Solid-State Chemistry of Pharmaceutical Co-Crystals, Amino Acids and other Materials

Thesis Submitted for
DOCTOR OF PHILOSOPHY

CARDIFF UNIVERSITY
December 2019

Okba Al Rahal

Abstract

This thesis reports structural and thermal properties of organic solids, focusing on pharmaceutical co-crystals and amino acids. Structural properties were determined primarily using state-of-the-art techniques for carrying out structure determination from powder X-ray diffraction (XRD) data, as well as using single-crystal XRD and solid-state NMR spectroscopy. Thermal properties were investigated using differential scanning calorimetry (DSC) and thermogravimetric analysis (TGA).

Chapter 1 gives background information on co-crystals and their applications, and the important topic of polymorphism is highlighted.

Chapter 2 discusses theoretical aspects of experimental techniques used in this thesis, including XRD (both single-crystal and powder XRD), solid-state NMR, DSC and TGA.

Chapter 3 describes the procedures for carrying out structure determination directly from powder XRD data, including details of the indexing, profile fitting, structure solution and structure refinement stages of the structure determination process. The use of periodic DFT-D calculations in conjunction with structure determination from powder XRD data is also discussed.

Chapter 4 explores structural properties, thermal properties and hydration-dehydration behaviour of two solid forms of the pharmaceutical co-crystal system (*S*)-ibuprofen:L-lysine. Interconversion between the two forms, which are anhydrous and monohydrate phases, is also established.

Chapter 5 reports structural and thermal properties of two solid forms of the pharmaceutical co-crystal system (*S*)-ibuprofen:L-proline. One form is an elusive anhydrous phase (obtained only once), while the other form is a quarter-hydrate that is obtained reproducibly. The dehydration behaviour of the quarter-hydrate form has been investigated.

Chapter 6 describes structural properties of a new polymorph of L-tryptophan prepared in this work, giving a detailed comparison to the structure of the previously reported polymorph. Periodic DFT-D calculations are used to assess the relative energetic properties of the two polymorphs.

Chapter 7 is focused on structural characterization of 1-iodoadamantane as a function of temperature, a material that exhibits complex phase transition behaviour.

Acknowledgments

None of the research reported in this thesis would have been possible without the help and support of many people. So I would like to thank all people who helped me during my PhD journey.

First of all, I would like to thank my supervisor, Professor Kenneth Harris for all of his support, advice, guidance and motivation he has given me during the course of my PhD. I would like to thank him for giving me the opportunity to be part of his research group and for the involvement in many projects during my PhD. I would also like to give special thanks to Dr Andrew Williams for all of his support and help. He was always ready to help.

I would also like to thank Dr Colan Hughes his help and Dr Benson Kariuki for recording single-crystal XRD data and for his help during my writing up period. My thanks also go to other members of Professor Harris research group, both past and present members, Yating Zhou, Rhian Patterson, and Christopher Smalley for their eagerness to help. It was an enjoyable and an unforgettable experience working with all of you.

I would like to thank Christopher Morgan for helping me in carrying out TGA experiments. I would also like to thank Dr David Apperley from School of Chemistry, Durham University for collecting solid-state NMR spectra. I am also grateful to Professor Simon Gaisford from School of Pharmacy, UCL for collecting DSC data of 1-iodoadamantane.

I am grateful to Diamond Light Source (beamline I11) and to UK National High Field Solid-State NMR Facility based at the University of Warwick.

Finally, I am grateful to Cardiff University and the Council for At-Risk Academics (CARA) for financial support.

Dedication

This thesis is dedicated to my parents (my father *Salah Al Rahal* and my mother *Mariam Al Rahal*) for all their prayers, encouragements, unconditional help and unlimited support. Without you, I would not be here. Thank you so much. I always tried to make you so proud.

To my dearest and soulmate wife (*Mariam Alamouri*) who has put every effort she could make to make the PhD journey easier for me. Without your help and unlimited assistance, none of this work would be possible. Thank you so much.

To my brothers and sisters: *Rouaa*, *Hafia*, *Allaa*, *Mohammad*, *Moawia*, *Haretha*, *Maen*, *Elham*, *Zahhra* and *Heba*. You are my best friends. I miss you and the old days' memories so much.

To my nephews and nieces: *Reem*, *Salam*, *Salah*, *Ryan*, *Sara*, *Amr* and *Ahmed*. I miss you so much.

Finally to the love of my life, to my heart and eyes, to my first baby which we expect to have on March. My sweet baby, I cannot wait to see you.

Table of Contents

List of Figures

List of Tables

Chapter 1: Introduction

1.1 Introduction to Co-crystals

In general, organic solid materials can be classified into two types: amorphous materials, where three dimensional (3D) long-range order is absent, and crystalline materials which exhibit 3D long-range order. The behaviour and physicochemical properties of solid materials are dependent on the presence or absence of the 3D long-range order, i.e. amorphous materials have different physicochemical properties from crystalline materials. For example, amorphous materials have higher solubility (see Section 1.2.1 for the definition of solubility) and higher dissolution rate than crystalline materials.[1] This could be advantageous in some cases such as fast-acting tablets in which the active pharmaceutical ingredient (API) needs to dissolve quickly so it can act fast. Examples of fast-acting tablets include painkiller tablets, where the painkiller should dissolve and act quickly to relieve pain. However, although amorphous materials can exhibit some advantages over crystalline materials, such as enhanced solubility and dissolution rate, the thermodynamic instability of amorphous materials is one of the biggest potential risks during the storage of these materials.[2-3] The thermodynamic instability of amorphous materials means that these materials might undergo crystallization to a more stable phase, leading to a fundamental change of the physicochemical properties. This can have a significant impact on the behaviour of solid materials.

By contrast, crystalline materials exhibit greater thermodynamic stability although some crystalline materials can undergo phase transitions as a function of temperature or time.[2] Although crystalline materials have higher thermodynamic stability than amorphous materials, these materials have lower solubility and lower dissolution rates compared to amorphous materials.[4] The target, therefore, is to enhance the physicochemical properties of solid materials whilst maintaining thermodynamic stability and thus maximizing their thermodynamic stability and behaviour. To achieve this target, co-crystals have the potential to modify the behaviour whilst conserving thermodynamic stability.

In spite of the fact that co-crystals have been studied for a long time, the definition is still a matter of debate. However, co-crystals can be broadly defined as materials that have two or more different molecules in the same crystal structure.[5-6]

Within the context of pharmaceutical applications, one molecule is usually called “the active molecule” and the other molecule is called “the co-former”. Co-crystals might also have solvent (e.g. water) molecules in the crystal structure, forming a solvate (hydrate) structure. This is due to the fact that the formation of co-crystals can involve crystallization from a solution which, in some cases, leads to the entrapment of solvent (water) molecules in the crystal structure of co-crystals, leading to co-crystal hydrates or co-crystal solvates. It should be noted that salt formation can be another way of improving the behaviour of solid materials. However, salt formation requires both the active material and the salt co-former to be ionizable. Due to the fact that a considerable number of active materials, particularly APIs, are not ionizable, salt formation is not feasible in many cases[7] and therefore co-crystal formation is a potential option for improving the behaviour of such materials.

Co-crystals have potential applications in many fields including pharmaceuticals, pigments and explosives. In the pharmaceutical context, it is well-known that a large number of APIs suffer from poor physicochemical properties including solubility and dissolution rates, leading to poor bioavailability and thus poor efficacy. In fact, APIs can be classified according to a bio-pharmaceutical classification system (BCS), which is based on two criteria: aqueous solubility and permeability.[8] This classification system is based on the fact that drugs have to dissolve in the gastrointestinal fluid (GI) and permeate through cell membranes to reach the site of action. Based on BCS, APIs can be classified into four classes. Class I involves materials with both high solubility and high permeability whereas class II involves materials with high permeability but low solubility. Class III has materials with low permeability and high solubility and class IV has materials with both low permeability and low solubility. It is clear that APIs in Class II and IV have significant challenges in formulating them in solid dosage forms such as tablets and capsules, given that they have low solubility. However, the co-crystal strategy can be a potential method to improve the behaviour of these materials and thus enhance their solubility, enabling the formulation of these materials as solid dosage forms. Introducing a new material, usually with high solubility, in the crystal structure of APIs leads to a new arrangement, consequently modifying the behaviour, leading to enhanced solubility and dissolution rate. It is important to note that in pharmaceutical co-crystals, the co-former molecule should be selected from the Generally Regarded As Safe “GRAS”

list.[9] Figure 1.1 shows a schematic diagram of a 1:1 pharmaceutical co-crystal, although these co-crystals can be formed in any stoichiometric ratio.

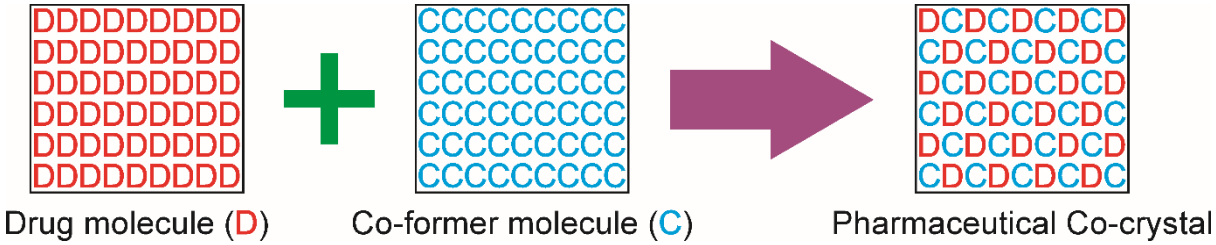

Figure 1.1. *A schematic diagram of a 1:1 pharmaceutical co-crystal.*

Given that co-crystals have to be in a stoichiometric ratio, the formation of co-crystalline materials is not always feasible. An alternative method of fine-tuning the physicochemical properties of solid materials is the formation of solid solutions. Solid solutions or molecular alloys can be defined as a sub-type of co-crystals in which one component is homogenously distributed within the crystal structure of another component.[10] These solid solutions, unlike co-crystals, are not restricted to a single stoichiometric ratio. In these systems, one atom/molecule is defined as an atomic/molecular solvent whereas the other atom/molecule is defined as an atomic/ molecular solute. The properties of the resulting material can be tailored by changing the ratio of the atomic/molecular solute to the atomic/molecular solvent. There are, in general, two types of solid solutions: substitutional solid solutions, where one atom/molecule is replaced or substituted with another of similar size and shape. The second type are interstitial solid solutions, where the atomic/molecular solute is much smaller and thus could fit within the interstitial spaces in the structures of the atomic/molecular solvent. Figure 1.2 shows a schematic diagram of these two types. An example of solid solutions, for which the structural properties have been reported, is the solid solutions of 3-chloro-*trans*-cinnamic acid (3-ClCA) and 3-bromo-*trans*-cinnamic acid (3-BrCA).[11]

1.2 Applications of Co-crystals

1.2.1 Solubility and Dissolution Rate

Solubility, the concentration of a solute which exists in equilibrium with a solid phase in a saturated solution at a specific temperature and pressure,[12] is an intrinsic property that plays a vital role in many fields. This definition of solubility refers to

thermodynamic solubility which can be measured by placing an excess amount of the solid solute in contact with the liquid at a specific temperature and pressure for enough time to reach the saturation state where the solid and solution are at equilibrium.

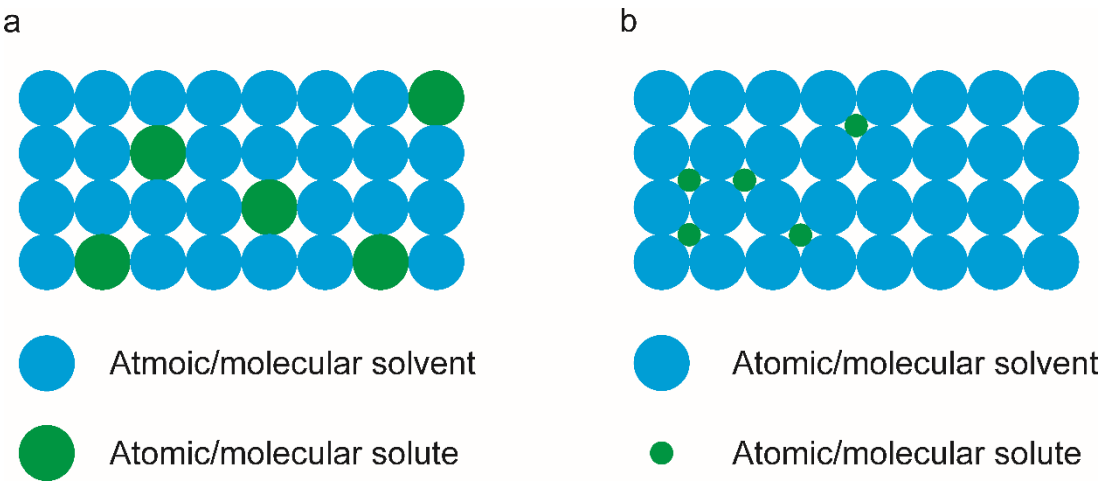

Figure 1.2. *A schematic diagram of (a) a substitutional solid solution, and (b) an interstitial solid solution.*

The co-crystal strategy can enhance the solubility and dissolution rate of APIs[13-14] and thus can increase their bioavailability.[15-16] However, it is worth noting that while co-crystals can improve the dissolution rate of APIs, there are some cases in which the formation of co-crystals leads to a lower dissolution rate. In fact, there are cases where high solubility means fast clearance of the API from the body and thus a higher number of doses is required to keep the drug concentration within therapeutic concentration. Decreasing the solubility is therefore desirable to reduce the clearance of API from the body and thus decrease the number of doses and increase patients' compliance. Examples of cases in which solubility is increased and decreased are now discussed.

The first example where co-crystallisation increases the solubility is the molecular drug resveratrol.[17] Resveratrol (Figure 1.3) has an anti-oxidant effect which can help the body to decrease free radicals and therefore decrease the risks of cancer and heart diseases. However, this drug molecule belongs to the BCS class II category,[18] meaning that it has a high permeability but low solubility. This makes it an attractive molecule for the co-crystal strategy to improve its solubility and therefore increase bioavailability and efficacy.

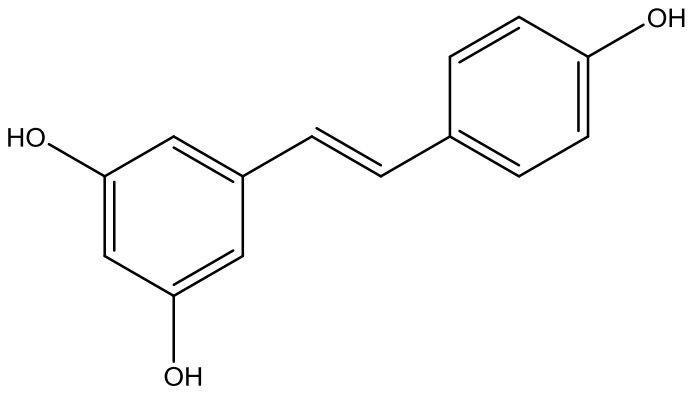

Figure 1.3. *The molecular structure of resveratrol.*

Two co-crystal forms have been reported[17] for this drug molecule and their physicochemical characterization has been carried out. One co-crystal was formed with 4-aminobenzamide, as a co-former, using liquid-assisted grinding whereas the other co-crystal was formed by rapid evaporation of an ethanolic solution containing resveratrol and isoniazid as a co-former. In the reported study, authors measured the solubility of both forms in different pH media and compared it with the solubility of the pure API. The authors found that both co-crystal forms have higher solubility than the pure API, with resveratrol:isoniazid co-crystals having the highest solubility. It is worth noting that the crystal structures of both co-crystal forms have not yet been reported.

Another example, where the co-crystal strategy has successfully been implemented in solubility enhancement, is the co-crystal formation of carbamazepine.[19-20] Carbamazepine (molecular structure; Figure 1.4) has been used as an anti-epilepsy drug for more than thirty years. However, its low solubility limits the bioavailability and efficacy of this drug. Moreover, its low solubility has a big impact on its therapeutic concentration leading to erratic concentration and consequently unstable therapeutic response. However, the solubility of this drug molecule has been effectively enhanced using the co-crystallization strategy.

It has been reported that carbamazepine can form many co-crystals with different co-formers giving the advantage of structural diversity.[19-20] For example, a one-dimensional hydrogen bonded chain-like structure has been formed by co-crystallizing carbamazepine with benzoquinone, terephthalaldehyde, 4,4′-bipyridine and nicotinamide.[19] Moreover, it has been reported that carbamazepine forms a co-crystal with saccharin using supercritical CO_2 as

anti-solvent and that two polymorphs of this system have been reported.[21] This example shows how co-crystals can provide a potential chance for improving the diversity[22] of solid state forms of a specific API and thus can enhance the patentability[23] (for the discussion of patentability, see Section 1.2.3).

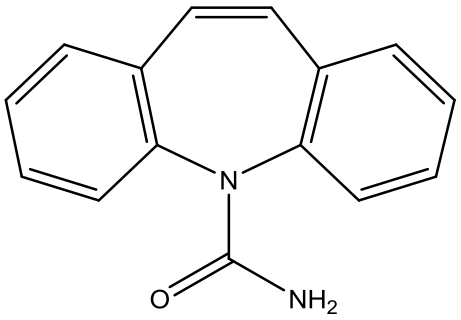

Figure 1.4. *The molecular structure of carbamazepine.*

Although co-crystals can enhance the solubility and dissolution rate in many APIs, it has been reported that co-crystals can decrease the dissolution rate in some APIs. For example, ribavirin (Figure 1.5) is an anti-viral drug with very high solubility in water.[24]

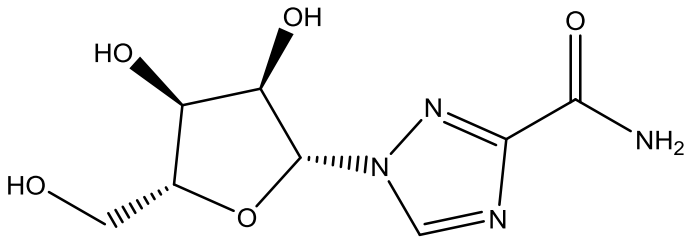

Figure 1.5. *The molecular structure of ribavirin.*

The high solubility leads to erratic peak-trough concentration in the body. It can also lead to fast clearance from the body; thus a high number of doses is required to maintain drug concentration within the therapeutic range. This in turn can cause undesirable side effects as a result of high concentration at the time of release. Reducing the dissolution rate of this drug can decrease the drug concentration at the time of release, thus minimizing the side effects and obtaining an optimized drug release with a lower number of doses.

The co-crystallization strategy has successfully been implemented to decrease the dissolution rate of ribavirin.[24] Three co-crystals of ribavirin with

3,5-dihydroxybenzoic acid (**I**), gallic acid (**II**) and barbituric acid (**III**) were prepared and the dissolution rate was compared.[24] The crystal structure of all co-crystals was determined by single-crystal X-ray diffraction.[24] The crystal structure of **I** contains sheets of 3,5-dihydroxybenzoic acid molecules hydrogen bonded with each other forming a channel where the ribavirin molecule lies in a chain-like fashion and hydrogen bonds with the 3,5-dihyroxybenzoic acid molecules. The crystal structure of **II** is shown to be a sheet like structure where ribavirin molecules are hydrogen bonded with gallic acid molecules *via* O−H···N and O−H···O bonds. The crystal structure of **III** consists of a one-dimensional hydrogen bonding arrangement sustained by N− H···O and O− H···O interactions. The dissolution rate of pure ribavirin was compared to the dissolution rate of the three co-crystals and it was shown that the pure drug has a higher dissolution rate compared to the co-crystal forms, meaning that the co-crystal strategy was effective in reducing the rate of drug release.[24] It was reported that co-crystal **I** has the lowest dissolution rate.[24]

1.2.2 Stability

The stability of an API is crucial to ensure that it is effective and safe for the shelf-life period. An API has to be chemically, physically, hygroscopically and thermodynamically stable. The co-crystal strategy can potentially increase the stability of APIs, leading to an optimum therapeutic efficacy. In this section, examples illustrating improvement of stability using the co-crystal strategy are given.

The first example concerns the chemical stability of the bioactive agent andrographolide (AP; molecular structure, Figure 1.6). AP is an herbal medicine with anti-viral, anti-inflammatory, anti-cancer and anti-malarial effects.[25] However, this drug molecule suffers from poor bioavailability due to the chemical instability as it transforms to the metabolite 14-deoxy-12-(R)-sulfoandrographolide (AP–SO_3H), leading to a big decrease in bioavailability.[26] To overcome the chemical instability and increase the bioavailability of this drug molecule, the co-crystal strategy has been implemented successfully.[27] Several co-formers such as vanillin (VAN), vanillic acid (VLA), salicylic acid (SLA), resorcinol (RES), and guaiacol (GUL) were used in co-crystal preparation.

To assess the chemical stability, the AP co-crystals were treated in similar conditions to the reaction that leads to the conversion of AP to AP-SO_3H. The authors

found that AP-SLA co-crystals had the highest chemical stability as no AP-SO_3H could be detected.[27] They argued that the carboxylic acid functional group of SLA inhibits the nucleophilic addition of the bisulfite ion (HSO_3^-), improving the chemical stability and consequently the bioavailability.[27]

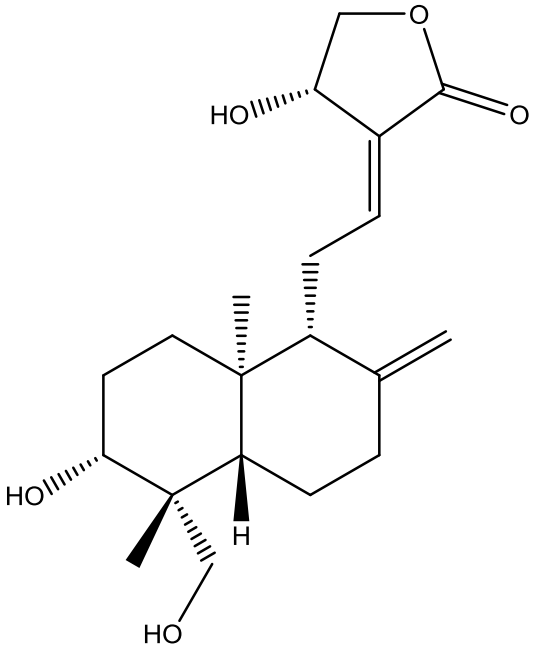

Figure 1.6. *The molecular structure of AP.*

The co-crystal strategy can also improve the hygroscopic stability of APIs. For example, oxiracetam (ox; molecular structure, Figure 1.7), an API used to treat cognitive disorders, is a chiral molecule with the (*S*) enantiomer having higher biological activity. However, the pure (*S*) enantiomer is very hygroscopic and it deliquesces completely to a liquid form at 87% relative humidity and ambient temperature within three days.[28] It has been reported that the hygroscopic stability of this drug molecule can be enhanced by forming co-crystals with many co-formers.[28]

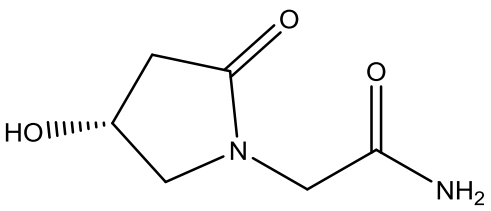

Figure 1.7. *The molecular structure of oxiracetam.*

In particular, gallic acid (ga) and 3,4-dihydroxybenzoic acid (dhba) were used as co-formers. The crystal structure of ox:ga (Figure 1.8a) is observed to be a sheet-like structure with O–H···O and N–H···O hydrogen bonds. The crystal structure of ox:dhba (Figure 1.8b) can also be described as a chain-like structure, again with O–H···O and N–H···O hydrogen bonds. The hygroscopic stability of both co-crystals was evaluated at different relative humidity conditions (43, 75, 85 and 98%). Both co-crystals showed higher hygroscopic stability than the pure (*S*) enantiomer with ox:ga having the highest hygroscopic stability.[28] Gallic acid has three hydroxyl groups whereas 3,4-dihydroxybenzoic acid has two hydroxyl groups. This means that gallic acid can form an additional hydrogen bond leading to stabilization of the hydrogen bond receptors of oxiracetam, preventing them from forming hydrogen bonds with water and consequently increasing its hygroscopic stability.[28]

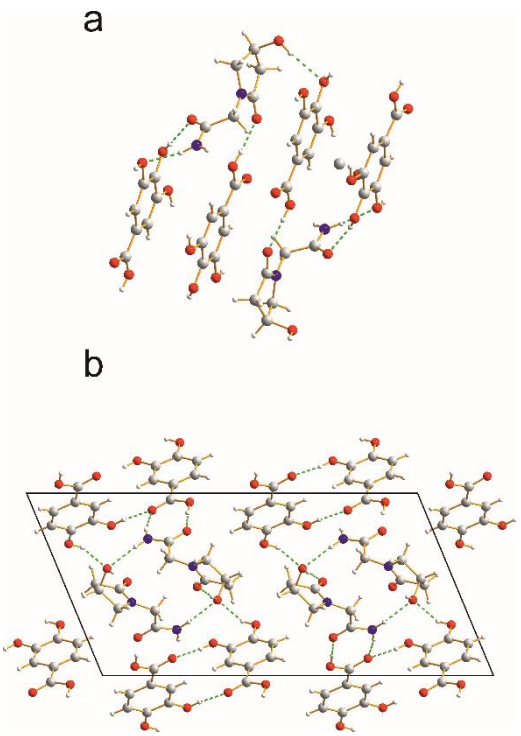

Figure 1.8. *The crystal structures of (a) ox:ga, (b) ox:dhba.*

In another study, Zaworotko *et al.*, investigated the hygroscopic stability of lithium chloride compared to the ionic co-crystals of lithium chloride with *a*-D-glucose at different relative humidities.[29] Lithium chloride is used in the treatment of bi-polar disorder.[30-31] Although this API is the drug of choice for treating bi-polar disorder, it suffers from poor hygroscopic stability as it deliquesces rapidly at low relative humidity (11.30%). This hygroscopic instability has a big impact on the storage

conditions and manufacturing procedures of the final dosage forms of lithium chloride. The study found that the ionic co-crystals are more stable up to a relative humidity of 40%.[29] However, at a higher relative humidity, the ionic co-crystals gained weight dramatically, meaning that the stability is lower when the relative humidity increases. These results are important in determining the correct storage conditions for the final products which contain lithium chloride as an API.[29]

Theophylline (Figure 1.9), used in the treatment of chronic obstructive pulmonary diseases such as asthma,[32] has low hygroscopic stability as the anhydrous phase can take up water and convert to the monohydrate form.[33-44] This hygroscopic instability has a big impact as the anhydrous phase has different physicochemical properties from the monohydrate phase. Controlling the hygroscopic stability is therefore vital to ensure that variability does not occur between different batches. The co-crystal strategy offers a potential solution as Jones *et al.*, have shown.[45] Their study was carried out using many co-formers to prepare co-crystals with theophylline, including dicarboxylic acids such as oxalic, malonic, maleic and glutaric acids. The molar ratio of all co-crystal was 1:1 except for oxalic acid where the molar ratio was 2:1. The authors determined the crystal structure of each co-crystal and studied the stability as a function of time and relative humidity.[45]

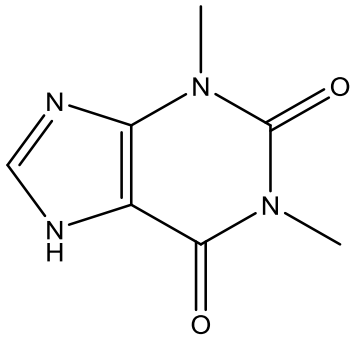

Figure 1.9. *The molecular structure of theophylline.*

The crystal structure of theophylline:oxalic acid (Figure 1.10a) consists of hydrogen bonded ribbons, where molecules of theophylline are hydrogen bonded to form dimers which are hydrogen bonded to oxalic acid. The crystal structure of theophylline:malonic acid (Figure 1.10b) is a chain-like structure where two molecules of theophylline are hydrogen bonded via N−H···O interactions, forming a dimer. Two molecules of malonic acid, which are hydrogen bonded by O−H···O,

connect the dimers of theophylline molecules by O − H···N hydrogen bonding, confirming the ratio of 1:1 of the co-crystals. The crystal structure of the theophylline:maleic acid co-crystal (Figure 1.10c) is also sustained by theophylline dimers (via N–H···O hydrogen bonding) which are hydrogen bonded to two molecules of maleic acid via O–H···N hydrogen bonding and again confirming the 1:1 ratio of the co-crystal. The crystal structure of the theophylline:glutaric acid co-crystal (Figure 1.10d) is a sheet-like structure sustained by the dimerization of theophylline molecules (*via* N− H···O hydrogen bonding) which are hydrogen bonded to glutaric acid molecules *via* O–H···N hydrogen bonding.

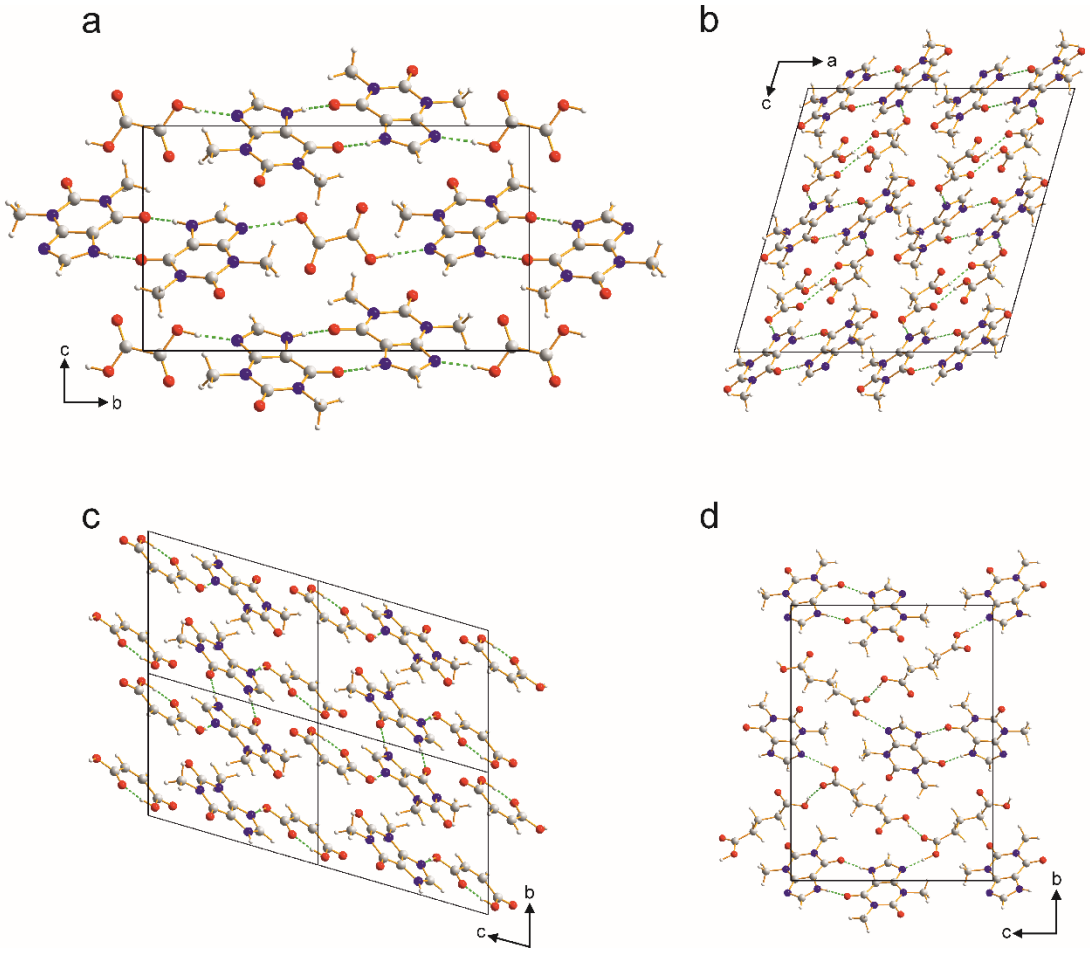

Figure 1.10. *The crystal structures of (a) theophylline:oxalic acid, (b) theophylline:malonic acid, (c) theophylline:maliec acid, (d) theophylline:glutaric acid.*

The hygroscopic stability of all theophylline co-crystals was compared to the hygroscopic stability of pure anhydrous theophylline as a function of both time and relative humidity.[45] The hygroscopic stability was assessed at different time intervals

between 1 day and 7 weeks. The stability was also assessed at different relative humidities. Although anhydrous theophylline showed hygroscopic stability up to 75% for 7 weeks, it transforms to the monohydrate form at 98%.[45] In comparison, the co-crystal of theophylline with oxalic acid was stable at high relative humidity for 7 weeks, offering a potential way to increase the hygroscopic stability of theophylline.

1.2.3 Patentability

The application of co-crystals is not limited to solubility and stability enhancement since this strategy can also play a role in patentability regulations. Patentability plays an important role as it allows for the extension of the life of a product in the market. Although the term patentable can refer to "anything under the sun that is made by man",[23] a patent will be eligible if it meets three criteria: novelty, utility and non-obviousness.[23] With regard to the first criterion, the co-crystal strategy can provide new solid-state modifications, which, in theory, exceeds the number of modifications offered by salt formation as the number of co-formers for co-crystal formation is much higher than the number of counter-ions for salt formation. With regard to the second criterion, the co-crystal strategy can improve physicochemical properties of solid materials, such as solubility and dissolution rate, making them of great utility in industrial applications. The non-obviousness criterion here can be interpreted analogously to the term "non-predictable", meaning that it is not feasible to predict the outcome of a co-crystallization experiment. This is due to the fact that many factors, including kinetics and thermodynamics, play a role in co-crystal formation, leading to difficulties in the prediction of, for example, the formation of a pure co-crystal phase rather than a mixture of phases from starting materials. In fact, the prediction of co-crystal formation involves the assumption that their constituents will interact favourably, meaning that the heterointeraction between the active molecule and the co-former must be higher than the homointeractions of active–active or co-former–co-former interactions. In addition, the prediction of a crystal structure of a co-crystal is challenging. In the light of these criteria, the co-crystal strategy meets all requirements to patentability and therefore can be an alternative way of extending the patentability.

1.3 Co-crystal Design and Preparation

In spite of the fact that co-crystals are often prepared based on a trial and error method, there are many strategies that help to design co-crystals in a rational way. For example, when an active molecule has specific functional groups, molecules with complementary functional groups, which have the ability to form hydrogen bonds with the active molecule, can be tested as co-formers.[46-47] Although this method might work for some materials, many geometric factors play an important role in the possibility of formation of hydrogen bonding between a specific donor and a specific acceptor.

Once a suitable co-former has been selected, the next stage is the preparation of co-crystalline materials. The preparation of co-crystalline materials can be carried out by solvent-based methods or non-solvent-based methods. While non-solvent-based methods lead intrinsically to samples with polycrystalline nature unsuitable for single-crystal X-ray diffraction (XRD),[48] solvent-based methods have the potential to give single crystals of sufficient size and quality for single-crystal XRD. However, many thermodynamic and kinetic factors play a vital role in co-crystallization, which can lead to polycrystalline samples rather than single crystals. In addition, it is not uncommon to obtain pure phases of the co-crystal components or a mixture of the pure phases with co-crystals rather than pure co-crystals using the solvent-based methods. In fact, solubility differences between the starting materials can have a big impact, as the component with the lower solubility will crystallize out first, leading to a mixture of the pure phases of the individual components rather than co-crystals.[49] By contrast, non-solvent-based methods such as neat grinding and liquid-assisted grinding (LAG) offer a potential way to prepare new co-crystals with no solvent or with a minimum amount of solvent, making it a more environmentally-friendly way of preparing new co-crystals. Solvent-based methods such as crystallization by cooling, crystallization by evaporation, anti-solvent methods and slurry crystallization, and non-solvent-based methods such as neat grinding, LAG, crystallization from the liquid phase (following melting) and crystallization from the gas phase (following sublimation) are discussed in more detail in the next sections.

1.3.1 Solvent-based Methods

The principle of solvent-based methods involves starting from a saturated or a supersaturated solution and gradually or immediately decreasing the solubility (in cooling) or increasing the concentration (in evaporation), leading to the growth of crystals. Upon decreasing solubility or increasing the concentration, a number of molecules gather to form nuclei in a process called nucleation[50] which is then followed by crystal growth where further molecules attach to the nuclei forming crystals.[50] There are many ways of achieving this principle. The cooling method of crystallization (Figure 1.11),[51] for example, can lead to the growth of a single crystal with a suitable size and quality for single-crystal XRD.

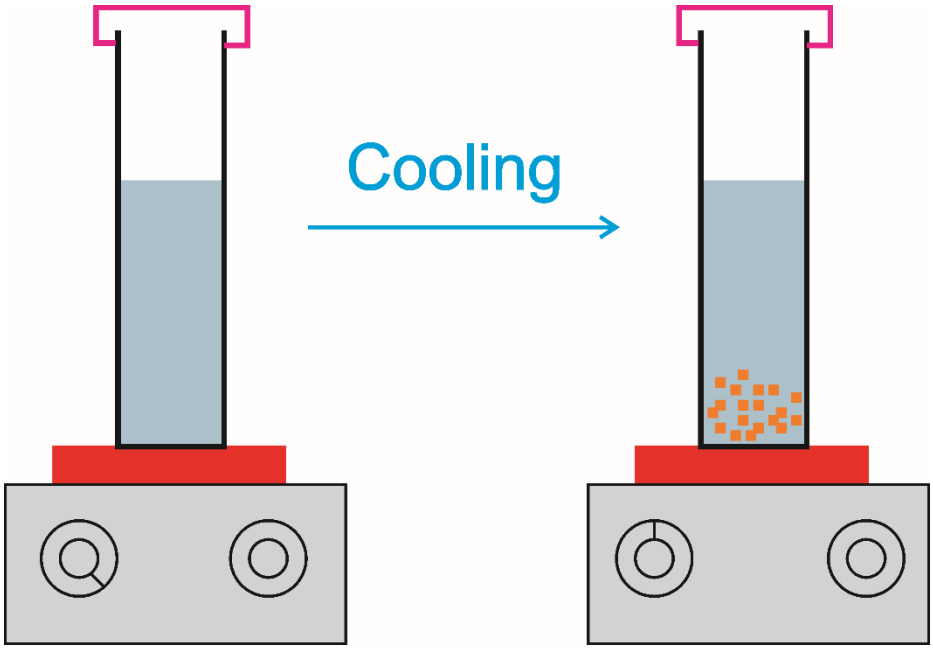

Figure 1.11. *A schematic diagram of crystallization by cooling.*

This method involves dissolving the constituents of a co-crystal in one solvent or a mixture of solvents at high temperature and then cooling down to obtain co-crystals. As the solubility of most materials decreases with lowering temperature, cooling down the hot solution leads to a decrease in solubility and thus crystallizing out co-crystals when the concertation of the solution matches the solubility. However, many factors have an important role and it is important to control these factors to obtain good quality crystals. For example, the cooling rate and the state of solution, whether it is a saturated or a supersaturated solution, may have a significant impact on the outcome. In comparison to crystallization of one component by cooling, the

crystallization of multi-component systems can be more complicated. This is because the two components may have different solubilities with respect to temperature and therefore one component might crystallize before the other when temperature decreases. As in all crystallization experiments, care must be taken that containers are clean, as any impurity present in the solution might act as a seed and trigger unwanted crystallizations.

Another method of solvent-based crystallization is the evaporation method (Figure 1.12).[52] It involves increasing the concentration of a sample in a solution by evaporation of the solvent. Although this method might work well for the crystallization of one-component materials, crystallization of multi-components materials might be more complicated. This is due to the fact that adding a new component to the solution can result in a change of solubility.

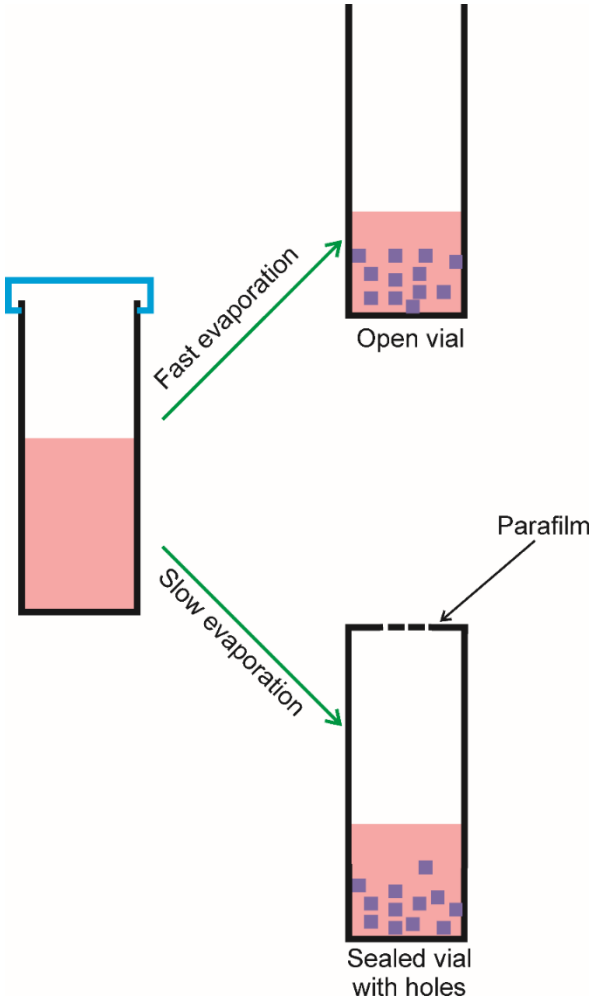

Figure 1.12. *A schematic diagram of crystallization by evaporation.*

The rate of evaporation plays an important role in determining whether a single crystal or a polycrystalline sample will be obtained.[52] The rate of evaporation can be varied either by leaving the vial, which contains the solution to be evaporated, open or by sealing it with parafilm and making a few holes in the parafilm. It is good practice to collect crystals before evaporating the whole solvent to avoid contamination with impurities or staring materials.

The anti-solvent method[53] (Figure 1.13) can also be used to grow single crystals even though it is not convenient for industrial applications. This method involves dissolving materials in one solvent and then decreasing the solubility by adding another miscible solvent, which is called anti-solvent. The solubility of materials in the anti-solvent should be low, allowing the materials to crystallize. This method can be applied either by fast addition of the anti-solvent or by slow diffusion of the anti-solvent into the main solvent.[54]

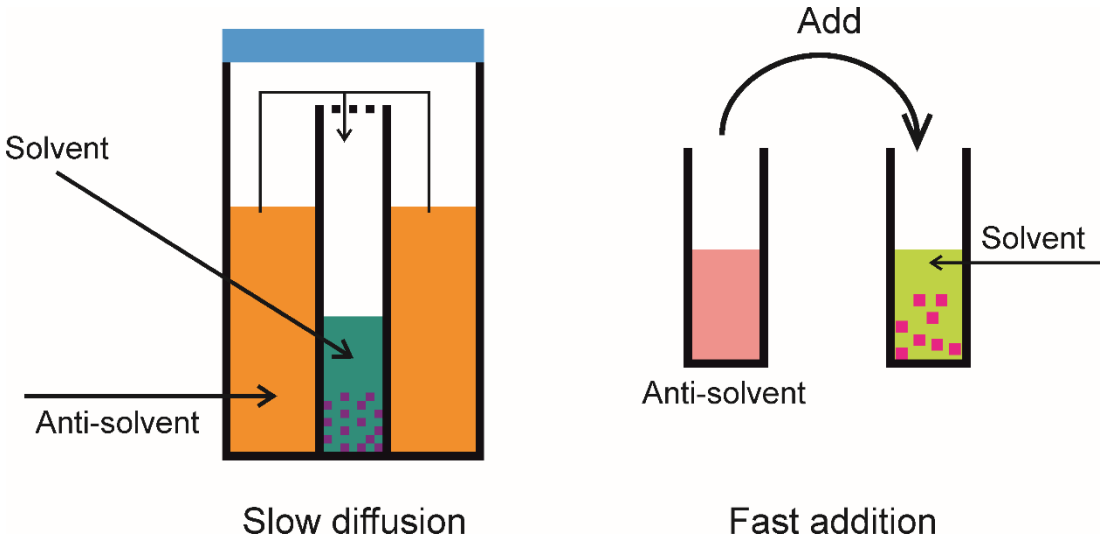

Figure 1.13. *A schematic diagram of crystallization by anti-solvent.*

Slurry crystallization is another potential solvent-based method to prepare co-crystals.[55] In this method, the constituents of a co-crystal are not dissolved but are dispersed in a solvent to form a slurry which is then dried to form final co-crystals. Dispersing the constituents in the slurry means that these constituents are supersaturated with respect to co-crystals, leading to the transformation of the individual components to co-crystals.[56] This method can overcome the problem of poor solubility of co-crystal constituents and their solubility differences. It has been reported that some co-crystals were prepared by this method.[57] In addition, this

method is used to study the stability of co-crystals as co-crystals tend to dissociate into their individual components upon dissolving in dissolution mediums.[58] It can also be used to investigate the stability of different polymorphs as a less stable polymorph transforms to a more stable polymorph in slurry experiments.

1.3.2 Non-solvent-based Methods

Neat grinding, which is usually carried out using a ball mill or planetary mill, uses mechanical energy, supplied by a number of metallic balls colliding with the samples of the pure solid phases of the individual components, inside a tightly-sealed jar.[48] In this method, the constituents of a co-crystal are weighed in a stoichiometric ratio and placed in a jar with a number of balls. The jar is then shaken, in a ball miller, or rotated, in a planetary miller, for a specific time at a predetermined frequency. The amount of mechanical energy needed to prepare co-crystals (the time of shaking or rotation and the frequency of shaking or rotation) can be varied depending on many factors such as the hardness of the constituents, their elasticity and plasticity and the stability of individual components relative to the stability of the final co-crystals.[48] Neat grinding can overcome the problem of poor solubility of constituents and the problem of solubility differences between the constituents of a co-crystal since there is no solvent involved. Moreover, as this method does not use solvents, it is a clean way to prepare new co-crystals even though it is inherently restricted to producing polycrystalline samples rather than single crystals.[48] It is worth noting that in this method the miscibility between starting materials has to be guaranteed during shaking or rotation time as grinding might lead to fine powders which can be segregated if the particle size difference is substantial.[48] It is therefore recommended, in some cases, to grind the components separately before preparing the co-crystals, to ensure that they have similar particle size, which will maximize the efficiency of mixing during shaking or rotation time.[48]

LAG is another non-solvent-based method to prepare co-crystalline materials.[48] In this method, the constituents are ground in a jar with a number of balls with a small amount of a liquid added; hence the name liquid-assisted grinding. The small amount of the liquid added in LAG experiments can increase the rate of co-crystallization as it can increase the mobility of molecules. Similar to neat grinding, a number of factors need to be controlled, such as the time of shaking or rotation, the frequency of shaking

or rotation, the number of balls and the volume of jars (as enough space for mixing materials during shaking or rotation should be used). In addition, the amount of liquid and the type of liquid can have a critical impact on the resulting crystalline phase due to the fact that using different liquids or using different amounts of the same liquid might lead to different polymorphs.[59] Jones *et al.*, showed that caffeine:anthranilic acid co-crystals exhibit polymorphism (polymorphism is discussed in Section 1.4), when prepared by LAG, by changing the amount of liquid and the type of liquid used.[59] They showed that form **I** of caffeine:anthranilic acid was obtained by neat grinding whereas form **II** was obtained when acetonitrile and/or ethylene glycol were used as liquids in LAG.[59] Form **III** of the co-crystals was obtained when 10 µ1 of 1-hexanol and/or 1-octanol and/or 1-dodecanol and/or ethyl acetate and/or 1,4-dioxan were used as liquids in LAG.[59] However, increasing the amount of 1-hexanol from 10 µl to 30 µl gave form **I** whereas increasing the amount of 1-octanol above 10 µl gave a mixture of form **I** and **III**.[59] When 1-dodecanol was increased from 10 µl to 20 µl and 30 µl, form **II** was obtained.[59] However, increasing the amount of 1-dodecanol above 30 µl gave form **I**.[59] These results clearly prove that the amount of liquid and the type of liquids can have a great impact on the purity and type of polymorphs obtained by LAG experiments.

Crystallization from the liquid phase following melting is another non-solvent-based method of preparing crystals, including co-crystals. In this method, if the melting point difference between the pure components is large, the component with higher melting point is melted and the other component is then added to the molten state while it is cooling down, at a temperature below the decomposition temperature.[60] Another way of preparing co-crystals is to melt both components together, in cases where the melting points of the two components is close to each other, and then leaving them to cool and crystallize. Controlling the cooling rate of molten states is important, as rapid cooling might result in a metastable phase rather than the most stable phase which is usually obtained by allowing the molten state to cool over a long period of time. Care must be taken not to increase the temperature to the decomposition point.

The last method of non-solvent-based methods described here is crystallization from the gas phase following sublimation. Sublimation is the transition of materials from a solid state to a gaseous state without passing through a liquid state.[61]

Sublimation is usually carried out under vacuum where the sample of interest is placed inside a sublimation apparatus which is then connected to a source of vacuum. Carrying out sublimation experiments under vacuum allows the material to transform from a solid state to a gaseous state at a lower temperature. Molecules from the gaseous state are deposited on a cold surface (usually a cold finger), which is kept cold by adding a mixture of acetone with dry ice, for example. It is worth noting here that changing the cold surface might lead to different polymorphs.[62-63] This can be useful as it provides a way to control polymorphism where the polymorph with desirable structural and physicochemical properties may be formed. Figure 1.14 shows a schematic diagram of a sublimation apparatus used during the course of the work described in this dissertation.

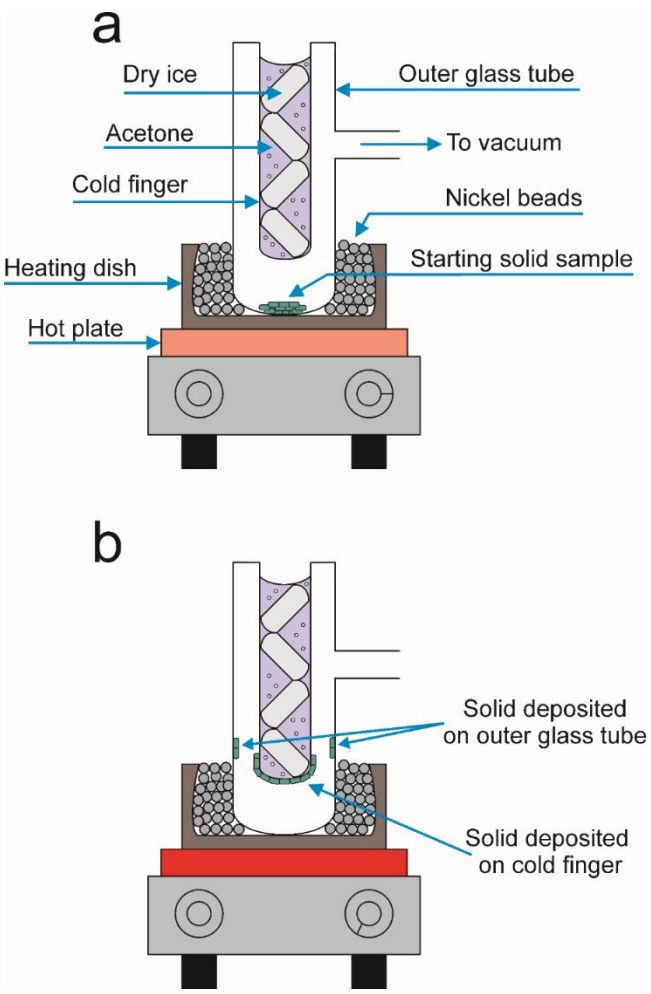

Figure 1.14. *A schematic diagram of a sublimation apparatus used for crystallization from the gas phase in this dissertation: (a) before sublimation, (b) after sublimation.*

Crystallization from the gas phase following sublimation has been used to prepare co-crystals of many materials, offering a potential way of obtaining new co-crystals, which might not be accessible by other crystallization methods. For example, Szell *et al.*[64] investigated the formation of halogen-bonded co-crystals using four halogen-bond donors (I_2, 1,4-diiodobenzene, 1,4-diiodotetrafluorobenzene, and 1,3,5-trifluoro-2,4,6-triiodobenzene) and four halogen-bond acceptors (2,3,5,6-tetramethylpyrazine, 1,4-diazabicyclo[2.2.2]octane, 2,2'-bipyridyl, and 1-adamantanecarbonitrile) through different crystallization methods including evaporation and co-sublimation. The authors found that the co-sublimation method is a relatively fast method for obtaining single crystals of sufficient size and quality for single-crystal XRD. Furthermore, it was reported that the co-crystal of 1,3,5-trifluoro-2,4,6-triiodobenzene with 1,4-diazabicyclo[2.2.2]octane is only accessible by the co-sublimation method.

Crystallization from the gas phase following sublimation has also been used to obtain new polymorphs of different materials by controlling factors which affect the sublimation experiment. Controlling the sublimation temperature, for example, was the key to obtain a new polymorph of 5-methoxy-salicylaldhyde azine.[65] In another study, the surface of the cold template, where solid materials are deposited, has been a key factor that leads to different polymorphs.[62] In the reported study, the control of polymorphism of carbamazepine (five polymorphs), metaxalone (two polymorphs), mefenamic acid (two polymorphs), paracetamol (two polymorphs), and ortho-, meta- and para-amino benzoic acids (one, four, and two polymorphs respectively) was carried out by controlling the type of surface of the cold template.[62]

1.4 Polymorphism

Polymorphism is the ability of a given material to crystallize in more than one crystal structure.[66] Given the fact that physicochemical properties of solid materials are determined by the arrangement of molecules in the crystal structure, different polymorphs have different physicochemical properties. The phenomenon of polymorphism might be advantageous in some cases but might be disadvantageous in others. It might be advantageous in cases where it allows, in principle, for a direct comparison of physicochemical properties between different polymorphs, allowing structure-property relationship to be established, and subsequently the prediction of

bulk properties depending on the arrangement of molecules in the crystal structure.[67-68] However, it might be disadvantageous in other cases, particularly for pharmaceuticals, where a specific amount of the API has to dissolve to reach the therapeutic concentration. Given the fact that different polymorphs have different solubilities, it is essential to use the "right" polymorph which gives a high enough concentration of API. However, during storage time, polymorphs can undergo phase transformations,[69] usually to the most stable form, leading to many problems with the formulation or with the solubility and bioavailability of APIs. More importantly, polymorphism can have a critical effect in the case of pharmaceuticals with a narrow therapeutic index (TI). TI is a quantitative measurement that relates the effective concentration and toxic concentration of an API.[70] If the margin between therapeutic and toxic concentrations of an API is relatively wide, the API is considered safe. Pharmaceuticals with a narrow TI have to dissolve to a specific amount so that the therapeutic concentration is reached but the toxic concentration is avoided.

There are different types of polymorphism. For example, molecular polymorphism refers to the situation where different polymorphs of a molecule have similar molecular structure but different crystal structure, i.e. different conformational arrangements of molecules in the crystal structure as a result of differences in the relative orientation of flexible functional groups. Disordered-ordered polymorphism can be observed in rotator phases such as 1-haloadamantanes (halo = fluorine, chlorine, bromine and iodine) where these phases undergo phase transformation upon cooling and/or heating. These materials[71] show positional order but orientational disorder upon crystallization from the liquid phase to the solid phase, meaning that they retain some properties (the orientational disorder) of the liquid phase. These materials usually show a high symmetry phase at high temperature and lower symmetry phases at lower temperature. This is due to the fact that, on cooling, the motion of the rotator phases could be frozen out, leading to more orientationally ordered phases even though some of the rotator phases may persist at very low temperatures.

Polymorphism can play an important role in the regulation and patentability of materials, particularly in pharmaceutical applications. The most famous example here is the case of ranitidine hydrochloride, which has the trade mark name "Zantac", made and marketed by GSK. GSK made form **I** of ranitidine hydrochloride in 1978 and

applied for a patent for this polymorph so no generic products could be produced. When the patent of this drug molecule was about to expire, GSK made another form of this drug molecule, called form **II**, and applied to extend the patentability. When the patent of form **I** expired, generic companies including Novapharm started producing the product according to a procedure described by GSK to produce form **I**. However, instead of producing form **I**, they produced form **II** which was protected by the new patent. Several repeats of the procedure to produce form **I** gave form **II** and Novapharm claimed that GSK produced form **II** originally in their first patent. GSK argued that Novapharm had produced form **II** because of the seeding effect of form **II**. They provided form **I** again, demonstrating that form **I** can be prepared in a pure form. Other researchers from independent institutions repeated the procedure that produces form **I** and obtained form **I** three times. These results led GSK to prevent Novapharm from producing form **II** of ranitidine hydrochloride before the expiry of its patent.[72]

Another example where polymorphism can play a critical role in the manufacturing process of pharmaceuticals is ritonavir.[73] Ritonavir is an anti-viral drug marketed by Abbot in 1996 to treat Acquired Immune Deficiency Syndrome (AIDS). Due to the fact that this drug molecule exhibits low solubility and low dissolution rate, the original form, denoted as form **I**, was formulated in a semi-solid gel. However, one of the subsequent batches failed the dissolution test and further examination revealed that the new batch was actually a new polymorph of ritonavir.[73] This new form, denoted as form **II**, showed lower solubility and lower dissolution rate and trials to reproduce form **I** led to the formation of form **II,** which had not passed the dissolution test. This failure led to the recall of ritonavir from the market.

As mentioned before, thermodynamic stability of different polymorphs plays an essential role as polymorphs can transform from a metastable phase to a more stable phase over time, leading to different physicochemical properties. It is therefore very important to understand the polymorphic behaviour of the system of interest to establish the most stable polymorph. The polymorphic behaviour in a specific system can be classified into two types: monotropic and enantiotropic.[74] In monotropic systems, the thermodynamic transition point (a point where the two polymorphs coexist at equilibrium) is always higher than the melting point of the lower melting polymorph (Figure 1.15a). The monotropic polymorphic transformation is

irreversible, meaning that once the least stable polymorph has been transformed to the most stable polymorph, the transformation cannot occur in the reverse direction. In enantiotropic systems, the thermodynamic transition point is below the melting point of the lower melting polymorph (Figure 1.15b). The polymorphic transition in enantiotropic systems is thermodynamically reversible, meaning that one polymorph could transform to another polymorph, and *vice versa*, on cooling or heating. The heat of fusion $\Delta_{fus}(H)$ rule is a good indicator of the behaviour of a polymorphic system. If the polymorphic system is monotropic, the form with higher melting point will have higher heat of fusion. If, on the other hand, the polymorphic system is enantiotropic, the form with higher melting point will have lower heat of fusion.

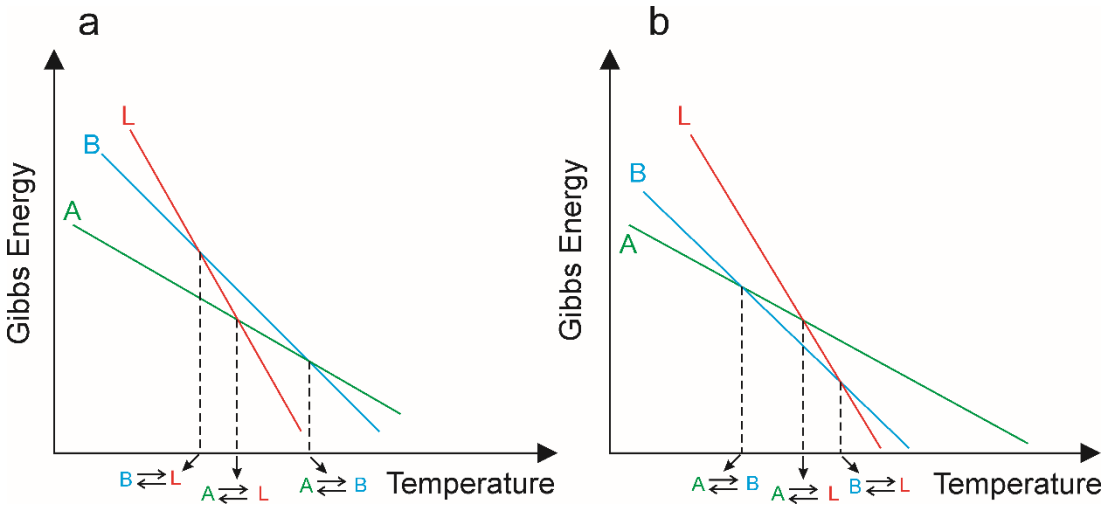

Figure 1.15. *(**a**) Monotropic behaviour, (**b**) enantoitropic behaviour, in polymorphic systems. A and B are solid phases, L is liquid phase.*

1.5 Aims of the Project

One of the aims of this project was to explore the structural properties of pharmaceutical co-crystals using modern techniques for structure determination from powder X-ray diffraction (XRD) data. Two pharmaceutical co-crystal systems were prepared and the structural and thermal properties of each system were determined using powder XRD, differential scanning calorimetry (DSC), thermogravimetric analysis (TGA) and solid-state nuclear magnetic resonance spectroscopy (SSNMR). In particular, (*S*)-ibuprofen, the biologically active enantiomer of the pain killer, has the potential to form many co-crystals with different amino acids. The two pharmaceutical co-crystal systems studied in this project are (*S*)-ibuprofen:L-lysine

and (*S*)-ibuprofen:L-proline. In these systems, the possibility to form hydrous and anhydrous phases was investigated using the analytical techniques mentioned above.

Given the importance of polymorphism in many fields, another aim of this project was to study polymorphism of amino acids. Amino acids are the building blocks for functional proteins; hence, they play an important role in biological systems. Of the 20 directly encoded proteinogenic amino acids, L-tryptophan plays an important role in cognitive disorders. Furthermore, the crystal structure of this amino acid has been reported to be remarkably complex with 16 molecules in the asymmetric unit. The aim of this project was to screen for new polymorphs for this important amino acid and then explore the structural properties using powder XRD data. Different crystallization methods were used for the screening of new polymorphs of this amino acid and structure determination of new polymorph prepared by crystallization from the gas phase was carried out from powder XRD data.

The polymorphic behaviour was studied for another molecular organic solid, i.e. 1-iodoadamantane (1-IA). 1-IA has been reported as a rotator phase. Given that rotator phases show multiple phase transitions upon cooling, as a result of the fact that the motion of the rotator phases are frozen out leading to a more ordered phase, the behaviour of this molecule as a function of temperature was studied using different analytical techniques including powder XRD, single-crystal XRD and DSC.

Chapter 2: Experimental Methods

Many analytical techniques can be used in structural and thermal characterization of crystalline and co-crystalline solid materials. For structural characterization, two of the main and most powerful techniques in structural characterization, X-ray Diffraction (XRD) and Solid-State Nuclear Magnetic Resonance (SSNMR) spectroscopy, are described. For thermal characterization, thermal analysis techniques (such as Differential Scanning Calorimetry DSC and ThermoGravimetric Analysis TGA) are the most common techniques. During the course of this research, single-crystal XRD, powder XRD, SSNMR, DSC and TGA were used in structural and thermal characterization of different solid materials prepared. These techniques are discussed in more details in this chapter.

2.1 X-ray Diffraction (XRD)

Since the discovery of X-rays in 1895 by the German physicist Wilhelm Conrad Roentgen,[75] this type of radiation has found a wide range of applications in the field of solid-state characterization, particularly for crystalline materials. For example, powder XRD can be used in the identification (fingerprinting) of crystalline materials due to the fact that different crystalline phases have different arrangements of atoms/molecules in their crystal structures and thus will have a unique powder XRD pattern when exposed to X-rays. In addition, diffraction techniques are the definitive way to confirm whether a solid material exists in a crystalline state or in an amorphous state. This is due to the fact that, unlike crystalline phases, amorphous materials do not give sharp peaks by diffraction techniques as a result of the fact that they do not have long-range order.[76] Another application of diffraction techniques is the study of the stability of crystalline phases as a function of external stimuli such as relative humidity, temperature or pressure. Such studies are carried out by recording the XRD patterns of crystalline materials as a function of the external stimulus and investigating changes that occur in the powder XRD data. Moreover, time-resolved powder XRD can be carried out. In principle, both laboratory-source XRD and synchrotron-source XRD (these two types of X-ray source are discussed in Section 2.1.3) can be used in time-resolved powder XRD experiments, although using synchrotron-source XRD is more desirable in such experiments due to its higher intensity compared with laboratory X-ray sources, allowing much better time-resolution in monitoring

structural changes over time. In addition, given that this technique is not sample-destructive (although some materials might be beam sensitive and might be damaged on exposure to X-rays) the sample can be recovered, allowing for other experiments to be carried out. There are two configurations of X-ray diffraction techniques in structural characterization, depending on the nature of the sample. If the sample is a single crystal of sufficient size and quality, 3D diffraction data are recorded. By contrast, if the sample is a polycrystalline powder, 1D diffraction data are recorded. Before discussing the key differences between these two configurations, diffraction theory is discussed.

2.1.1 Diffraction Theory

In a crystalline material, the constituents (such as atoms, molecules or ions) are infinitely repeated in three dimensions in a regular array. The 3-dimensional periodicity of crystalline phases can be represented by planes with each plane uniquely defined by a set of three integers (*hkl*) called Miller indices. When a beam of X-rays interacts with a crystalline sample, the X-rays are scattered, by the electrons of atoms in the sample, in all directions. Due to the periodicity of crystalline materials, X-rays scattered in certain directions are in phase with each other, producing intense maxima, while the diffracted beams in all other directions are out of phase, leading to zero intensity. When the scattered beams are in phase, the result is a constructive interference whereas if the scattered beams are out of phase, the result is a destructive interference.

In order for X-ray diffraction to occur in crystalline materials, Bragg's law[77] must be satisfied. Lawrence Bragg showed that for X-rays to be diffracted by a crystalline material, the crystal must have specific orientations with respect to the incident X-ray beam. In this situation, the geometry of the diffraction process can be understood by thinking of the incident beam as if it acts like a beam of light hitting a mirror. When the beam of light hits the mirror, the beam is reflected, obeying the law of reflection which states that the angle of incidence should be equal to the angle of reflection. In an analogous situation in Bragg's law, the incident X-ray beam is considered to hit a set of lattice planes at an angle of θ and then gets reflected at the same angle as shown in Figure 2.1.

In Figure 2.1, we consider two X-ray beams reflected from a set of lattice planes, with angle of incidence detonated θ.

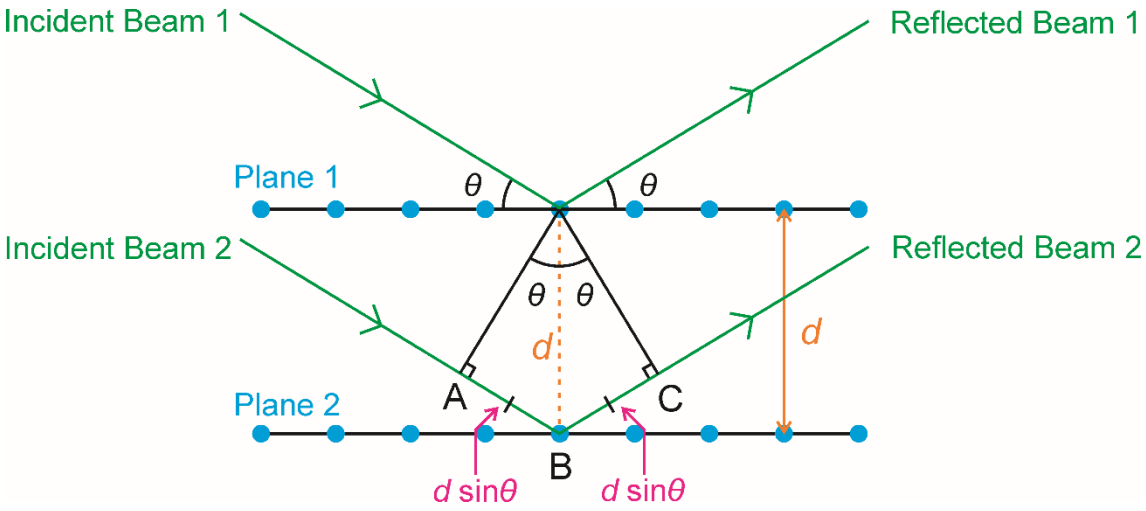

Figure 2.1. *A schematic diagram of lattice points in a crystal, showing the derivation of Bragg's law.*

If the two beams are in phase, the interference between these two beams is constructive and thus diffraction occurs. When the X-rays are reflected from plane 1 and plane 2 as illustrated in Figure 2.1, the two reflected rays will be in phase if the path difference between these two reflected rays is an integer multiple of the wavelength. From Figure 2.1, the path difference between two reflected rays in phase can be written as:

$$AB + BC = n\lambda \tag{2.1}$$

Using rules of trigonometry, AB and BC can be written in terms of d-spacing and θ as:

$$AB = BC = d \sin \theta \tag{2.2}$$

Now if we substitute equation (2.2) in equation (2.1), the final version of Bragg's law is obtained as follows:

$$n\lambda = 2d \sin \theta \tag{2.3}$$

where n is a positive integer representing the diffraction order, λ is the X-ray wavelength, d is the spacing between adjacent lattice planes and θ is the angle between the incident X-ray and the lattice plane.

The intensity of a diffracted X-ray beam is related to the structure factor which depends upon the distribution of electron density in the sample. The intensity (I_{hkl}) of the Bragg reflection with Miller indices of *hkl* is proportional to the square of the magnitude of the structure factor (F_{hkl}):

$$I_{hkl} \propto |F_{hkl}|^2$$

The structure factor F_{hkl}, for a specific set of Miller indices, can be calculated using the following equation:

$$F_{hkl} = \sum_{j=1}^{n} f_j N_j e^{2\pi i(hx_j + ky_j + lz_j)} \exp\left(\frac{-B_j \sin^2\theta}{\lambda^2}\right) \tag{2.4}$$

where the summation is over all atoms in the unit cell, f_j is the atomic scattering factor for the j^{th} atom in the unit cell, N_j is the site occupancy (the probability of finding the atom at a specific position), x_j, y_j and z_j are the fractional coordinates of the j^{th} atom in the unit cell and B_j is the isotropic atomic displacement parameter for the j^{th} atom. The isotropic atomic displacement parameter measures the magnitude of atoms displacement from their equilibrium positions and depends on many factors such as thermal motion, dynamic disorder and static disorder. The isotropic atomic displacement parameter (B_{iso}) can be written in terms of another commonly used factor U_{iso} as:

$$U_{iso} = \frac{B_{iso}}{8\pi^2} \tag{2.5}$$

The atomic scattering factor, which measures the scattering amplitude of the j^{th} atom, depends on the type of atom, the diffraction angle and the type of radiation. This factor can be calculated using the following equation:

$$f = c + \sum_{i=1}^{4} a_i \exp\left(\frac{-b_i \sin^2\theta}{\lambda^2}\right) \tag{2.6}$$

where a_i, b_i, and c are coefficients, the values of which depend on the electronic structure of the scattering atom and can be determined by fitting a simulated atomic scattering curve.[78] The atomic scattering factor is proportional to atomic number, thus atoms with higher atomic number are stronger scatteres of X-ray. As a consequence,

hydrogen atoms are weak scatterers of X-rays due to the fact that they only have one electron. Given that hydrogen atoms are weak scatterers of X-ray, their positions cannot be accurately determined from the X-ray diffraction data. By contrast, neutron diffraction[79] is more accurate than X-ray diffraction in determining the position of hydrogen atoms. In this technique, the diffraction does not depend on the distribution of electron density but rather happens as a result of the interaction of neutrons with the nuclei within the sample.

2.1.2 Single-Crystal XRD versus Powder XRD

We now consider the differences between single-crystal XRD and powder XRD. In single-crystal XRD, the sample of interest must be a single crystal of sufficient size and quality. The typical size of the single crystal is about 30-300 μm with an average ideal size of 150-250 μm. A high quality single crystal needs to have well-formed faces with no deformation. In addition, the crystal should be optically clear and should not be fractured, twinned or growing "baby crystals".

To carry out a single-crystal XRD measurement, the single crystal is mounted on a goniometer and exposed to an incident monochromatic X-ray beam. The single crystal must be rotated so that a full array of reflections is recorded. The reflections are recorded using a 2D detector (area detector) which records each reflection as a well-resolved spot. Figure 2.2 shows a schematic diagram of a single-crystal XRD measurement. From the positions of the "spots" and their intensities, an electron density map (and consequently a structural model) can be calculated through the structure solution and refinement processes.

Although single crystal XRD is the most accurate method to determine crystal structures, this method needs a sufficiently large single crystal of sufficient quality. Growing such a single crystal is not always feasible given the fact that many thermodynamic and kinetic factors contribute to crystallization outcomes, leading, in many cases, to polycrystalline samples rather than a single crystal of high quality and suitable size. In addition, one single crystal might not represent the entire crystallized sample, as several different phases may be present, and care must be taken to isolate and characterize all possible phases. In the light of these limitations of single-crystal XRD, powder XRD is an alternative way to determine crystal structures. In addition,

powder XRD is practically the technique of choice for the identification ("fingerprinting") of crystalline phases.

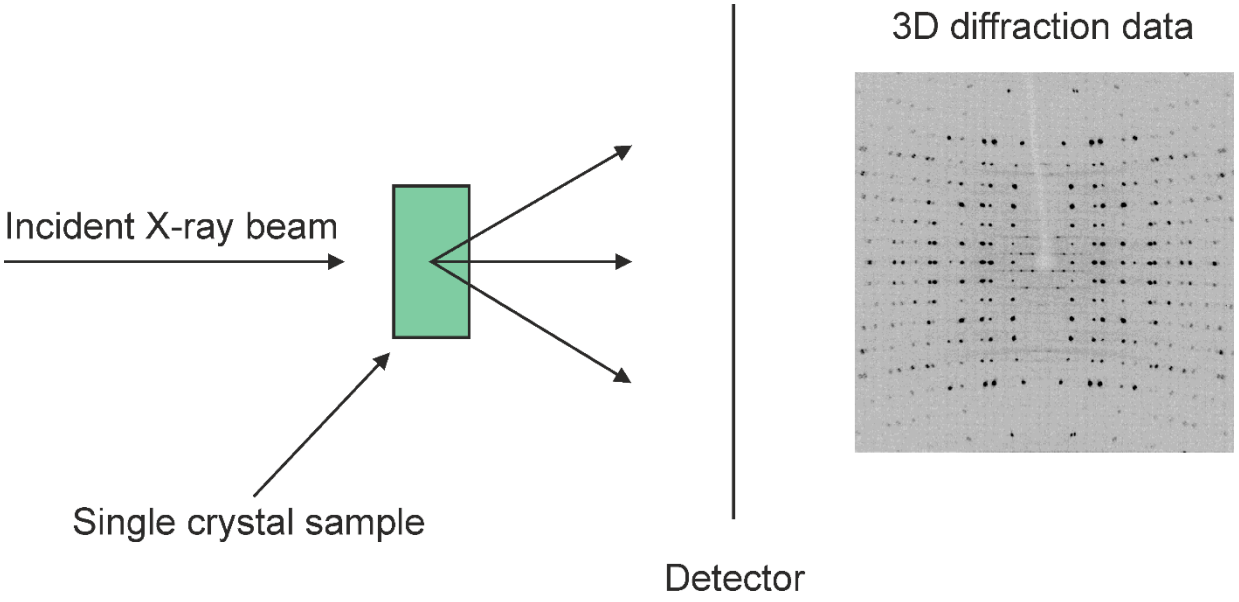

Figure 2.2. *A schematic diagram of a single-crystal X-ray diffraction measurement.*[80]

In powder XRD, a polycrystalline sample is used to record high quality XRD data for structure determination. The polycrystalline sample contains many microcrystals which, in an ideal situation, are randomly oriented. The physical phenomenon of XRD is the same in single-crystal XRD and powder XRD, but the form of the recorded diffraction pattern is different in each case. The polycrystalline sample in powder XRD comprises a large number of small crystallites in random orientations and each crystallite behaves in a similar way to a single crystal in single-crystal XRD. As a consequence, the collective scattering from the whole powder sample is recorded. This collective scattering pattern appears as coaxial cones of scattered radiation (see Figure 2.3).

The 1D detector, in powder XRD, records diffraction maxima as a function of one spatial variable, i.e. the diffraction angle 2θ. Figure 2.3 shows a schematic diagram of a powder XRD measurement. The fact that powder XRD records the diffraction intensity as a function of only one spatial variable (the diffraction angle 2θ), leads to the "compression" of the 3D diffraction data into 1D, making it more challenging for structure determination, especially when there is significant peak overlap. Peak overlap is more likely to be severe for materials with large unit cells and/or low symmetry, leading to more difficulties in structure determination. However, these

challenges can be overcome by techniques such as the direct-space strategy for structure solution (details of this strategy are given in Chapter 3), which takes peak overlap implicitly into consideration, allowing successful structure determination of organic materials of moderate complexity.[81-89]

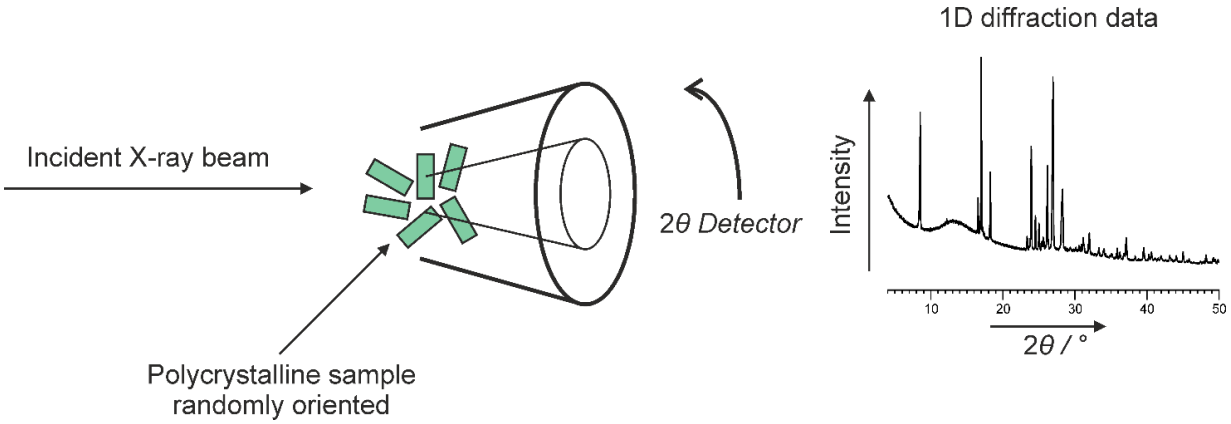

Figure 2.3. *A schematic diagram of a powder XRD measurement.*[80]

Although structure determination from powder XRD data is more challenging, there are many situations in which the use of powder XRD data in structure determination is unavoidable.[48, 85, 88-101] For example, the use of mechanochemical methods for sample preparation, such as LAG and neat grinding, lead inherently to polycrystalline samples.[48] Furthermore, even solvent-based crystallization methods lead, in many cases, to polycrystalline samples rather than large and high quality single crystals. In addition, materials produced by desolvation processes (such as dehydration) or materials produced by solid state reactions or solid-solid phase transitions are usually produced in a polycrystalline form.[102-103] In all these cases, powder XRD must be used to record high quality XRD data for structure determination.

For polycrystalline samples, to obtain a high-quality powder pattern for indexing and structure solution, it is recommended that a number of procedures are followed. For example, depending on the sample of interest, it is sometimes desirable to grind the powder to reduce the effect of "preferred orientation". This preferred orientation is greater when crystallites have anisotropic shapes (such as needles or plates), making them preferably oriented rather than randomly oriented. In some cases, preferred orientation has a significant effect on structure determination from powder XRD data, and it is therefore essential to reduce this effect before attempting structure

determination. One way to investigate if a powder sample has preferred orientation is to measure the powder XRD pattern of the sample using a diffractometer with a different configuration (such as using a diffractometer with an area (2D) detector). If the intensity of the cone (scattered radiation) is uniform, this means that there is no preferred orientation. If, however, the intensity of the cone is not uniform, this means that the sample suffers from preferred orientation. Figure 2.4 shows an example of a powder sample with preferred orientation. Another way of investigating preferred orientation is by measuring the powder XRD pattern of the sample using different ways of packing the sample. For example, the sample can be packed in a capillary or can be packed between two layers of an amorphous tape. If the relative intensities are different in the powder XRD data recorded using these methods, the sample clearly has preferred orientation.

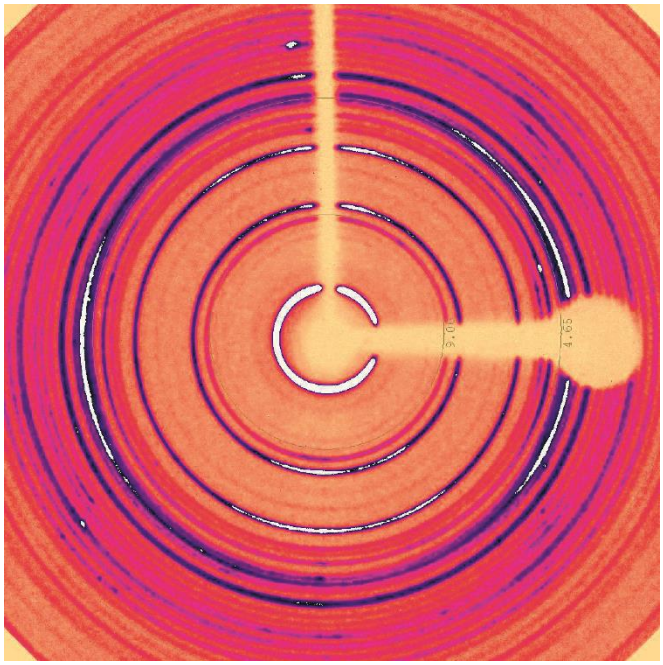

Figure 2.4. *A 2D scan of a powder sample, showing the non-uniform intensity of the ring of scattered radiation, indicative of preferred orientation.*

There are many procedures which can alleviate the extent of preferred orientation in a powder sample. One procedure is to use capillaries, rather than compressing the sample between two pieces of an amorphous tape (microcrystals have a higher chance of orienting themselves more randomly in a capillary). A second procedure is to grind the sample so needle or plate crystallites can be broken, thus decreasing the anisotropic morphology and increasing the chance of random

orientations in the powder. However, it should be noted that overgrinding the sample might affect the crystallinity and thus lead to broad peaks in the powder XRD pattern. In addition, overgrinding the sample might lead to more electrostatic interactions, making the sample stickier and thus more difficult to pack into capillary. Furthermore, care must be taken when the sample is ground due the fact that grinding might stimulate phase transition, leading to the transformation of solid material from one phase to another phase. A third procedure that might reduce the effect of preferred orientation is to mix the sample with an amorphous material (e.g. starch) to increase the likelihood that the crystallites will be randomly oriented.

The geometry of powder diffractometer used during the course of this research was the transmission mode (Debye-Scherrer). In this mode, the sample is held between two layers of an amorphous tape or packed into a number of capillaries, (typically three), which are spun to reduce the effect of preferred orientation (Figure 2.5).

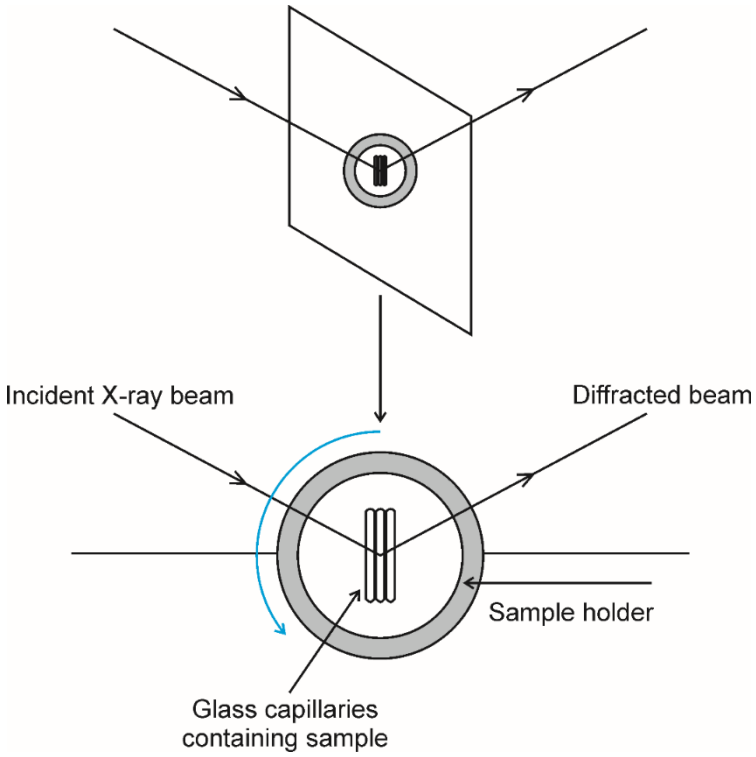

Figure 2.5. *A schematic diagram of the transmission geometry of Debye-Scherrer diffractometer used in this dissertation, showing a sample holder with three capillaries containing the sample. The sample holder and capillaries spin in the direction of the blue arrow.*

The use of transmission mode over other modes of powder XRD (such as Bragg-Brentano reflection) has many advantages such as higher resolution and less likelihood of preferred orientation. It is therefore desirable to use the transmission geometry to collect high quality powder XRD data for the structure determination process, especially for organic solid materials, due to the fact that these materials tend to have large unit cells or low symmetry, leading to greater peak overlap.

2.1.3 X-ray Sources

There are two main methods for generating X-rays: a laboratory-based method and a synchrotron-based method. In the laboratory-based method (Figure 2.6), a negatively charged filament (cathode) is heated to release electrons which are then accelerated, in vacuum, by a high electric field. These accelerated electrons hit a positively charged metal target (anode), generating X-rays in all directions. When the accelerated electrons hit the metal target, electrons are excited from the core shell (e.g. 1*s* orbital) to generate a "core hole". The core hole is then filled by an electron from a larger energy orbital, with the emission of X-rays. If an electron transition from the L shell (2*p* orbital) to the K shell (1*s* orbital), Kα radiation is produced. On the other hand, Kβ radiation is produced if the electron transition is from the M shell (3*p* orbital) to the K shell. In fact, Kα radiation contains two wavelengths ($K\alpha_1$ and $K\alpha_2$) due to the fact that electrons in the *p* orbital can have different spin states.[104] The preferred radiation type in laboratory powder XRD is Cu $K\alpha_1$. The $K\alpha_1$ radiation is selected using a single crystal monochromator, which is usually made of germanium.

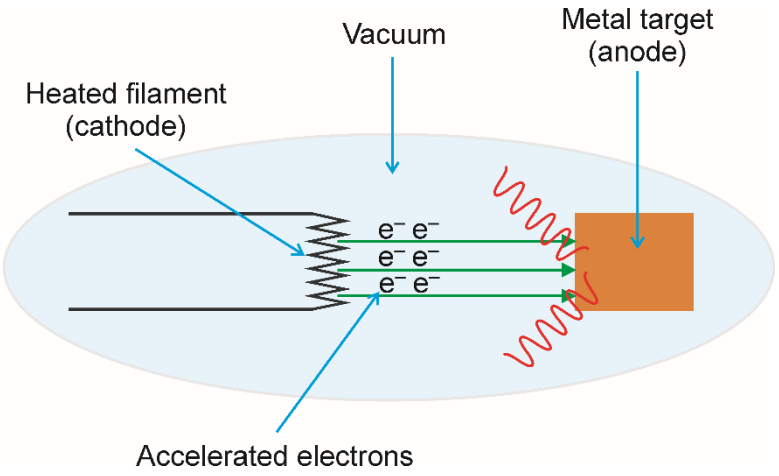

Figure 2.6. *A schematic diagram of generating X-rays using a laboratory-source.*

In the synchrotron-based method[105] (Figure 2.7), electrons are generated using an electron gun. These electrons are then accelerated approximately to the speed of light using a linear accelerator (linac) and booster synchrotron before injecting them into a circular ring called a storage ring. To maintain the circular motion of electrons in the storage ring, bending dipole magnets are used. When the electrons move past the bending magnet, they are accelerated as their directions change, emitting X-rays of different wavelengths. X-rays of a specific wavelength can be selected using suitable monochromators. The X-rays generated by a synchrotron source are highly polarized and have much higher intensity than X-rays from a laboratory source (this is why diffraction peaks have better signal-to-noise ratio when a synchrotron source is used compared to the laboratory source).[105] In addition, diffraction peaks are much sharper using a synchrotron source due to the fact that the synchrotron produces much narrower beams than the laboratory source.

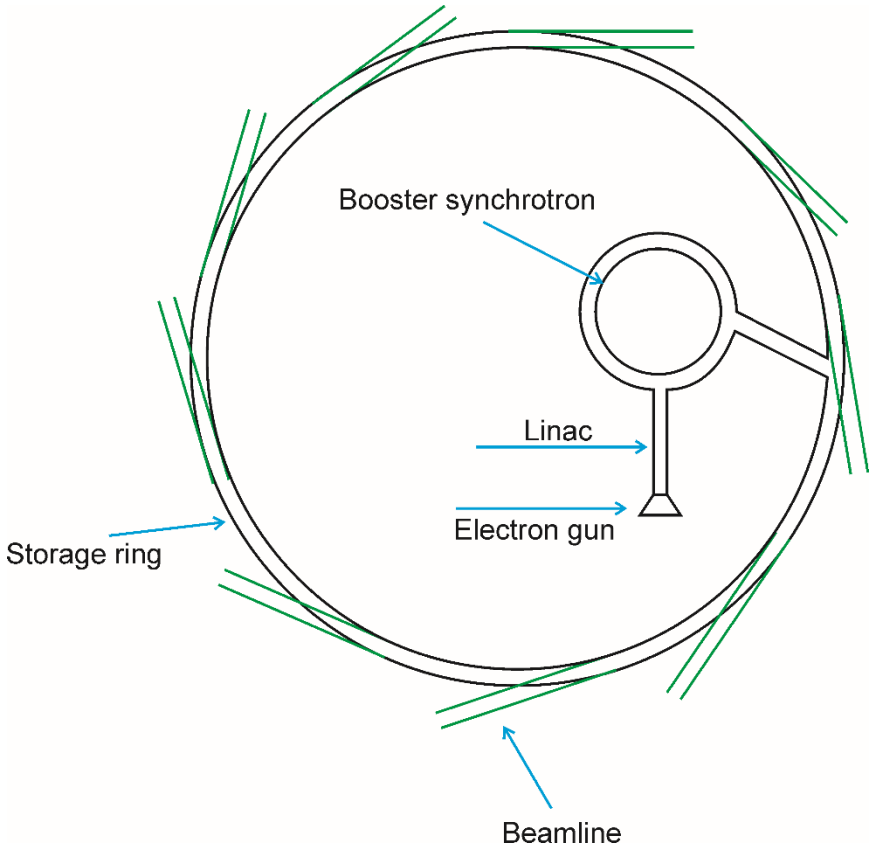

Figure 2.7. *A schematic diagram of generating X-rays using a synchrotron source.*

2.2 Solid-state Nuclear Magnetic Resonance (SSNMR) Spectroscopy

NMR spectroscopy[106] is one of the most powerful techniques used in structural characterization of different materials including solid and liquid phases. Depending on the nature of the samples, there are two types of NMR spectroscopy: liquid-state NMR spectroscopy and solid-state NMR spectroscopy. In this section, we focus on solid-state NMR spectroscopy, although the principle of NMR spectroscopy is similar in both liquid-state NMR and solid-state NMR spectroscopy.

Solid-state NMR spectroscopy can be used to study structural and dynamical properties of a range of solid materials including crystalline and amorphous phases. Unlike diffraction techniques, where the material of interest has to be in a crystalline form to give sharp peaks, solid-state NMR spectroscopy can be used to study amorphous phases (where it can study short-range order of amorphous materials) and highly disordered materials. In addition, this technique can be used in crystallography as a complementary technique to diffraction, leading to a better understanding of structure determination processes (details of structure determination from powder XRD data are discussed in Chapter 3). In this regard, SSNMR can be used to assess the composition of the asymmetric unit of a crystal structure, prior to the structure determination calculation. Moreover, the connectivity and geometry of molecules can be established using SSNMR spectroscopy. In addition, in the case of amorphous materials with short-range order or materials with highly disordered structures, this technique can reveal structural and geometrical information such as internuclear distances and bond angles when no other analytical method can provide such information.[106]

Solid-state NMR spectroscopy can be the technique of choice to study molecular mobility in solid materials. This is due to the fact that the timescale of molecular mobility in these materials is suitable for investigation by NMR techniques, leading to better understanding of the dynamical properties of these solid materials. For example, the size of the force, which can be applied onto solid materials as stress before breaking them, depends on the degree of molecular flexibility.[106] Another example, where understanding molecular mobility is the key to understanding solid state properties, is solid-solid phase transformations. Certain types of solid-solid phase transformations occur as a result of molecular motion where atoms or molecules have enough energy to overcome the energy barrier of transformation. Identifying and

understanding phase transitions in solid materials is crucial in many industries such as pharmaceuticals.

2.2.1 Theory

NMR spectroscopy studies the effects of an applied magnetic field on the spin resonance of an ensemble of nuclei. An ensemble of nuclei has magnetic moments and thus can interact with an external applied magnetic field $\mathbf{B_0}$. In the absence of an external magnetic field, the net magnetization of nuclei in the sample is zero due to the random orientations of their magnetic moments. However, in the presence of an external magnetic field, the magnetic moments of the nuclei partially align with $\mathbf{B_0}$, giving rise to a bulk magnetization. The components of the magnetization can be parallel or antiparallel to the external applied magnetic field depending on the nuclei. When an external magnetic field is applied to the nuclei, it causes the energy states of the nuclear spin to split, otherwise known as the Zeeman effect. A small excess of spins in the lower energy level(s) gives rise to the bulk magnetization.

The chemical shift is the most commonly investigated interaction in NMR spectroscopy. While the fast tumbling of molecules in solution leads to isotropic chemical shifts in liquid-state NMR, the restricted mobility in solid materials and the orientation dependence of chemical shift in solid-state NMR leads to chemical shift anisotropy. Chemical shift interactions can give information about the chemical environment which can arise as a result of bond types, bond angles or bonding to different atoms.

Given that chemical shift interactions are averaged out in liquid-state NMR leading to isotropic chemical shifts, the liquid-state NMR spectra always show sharp peaks, whereas the chemical shift anisotropy observed in solid-state NMR leads to broad lineshapes. In a polycrystalline sample, each microcrystal with a distinct orientation relative to $\mathbf{B_0}$ has nuclei in different orientation, leading to peak broadening. To improve the resolution of NMR spectrum, Magic Angle Spinning (MAS) can be applied whereas Cross Polarization (CP) [107] can be used alongside MAS to enhance signal-to-noise ratio.

2.2.2 Magic Angle Spinning (MAS)

MAS can be used to remove the anisotropic NMR interactions and enhance the resolution of spectra in solid-state NMR spectroscopy. In this technique, a polycrystalline sample is packed into a rotor which is spun at a predetermined frequency around a spinning axis which forms an angle of 54.74° (the "magic angle") with respect to the applied magnetic field (see Figure 2.8).

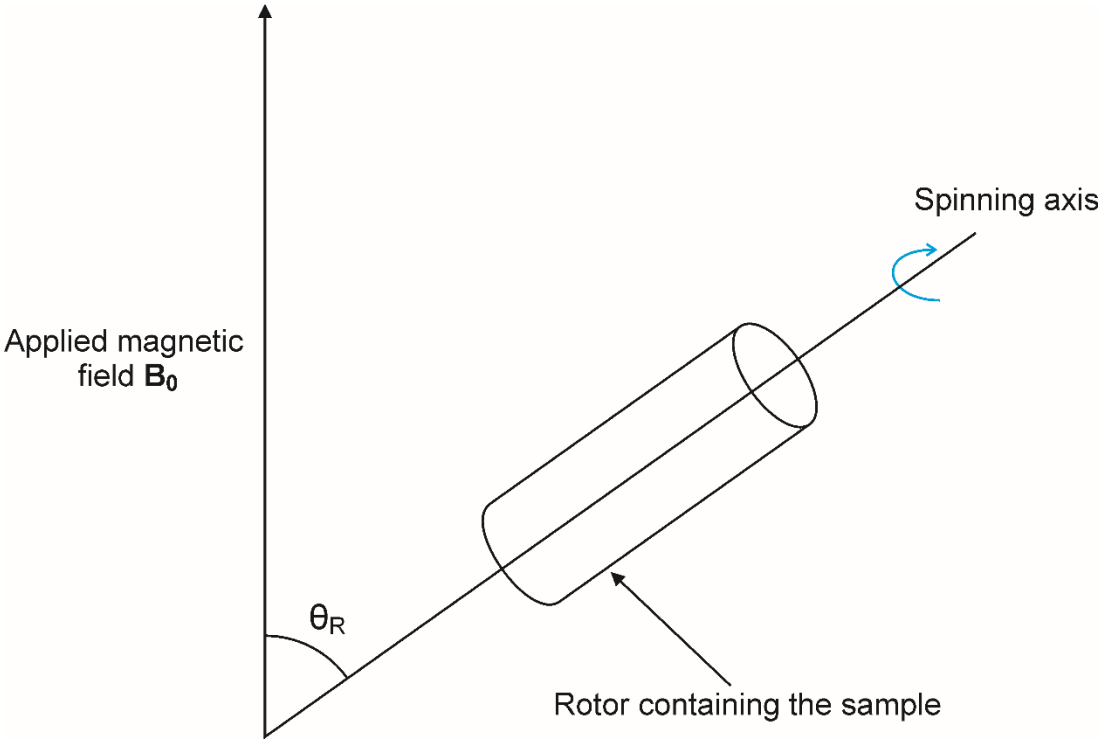

Figure 2.8. *A schematic diagram showing MAS (θ_R) in SSNMR experiments.*

MAS can reduce or even eliminate the effect of chemical shift anisotropy.[106] However, in order for MAS to achieve this goal, the spinning of the rotor must be fast enough to overcome the various interactions. If the spinning frequency is not fast enough, spinning sidebands will be observed in SSNMR spectra. Spinning sidebands are peaks which appear at positions from the centerbands equal to integer multiple of the spinning frequency. The intensities of the sidebands depend on the rate of spinning, with slower spinning giving more intense sidebands. In fact, the intensity of sidebands can even be bigger than the intensity of centerbands at slow spinning frequencies. One way to differentiate sidebands from centerbands is to record the spectra at different spinning frequencies since the centerbands will stay at the same position at all rates of

spinning whereas the spinning sidebands will move according to the spinning frequency.

2.2.3 Cross Polarization (CP)

Although MAS can improve the resolution of SSNMR spectra, nuclei with low natural abundance such as ^{13}C give, unavoidably, low signal-to-noise ratio. In addition, these nuclei tend to have a longer relaxation time and thus longer period of time is required between scans, meaning that collecting a high quality solid-state NMR spectrum can take a relatively long time. A technique that can be applied, alongside MAS, to improve the signal-to-noise ratio in samples with low natural abundance is Cross Polarization (CP)[107] and it is often used to record SSNMR spectra of organic solids. In CP, magnetization is transferred from nuclei with high natural abundance and high Larmor frequency to nuclei with low natural abundance and low Larmor frequency. This can be achieved by applying a 90° radio-frequency (rf) pulse which rotates the ^{1}H magnetization onto the y axis. Another 90° rf pulse, which is called a spin-lock pulse as it spin-locks the ^{1}H magnetization, is applied to the ^{1}H channel. A simultaneous rf pulse is applied to the X channel and during the contact time (the time when both rf pulses are simultaneously applied to both ^{1}H and X channels), the magnetization will transfer from ^{1}H to X. The NMR signal is recorded during the acquisition time for X nuclei while carrying out ^{1}H decoupling. ^{1}H decoupling can be carried out by irradiating the ^{1}H channel continuously or by applying a sequence of pulses such as SPINAL 64.[108] Figure 2.9 shows a schematic diagram for a CP experiment.

Given that nuclei with higher Larmor frequency have higher gyromagnetic ratio than nuclei with lower Larmor frequency, there is an enhancement of signal-to-noise ratio, equivalent to the ratio of the gyromagnetic ratios of the nuclei with high Larmor frequency and the low Larmor frequency $\omega_0(^{1}H)/\omega_0(X)$. Furthermore, given that magnetization was originally transferred from ^{1}H, which has a shorter relaxation time, signal recovery will depend on the relaxation time of ^{1}H and therefore will allow high resolution spectra of materials with low natural abundance nuclei to be recorded in a relatively shorter time.

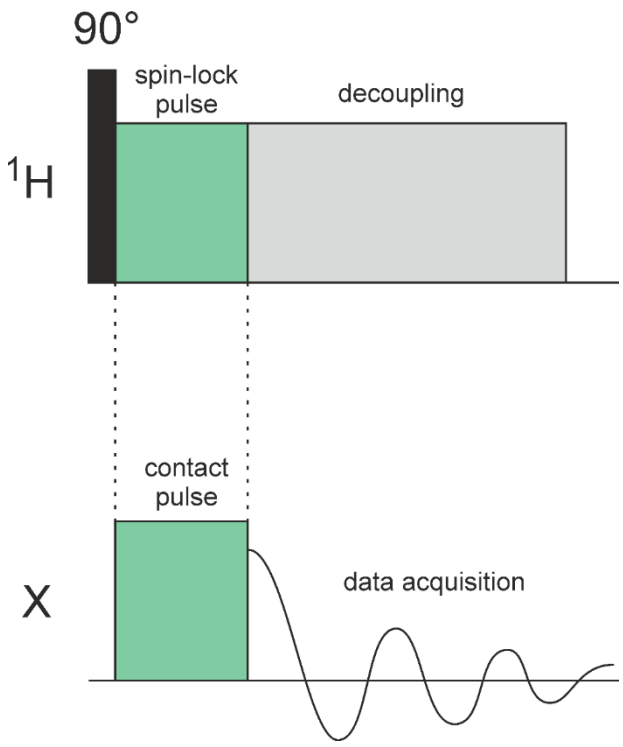

Figure 2.9. *A schematic diagram showing pulse sequences of a simple cross polarization experiment in SSNMR.*

2.3 Differential Scanning Calorimetry (DSC)

DSC[109] is one of the most powerful analytical techniques used to characterize thermal properties of materials including melting points, phase transitions, glass transitions and heat capacities. In addition, this technique can be used to investigate polymorphism in organic materials.[110] Furthermore, this technique can be used to study the crystallinity and purity of crystalline materials as well as kinetic crystallization of amorphous materials.[111] The principle of this technique involves heating and/or cooling a reference pan and a sample pan over a temperature program.

In DSC, the calorimeter measures heat flow to the sample pan compared with heat flow to the reference pan and then plots heat flow difference as a function of temperature. This allows for different thermal events such as phase transitions, melting, glass transitions and recrystallization to be detected since the sample pan and the reference pan have different heat capacities. A schematic diagram of heat flux DSC with a turret-type[109] measuring system (TA instruments), which was used in the course of this research, is displayed in Figure 2.10.

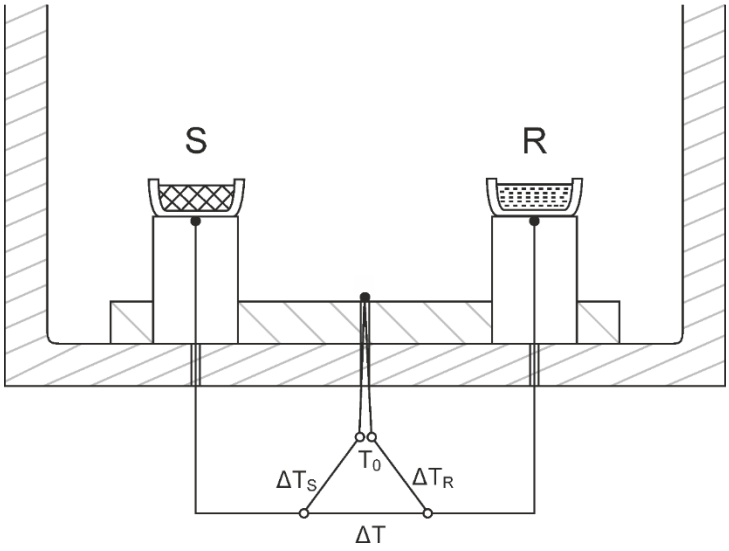

Figure 2.10. *A schematic diagram of heat flux DSC with a "turret-type" measuring system. S is the sample pan, R is the reference pan. T_0 is the temperature of the furnace, ΔT_R is the temperature difference between the furnace and the reference pan, ΔT_S is the temperature difference between the furnace and the sample pan, ΔT is the temperature difference between the reference pan and the sample pan.*

When a thermal event, such as melting, phase transition, glass transition or recrystallization takes place, the heat flow of the sample pan will change compared to the reference pan. This change is recorded as a peak in a direction determined by the type of thermal event. In endothermic events, such as melting, the sample absorbs heat. By contrast, in exothermic events such as recrystallization, the system releases heat. A schematic diagram of a typical DSC thermogram is shown in Figure 2.11a. As can be observed, heating a sample might lead to different thermal events including a solid-solid phase transition, where the solid material transforms from one solid phase to another solid phase, and melting, where the sample transforms from a solid state to a liquid state (usually the enthalpy of melting is higher than the enthalpy of solid-solid phase transitions).

On cooling, the sample might undergo recrystallization, giving an exothermic peak. In some cases, hysteresis can be observed upon cooling the sample as a result of the formation of a cooled or super-cooled liquid. Another thermal event that might be observed upon cooling is glass transition where the sample transforms from a liquid state to a glassy state. This event can be detected in DSC thermogram as a change of the heat flow and will be recorded as a curve (change of heat flow). It is worth noting here that the onset temperature (Figure 2.11b) of a thermal event should be recorded

and quoted, as this temperature does not depend on the heating/cooling rate. By contrast, the temperature of the peak maximum of a thermal event depends on the heating/cooling rate. The onset temperature can be determined by drawing a tangent of the peak and interpolating the background. The point of intersection between the tangent and the interpolated background is the onset temperature (Figure 2.11b).

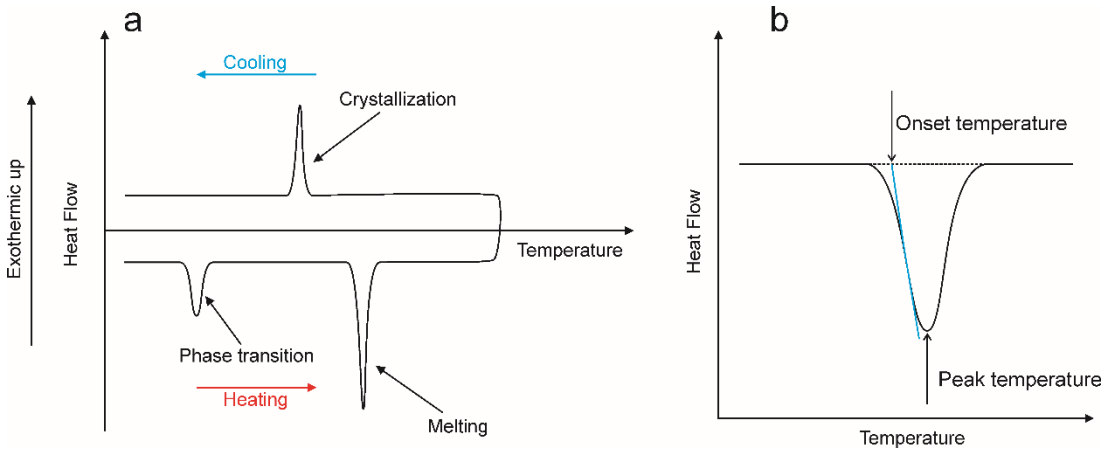

Figure 2.11. *(**a**) A schematic diagram of a DSC thermogram showing different thermal events that can be observed during a DSC experiment, (**b**) a schematic diagram of a peak showing the onset temperature and the peak temperature (the onset temperature is the intersection point between the tangent and the baseline interpolation).*

2.4 Thermo-Gravimetric Analysis (TGA)

TGA is another analytical method which can be used to characterize the physicochemical properties of solids. In this technique, temperature is increased at a specific rate and mass is recorded as a function of temperature. TGA can also be carried out isothermally, where temperature is fixed and mass is recorded as a function of time. The major component of this technique is a very sensitive balance which is placed inside a furnace. The furnace and the balance are connected to a thermocouple which measures the temperature of the sample. TGA can be used to investigate whether solids are anhydrous or solvates (including hydrates). Anhydrous forms do not show any mass loss as temperature increases until temperature reaches a decomposition point, where a substantial mass loss is observed as a result of decomposition of the material (Figure 2.12a). Mass loss due to decomposition of the sample usually results from gas release due to bond cleavage. Solvate (hydrate) materials, on the other hand, will show a partial mass loss due to loss of the solvent

(which corresponds to the stoichiometry of the solvent), before the temperature reaches the decomposition point. If one partial mass loss is observed in the TGA thermogram, this implies that the sample undergoes one desolvation (or dehydration) process before decomposition (Figure 2.12b). If, however, two partial mass losses are observed, this implies that the sample undergoes two desolvation processes. For example, if the sample exists as a dihydrate form, we may observe two partial mass losses in the TGA thermogram (Figure 2.12c). The first partial mass loss could correspond to the transformation of the dihydrate to a monohydrate, and the second partial mass loss may correspond to transformation of the monohydrate to an anhydrous form.

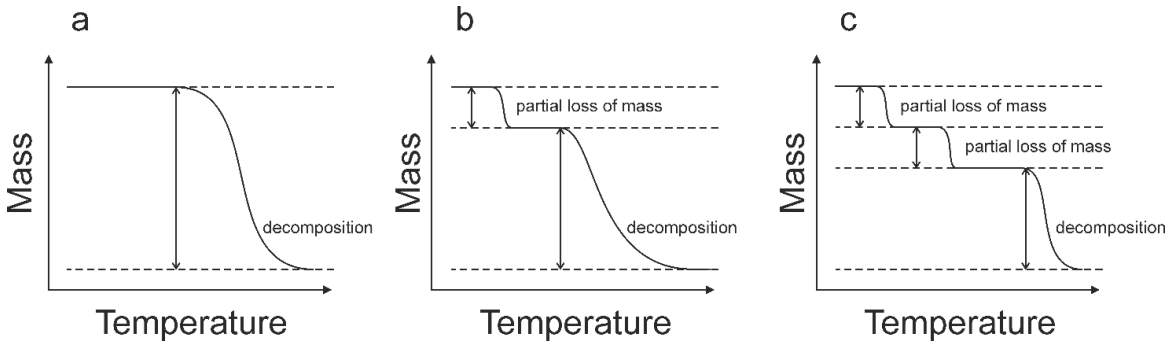

Figure 2.12. *A schematic diagram of a typical TGA thermogram of (a) an anhydrous material showing no mass loss until decomposition of the material where a large loss of the mass is observed, (b) a solvate (hydrate) material showing one desolvation (dehydration) process where one partial mass loss is observed before decomposition, (c) a solvate (hydrate) material showing two desolvation (dehydration) processes where two partial mass losses are observed before decomposition.*

TGA can identify the presence of any solvates or hydrates and thus determine their stoichiometry which can be very useful in structure determination from powder X-ray diffraction. This allows for the determination of the composition of the asymmetric unit, and thus for setting up structure solution calculations, i.e. whether we need to include additional structural variables to account for water or solvent molecules.

The combination of DSC and TGA is very common in solid-state characterization as these two techniques are complementary and allow for full thermal characterization of solids. Using DSC or TGA alone can be misleading and, therefore, it is strongly recommended that a combination of these two techniques is used. For

example, if a small endothermic peak is observed before melting in a DSC thermogram, it can be uncertain whether this small peak is due to desolvation (dehydration) or a phase-transition event. This uncertainty can be clarified if TGA is used along with DSC. If the TGA experiment shows a mass loss at a similar temperature of the small peak observed in DSC thermogram, desolvation (dehydration) can be confirmed. If, however, no mass loss is observed in TGA thermogram, desolvation (dehydration) can be ruled out and the small peak in DSC thermogram can be assigned to a phase-transition event.

Chapter 3: Structure Determination from Powder XRD Data

Although the most accurate method to obtain crystal structures is single-crystal XRD,[112-114] using this technique requires a single crystal of enough size and quality. However, for many materials, single crystals of suitable size and quality cannot be prepared. Furthermore, in many cases, solid-state preparation procedures inherently produce polycrystalline samples, such as neat grinding and liquid-assisted grinding [48, 115]. In such cases single-crystal XRD is again not suitable for structure determination. In these cases, the alternative for structure determination is to use powder XRD, although it is significantly more challenging as discussed in Chapter 2. In the case of organic materials, peak overlap is significant, making the process of structure determination especially challenging. Nevertheless, advancement in structure determination techniques in the past twenty-five years has made the process of structure determination from powder XRD data more feasible although it is still not trivial.[96, 113, 116-129] The direct-space strategy in particular has opened up the opportunity for structure determination of organic materials directly from powder XRD data.[94, 130-140]

The process of structure determination from powder XRD data can be divided into a number of consecutive steps, with each step playing an important role in the structure determination process. It is therefore necessary to optimize each step in order to carry out structure determination from powder XRD data successfully. For example, the optimization of sample preparation might include grinding the sample or mixing it with starch to reduce the effects of preferred orientation, which can make it impossible to determine the crystal structure from powder XRD data.

Assuming that high quality powder XRD data have been recorded, the next step in the structure determination process is indexing the powder pattern to determine approximate values of the unit-cell parameters and to assign plausible space groups. Once the powder pattern has been indexed correctly, the next step is to carry out profile fitting to refine the unit-cell parameters, to confirm the space group assignment and to establish the lineshape and linewidth parameters that describe peaks in the powder XRD pattern. The next step is to carry out structure solution, for example using the direct-space strategy, to obtain the approximate structural model that best fits the experimental data. In the final stages, the structure is then optimized using the Rietveld refinement technique. The refined structure can be further validated by carrying out

energy minimization calculations, usually using periodic DFT. These steps are explained in more detail in this chapter. Figure 3.1 shows a schematic diagram for the consecutive steps in structure determination process from powder XRD data.

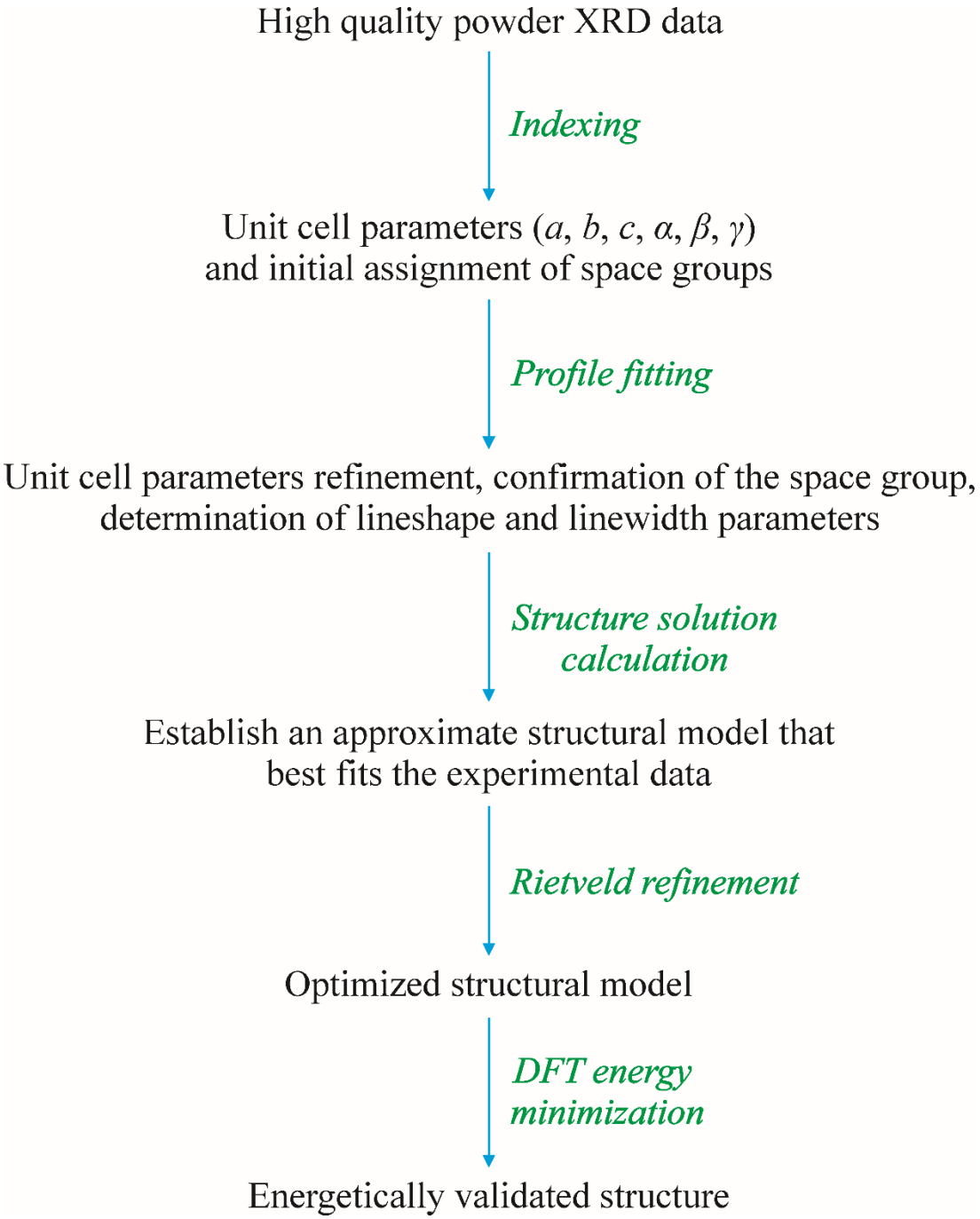

Figure 3.1. *A schematic diagram of structure determination from powder XRD data.*

3.1 Indexing (Unit Cell Determination)

The first stage in structure determination from powder XRD data is the indexing of the powder XRD pattern. Indexing a powder XRD pattern means obtaining

approximately correct unit-cell parameters (a, b, c, α, β, γ) using a set of algorithm packages, such as the CRYSFIRE package[141-142] which uses a range of different indexing algorithms (such as ITO,[143] TREOR,[144] DICVOL,[145] FJZN[146] and XCELL[147]). These algorithms use peak positions (at least 20 peaks preferably at low 2θ angle) extracted from the powder pattern and apply different types of search methods to find the Miller indices (*hkl*) for each selected peak. Once the Miller indices (*hkl*) of each peak are calculated, the unit-cell parameters can be determined. The determination of unit-cell parameters allows for the determination of unit-cell volume which allows for approximating the density, given that the chemical composition of the material of interest is known. The density can be estimated by multiplying the mass of the formula unit by an integer n ($n \geq 1$), representing the number of molecules in the asymmetric unit, and then dividing by the unit cell volume. The determination of density, at this stage of structure determination, serves as an extra check for the plausibility of unit-cell parameters as the estimated density can be compared with an experimental density, or with known densities of other polymorphs or similar materials. It is worth noting that the indexing of a powder XRD pattern requires that the crystalline material exists as a pure phase. If the material of interest exists as a mixture of crystalline phases, indexing becomes virtually impossible (unless the identities of all the "impurity" phases are known).[80]

3.2 Profile Fitting

After determining the unit-cell parameters in the indexing stage, the next stage is to carry out profile fitting. The aim of profile fitting is to improve the accuracy of the unit-cell parameters, to prepare the intensity data for space group assignment, and to determine the lineshape and linewidth parameters for subsequent structure solution calculations. There are two methods for carrying out profile fitting: the Pawley method[148] and the Le Bail method[149] (the Le Bail method can be carried out by the program GSAS).[150] The aim of the profile fitting stage is to fit the whole experimental powder XRD profile by refining parameters that describe: (i) peak positions (which depend on the unit-cell parameters and the instrumental zero shift, a shift that occurs as a result of detector misalignment), (ii) peak lineshape, (iii) peak linewidth, (iv) background intensity distribution, and (v) peak intensities. As the unit-cell parameters are refined in the profile fitting stage, the refined parameters are more accurate representations of the true unit-cell parameters. At this stage, the intensity values are

refined to obtain an optimal fit that best describes the profile parameters for subsequent structure solution. It is worth emphasising that the intensity values obtained in this stage are not used in subsequent structure solution using the direct-space strategy and that only variables (i)-(iv) are used to construct the calculated powder XRD patterns for each trial structure in direct-space structure solution (together with the intensities calculated for the trial structures).

The assignment of space group at this stage can be carried out by identifying systematic absences in the intensity data. However, if more than one space group has the same systematic absences or if many space groups are plausible, profile fitting and further structure solution must be carried out for all possible space groups. It is worth emphasising that no structural model is used in the profile stage of structure determination from powder XRD data, apart from the unit-cell parameters, as the aim of profile fitting is to establish the profile parameters, which describe the shape and the width of peaks in the powder XRD pattern, and to determine accurate values of the unit cell parameters.

3.3 Structure Solution

After obtaining unit-cell and profile parameters from the indexing and profile-fitting stages, structure solution is the next stage. At this stage, the experimental information that we have is a 1D powder XRD pattern, and the only structural knowledge (apart from the unit-cell parameters) is the chemical composition of the material of interest with the connectivity and geometry of the molecule, although in some cases the connectivity and molecular geometry may not be known. This means that 3D data (a 3D crystal structure) has to be deduced from 1D powder XRD data. This imposes many challenges, particularly if the material has low symmetry or a large unit cell, which leads to substantial peak overlap in the 1D powder XRD data.

There are two strategies for structure solution from powder XRD data: the traditional strategy and the direct-space strategy. In the traditional strategy, which follows a close approach to crystal structure solution using single-crystal XRD data, the integrated intensity data extracted for each peak in the experimental powder XRD pattern in the profile fitting stage are used. Several techniques (such as direct methods,[151-152] Patterson methods[153] and the charge-flipping method[154-156]) are then

used to solve the crystal structure from the integrated intensity data in a similar way to using single-crystal XRD data. However, given that the vast majority of organic compounds display severe peak overlap, this peak overlap poses serious challenges for extracting accurate intensities and thus reliable values for structure factors. By contrast, the direct-space strategy[94, 131, 134, 138-139] can successfully be used to overcome the problem of peak overlap.

Before discussing the principles of the direct-space strategy, we need to understand the link between a crystal structure and its diffraction pattern. If the crystal structure of a material is known, the powder XRD pattern can be calculated straightforwardly. A powder XRD profile is mainly defined by the positions of diffraction maxima, which depend on the size of the unit cell as defined by lattice parameters (a, b, c, α, β, γ), and the relative intensities of diffraction maxima, which depend on the distribution of the X-ray scattering matter (the distribution of electron density) in the unit cell. The intensity of each diffraction maximum is related to the structure factor $F(\boldsymbol{H})$, where $\boldsymbol{H}$ is the scattering vector in reciprocal space given by $\boldsymbol{H} = h\boldsymbol{a}^* + k\boldsymbol{b}^* + l\boldsymbol{c}^*$ (hkl are the Miller indices for the diffraction maximum and $\boldsymbol{a}^*$, $\boldsymbol{b}^*$ and $\boldsymbol{c}^*$ are the reciprocal lattice vectors). The structure factor, which links the crystal structure to its XRD pattern, has magnitude $|F(\boldsymbol{H})|$ and phase $\alpha(\boldsymbol{H})$, and is related to the electron density $\rho(\boldsymbol{r})$ within the unit cell by the following equation:

$$F(\boldsymbol{H}) = |F(\boldsymbol{H})| \exp[i\alpha(\boldsymbol{H})] = \int \rho(\boldsymbol{r}) \exp(2\pi i \boldsymbol{H} \,.\, \boldsymbol{r}) d\boldsymbol{r} \qquad (3.1)$$

where $\boldsymbol{r}$ is the vector $\boldsymbol{r} = x\boldsymbol{a} + y\boldsymbol{b} + z\boldsymbol{c}$ in direct space and $\boldsymbol{a}$, $\boldsymbol{b}$ and $\boldsymbol{c}$ are the lattice vectors defining the periodicity of the crystal structure, and the integration is over all vectors $\boldsymbol{r}$ in the unit cell. The electron density in equation (3.1) can be calculated through the inverse Fourier transform as follows:

$$\rho(\boldsymbol{r}) = (1/V) \sum_{\boldsymbol{H}} |F(\boldsymbol{H})| \exp[i\alpha(\boldsymbol{H}) - 2\pi i \boldsymbol{H} \,.\, \boldsymbol{r}] \qquad (3.2)$$

where V is the volume of the unit cell and the summation is over all vectors $\boldsymbol{H}$. This equation shows that the electron density, and thus the crystal structure, can be calculated if both the magnitude $F(\boldsymbol{H})$ and phase $\alpha(\boldsymbol{H})$ of the structure factors are known from the XRD pattern. However, while the magnitudes of the structure factors are known from the intensities of diffraction maxima, the phases of the structure factors cannot be measured from the experimental XRD data, leading to the "the phase

problem" in crystallography. Although many methods have been developed to overcome this challenge to determine electron density from experimental data, the problem of peak overlap in powder XRD data leads to inaccurate intensity values, and failure to traditional structure solution methods. However, the development of the direct-space strategy provides a way around the challenge of peak overlap, and enables structure determination from powder XRD data for many materials without requiring the integrated intensities of individual reflections to be extracted from the experimental powder XRD data.

In the direct-space strategy, a reverse procedure is used, i.e. trial crystal structures are generated independently of the observed powder XRD data and their XRD patterns are calculated using equation (3.1) as an approximate description of the electron density $\rho(\boldsymbol{r})$ is known for each trial structure. The calculated powder XRD patterns of the trial structures are then compared point-by-point with the experimental powder XRD pattern. Given that the calculated and experimental powder XRD profiles are compared point-by-point, rather than comparing the integrated intensities of each peak, the problem of peak overlap is implicitly taken into account.

In the direct-space strategy, a structural model could be defined in two ways. The first way discards any prior knowledge of molecular connectivity or molecular geometry and defines the structural model as a set of structural variables which could be taken as the coordinates $\{x, y, z\}$ of all atoms in the asymmetric unit. The number of structural variables in this case would be 3N where N is the number of atoms in the asymmetric unit. However, for organic materials, the molecular connectivity and geometry, in general, is already known prior to structure determination from powder XRD data. Given that the molecular connectivity and geometry is known, the second way of defining a structural model is preferred. In this method, the bond lengths and angles are fixed at standard values, while the torsion angles which describe the conformation of the molecule are allowed to vary. Thus, a structural model can be defined on the basis of the position of the molecule in the unit cell (defined by the coordinates $\{x, y, z\}$[84] of a selected atom), the orientation of the molecule relative to the unit cell (defined by the rotation angles $\{\theta, \phi, \psi\}$) and a number of torsion angle variables $\{\tau_1, \tau_2, \tau_3, \ldots, \tau_n\}$. Thus for each molecule in the asymmetric unit, there are $6 + n$ variables, $\boldsymbol{\Gamma} = \{x, y, z, \theta, \phi, \psi, \tau_1, \tau_2, \tau_3, \ldots, \tau_n\}$, where n is the number of torsion angle variables. However, it is worth noting here that, for some structures, a molecule

could be fixed due to symmetry. For example, in the case of an inversion center or a rotation axis, one molecule may be fixed on an inversion center or on a rotation axis, reducing the number of positional variable for this fixed molecule. Figure 3.2 shows a schematic diagram of one molecule in the asymmetric unit which is located at a general position with structural variables defining the molecule. In this case, there are nine structural variables.

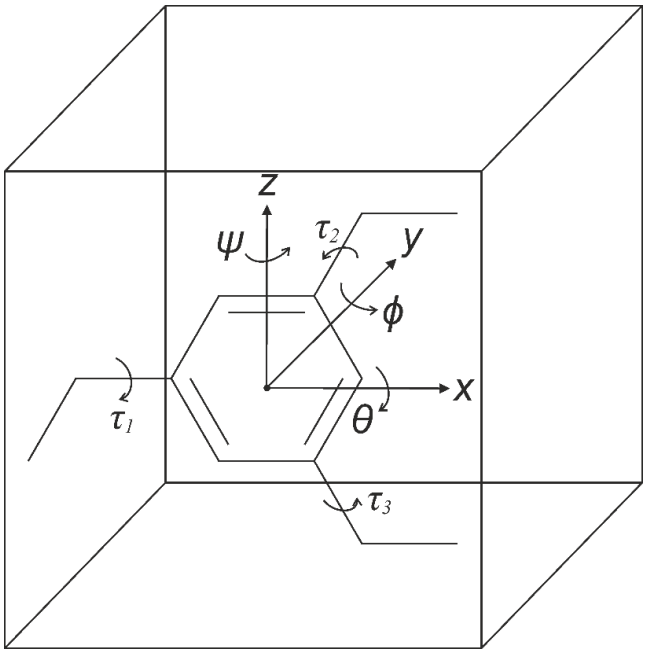

Figure 3.2. *A schematic diagram of one molecule in the asymmetric unit with structural variables defining the structural model. {x, y, z} are positional variables, {θ, ϕ, ψ} are orientational variables, {τ_1, τ_2, τ_3} are torsion angle variables.*

As mentioned above, the direct-space strategy involves generating trial structures in direct space to explore the hypersurface $\boldsymbol{\Gamma}$, assessing the quality of agreement between the calculated and experimental powder XRD patterns for each trial structure. The quality of agreement, or the "goodness of fit", can be judged using a suitable figure of merit which takes into account the comparison, point-by-point, between experimental and calculated powder XRD patterns. The most common comparison in the direct-space strategy uses the weighted (R_{wp}) and unweighted (R_p) profile *R*-factors, which are defined as follows:

$$R_p = 100 \times \frac{\sum_i \left| y_i - y_{ci} \right|}{\sum_i \left| y_i \right|} \tag{3.4}$$

$$R_{wp} = 100 \times \sqrt{\frac{\sum_i w_i \left(y_i - y_{ci} \right)^2}{\sum_i w_i y_i^2}} \tag{3.3}$$

where y_i is the intensity of the ith point in the digitized experimental powder XRD pattern, y_{ci} is the intensity of the ith point in the calculated powder XRD pattern, w_i is a weighting factor for the ith intensity point defined as $w_i = 1/y_i$ and the summation is over all the points in the powder XRD pattern. These whole-profile R-factors have the advantage that the whole digitized experimental data is used as recorded, and compared point-by-point with the calculated pattern, thus taking peak overlap into account implicitly. These R-factors are used in profile-fitting, structure solution, and Rietveld refinement stages.

The direct-space strategy handles structure solution as a global optimization procedure. Although, in principle, many search methods, such as Monte Carlo (simulated annealing)[124-125, 157-159] and differential evolution[160-161] can be used in this strategy, the genetic algorithm (GA) technique,[80, 84, 94, 96, 119-120, 131, 139, 162] which mimics genetic evolution in biological systems (and hence the name GA), is the most efficient technique in this regard. Structure solution calculations using the GA technique can be carried out in parallel using a number of independent processors. In GA, an initial population (P_0), which contains a number of randomly-generated trial structures (N_p), is used. These trial structures are generated randomly by assigning random values to the variables in the set $\boldsymbol{\Gamma}$.[84] This (P_0) population then evolves to the next generation (P_{j+1}) through evolution operations of mating, mutation and natural selection. Figure 3.3 shows a schematic diagram of the GA.

In mating operations, N_m pairs of randomly-selected trial structures are allowed to mate, producing $2N_m$ offspring and thus giving an intermediate population of N_p+2N_m. This mating process can be applied by different procedures such as "single point crossover" in which the structural variables are exchanged between a pair of parent structures at a defined point.[84] For example, for a rigid molecule, if one of the parent structures has a set $\boldsymbol{\Gamma}$ of $\{x_1, y_1, z_1, \theta_1, \phi_1, \psi_1\}$ and the other structure has a set

$\boldsymbol{\Gamma}$ of $\{x_2, y_2, z_2, \theta_2, \phi_2, \psi_2\}$, mating can be carried out by exchanging the positional variables $\{x, y, z\}$ and orientational variables $\{\theta, \phi, \psi\}$ to generate two offspring $\{x_1, y_1, z_1, \theta_2, \phi_2, \psi_2\}$ and $\{x_2, y_2, z_2, \theta_1, \phi_1, \psi_1\}$. For more complicated systems with higher number of variables in the set $\boldsymbol{\Gamma}$ (e.g. flexible molecules with n torsion angles), more complex rules of mating can be applied. To maintain the diversity within the population and reduce the chance of stagnation, mutation operations are applied, generating N_x mutants from the intermediate population.

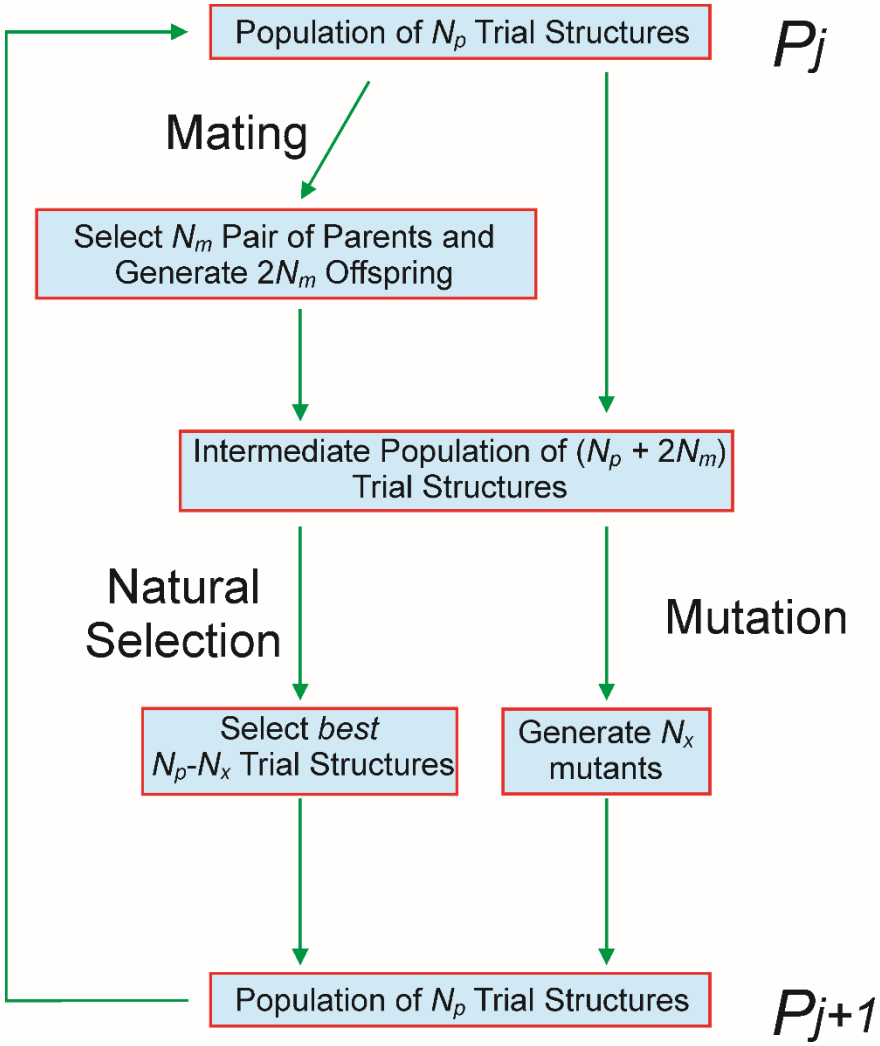

Figure 3.3. *A schematic diagram of the GA used in the direct-space strategy for structure solution from powder XRD data. This GA technique is implemented in the program EAGER which was used in structure determination during the course of this research.*

Mutation can be carried out by selecting random *Nx* structures from the intermediate population and then assigning random value(s) to one or more variables

in the set $\boldsymbol{\Gamma}$.[84] It is worth noting here that while the mating operation leads to a redistribution of the values of variables in the set $\boldsymbol{\Gamma}$, the mutation operation produces new values for variables in the set $\boldsymbol{\Gamma}$. A selection process, mimicking natural evolution where the best fit survives, will then select $N_p - N_x$ best trial structures from the intermediate population to the next generation P_{j+1}. This process of mating, mutation and natural selection can be repeated for any number of generations until the global minimum is successfully located. The ideal situation, in structure solution using GA, is that many processors converge on the same structural model confirming that this structural model is the global minimum. The program exploiting the GA technique for structure determination from powder XRD data, which was used in the course of this research, is EAGER.[103, 137, 163-166]

3.4 Structure Refinement

Having obtained a structural model that gives a good fit to the experimental data from the structure solution stage, this structural model can be optimized using the Rietveld refinement technique.[167] In Rietveld refinement, the variables that define the powder XRD profile, such as unit cell parameters, instrumental zero shift, peak shape and peak width, and atomic coordinates in the asymmetric unit (which control the peak intensities in the powder XRD pattern) are refined to improve the quality of fit between experimental and calculated powder XRD data (i.e., minimum R_{wp}). In addition, a scale factor, which determines peak intensities of the calculated powder pattern relative to the intensities of the experimental powder XRD pattern, is refined. These variables are usually refined in Rietveld refinement using a least squares procedure, which attempts to minimize the difference between the calculated and experimental powder pattern. The scale factor is usually refined first, which is then followed by refining atomic coordinates as a common practice. Unlike profile fitting, where the intensities are assigned arbitrary values to optimize the fit, the intensity in Rietveld refinement comes directly from the position of atoms in the asymmetric unit (and isotropic displacement parameter). Refining atomic positions, therefore, will improve the crystal structure by allowing the peak intensities to be optimized. However, allowing the atomic positions to change during the refinement may lead to an unstable refinement, resulting in divergence of the refinement rather than a convergence. To avoid this problem, geometric restraints (soft constraints) such as bond-length and bond-angle restraints, which can be extracted from similar structures in the Cambridge

Structural Database (CSD)[168] or based on standard bond lengths and bond angles,[169] should be applied to ensure stable and convergent refinement. Depending on the molecular structure, planarity restraints might also be applied. In addition, an isotropic displacement factor is refined (usually as a common value for all non-hydrogen atoms), with the value of the hydrogen atoms set to 1.2 times that for non-hydrogen atoms. It is generally recommended that the applied restraints should be tight, i.e. not allowing the atoms to move in big steps from their positions at the beginning of refinement. If the refinement is stable, atom positions are then allowed to move in bigger steps, by releasing the restraints.

3.5. Structure Optimization by Energy Minimization

Given that the structural model obtained from structure solution fits the experimental powder XRD data, there is another criterion for this structural model to be considered as "correct structure". The structural model has to be energetically stable, meaning that energy minimization of the structure should remain close to the final structure obtained in the Rietveld refinement. The similarity between the energy-minimized structure and the Rietveld structure can be established by calculating the root-mean-square deviation (RMSD) of atomic positions. The lower the value of the RMSD, the closer the atomic positions of the refined structure are to the energy-minimized structure. Energy minimization can be carried out using the program CASTEP[170] which uses Density Functional Theory (DFT)[171] to calculate the final energy of the structure. Energy values obtained from DFT can also be used in comparing different polymorphs to investigate which polymorph has the lowest energy and therefore is more stable.

Periodic DFT calculations are a powerful method for determining the energies of crystal structures, and as a validation tool for establishing whether a crystal structure determined from experimental diffraction data represents a true energy minimum. However, the reliability and accuracy of DFT calculations depend on the type of functional used and the method for implementing dispersion correction (which takes into account the effects of van der Waals interactions). Commonly used functionals are the semi-local density functional PBE[172] and the hybrid functional PBE0,[173] which may be combined together with dispersion corrections using the method of Tkatchenko and Scheffler (TS)[174] or the method of many-body dispersion

(MBD),[175] leading to a range of strategies for carrying out DFT calculations on molecular crystals. In general, the fastest method for calculating the energy of a crystal structure is the PBE-TS method. This method is commonly used to carry out geometry optimization of molecular crystal structures (for example, in the present work, to establish that a crystal structure determined from powder XRD data is close to an energy minimum). However, in terms of calculating accurate energies of crystal structures to allow reliable ranking of the relative energies of polymorphs, it has been shown that the PBE0-MBD method (which is significantly more computationally expensive than PBE-TS) is the most reliable and accurate approach,[176] and represents the current benchmark in this area of application of DFT calculations. In the context of establishing a reliable energy ranking of polymorphs, the currently accepted strategy is to carry out geometry optimization of the different polymorphs using the PBE-TS method, and then to calculate the energy of the resultant optimized structure of each polymorph using a single-point PBE0-MBD calculation. The energies calculated using the PBE0-MBD method are then used in the energy ranking of the different polymorphs.

Chapter 4: Structural, Thermal and Hydration/Dehydration Characterization of the (*S*)-ibuprofen:L-lysine Co-crystal System

4.1 Introduction

Co-crystallization is a well-established technique for modifying the behaviour of solid materials, for example to enhance physicochemical properties such as dissolution rate. Although the subject of co-crystals has been extensively studied and a large number of co-crystals has been reported, the definition of a co-crystal is still controversial. In relation to the research reported in this thesis, co-crystals are defined as *"solids that are crystalline materials composed of two or more molecules in the same crystal structure"*.[5-6]

Ibuprofen, a widely used painkiller due to its safety and efficacy, is listed on the WHO Essential Medicine List.[177] This drug molecule is chiral and exists as two enantiomers. The biologically active form is the (*S*) enantiomer (molecular structure, Figure 4.1a), but an enzymatic transformation occurs *in vivo*[178] to convert the (*R*) enantiomer to the biologically active (*S*) enantiomer. Thus, for a racemic sample of ibuprofen, the (*R*) enantiomer is converted to the (*S*) enantiomer in the biological environment. The aqueous solubility of ibuprofen is poor, leading to limited bioavailability and difficulties in manufacturing processes.[179]

L-lysine (molecular structure, Figure 4.1b) has been reported as a co-former to improve the dissolution rate of ibuprofen.[180] In addition, L-lysine was used in chiral resolution of racemic (rac) ibuprofen by enrichment crystallization, leading to (*R*)-ibuprofen:L-lysine and (*S*)-ibuprofen:L-lysine.[181] While the crystal structure of rac-ibuprofen:rac-lysine was reported,[182] the crystal structures of (*S*)-ibuprofen:L-lysine and (*R*)-ibuprofen:L-lysine have yet not been reported. Significantly, the (*S*)-ibuprofen:L-lysine co-crystal has higher a dissolution rate than (*R*)-ibuprofen:L-lysine and rac-ibuprofen:rac-lysine.[181]

In this chapter, the structural and thermal properties of two new solid forms of (*S*)-ibuprofen co-crystallized with L-lysine are reported. One form was found to be anhydrous (denoted **IL-AH**) while the other form was found to be a monohydrate (denoted **IL-MH**). The interconversion between these two phases through hydration/dehydration processes was also studied.

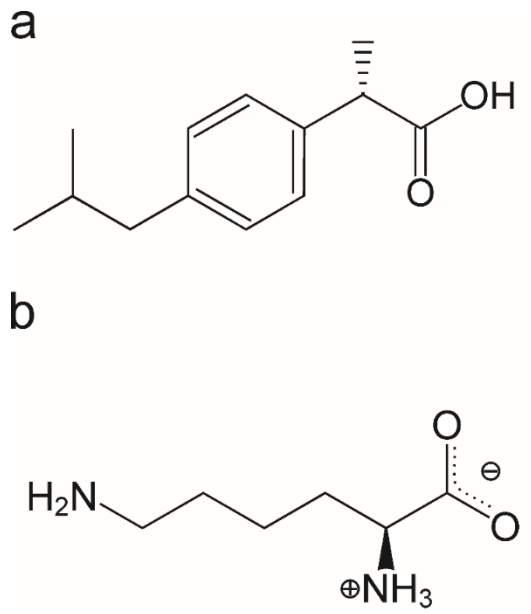

Figure 4.1. *Molecular structures of (a) (S)-ibuprofen and (b)* L*-lysine.*

Preparation of **IL-MH** was carried out by crystallization from solution (solvent evaporation), although large single crystals could not be grown. On the other hand, liquid-assisted grinding was used to prepare **IL-AH**. As both forms were produced as polycrystalline powders, crystal structure determination was carried out directly from powder XRD data. We recall that structure determination from powder XRD data is significantly more challenging than from single crystal XRD data. However, recent advances in methodology for structure determination from powder XRD data are such that crystal structures of moderate complexity can now be determined by this approach.[85-86, 94, 97-99, 101, 127, 183-188] In this regard, the direct-space strategy for structure solution[89, 93, 95, 100, 189] has created considerable opportunities to solve structures of organic molecular materials directly from powder XRD data. In this chapter, the direct-space strategy was used to solve the crystal structures of **IL-AH** and **IL-MH**, followed by Rietveld refinement. Periodic DFT-D calculations were also used in validation of the structures.

4.2 Experimental Section

4.2.1 Co-crystal Preparation

IL-AH was prepared by liquid assisted grinding. A 1:1 molar ratio of (*S*)-ibuprofen and L-lysine was weighed accurately and co-ground in a ball mill for 30 minutes in the presence of a few drops of ethanol. Milling was carried out at a

frequency of 30 Hz using a MM400 Retsch ball mill with 4 stainless steel balls (ball diameter, 3.18mm) inside the sample jar (grinding jar size, 1.5 ml).

IL-MH was prepared by crystallization from a solution containing a 1:1 molar ratio of (*S*)-ibuprofen and L-lysine. The solution was prepared by dissolving (*S*)-ibuprofen in ethanol and dissolving L-lysine in water, before mixing the two solutions. Slow solvent evaporation produced a microcrystalline powder (later identified as **IL-MH**), which was collected after a few days.

4.2.2 Thermal Analytical Measurements

Thermal analysis was carried by DSC (using a TA Instruments Q100) and TGA (using a Perkin Elmer 4000 ThermoGravimetric Analyser).

For DSC experiments, a few milligrams (typically 5 – 10 mg) of the sample was weighed accurately in an aluminium pan prior to hermetic sealing. The sample was heated from 20 °C to 200 °C and then cooled to –100 °C, followed by heating back to 20 °C (heating/cooling rate, 10 °C/min; nitrogen flow rate, 50 ml/min). In another experiment for **IL-MH**, the sample was heated from 20 °C to 110 °C and then cooled to 20 °C (heating/cooling rate, 10 °C/min). Another cycle of heating/cooling was applied using the same conditions. In another experiment for **IL-AH**, the sample was heated from 20 °C to 100 °C, then cooled to 20 °C (heating/cooling rate, 10 °C/min) followed by a second cycle of heating/cooling under the same conditions.

TGA experiments were carried out on 10 – 20 mg of the sample in an open aluminium pan using the following parameters: initial temperature, 20 °C; final temperature, 300 °C; heating rate, 10 °C/min; nitrogen flow rate, 50 ml/min.

4.2.3 Hydration/Dehydration Studies

To investigate hydration of **IL-AH**, a few milligrams of this phase were added to an open vial, which was then placed in a beaker partially filled with water. The beaker was covered with parafilm to ensure that a high saturated relative humidity was established within the system. After a few hours, the vial was removed from the beaker and powder XRD data were recorded on the solid sample recovered from the vial.

To study dehydration of **IL-MH**, a few milligrams of this phase were heated in a DSC instrument beyond the point of dehydration (at a temperature established from

TGA studies), and then cooled back to ambient temperature. The powder sample was recovered and powder XRD data were recorded.

4.2.4 Measurement of Powder XRD Data for Structure Determination

High-quality powder XRD data for structure determination were recorded using a Bruker D8 instrument (Ge-monochromated CuKα_1 radiation) operating in transmission mode. Each powder sample was packed into three 0.7 mm glass capillaries, which were then sealed and attached to the disc sample holder of the powder XRD instrument. The data were recorded over a 2θ range of 3.35° – 70° (step size 0.017°) with a total recording time of 17 hr.

Powder XRD data for **IL-AH** were recorded at ambient temperature and after heating to 80 °C on beamline I11 at Diamond Light Source. The sample was contained in a borosilicate glass capillary (0.7 mm), which was spun around the capillary axis to alleviate the effects of preferred orientation. Temperature was controlled using an Oxford Cryostream Plus. The data were recorded using a Multi-Analyser-Crystal (MAC) detector (λ = 0.824656 Å; step size, 0.001°; 2θ range, 1° – 150°; data collection time, 15 min).

4.2.5 High-resolution Solid-state ^{13}C NMR Spectroscopy

High-resolution solid-state ^{13}C NMR data were recorded for **IL-AH** and **IL-MH** using a Bruker AVANCE III spectrometer at the UK 850 MHz Solid-State NMR Facility (^{13}C Larmor frequency, 213.82 MHz; 4 mm HXY probe; zirconia rotor; 20 °C). The solid-state ^{13}C NMR spectra were recorded using ramped ^{1}H→^{13}C cross-polarization (CP)[190] together with ^{1}H decoupling using SPINAL-64[191][191][190][189][188][187][186][191][190][189][188][188][187][186] and magic-angle spinning (MAS) at 10 kHz. The solid-state ^{13}C NMR spectrum was also recorded for **IL-AH** at 80 °C using CP-MAS and a spinning speed of 10 kHz. The sample was then cooled to ambient temperature (25 °C) and the solid-state ^{13}C NMR spectrum was recorded.

4.2.6 Periodic DFT-D Calculations

Periodic Density Functional Theory (DFT-D) calculations were carried out using the program CASTEP[170] (Academic Release version 8.0). The calculations were carried out using a basic set cut-off energy of 700 eV and a Monkhorst-Pack[192]

grid of minimum sample spacing 0.05 × 2π Å, ultrasoft pseudopotentials,[193] PBE functional,[172] semi-empirical dispersion corrections (TS correction scheme),[174] fixed unit cell, preserved space group symmetry and periodic boundary conditions.

4.3 Results and Discussion

Two new solid forms of (*S*)-ibuprofen:L-lysine were prepared using liquid-assisted grinding and conventional crystallization from solution. One form was found to be an anhydrous phase (denoted **IL-AH**) and the other form was found to be a monohydrate phase (denoted **IL-MH**). The crystal structures of **IL-AH** and **IL-MH** were determined directly from powder XRD data. The hydration/dehydration behaviour of **IL-AH** and **IL-MH** was also investigated.

4.3.1 Thermal Analysis and Phase Behaviour

The presence or absence of water in the two phases was assessed initially by thermal analysis (DSC and TGA). DSC data for **IL-AH** (Figure 4.2) show a small endothermic peak at *ca.* 62 °C, followed by a large endothermic peak at *ca.* 178 °C (assigned to melting). TGA data (Figure 4.3) show no mass loss in the temperature region of *ca.* 62 °C, suggesting that the peak at *ca.* 62 °C in the DSC data is due to a solid-solid phase transition rather than a dehydration process. On cooling from the molten phase, a glass transition is observed at *ca.* 50 °C, indicating that the sample had transformed from the molten state to a glass state with no observation of a recrystallization process.

The occurrence of a solid-solid phase transition was also supported by a DSC experiment (Figure 4.4) in which the sample was heated from ambient temperature to 100 °C (i.e. above the temperature of the endotherm at *ca.* 62 °C but lower than the melting temperature) and then cooled back to ambient temperature, followed by another heating/cooling cycle. It is clear from Figure 4.4 that the thermal event giving rise to the endothermic peak at *ca.* 62 °C is reversible (with slight hysteresis), consistent with a solid-solid phase transition rather than a dehydration event. This phase transition was further confirmed from variable-temperature powder XRD data recorded on beamline I11 at Diamond Light Source (Figure 4.5), which shows clearly that the powder XRD pattern at 80 °C (i.e. above the phase transition temperature) is different from the powder XRD pattern recorded at ambient temperature (i.e. the

IL-AH phase). Solid-state ^{13}C NMR data (Figures 4.9 and 4.10) also confirm that the structural properties are different at ambient temperature (20 °C) and 80 °C, consistent with the occurrence of a solid-solid phase transition between these temperatures. At this stage, we refer to the unknown high-temperature phase produced by heating **IL-AH** above *ca*. 62 °C as **IL-X**.

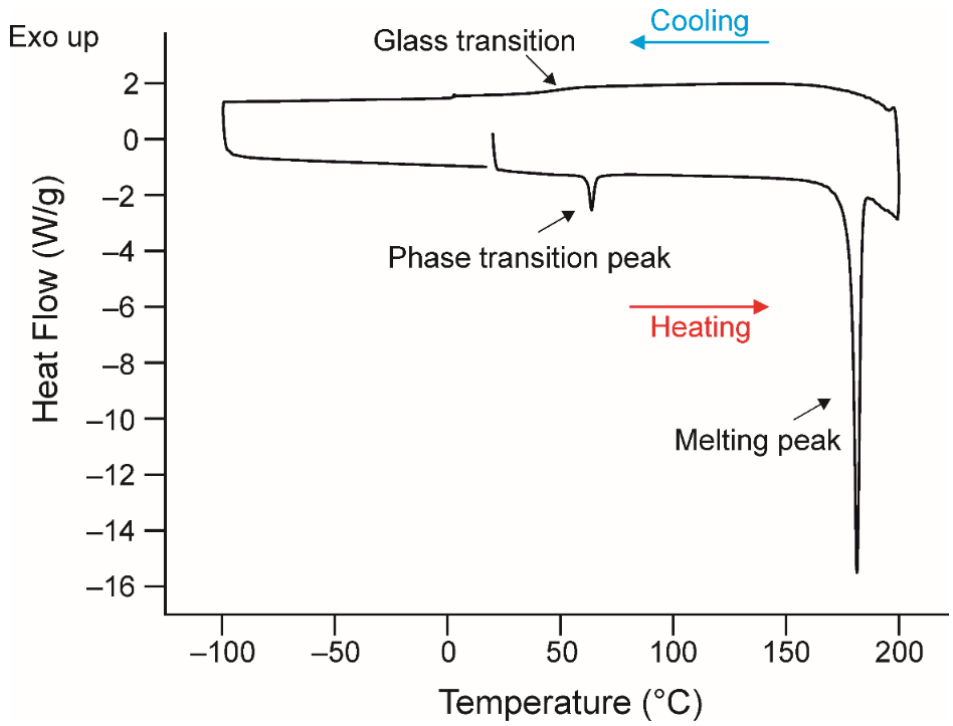

Figure 4.2. *DSC data for* ***IL-AH****.*

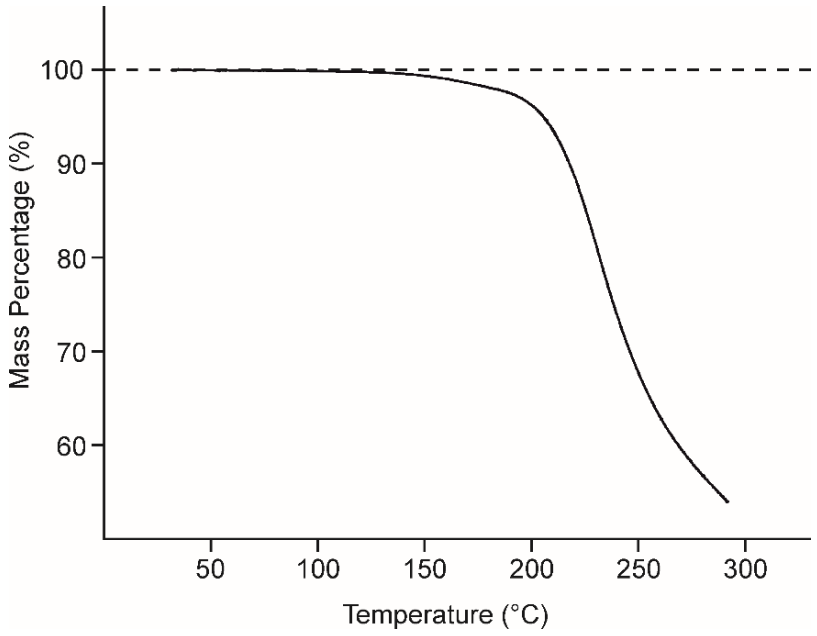

Figure 4.3. *TGA data for* ***IL-AH****, showing no mass loss before decomposition.*

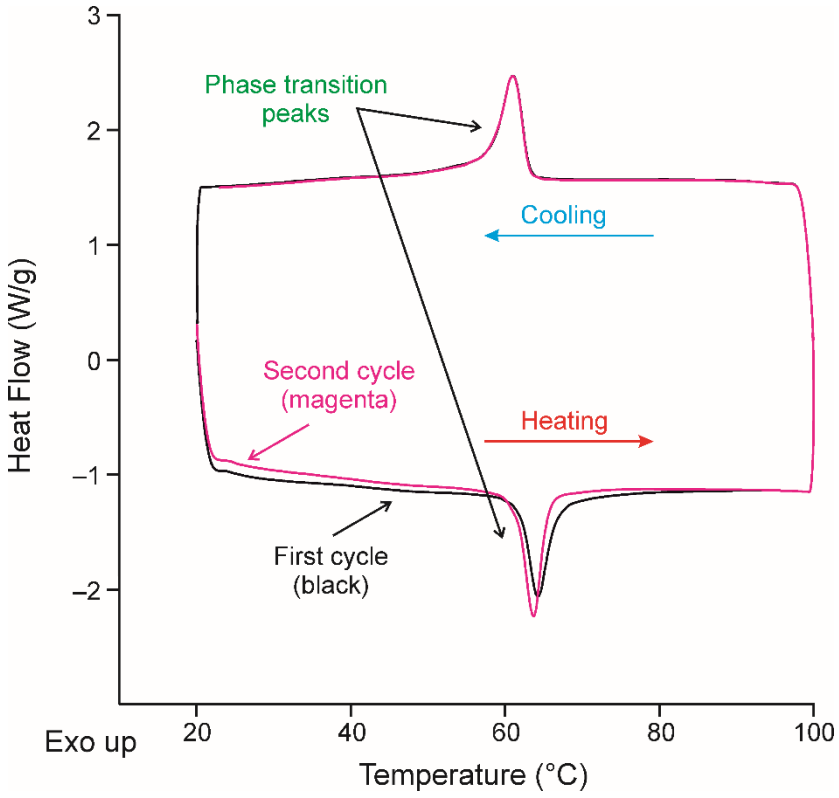

Figure 4.4. *DSC data for* ***IL-AH*** *recorded for two cycles of heating and cooling between 20 °C and 100 °C, showing a reversible solid-solid phase transition.*

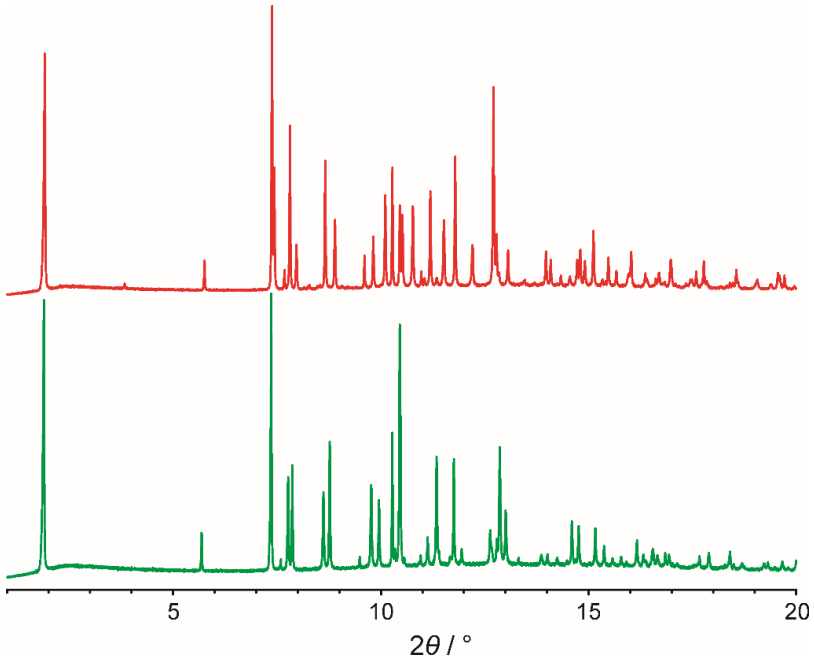

Figure 4.5. *Powder XRD data for* ***IL-AH*** *recorded at ambient temperature (red) and for* ***IL-X*** *at 80 °C (i.e. after heating* ***IL-AH*** *above the solid-solid transition at ca. 62 °C) (green).*

The presence of water in **IL-MH** was established by TGA (Figure 4.6). The TGA data shows a mass loss of 5% between *ca.* 50 °C and *ca.* 100 °C, followed by a substantial mass loss from *ca.* 190 °C due to decomposition of the sample. The mass loss of 5% corresponds to an equivalent of one molecule of water, confirming that **IL-MH** is a monohydrate. The assignment of this material as a monohydrate was also confirmed by structure determination from powder XRD data (see Section 4.3.6).

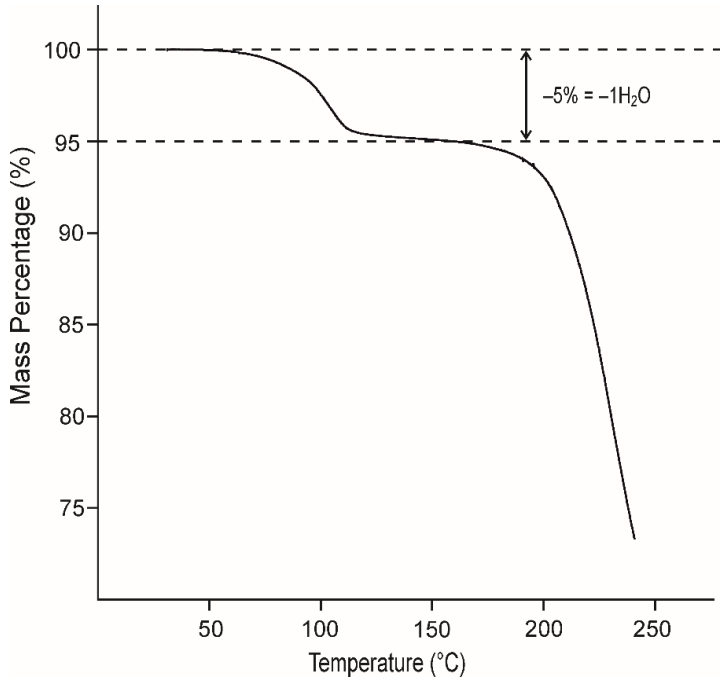

Figure 4.6. *TGA data for* ***IL-MH****, showing a mass loss corresponding to one equivalent of water.*

DSC data for **IL-MH** (Figure 4.7) show an endothermic peak at *ca.* 96 °C, followed by an endothermic melting peak at *ca.* 176 °C (this temperature is similar to the melting temperature of the **IL-AH** phase; Figure 4.2). The peak at *ca.* 96 °C corresponds to the dehydration event observed in the TGA data. On cooling from the molten phase, the sample undergoes a glass transition at *ca.* 5 °C, transforming from the molten state to a glass state, with no crystallization observed.

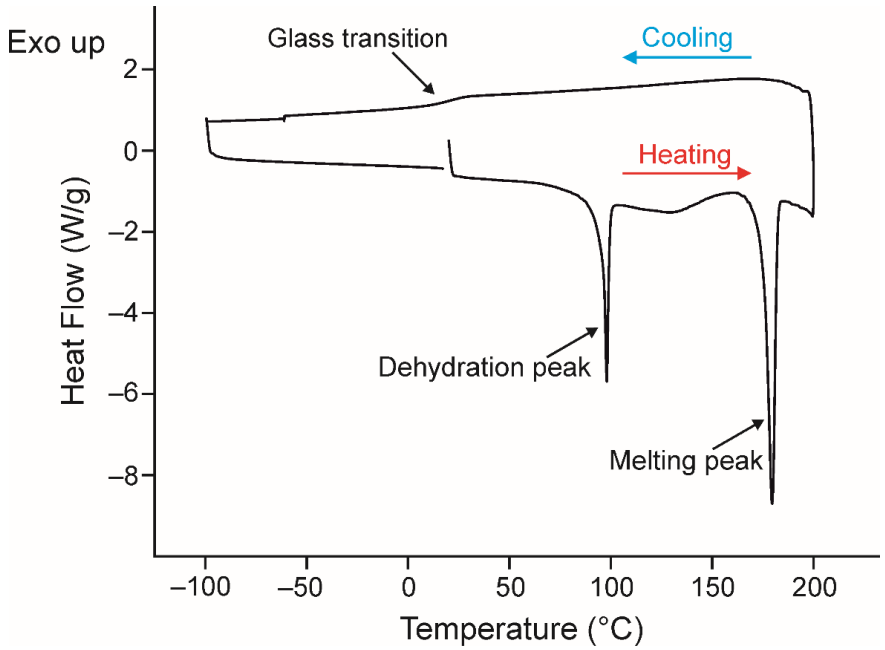

Figure 4.7. *DSC data for* ***IL-MH****.*

4.3.2 Hydration/Dehydration Behaviour

As **IL-AH** and **IL-MH** are anhydrous and monohydrate phases, respectively, a relevant question is what happens on hydration of **IL-AH** and on dehydration of **IL-MH**, and does the hydration/dehydration behaviour of this system occur in a reversible or irreversible manner? To address these questions, studies of hydration of **IL-AH** and dehydration of **IL-MH** were carried out.

Hydration of **IL-AH** was investigated by placing a vial containing **IL-AH** in an environment at a high saturated relative humidity (see Section 4.2.3). The powder XRD pattern of the sample recovered after this experiment is identical to the powder XRD pattern of **IL-MH**, confirming that **IL-AH** undergoes hydration at this relative humidity to produce **IL-MH**.

Dehydration of **IL-MH** was studied by heating a sample of **IL-MH** in a DSC experiment above the temperature of the dehydration peak (observed in the DSC data in Figure 4.6) but below the melting temperature, followed by cooling to ambient temperature and another cycle of heating/cooling was then applied. The results from this experiment are shown in Figure 4.8.

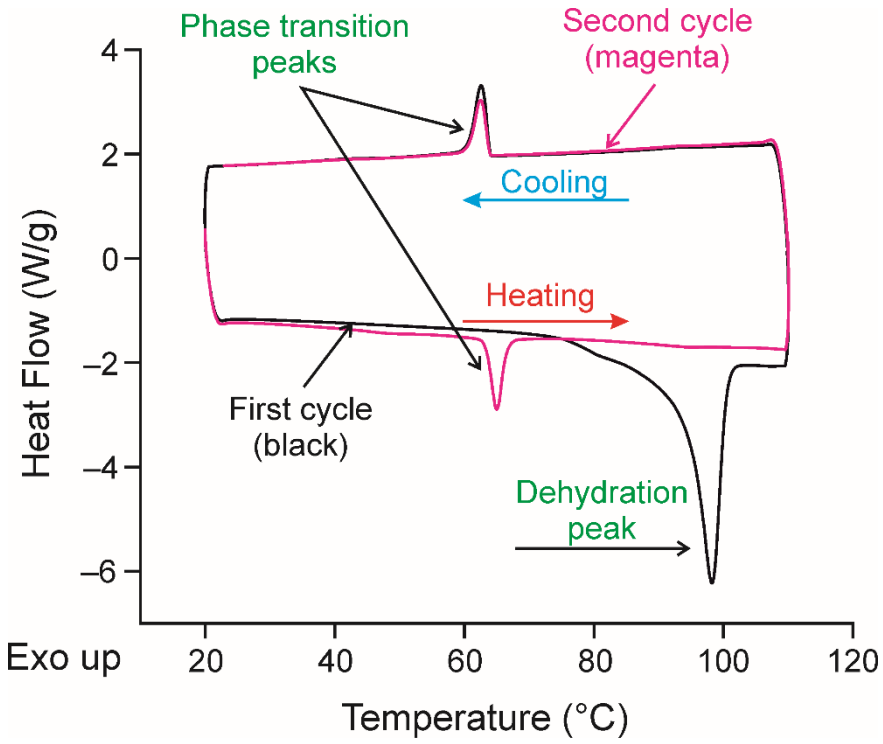

Figure 4.8. *DSC data for* ***IL-MH*** *showing the two cycle of heating/cooling. The sample was heated above the dehydration temperature, followed by cooling to ambient temperature.*

On heating the sample in the first cycle, an endothermic peak is observed, corresponding to dehydration of **IL-MH**. On cooling sample in the first cycle, an exothermic peak is observed at *ca.* 63 °C (very close to the temperature of the solid-solid phase transition observed for **IL-AH**; Figures 4.2 and 4.4). In the second cycle of heating/cooling a reversible phase transition (similar to that observed for **IL-AH**; Figure 4.4) is observed. The powder XRD pattern of the material recovered (at ambient temperature) is identical to the powder XRD pattern of **IL-AH**. Observation of the solid-solid phase transition at *ca.* 63 °C in the cooling stage of this experiment strongly suggests that the cooling process is associated with the phase transition from the high-temperature anhydrous phase **IL-X** to **IL-AH**, and therefore that the anhydrous material produced directly on dehydration of **IL-MH** is **IL-X**.

4.3.3 Solid-state ^{13}C NMR Spectroscopy of IL-AH and IL-X

The high-resolution solid-state ^{13}C NMR spectrum of **IL-AH** recorded at 20 °C is shown in Figure 4.9.

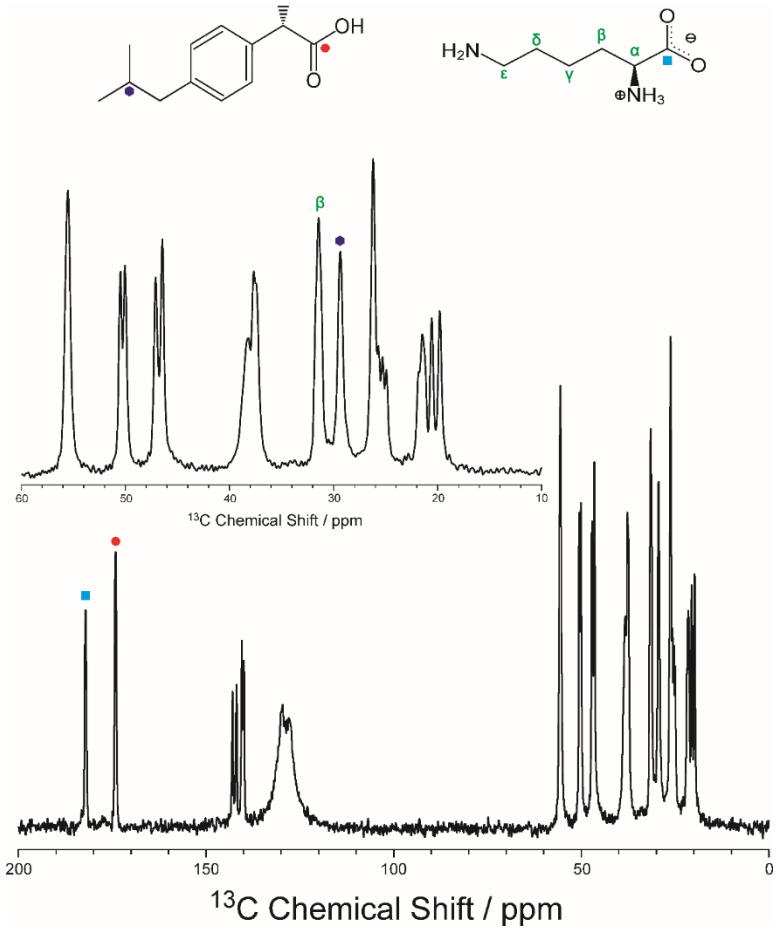

Figure 4.9. *High-resolution solid-state ^{13}C NMR spectrum of* ***IL-AH*** *recorded at ambient temperature. The red circle and blue square indicate peaks due to the carboxylate groups of (S)-ibuprofen and* L*-lysine.*

There are two isotropic peaks in the chemical shift range from 175 ppm to 185 ppm, assigned to the carboxylate groups of (*S*)-ibuprofen and L-lysine, suggesting that there is one (*S*)-ibuprofen molecule and one L-lysine molecule in the asymmetric unit. One peak is observed at *ca.* 32 ppm, assigned to the β carbon of L-lysine (Figure 4.9), and one peak is observed at *ca.* 30 ppm, assigned to the CH environment of (*S*)-ibuprofen (Figure 4.9). These observations are consistent with the presence of one L-lysine molecule and one (*S*)-ibuprofen molecule in the asymmetric unit.

As mentioned above, DSC and powder XRD data suggest that a solid-solid phase transition occurs on heating **IL-AH**, which is also supported by the high-resolution solid-state ^{13}C NMR results (Figure 4.10).

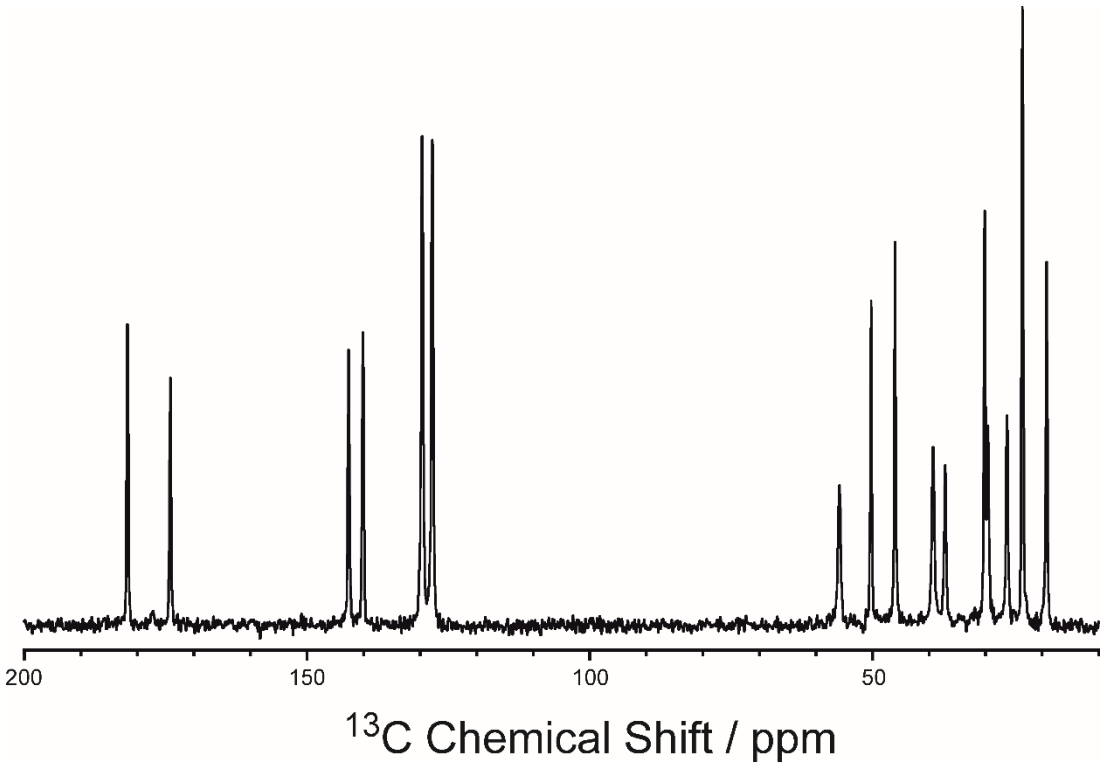

Figure 4.10. *High-resolution solid-state ^{13}C NMR spectrum of **IL-X** recorded on heating the **IL-AH** phase to 80 °C.*

The peaks for the phenyl ring of (*S*)-ibuprofen are between 125 and 145 ppm (Figure 4.9). On increasing temperature to 80 °C (to produce the **IL-X** phase), these peaks coalesce (Figure 4.10), probably due to mobility of the phenyl ring in (*S*)-ibuprofen at this temperature. Other significant changes in the high-resolution solid-state ^{13}C NMR spectrum are observed between ambient temperature and 80 °C (see, for example, the region around 20 ppm, arising from signals due to methyl groups in (*S*)-ibuprofen), consistent with significant structural changes between the **IL-AH** and **IL-X** phases. We note that the solid-state ^{13}C NMR spectrum recorded after cooling to ambient temperature is identical with the original spectrum of **IL-AH** recorded at ambient temperature before heating, indicating that the phase transition is reversible (in agreement with the DSC results).

4.3.4 Structure Determination of IL-AH from Powder XRD Data

Indexing and Profile Refinement

The powder XRD pattern of **IL-AH** was indexed using the program LZON[194] within the CRYSFIRE[195] package, giving the following unit cell with monoclinic

metric symmetry: a = 8.97 Å, b = 9.18 Å, c = 24.79 Å, β = 98.06°. Density considerations suggest that the unit cell contains four molecules of (*S*)-ibuprofen and four molecules of L-lysine. From systemic absences, the space group is assigned as *C*2; thus, the asymmetric unit contains one molecule of (*S*)-ibuprofen and one molecule of L-lysine. This conclusion is consistent with the solid-state ^{13}C NMR data for **IL-AH** (Figure 4.9), which suggests that the asymmetric unit contains one molecule of (*S*)-ibuprofen and one molecule of L-lysine.

The unit cell parameters from the indexing stage together with the assigned space group were used for profile fitting using the Le Bail method[149] incorporated in the program GSAS,[150] leading to a good quality of fit (R_{wp} = 3.39%, R_p = 2.25%; Figure 4.11a) with the following refined unit cell parameters: a = 8.977(20) Å, b = 9.188(20) Å, c = 24.799(7) Å, β = 98.066(19)°, V = 2025.35(8) Å^3.

Structure Solution

Structure solution of **IL-AH** was carried out using the direct-space genetic algorithm (GA) technique[89, 93, 95, 189] incorporated in the program EAGER.[81-82, 87, 90, 196-198] In the GA structure solution calculations, the L-lysine molecule was defined by 11 structural variables (2 positional, 3 orientational and 5 torsion-angle variables); we note that the *y*-coordinate of one molecule can be fixed for space group *C*2 (thus, there are only two positional variables for this molecule). The (*S*)-ibuprofen molecule was defined by 10 structural variables (3 positional, 3 orientational and 4 torsion-angle variables). Thus, the total number of structural variables was 20. In the GA structure solution calculations, the population size was 500 and the evolution was carried out for 300 generations. In each generation, 50 mating operations and 250 mutation operations were applied. In total, 16 independent GA calculations were carried out in parallel. After 300 generations, the same structure with the lowest R_{wp} was found in four of the 16 independent GA calculations.

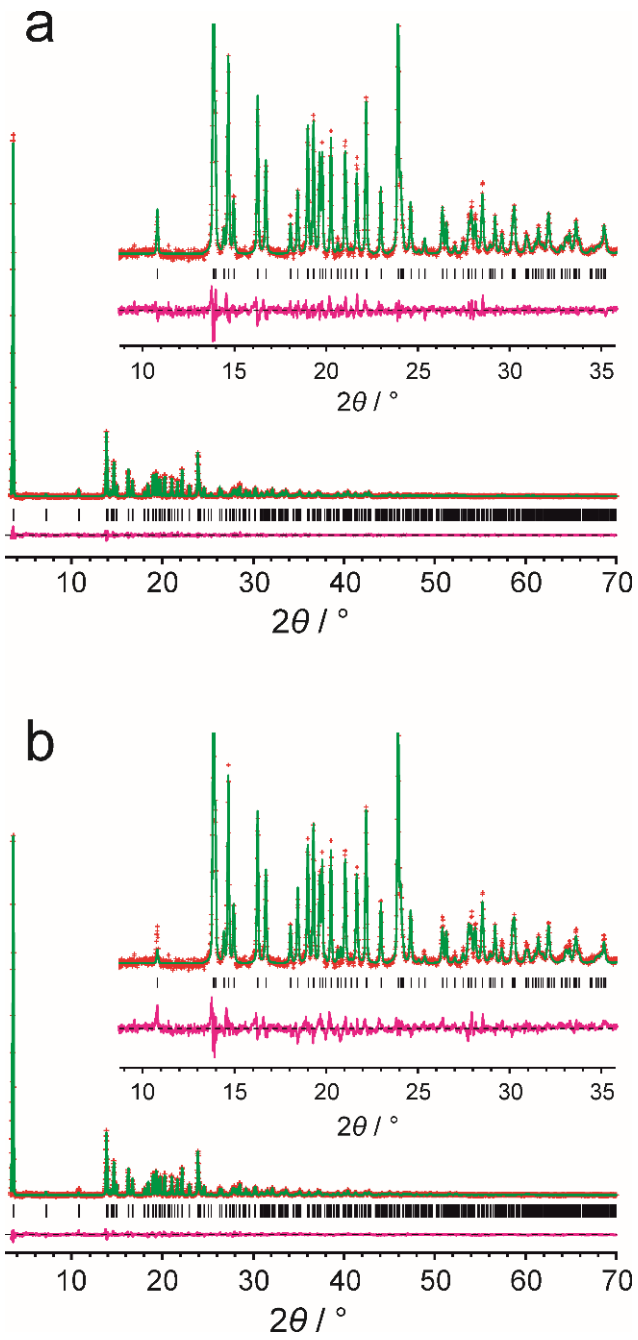

Figure 4.11. *(a) Le Bail fitting of the powder XRD pattern of* ***IL-AH****, (b) final Rietveld refinement of* ***IL-AH****. (Red crosses, experimental powder XRD pattern following background subtraction; green line, calculated powder XRD pattern; black tic marks, predicted peak positions; magenta line, difference plot).*

Structure Refinement

The best structure (with lowest R_{wp}) obtained in the GA structure solution calculations was used as the initial structural model for Rietveld refinement,[167] which was carried out using the program GSAS.[150] In the Rietveld refinement, standard

restraints[169] were applied to bond lengths and bond angles, and planar restraints were applied to the carboxylate groups of (*S*)-ibuprofen and L-lysine, and the phenyl ring of (*S*)-ibuprofen. A common isotropic displacement parameter was refined for all non-hydrogen atoms, and the value for hydrogen atoms was set at 1.2 times the value of non-hydrogen atoms. The final Rietveld refinement gave good agreement between calculated and experimental powder XRD patterns (R_{wp} = 4.26%, R_p = 3.04%; Figure 4.11b) with the following refined parameters: a = 8.978(27) Å, b = 9.188(28) Å, c = 24.796(10) Å, β = 98.066(25)°, V = 2025.13(13) Å^3 (2θ range, 3.35° – 70°; 4093 profile points; 187 refined variables).

The refined structure was subjected to DFT-D geometry optimization (with fixed unit cell), carried out using the program CASTEP[170] (Academic Version 8.0). The geometry-optimized structure showed only very minor atomic displacements (RMSD = 0.31 Å for non-hydrogen atoms) from the refined structure, indicating that the refined structure is very close to an energy minimum.

4.3.5 Structure Determination of IL-X from Powder XRD Data

Indexing and Profile Fitting

The powder XRD pattern of **IL-X** was indexed using the program DICVOL[199] in the CRYSFIRE[195] package, giving the following unit cell parameter with monoclinic metric symmetry: a = 9.16 Å, b = 9.21 Å, c = 25.22 Å, β = 98.9°, V = 2103 Å^3. Based on systematic absences, the space group was assigned as $C2$. Profile fitting was carried using the Le Bail method[149] in the program GSAS,[150] with initial unit cell parameters taken from the indexing stage. Profile fitting gave a good quality fit to the experimental powder XRD data (R_{wp} = 4.98%; R_p = 3.83%; Figure 4.12), confirming the assignment of space group as $C2$. The refined unit cell parameters were: a = 9.14945(10) Å, b = 9.20255(9) Å, c = 25.19385(29) Å, β = 98.9121(8)°, V = 2095.67(5) Å^3.

Density considerations indicate that the unit cell contains four molecules of (*S*)-ibuprofen and four molecules of L-lysine; thus, it was deduced that the asymmetric unit comprises one molecule of (*S*)-ibuprofen and one molecule of L-lysine. This observation is consistent with the high-resolution solid-state ^{13}C NMR spectrum of **IL-X** (Figure 4.10), which shows two peaks in the region 175 – 185 ppm (assigned to

carboxylate groups of (*S*)-ibuprofen and L-lysine), suggesting that the asymmetric unit comprises one molecule of (*S*)-ibuprofen and one molecule of L-lysine.

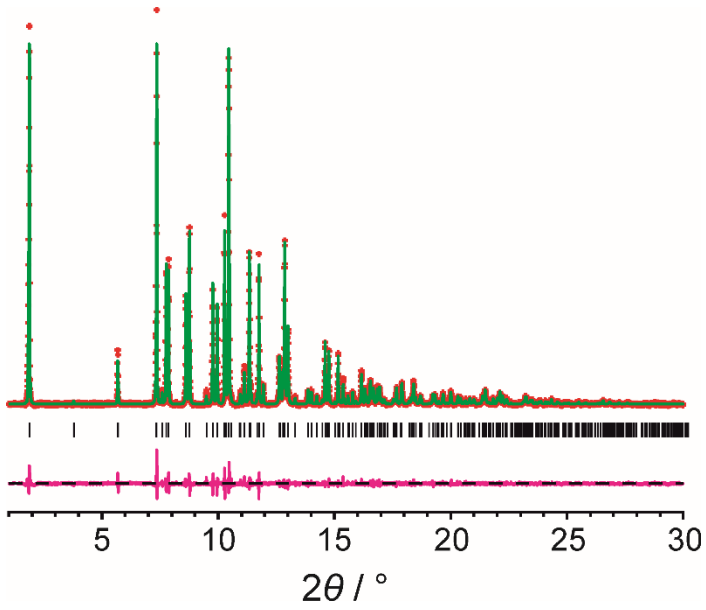

Figure 4.12. *Le Bail fitting of the powder XRD pattern of* ***IL-X****. (Red crosses, experimental powder XRD pattern following background subtraction; green line, calculated powder XRD pattern; black tic marks, predicted peak positions; magenta line, difference plot).*

Structure Solution

Structure solution of **IL-X** was carried out using the program EAGER,[81-82, 87, 90, 196-197] which implements the GA technique for direct-space structure solution. The structural fragment, comprising one molecule of (*S*)-ibuprofen and one molecule of L-lysine, was set up as described above for structure solution of **IL-AH**. For the direct-space structure solution calculations of **IL-X** in space group *C*2, the position of one molecule can be fixed along the *b*-axis (as was the case for **IL-AH**); hence, there were only two positional variables for this molecule, and thus the total number of structural variables in the direct-space structure solution calculation was 20.

In the GA structure solution calculations, the population size was 500 and the evolution was carried out for 500 generations. In each generation, 50 mating operations and 250 mutation operations were applied. In total, 16 independent GA calculations were carried out in parallel. After 500 generations, two processors converged on approximately the same structural model giving the best fit to the

experimental powder XRD data (i.e. lowest R_{wp}). This structure was used as the initial model for Rietveld refinement.

Structure Refinement

The method for Rietveld refinement of **IL-X** was similar to that described above for **IL-AH**. However, at the stage of completing this thesis, the quality of fit obtained in the Rietveld refinement was not considered satisfactory to represent a final refined structure. Thus, further work is required to complete the structure determination of **IL-X**, and this work remains "in progress" at this stage.

4.3.6 Structure Determination of IL-MH from Powder XRD Data

Indexing and Initial Profile Refinement

The powder XRD pattern of **IL-MH** was indexed using the program DICVOL[199] in the CRYSFIRE package, giving the following unit cell with orthorhombic metric symmetry: a = 5.17 Å, b = 41.22 Å, c = 9.71 Å. As it was not possible to assign the space group unambiguously based on systematic absences, profile fitting and subsequent structure solution were carried out for all possible chiral space groups in the orthorhombic system. In these structure solution calculations, a chemically and structurally acceptable structure was obtained only for space group $P2_12_12$. Profile fitting for space group $P2_12_12$, using the Le Bail method, gave a good quality of fit (R_{wp} = 3.05%; R_p = 2.29%) with the following refined unit cell parameters: a = 5.1799(15) Å, b = 41.2238(16) Å, c = 9.7099(5) Å, V = 2073.44(12) Å^3.

Initial Structure Solution

At this stage, the high-resolution solid-state ^{13}C NMR spectrum of **IL-MH** had not been recorded and therefore we did not have an experimental assessment of the number of independent molecules in the asymmetric unit. Based on the results from profile fitting, density considerations suggest that there are four molecules of (*S*)-ibuprofen and four molecules of L-lysine in the unit cell (and therefore also four molecules of water). For space group $P2_12_12$ (which has multiplicity of 4), the asymmetric unit therefore comprises one molecule of (*S*)-ibuprofen, one molecule of L-lysine molecule and one molecule of water.

Structure solution of **IL-MH** was carried out using the direct-space GA technique[89, 93, 95, 100, 189] incorporated in the program EAGER[81-82, 87, 90, 196-198] for the orthorhombic system with space group $P2_12_12$. The (*S*)-ibuprofen molecule was defined by 10 structural variables (3 positional variables, 3 orientational variables and 4 torsion angles), the L-lysine molecule was defined by 11 structural variables (3 positional variables, 3 orientational variables and 4 torsion angles), and the water molecule was defined by 6 structural variables (3 positional variables and 3 orientational variables). Thus, the total number of structural variables was 27. The population size was 500 and the GA calculation was run for 600 generations. In each generation, 50 mating operations and 250 mutation operations were applied. In total, 64 independent GA calculations were carried out in parallel. After 600 generations, four independent processors converged to the same structural model with the lowest R_{wp}.

Initial Rietveld Refinement

The best structure (i.e. with lowest value of R_{wp}) obtained in the GA structure solution calculations was used as the initial structural model for Rietveld refinement.[167] Standard restraints[169] were applied to bond lengths and bond angles, and planar restraints were applied to the carboxylate groups of (*S*)-ibuprofen and L-lysine, and to the phenyl ring of (*S*)-ibuprofen. Good agreement between calculated and experimental powder XRD patterns was obtained (R_{wp} = 3.42%, R_p = 2.54%), with the following refined unit cell parameters: a = 5.17909(20) Å, b = 41.2244(22) Å, c = 9.7098(5) Å, V = 2073.08(16) Å^3, (2θ range = 3.5 – 70°, 4090 profile points and 198 variables).

Solid-state ^{13}C NMR Spectroscopy

After completion of the Rietveld refinement of **IL-MH** based on the orthorhombic structure discussed above, the high-resolution solid-state ^{13}C NMR spectrum of **IL-MH** was recorded at 20 °C (Figure 4.13). Clearly, there are four peaks between 175 ppm and 185 ppm, assigned to the carboxylate groups of (*S*)-ibuprofen and L-lysine; this observation strongly suggests that the asymmetric unit actually contains two independent molecules of (*S*)-ibuprofen and two independent molecules of L-lysine. In addition, there are two peaks at *ca.* 32 ppm, assigned to the β carbon of L-lysine (Figure 4.13), and there are two peaks at *ca.* 30 ppm, assigned to the CH group

of (*S*)-ibuprofen. The solid-state ^{13}C NMR results therefore provide convincing evidence that there are two molecules of L-lysine and two molecules of (*S*)-ibuprofen (and hence also two molecules of water) in the asymmetric unit.

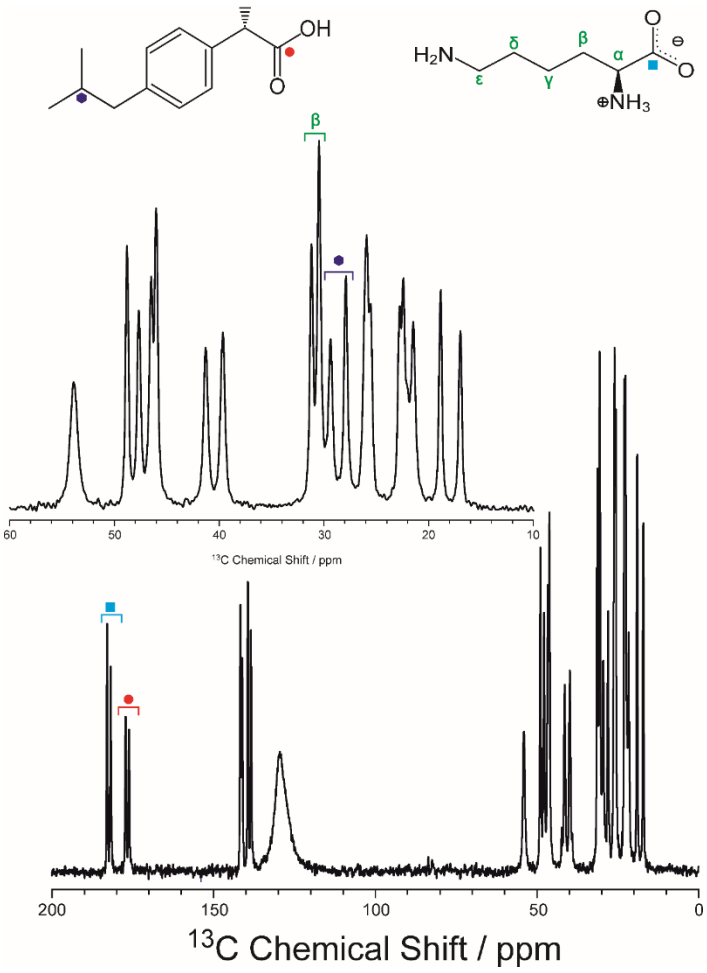

Figure 4.13. *High-resolution solid-state ^{13}C NMR spectrum of* ***IL-MH*** *recorded at 20 °C. Specific peaks discussed in the text are labelled.*

As this description of the asymmetric unit is not compatible with the orthorhombic structure determined in the initial structure determination of **IL-MH**, it was clearly necessary to revise the description of the structure of **IL-MH**. Our first approach was to explore the possibility that the orthorhombic structure (space group $P2_12_12$, which has multiplicity of 4) should be described more correctly as monoclinic (space group $P2_1$, which has multiplicity of 2). For this reason, the symmetry of the orthorhombic structure (with the same unit cell) was dropped to $P2_1$ (a subgroup of $P2_12_12$). In the $P2_1$ description, the asymmetric unit contains two molecules of (*S*)-ibuprofen and two molecules of L-lysine, consistent with the solid-state ^{13}C NMR

data. Space group $P2$ was ruled out as structure solution calculations using this space group produced structures that were not structurally or chemically sensible.

Revised Profile Fitting in the Monoclinic System

Given the change of crystal symmetry to monoclinic, profile fitting was carried out again, starting from the orthorhombic unit cell parameters but with the β angle (initially 90° from the orthorhombic unit cell) now allowed to vary. Le-Bail fitting in space group $P2_1$ gave a good fit to the powder XRD data (R_{wp} = 3.00%, R_p = 2.24%; Figure 4.14a) with the following refined unit cell parameters: a = 5.17769(20) Å, b = 41.2401(15) Å, c = 9.7059(4) Å, β = 89.948(14)°, V = 2072.5(14) Å^3. The quality of the Le Bail fitting for the monoclinic description in space group $P2_1$ (Figure 4.14a) is better than that for the orthorhombic description.

Final Rietveld Refinement

The initial model for Rietveld refinement for the monoclinic structure, was obtained by taking the refined orthorhombic structure and dropping the symmetry from $P2_12_12$ to $P2_1$. This was carried out by taking the coordinates of the asymmetric unit of the orthorhombic structure and applying one of the symmetry operations for $P2_12_12$, specifically the 2-fold rotation axis parallel to the c-axis. Thus, the monoclinic structure had one copy of molecules that were the same as the asymmetric unit of the orthorhombic structure (x, y, z) and one copy that had been transformed by the operation ($\bar{x}$, $\bar{y}$, z). The conventional unit cell setting for the monoclinic system was used with the b-axis as the unique axis.

Rietveld refinement was carried out for the monoclinic structure with space group $P2_1$ using the same refinement strategy described above for the orthorhombic structure. The final refined monoclinic structure (Figure 4.14b) gave a better fit (R_{wp} = 3.35%; R_p = 2.49%) than the refined orthorhombic structure, further supporting the monoclinic structure as the correct description. The final refined parameters for the monoclinic structure are: a = 5.179(32) Å, b = 41.222(34) Å, c = 9.711(7) Å, β = 90.078(19)°, V = 2073.28 Å^3 (2θ range, 3.35° – 70°; 4090 profile points; 195 refined variables).

A DFT-D geometry optimization calculation was carried out for the final refined structure (with fixed unit cell) and showed only minor atomic displacements, confirming that the refined structure is close to an energy minimum.

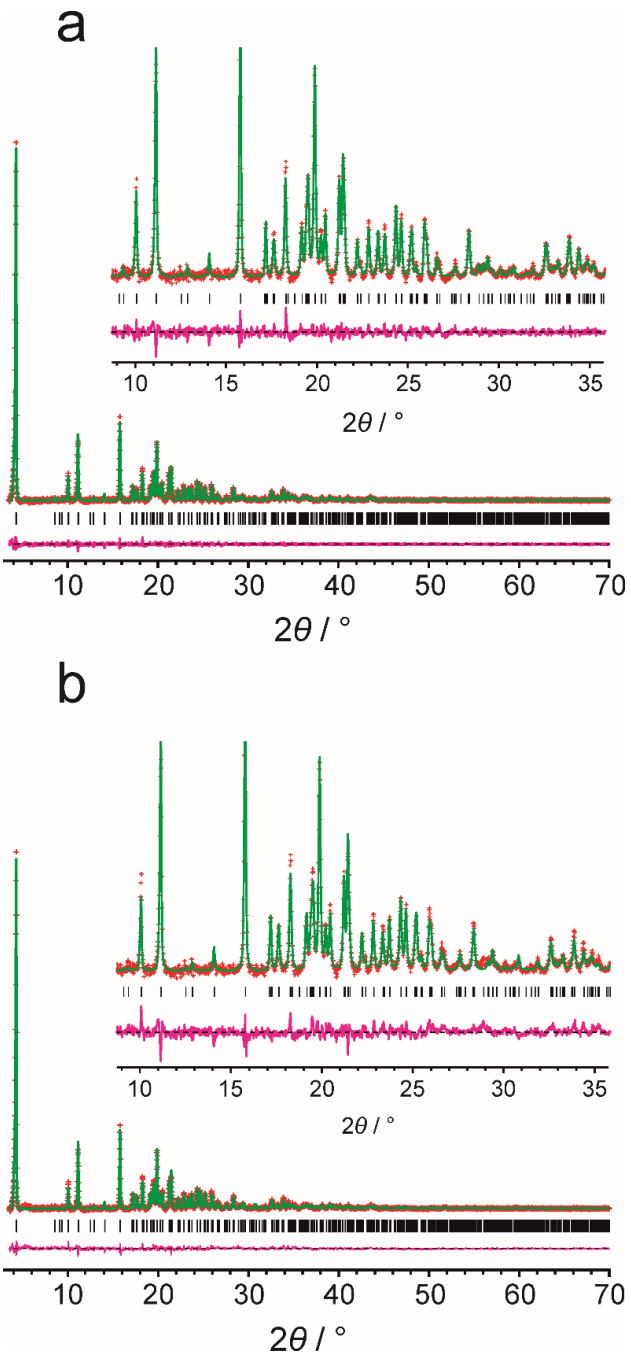

Figure 4.14. *(a) Le Bail fitting of the powder XRD pattern of* ***IL-MH*** *(with monoclinic system), and (b) final Rietveld refinement of* ***IL-MH*** *(with monoclinic system). (Red crosses, experimental powder XRD pattern following background subtraction; green line, calculated powder XRD pattern; black tic marks, predicted peak positions; magenta line, difference plot).*

To confirm that the monoclinic description (space group $P2_1$) represents a more correct representation of the structure than the orthorhombic description (space group $P2_12_12$), the energy of each structure was calculated by DFT-D. The monoclinic

structure has lower energy by *ca.* 10 kJ mol^{-1}. Furthermore, the hydrogen bonding arrangement is structurally and chemically more plausible for the monoclinic structure, particularly with regard to the hydrogen bonding involving the water molecules (this issue is discussed in more detailed in Section 4.3.8). Furthermore, the solid-state ^{13}C NMR spectrum calculated for the monoclinic structure is in good agreement with the experimental solid-state ^{13}C NMR spectrum (Figure 4.15), further suggesting that the monoclinic structure is more correct. The combination of Rietveld refinement, solid-state ^{13}C NMR results and DFT-D calculations leads to the conclusion that the monoclinic description of the structure of **IL-MH** is correct.

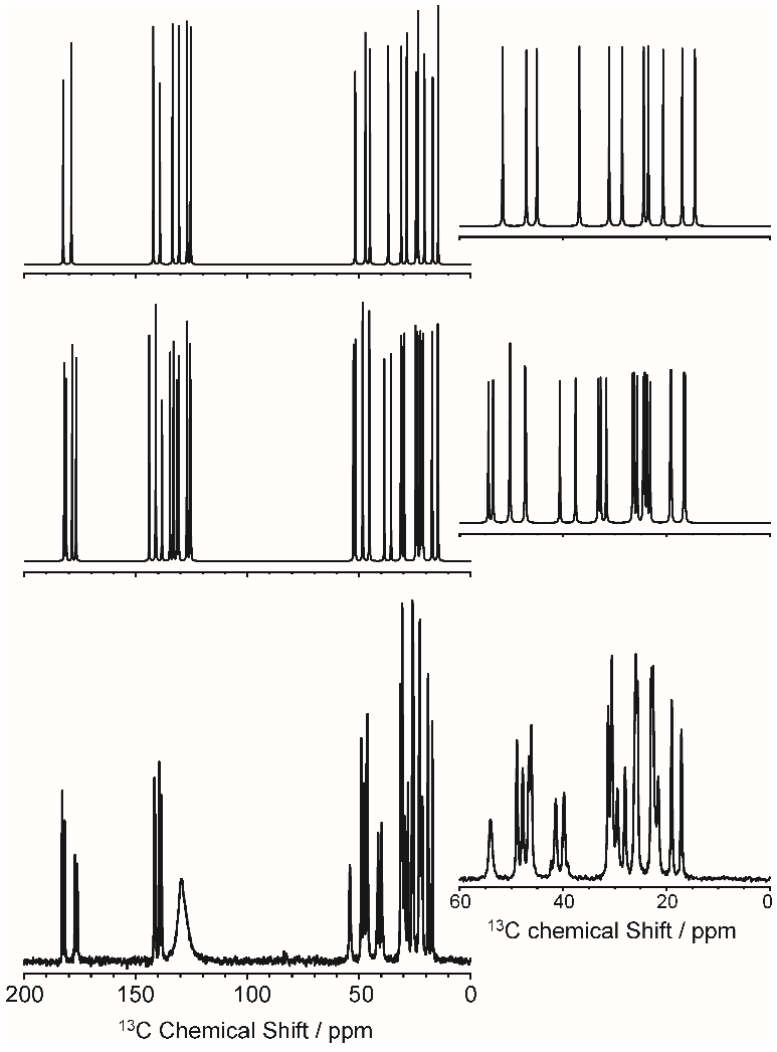

Figure 4.15. *Solid-state ^{13}C NMR spectrum calculated for the refined orthorhombic structure of* ***IL-MH*** *(top), solid-state ^{13}C NMR spectrum calculated for the refined monoclinic structure of* ***IL-MH*** *(middle), and the experimental ^{13}C NMR spectrum of* ***IL-MH*** *(bottom). The better agreement between the middle and bottom spectra suggests that the monoclinic structure is more plausible.*

4.3.7 Structural Properties of IL-AH

The crystal structure of **IL-AH** (Figure 4.16) is a layered structure, comprising a hydrophilic region and a hydrophobic region.

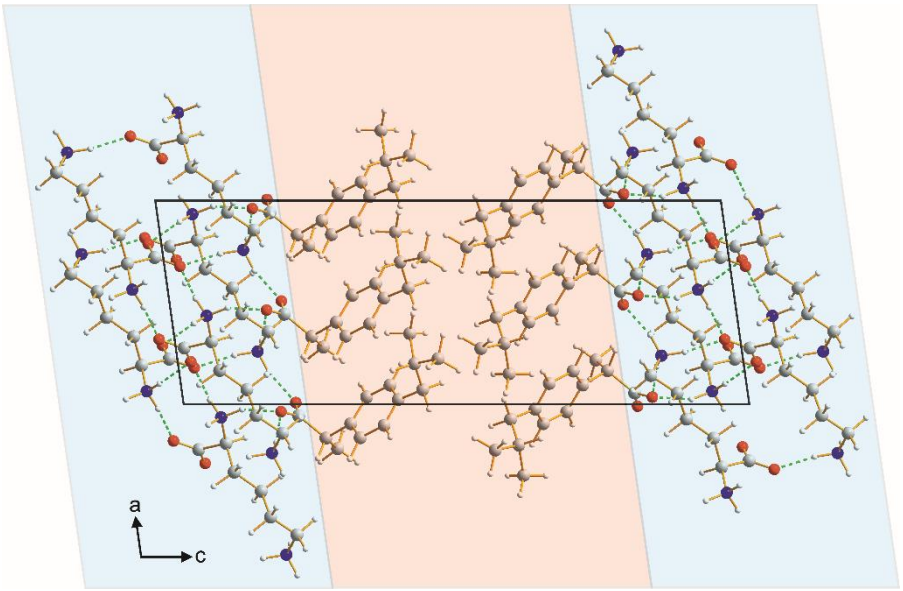

Figure 4.16. *Crystal structure of* ***IL-AH*** *viewed along the b-axis, showing the hydrophilic region (blue shading) and hydrophobic region (red shading). Hydrogen bonds are indicated by green dashed lines.*

In the hydrophilic region (blue shaded region in Figure 4.16), L-lysine molecules are hydrogen bonded to each other, forming layers parallel to the *ab*-plane (Figure 4.17). Within each layer, pairs of L-lysine molecules interact in a head-to-head manner (Figure 4.18) involving two N–H···O hydrogen bonds; in each case, an N–H bond of the head-group ammonium of one L-lysine molecule is hydrogen-bonded to the carboxylate group of the other L-lysine molecule, and *vice versa*. In addition, pairs of L-lysine molecules interact in a head-to-tail manner (Figure 4.18) involving two N–H···O hydrogen bonds; in each case, an N–H bond of the side-chain ammonium of one L-lysine molecule is hydrogen-bonded to the carboxylate group of the other L-lysine molecule, and *vice versa*. The layers of L-lysine molecules are connected through N–H···O hydrogen bonds.

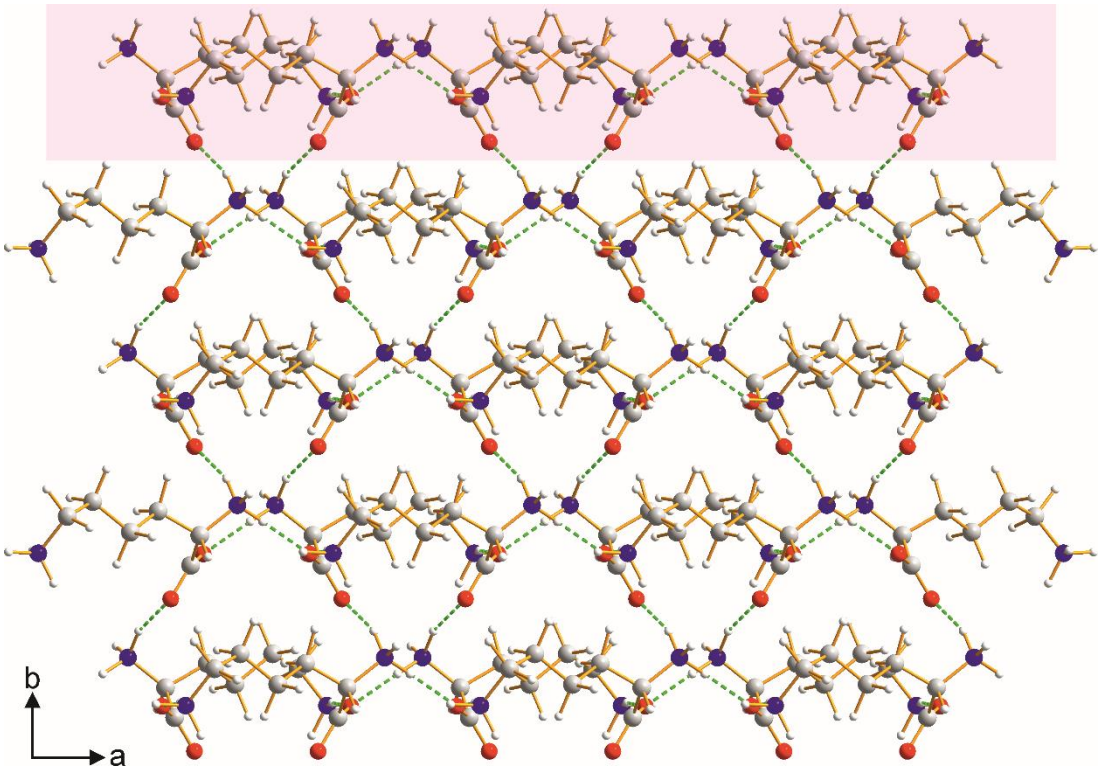

Figure 4.17. *A single layer of* L*-lysine in the crystal structure of* ***IL-AH*** *viewed along the c-axis, perpendicular to the plane of the layer (which is parallel to the ab-plane). To show the hydrogen bonding more clearly within the layer, the shaded part in magenta is viewed along the b-axis in Figure 4.18. Hydrogen bonds are defined by green dashed lines.*

We note that the interactions between L-lysine molecules in this structure differ from those in the crystal structure of pure anhydrous L-lysine.[200] While the structure of **IL-AH** contains N–H···O head-to-head and N–H···O head-to-tail interactions between L-lysine molecules, the crystal structure of pure anhydrous L-lysine contains N–H···N tail-to-tail (side chains) and N–H···O head-to-head (head groups) hydrogen bonds.

The hydrogen bonding between (*S*)-ibuprofen and L-lysine molecules in the structure of **IL-AH** is shown in Figure 4.18. The (*S*)-ibuprofen molecules interact with L-lysine molecules at the periphery of L-lysine layer through N–H···O hydrogen bonding, with the side-chain ammonium group of L-lysine as the donor and an oxygen of the carboxylate group of (*S*)-ibuprofen as the acceptor. The other oxygen of the carboxylate group of (*S*)-ibuprofen acts as an acceptor in an N–H···O hydrogen bond with the head-group ammonium of another L-lysine molecule as the donor.

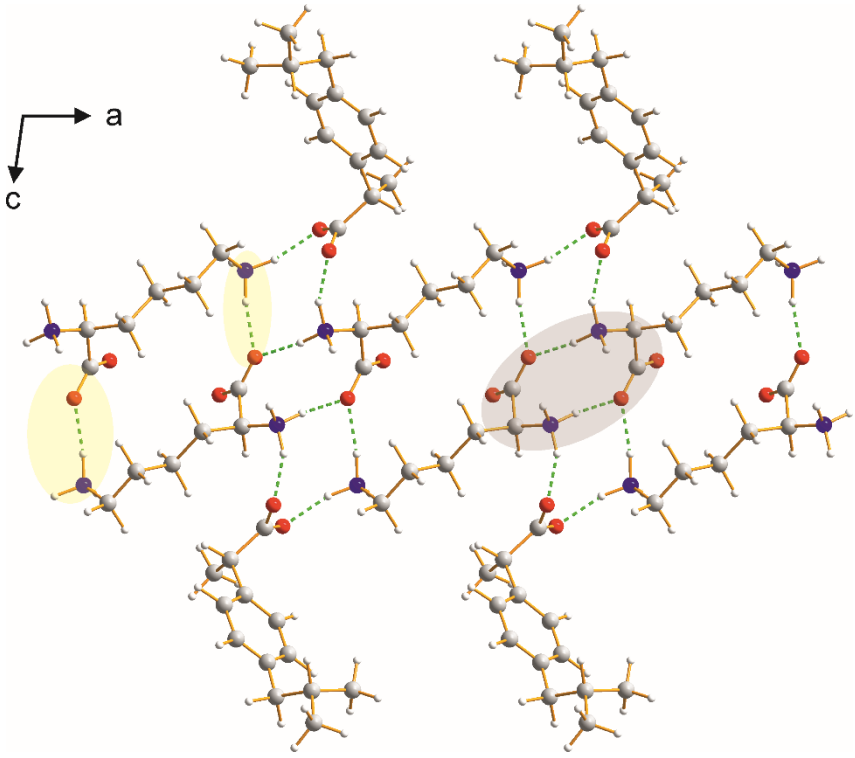

Figure 4.18. *Part of a single layer of L-lysine molecules (corresponding to the magenta-shaded box in Figure 4.17), highlighting the head-to-head (shaded in brown) and head-to-tail (shaded in yellow) interactions between L-lysine molecules. The (S)-ibuprofen molecules that interact through N–H···O hydrogen bonds at the periphery of the L-lysine layer are also shown. Green dashed lines indicate hydrogen bonding.*

The hydrophobic region of **IL-AH** is a bilayer involving the phenyl rings and isobutyl groups of (*S*)-ibuprofen molecules (Figure 4.19). In each single layer of the hydrophobic bilayer, the (*S*)-ibuprofen molecules are arranged such that the planes of the phenyl rings are parallel to each other (Figure 4.20). The other layer of the hydrophobic bilayer is oriented such that the planes of the phenyl rings form acute angles with respect to the planes of the phenyl rings of the other layer. Figure 4.21 shows the arrangement of the hydrophobic bilayer in **IL-AH**.

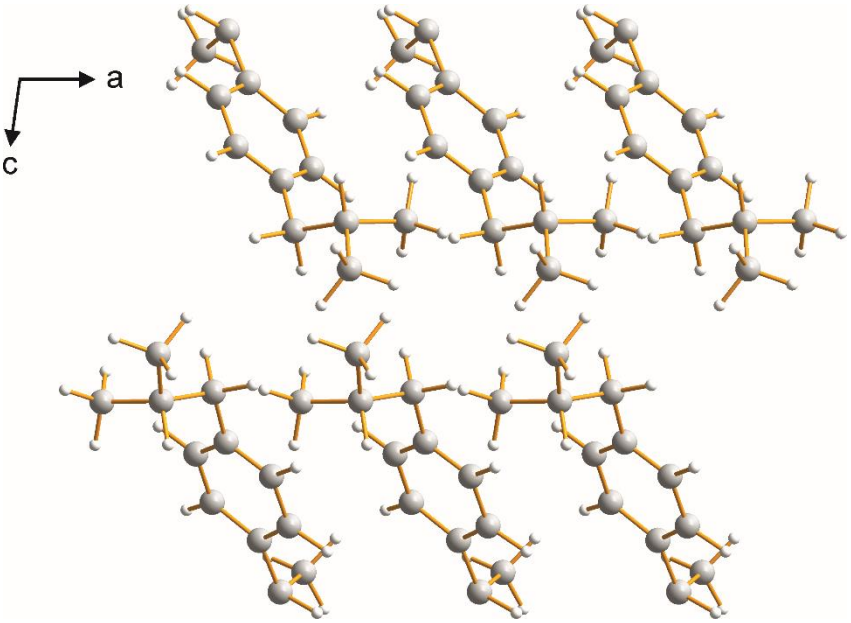

Figure 4.19. *The hydrophobic bilayer of* ***IL-AH*** *viewed along the b-axis. The carboxylate groups of (S)-ibuprofen molecules are omitted for clarity.*

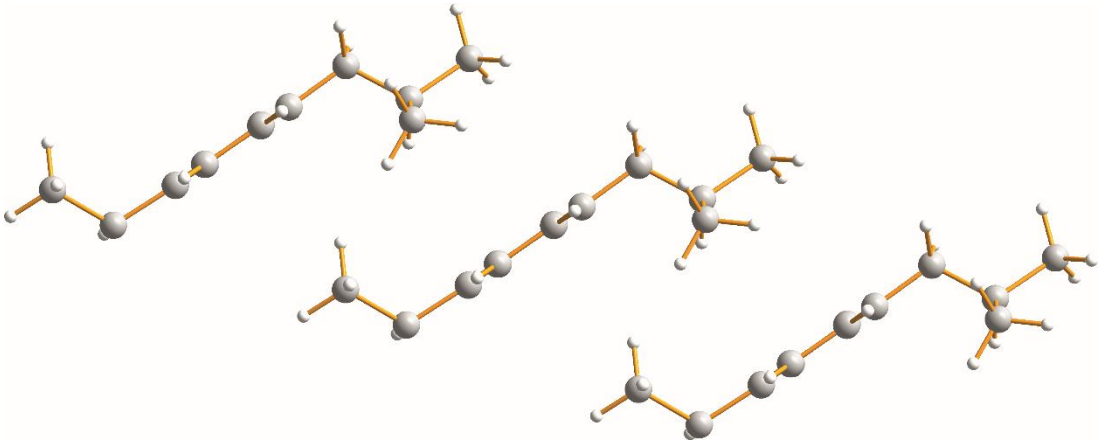

Figure 4.20. *A single layer of the hydrophobic bilayer of (S)-ibuprofen molecules in* ***IL-AH****, showing that the planes of the phenyl rings are parallel to each other. The carboxylate groups of the (S)-ibuprofen molecules are omitted for clarity.*

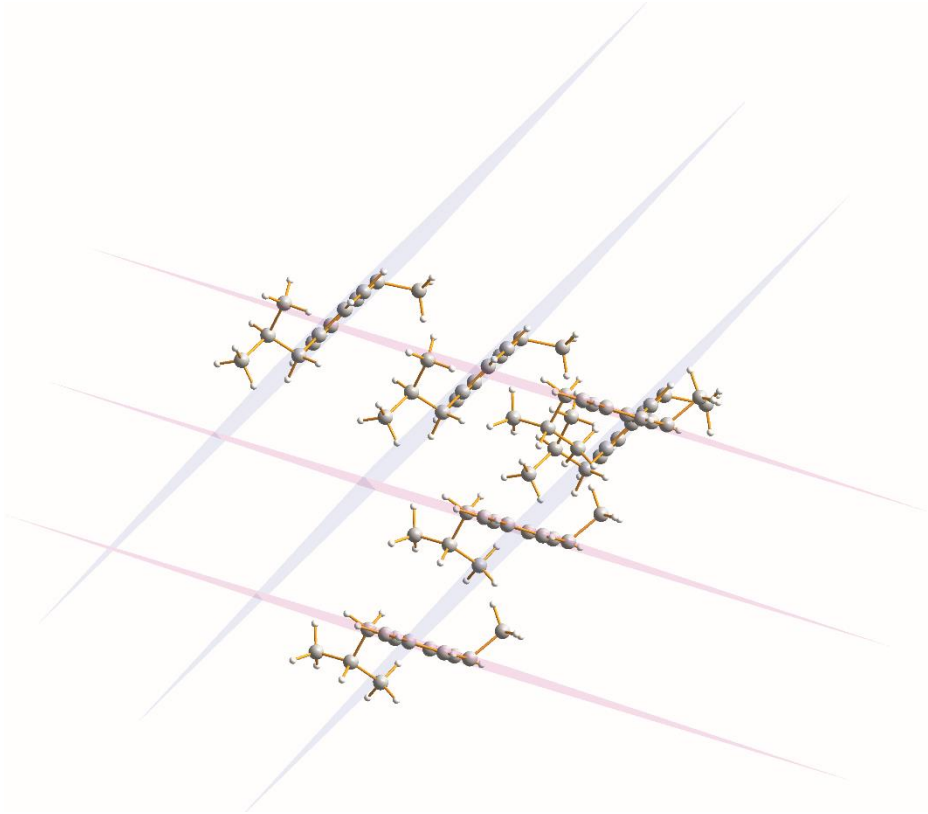

Figure 4.21. *Arrangement of (S)-ibuprofen molecules in the bilayer of the hydrophobic layer in* ***IL-AH****. The carboxylate groups of the (S)-ibuprofen molecules are omitted for clarity.*

4.3.8 Structural Properties of IL-MH

The crystal structure of **IL-MH** (as refined in the monoclinic system) is now described. First, we recall that the orthorhombic description of the structure gave a good fit to the powder XRD data, so clearly it is a reasonable approximation to the correct structure. Clearly, it is relevant to discuss this matter and to highlight the differences (particularly relating to the water molecules) that arise in the monoclinic description. Figure 4.22 shows an overlay between the monoclinic and orthorhombic descriptions of the structure. The two structures are very similar, with some differences in the conformations of the (*S*)-ibuprofen and L-lysine molecules but with greater differences in terms of the positions and orientations of the water molecules. In the orthorhombic description, there is one water molecule in the asymmetric unit, and therefore the two water molecules in close proximity of each other are related by a 2-fold rotation axis parallel to the *c*-axis. As a consequence, the two water molecules in the orthorhombic description cannot (at least in an ordered structure) be engaged in

hydrogen bonding with each other, given the unsymmetric nature of the O–H···O hydrogen bond. In contrast, in the monoclinic description, the two water molecules are engaged in an O–H···O hydrogen bond with each other, and also form a very plausible hydrogen bonding arrangement with (*S*)-ibuprofen and L-lysine molecules in their immediate neighbourhood. Figure 4.23 shows a comparison of the hydrogen bonding regions involving the water molecules in the monoclinic and orthorhombic descriptions.

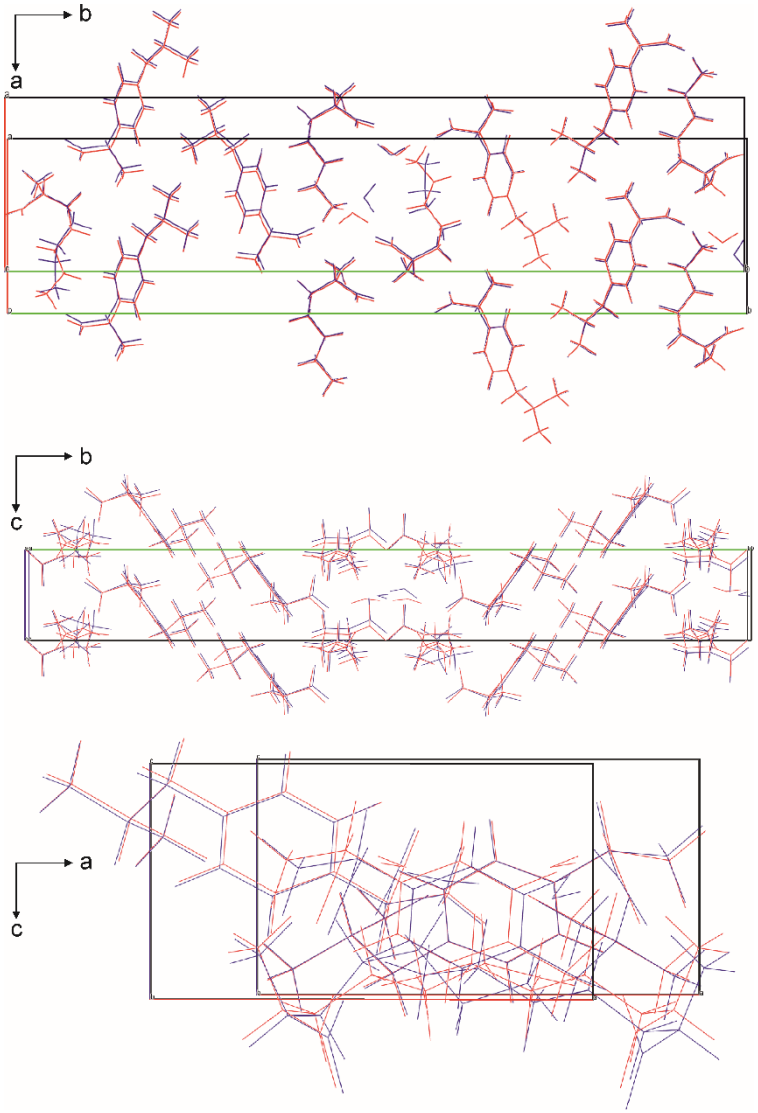

Figure 4.22. *Overlay of the monoclinic (blue) and orthorhombic (red) descriptions of the structure of* ***IL-MH****, viewed in different directions, showing that the two structures are similar. However, there are some conformational differences concerning the (S)-ibuprofen and L-lysine molecules, and a significant difference in the orientations of the water molecules*

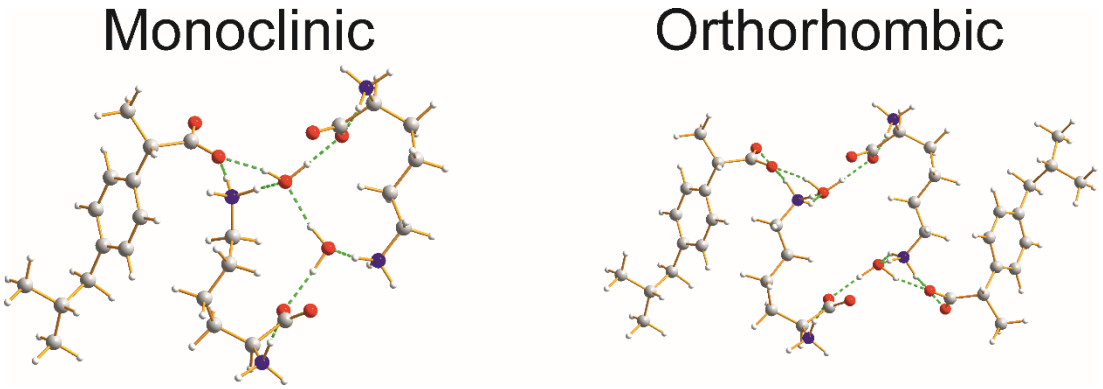

Figure 4.23. *Comparison of hydrogen bonding arrangements involving the engagement of water molecules in hydrogen bonding in the monoclinic and orthorhombic descriptions of the structure of* ***IL-MH****.*

Now, we focus only on the monoclinic description of the crystal structure of **IL-MH** (Figure 4.24), which is a layered structure with both hydrophilic and hydrophobic regions. The hydrogen-bonding scheme in the hydrophilic region and the arrangement of molecules in the hydrophobic region are significantly different from **IL-AH**.

In the hydrophilic region of **IL-MH** (blue shaded region in Figure 4.25), the L-lysine molecules are arranged in hydrogen-bonded layers parallel to the *ac*-plane, with a single layer shown in Figure 4.25. Within the hydrogen-bonded layer (Figure 4.26), the only hydrogen bonds between L-lysine molecules are head-to-head N–H···O hydrogen bonds (involving the ammonium head-group as the donor and the carboxylate group as the acceptor), and there are no head-to-tail N–H···O hydrogen bonds between L-lysine molecules involving the side-chain ammonium group as the donor. Instead, the side-chain ammonium group acts as the donor in an N–H···O hydrogen bond with the oxygen atom of water as the acceptor (Figure 4.26). The two independent water molecules interact with each other through an O–H···O bond (Figure 4.26). The water molecule that is the acceptor in this interaction is also the donor in two O–H···O hydrogen bonds, involving the carboxylate group of an L-lysine molecule one acceptor and the carboxylate group of an (*S*)-ibuprofen molecule as the other acceptor. The water molecule that is the donor in the O–H···O hydrogen bond between the two water molecules is also the donor in an O–H···O hydrogen bond with the carboxylate group of an L-lysine molecule as the acceptor.

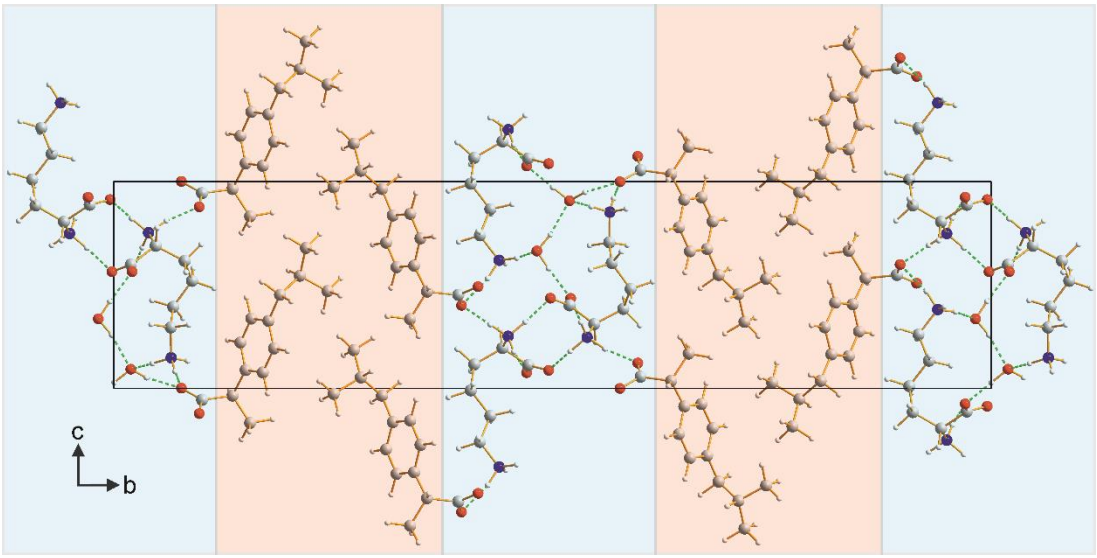

Figure 4.24. *Crystal structure of* ***IL-MH*** *viewed along the a-axis, showing the hydrophilic region (blue shaded area) and hydrophobic region (red shaded area). Hydrogen bonding is indicated by green dashed lines.*

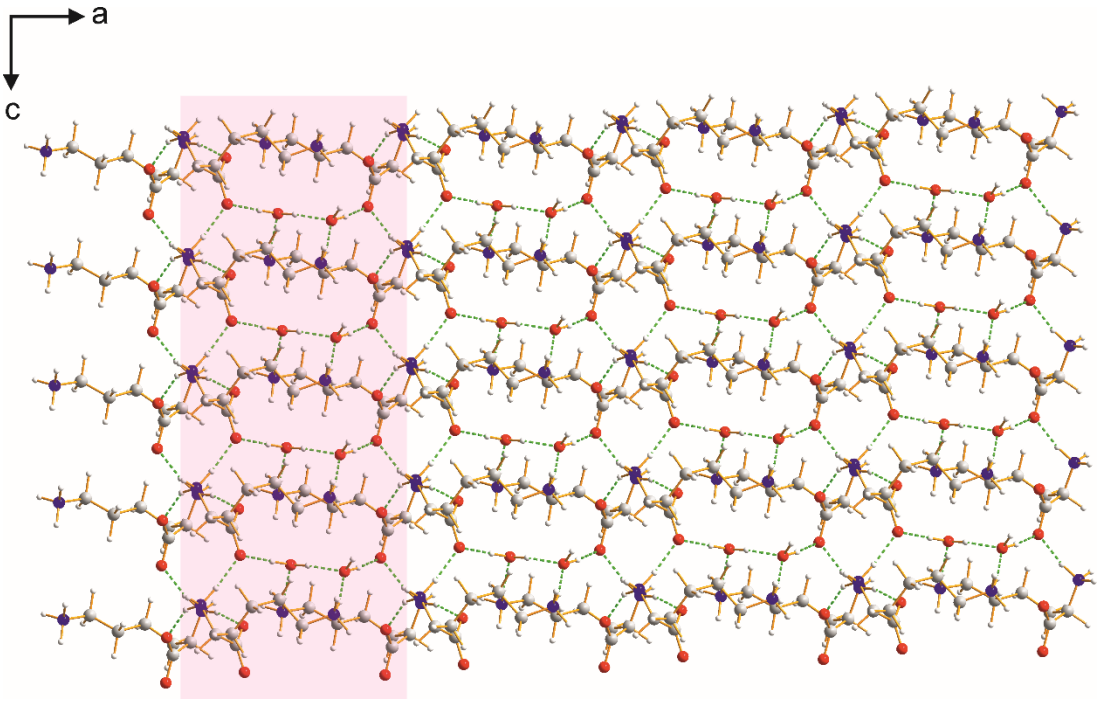

Figure 4.25. *A single layer of* L*-lysine molecules viewed along the b-axis perpendicular to the plane of the layer (which is parallel to the ac-plane) of the crystal structure of* ***IL-MH****. To view the hydrogen bonding more clearly, the magenta-shaded rectangle is viewed along the a-axis in Figure 4.26. Green dashed lines indicate the hydrogen bonding.*

The (*S*)-ibuprofen molecules interact with L-lysine through N–H···O hydrogen bonding at the periphery of the layers of L-lysine molecules (Figure 4.26), involving both ammonium head-groups and side-chain ammonium groups of L-lysine as donors and carboxylate groups of (*S*)-ibuprofen as acceptors.

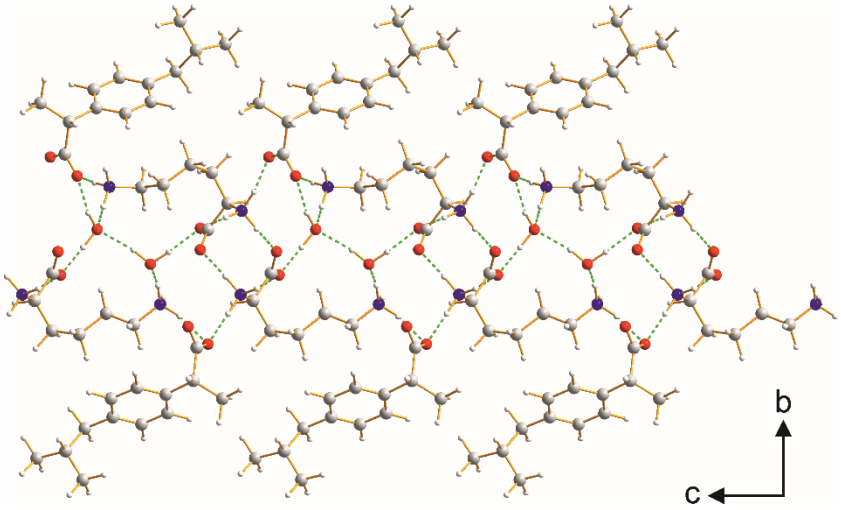

Figure 4.26*. Part of a single layer of L-lysine molecules (corresponding to the magenta-shaded box in Figure 4.25), showing the head-to-head interactions between L-lysine molecules. The hydrogen bonding of water molecules and the (S)-ibuprofen molecules that interact through N–H···O hydrogen bonds at the periphery of the L-lysine layer are also shown.*

The hydrophobic region of **IL-MH** is a bilayer (Figure 4.27) involving the phenyl rings and isobutyl groups of (*S*)-ibuprofen molecules, similar to the hydrophobic bilayer in **IL-AH**. However, the arrangement of phenyl rings and isobutyl groups of (*S*)-ibuprofen molecules in the bilayer of **IL-MH** is different from that in the bilayer of **IL-AH**. While the (*S*)-ibuprofen molecules in the bilayer of **IL-AH** are arranged such that the planes of the phenyl rings form an acute angle with respect to each other (Figure 4.21), the (*S*)-ibuprofen molecules in **IL-MH** are arranged with the planes of the phenyl rings nearly parallel to each other (Figure 4.27). In each single layer of the bilayer in **IL-MH**, the (*S*)-ibuprofen molecules are arranged next to each other in a side by side manner (Figure 4.28), whereas the (*S*)-ibuprofen molecules in each single layer of the bilayer of **IL-AH** are arranged such that the planes of the phenyl rings are parallel to each other (Figure 4.20).

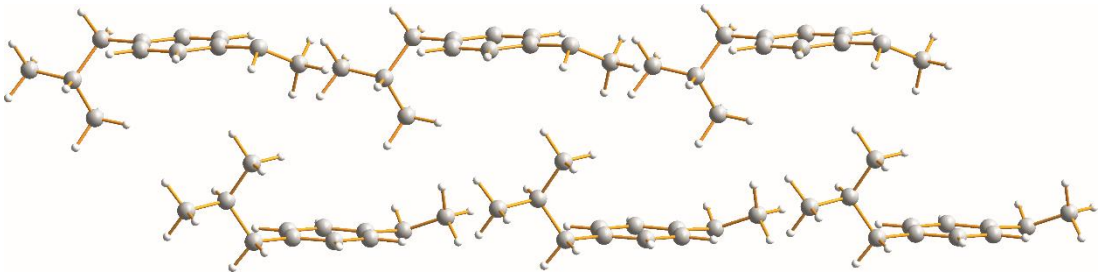

Figure 4.27. *Arrangement of (S)-ibuprofen molecules in the bilayer of* ***IL-MH****, showing the nearly parallel arrangement of phenyl rings. The carboxylate groups of (S)-ibuprofen molecules are omitted for clarity.*

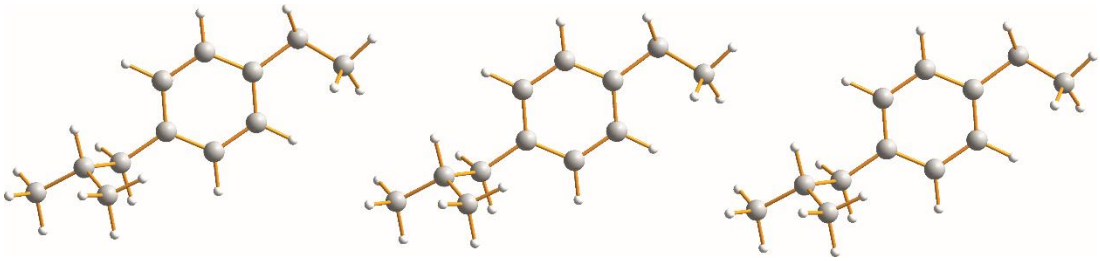

Figure 4.28. *Arrangement of (S)-ibuprofen molecules in a single layer of the bilayer in* ***IL-MH****. The carboxylate groups of the (S)-ibuprofen molecules are omitted for clarity.*

4.4 Concluding Remarks

In conclusion, the structural, thermal and hydration/dehydration characterization of two solid forms of (*S*)-ibuprofen:L-lysine (an anhydrous form and a monohydrate form) have been reported. The structures of both **IL-AH** and **IL-MH** contain alternating hydrophilic and hydrophobic regions, although the hydrogen bonding scheme in the hydrophilic region and the arrangement of molecules in the hydrophobic region differ significantly between the two structures. The hydration levels of **IL-AH** and **IL-MH** were determined by thermal analysis (TGA and DSC) and confirmed by subsequent structure determination. High-resolution solid-state ^{13}C NMR data played a significant role in structure determination of **IL-MH**, as it gave crucial information on the number of molecules in the asymmetric unit. Studies of hydration/dehydration behaviour of this system revealed that **IL-AH** transforms to **IL-MH** at high relative humidity whereas **IL-MH** converts to the high-temperature anhydrous phase **IL-X** upon heating. It has been shown by DSC and variable-temperature powder XRD that the low-temperature anhydrous phase **IL-AH** transforms to the high-temperature anhydrous phase **IL-X** at *ca*. 62 °C on heating, and the reverse transformation from

IL-X to **IL-AH** occurs on cooling at approximately the same temperature. Structure determination of the **IL-X** phase from powder XRD data is in progress.

Chapter 5: Exploring the Co-crystal Landscape of (*S*)-ibuprofen and L-proline

5.1 Introduction

Racemic ibuprofen is an effective, cheap and safe painkiller. The (*S*) enantiomer of ibuprofen (Figure 5.1) is the biologically active form and the (*R*) enantiomer is converted into the (*S*) enantiomer in the human body by enzymatic activity.[178] In spite of the efficacy and safety of this drug, its low solubility and low dissolution rate limit the bioavailability when taken orally, which is the most convenient route for drug administration. Furthermore, it suffers from poor compressibility leading to difficulties in the manufacturing process.[179] The prospects to improve these properties by co-crystal formation strategies is therefore a promising line of research. Furthermore, the co-crystal strategy can potentially provide new modifications of a solid material, and thus can increase structural diversity, allowing the selection of a specific solid form for a targeted materials application.

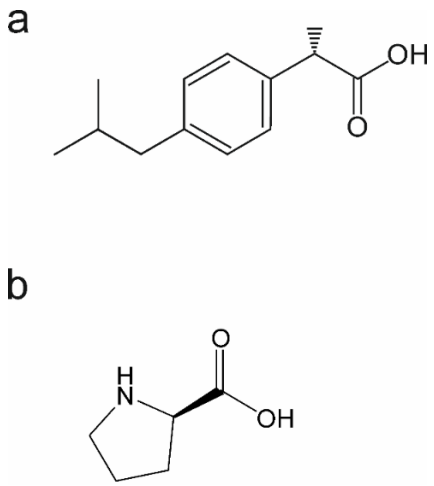

Figure 5.1. *Molecular structures of (a) (S)-ibuprofen and (b) L-proline.*

In this chapter, two new co-crystal phases of (*S*)-ibuprofen with the amino acid L-proline (Figure 5.1) are reported and structurally characterized. One co-crystal phase is anhydrous (denoted **AH**) and the other is quarter-hydrate (denoted **QH**). In both phases, (*S*)-ibuprofen and L-proline are present in 1:1 molar ratio. The **QH** phase was prepared by slow evaporation from solution, although single crystals of suitable size and quality for single-crystal XRD were not obtained. The **AH** phase was prepared by a solid-state mechanochemical procedure, which inherently gives a polycrystalline sample. As both phases were prepared as polycrystalline powders, the structural

properties have been determined directly from powder XRD data.[85, 89-90, 94-95, 97-99, 201] The dehydration behaviour of the **QH** phase is also reported in this chapter

5.2 Experimental Section

5.2.1 Co-crystal Preparation

The **AH** phase was prepared by liquid-assisted grinding (LAG),[48] with a drop of methanol added to a physical mixture of polycrystalline samples of pure (*S*)-ibuprofen and pure L-proline in 1:1 molar ratio. The mixture was placed inside a milling jar (grinding jar size, 1.5 ml) containing four stainless steel balls (ball diameter, 3.18 mm), and milling was carried out using a MM400 Retsch ball mill at 30 Hz for 30 min. The first time this procedure was carried out, the **AH** phase was obtained. However, all repeated experiments using ostensibly the same experimental procedure instead produced the **QH** phase. As the **AH** phase was produced only on one occasion, only a limited amount of characterization techniques could be applied to the **AH** phase, as discussed below.

The **QH** phase was prepared by slow evaporation of solvent from a solution containing a 1:1 molar ratio of (*S*)-ibuprofen and L-proline in ethanol. The solution was heated to *ca.* 40 °C to achieve complete dissolution, then cooled to ambient temperature; the solution was then maintained at ambient temperature to allow slow evaporation. After a few days, a microcrystalline powder was collected. The **QH** phase was obtained reproducibly by this procedure.

5.2.2 Powder XRD

For structure determination, high-quality powder XRD data were recorded on a Bruker D8 instrument (Ge-monochromated Cu$K\alpha_1$ radiation) operating in transmission mode. A polycrystalline sample of each phase was packed into three glass capillaries, which were then sealed and attached to the disc sample holder of the powder XRD instrument (2θ range, 3.5 – 70°; step size, 0.017°; data collection time, 17 hr for **AH**, 64 hr for **QH**). Powder XRD data for structure determination were recorded at ambient temperature (293 K).

To study dehydration of the **QH** phase, powder XRD data were recorded as a function of temperature on an Agilent SuperNova Dual Atlas diffractometer with a mirror monochromator using Cu$K\alpha_1$ (λ = 1.5418 Å) radiation. The sample was packed

in a glass capillary tube which was then sealed. The temperature was controlled using an Oxford Cryosystems 700 Series Cryostream cooler. Two-dimensional powder XRD data were recorded for five detector and sample positions, with the sample rotated about the capillary axis for each position. Intensity integration of the images produced a conventional one-dimensional powder XRD pattern (intensity *versus* 2θ) in the range 2θ = 6 – 120°. The powder XRD pattern was recorded at ambient temperature. The capillary was then opened and a powder XRD pattern was recorded at 80 °C.

5.2.3 Thermal Analysis

Differential Scanning Calorimetry (DSC) was carried out using a Q100 DSC (TA Instruments) and Thermogravimetric Analysis (TGA) was carried out using a 4000 TGA (Perkin Elmer) instrument. In the DSC experiments, polycrystalline samples of the **AH** and **QH** phases (*ca*. 5 – 10 mg) were placed in a hermetically-sealed pan and heated at 10 °C/min from ambient temperature to 150 °C followed by cooling to –100 °C at –10 °C/min, and then heating back to ambient temperature. In the TGA experiments, the mass of polycrystalline samples of the **AH** and **QH** phases (starting mass *ca*. 10 – 20 mg) were recorded as a function of temperature. For the **AH** phase, the sample was heated to 300 °C at 5 °C/min. For the **QH** phase, initial TGA experiments showed that mass loss begins close to ambient temperature. To minimize the likelihood of mass loss before commencing the actual TGA experiment, the sample was placed in an open aluminium pan which was then stored in a fridge for two days before carrying out the TGA measurement. In the TGA measurement, the sample was heated from ambient temperature to 200 °C at 5 °C/min, with no flow of nitrogen purge (in order to minimize any loss of water from **QH** before commencing the TGA measurement).

For the **QH** phase, an isothermal TGA experiment was also carried out. The sample (*ca.* 10 mg) was held at ambient temperature for 30 min, with the mass of the sample recorded as a function of time.

5.2.4 High-resolution Solid-state ^{13}C NMR

High-resolution solid-state ^{13}C NMR data were recorded for the **QH** phase using a Bruker AVANCE III spectrometer at the UK 850 MHz Solid-State NMR Facility

(^{13}C Larmor frequency, 213.82 MHz; 4 mm HXY probe in double-resonance mode; zirconia rotor; 20 °C). The ^{13}C NMR spectra were recorded using ramped ^{1}H→^{13}C cross-polarization[202] together with ^{1}H decoupling using SPINAL-64[108] and magic-angle spinning (MAS) at frequencies of 11 kHz and 12 kHz.

5.2.5 DFT-D Calculations

Periodic density functional theory (DFT-D) calculations were carried out using the program CASTEP[170] (Academic Release version 8.0). The calculations utilized ultrasoft pseudopotentials,[193] the PBE functional,[172] semi-empirical dispersion corrections (TS correction scheme),[174] fixed unit cell, preserved space group symmetry, periodic boundary conditions, a basis set cut-off energy of 700 eV and a Monkhorst-Pack grid[192] of minimum sample spacing $0.05 \times 2\pi$ Å^{-1}.

5.3 Results and Discussion

Two new solid forms of (*S*)-ibuprofen:L-proline were prepared in this work, denoted the **AH** phase and the **QH** phase. The **AH** phase was elusive and was obtained only once by a mechanochemical preparation procedure. Repeating this procedure under ostensibly identical conditions instead yielded the **QH** phase. Several attempts were also made to obtain the **AH** phase by changing the conditions of the mechanochemical procedure (e.g. using dry-grinding or repeating the LAG experiment with different solvents and/or increasing the amount of solvent), but only the **QH** phase was obtained. These observations suggest that the **AH** phase was obtained only under very exact conditions. In contrast, the procedure to prepare the **QH** phase (involving solvent evaporation from a solution of (*S*)-ibuprofen and L-proline in ethanol) was reproducible.

5.3.1 Thermal Analysis

The presence (or absence) of water in the **AH** phase and the **QH** phase was assessed by thermal analysis (DSC and TGA) and further confirmed by structure determination from powder XRD data. The DSC data for **AH** (Figure 5.2) shows a single endothermic peak at *ca*. 122 °C, which is assigned to melting. On cooling the sample from the liquid phase, an exothermic peak, assigned to recrystallization, is observed. Some hysteresis is observed between the melting and the recrystallization

processes. No further thermal events are observed on cooling to –100 °C and on heating back to ambient temperature.

TGA data (Figure 5.3) for the **AH** phase show no mass loss below the melting temperature (122 °C). After melting, a significant mass loss is observed, beginning at *ca*. 130 °C, which may be attributed to decomposition. The fact that the TGA data show no mass loss up to *ca.* 130 °C is consistent with the assignment that the **AH** phase contains no water (at least, no water that is released from the solid below the melting temperature). Structure determination from powder XRD data confirms the assignment of this material as an anhydrous phase (see Section 5.3.3).

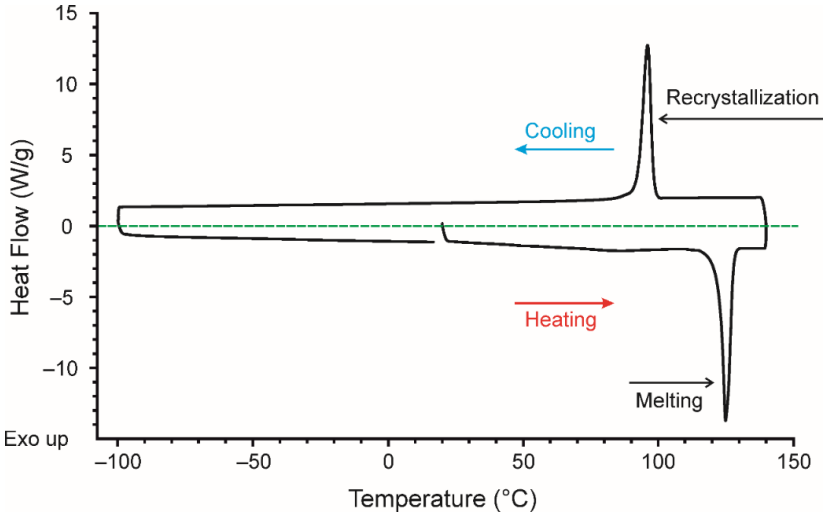

Figure 5.2. *DSC data for the* ***AH*** *phase.*

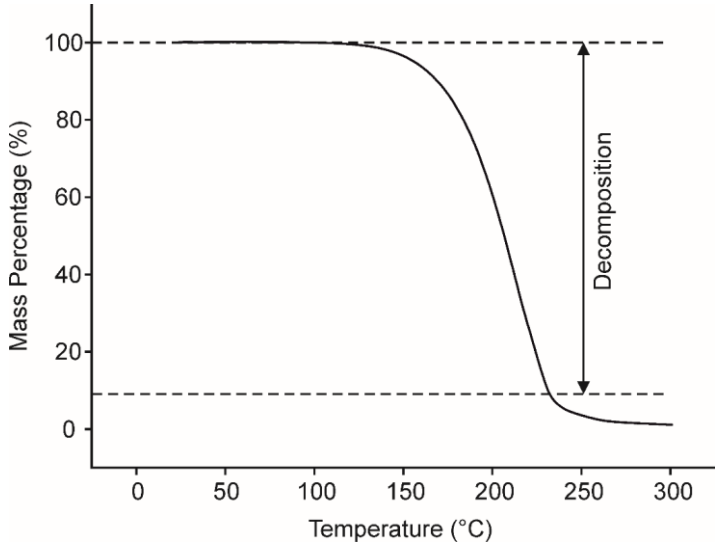

Figure 5.3. *TGA data for the* ***AH*** *phase, showing that no mass loss occurs below the melting temperature (122 °C).*

TGA data for the **QH** phase are shown in Figure 5.4. On heating, a step is observed from just above ambient temperature to *ca*. 100 °C, corresponding to a percentage mass loss of *ca*. 1.33%. On the assumption (subsequently confirmed from solid-state ^{13}C NMR data; see Section 5.3.2) that the **QH** phase contains (*S*)-ibuprofen and L-proline in 1:1 molar ratio, the mass loss of 1.33% corresponds to a quarter equivalent of water.

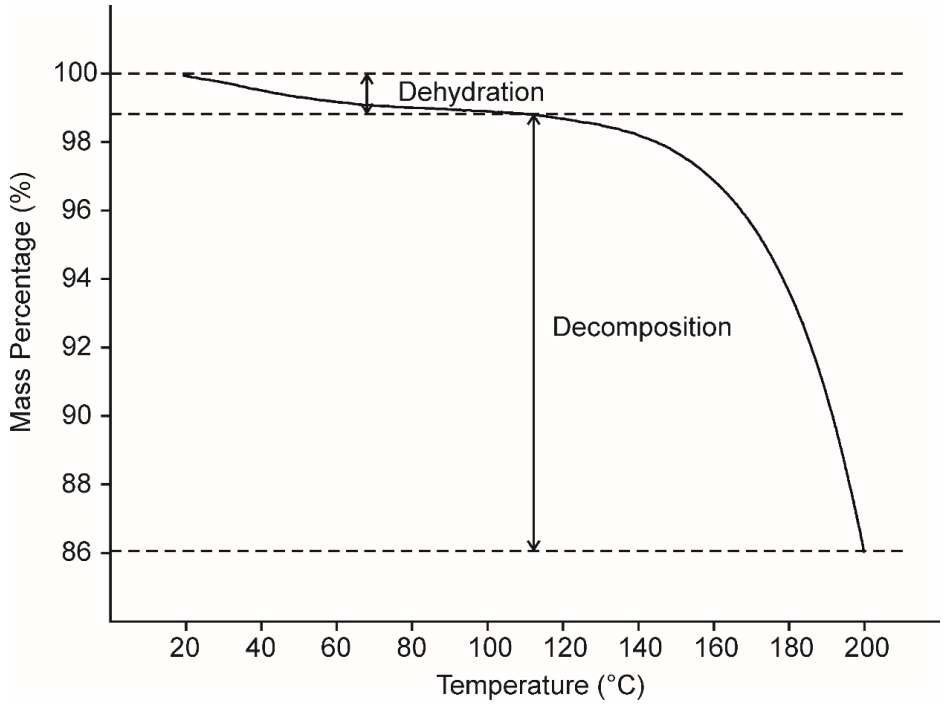

Figure 5.4. *TGA data for the* ***QH*** *phase, showing an initial mass loss due to dehydration followed by a significant mass loss due to decomposition.*

To confirm that the initial mass loss observed in the TGA data in Figure 5.4 is due to dehydration (and not, for example, due to decomposition), an isothermal TGA experiment was carried out at ambient temperature, with the mass of the sample recorded as a function of time. As shown Figure 5.5, a mass loss of *ca.* 1% is observed over 30 min, consistent with the assignment that the initial mass loss observed in the TGA data recorded as a function of temperature (Figure 5.4) is due to dehydration rather than decomposition.

DSC data for the **QH** phase (Figure 5.6) show small endothermic peaks at *ca*. 60 °C and 100 °C followed by a large endothermic peak at *ca.* 118 °C, assigned as melting. On cooling, a peak due to recrystallization is observed at *ca.* 87 °C. No further thermal events are observed on further cooling to –100 °C and heating back to ambient

temperature. The DSC data for **QH** phase are reproducible (other DSC data for the **QH** phase are shown in the Appendix B), indicating that the small features observed at *ca.* 60 and 100 °C are reproducible. However, at this stage, the thermal events giving rise to these peaks have not been assigned.

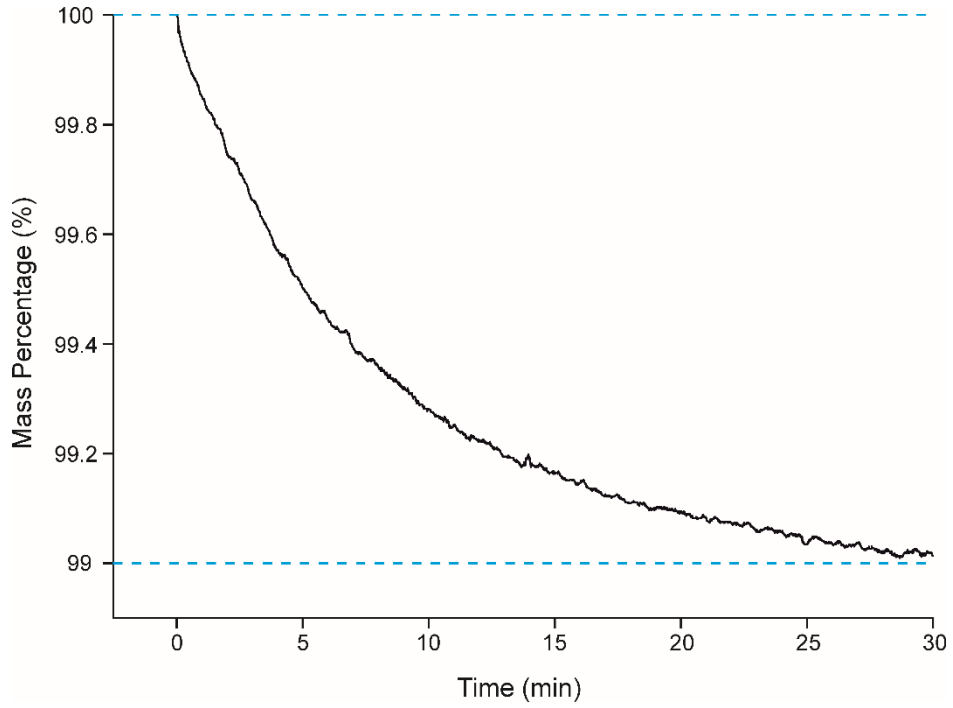

Figure 5.5. *Isothermal TGA data recorded for the* ***QH*** *phase as a function of time at ambient temperature.*

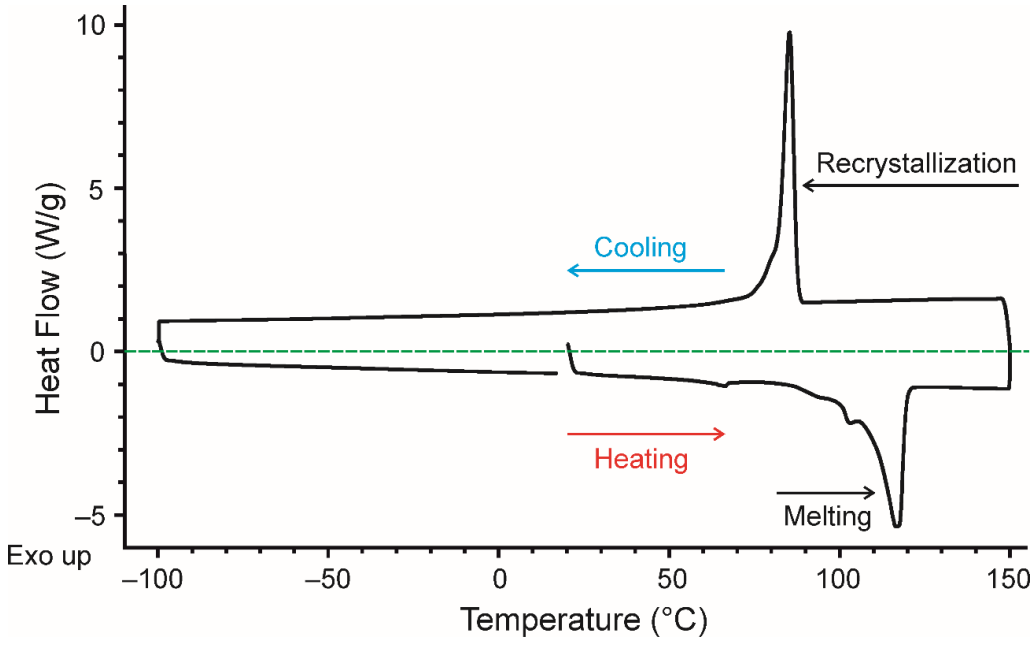

Figure 5.6. *DSC data for the* ***QH*** *phase.*

To investigate the structural changes that occur on dehydration of the **QH** phase, variable-temperature powder XRD data were recorded at ambient temperature and 80 °C. The results are discussed in Section 5.3.7.

5.3.2 High-resolution Solid-state ^{13}C NMR Spectroscopy

High-resolution solid-state ^{13}C NMR data for the **QH** phase was used in conjunction with structure determination from powder XRD data to provide an independent assessment of the number of molecules in the asymmetric unit. In the solid-state ^{13}C NMR spectrum (Figure 5.7), two peaks are observed with isotropic chemical shift in the region of 60 ppm, assigned to the carbon environment of L-proline labelled with the blue circle in Figure 5.7.

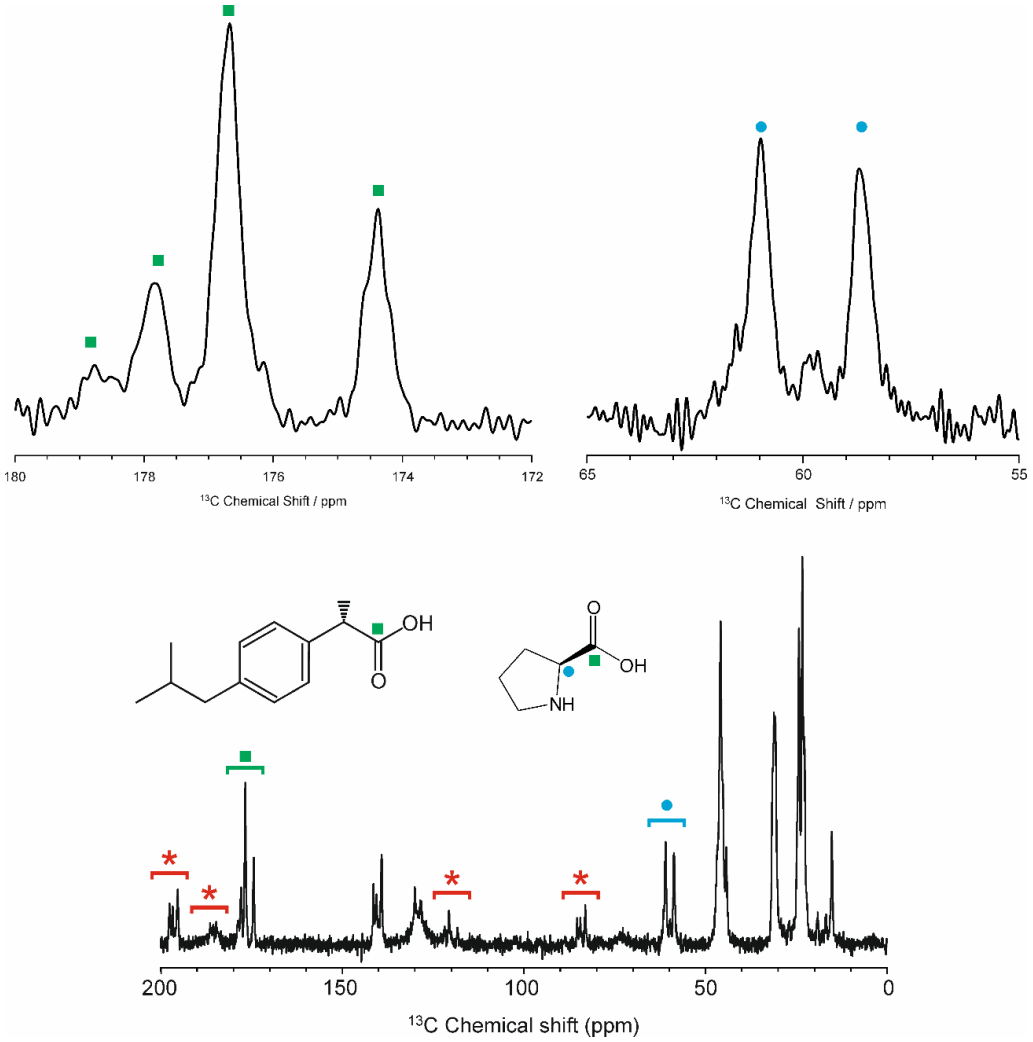

Figure 5.7. *High-resolution solid-state ^{13}C NMR data for the **QH** phase. Red asterisks indicate spinning sidebands.*

The presence of two peaks indicates that there are two independent molecules of L-proline in the asymmetric unit. In addition, four peaks are observed with isotropic chemical shift in the region *ca*. 174 – 180 ppm, assigned to the carboxylic acid group of (*S*)-ibuprofen and the carboxylate group of L-proline, suggesting that there are two molecules of L-proline and two molecule of (*S*)-ibuprofen in the asymmetric unit. As thermal analysis indicates that the material contains one quarter equivalent of water, and as the asymmetric unit contains two molecules of L-proline and two molecules of (*S*)-ibuprofen (established from solid-state ^{13}C NMR), we deduce that the asymmetric unit contains two molecules of (*S*)-ibuprofen, two molecules of L-proline and one half molecule of water. This information is crucial in setting up the direct-space structure solution calculation from powder XRD data.

As only a limited amount of the **AH** phase was obtained in this work (see Section 5.2.1), it was not possible to record solid-state ^{13}C NMR data for this phase.

5.3.3 Structure Determination of the AH Phase from Powder XRD Data

Indexing and Profile Fitting

The powder XRD pattern of the **AH** phase was indexed using the program TREOR[203] within the CRYSFIRE package,[141] giving the following unit cell with monoclinic metric symmetry: a = 14.43 Å, b = 5.81 Å, c = 21.81 Å, β = 97.10°, V = 1814 Å^3. As the **AH** phase contains single enantiomers of (*S*)-ibuprofen and L-proline, the space group must be chiral. On the basis of systematic absences, space group *C*2 may be ruled out, but it was not possible to conclude whether the space group is *P*2 or *P*2$_1$. For this reason, profile fitting using the Le Bail method[149] in the GSAS program[150] was carried out for both space groups *P*2 and *P*2$_1$.

A comparable quality of fit was obtained for both space groups. For space group *P*2$_1$, the result of profile fitting (R_{wp} = 3.11%, R_p = 2.33%) is shown in Figure 5.8a, with the following refined unit cell parameters: a = 14.4285(8) Å, b = 5.80902(15) Å, c = 21.8144(8) Å, β = 97.1153(21)°, V = 1814.3(13) Å^3. To resolve the question of whether the correct space group is *P*2 or *P*2$_1$, structure solution calculations were carried out for both space groups.

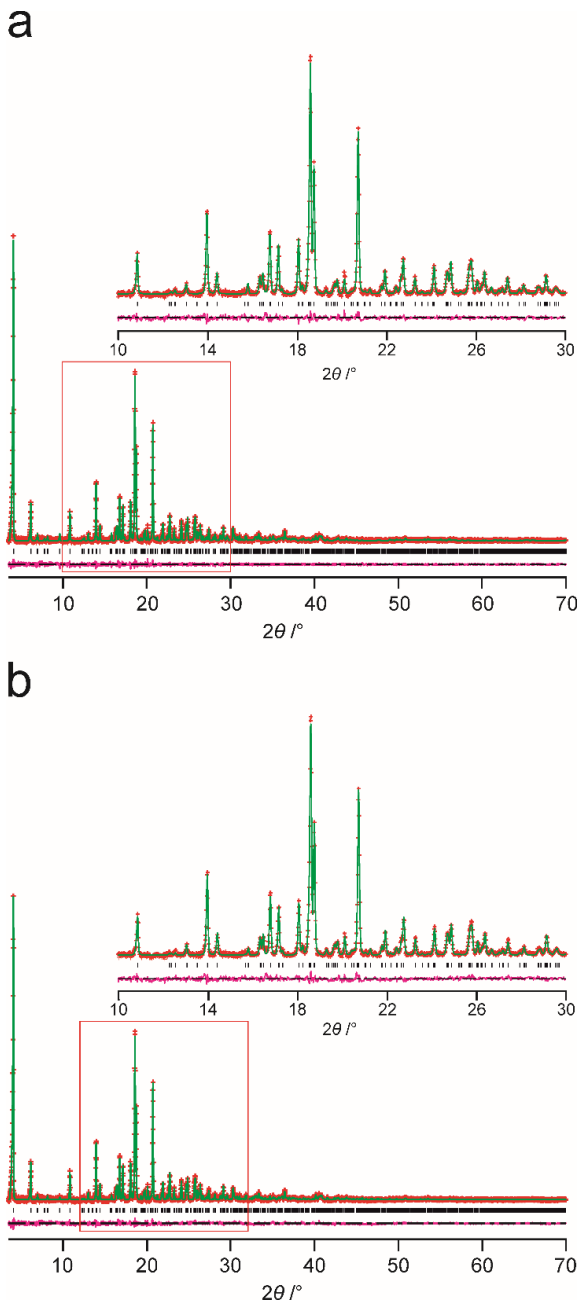

Figure 5.8. *(a) Le Bail fitting and (b) final Rietveld refinement for the* ***AH*** *phase. Red crosses, experimental data following background subtraction; green line, calculated data; magenta line, difference plot; black tick marks, predicted peak positions.*

Structure Solution

Structure solution calculations for the **AH** phase were carried out independently for both space groups *P*2 and $P2_1$ using the direct-space genetic algorithm (GA) technique[95] implemented in the program EAGER.[81-82, 89-90, 98-99, 204] Density considerations suggest that the unit cell contains four molecules of (*S*)-ibuprofen and four molecules of L-proline, and thus the asymmetric unit contains two molecules of

(*S*)-ibuprofen and two molecules of L-proline, either for space group $P2$ or space group $P2_1$ (as both of these space groups have $Z' = 2$). Given that the **AH** phase was obtained only as a small amount of sample in one preparation, the solid-state ^{13}C NMR spectrum was not recorded for this phase, so an independent assessment of the number of molecules in the asymmetric unit could not be carried out.

In the GA structure solution calculations, each (*S*)-ibuprofen molecule was defined by 10 structural variables (3 positional, 3 orientational and 4 torsion-angle variables) and each L-proline molecule was defined by 7 structural variables (3 positional, 3 orientational and 1 torsion-angle variables). The conformation of the ring in the L-proline molecules was fixed in the GA calculations, with the geometry of the ring taken from the reported structure of L-proline[205] (REF Code: PROLIN). For both space groups $P2$ and $P2_1$, one L-proline molecule was fixed along the *b*-axis, reducing the number of positional variables to 2 for this molecule. Thus, the total number of structural variables in the direct-space structure solution calculation was 33. The GA calculations for each space group involved the evolution of a population size of 500 trial structures for 600 generations, with 50 mating operations and 250 mutation operations per generation. In total, 16 independent GA structure solution calculations were carried out in parallel.

Only the structure solution calculations for space group $P2_1$ gave acceptable structures that made chemical and structural sense, and gave a good fit to the experimental powder XRD data, indicating that $P2_1$ is the correct space group. For space group $P2_1$, four of the 16 independent GA calculations produced the same structure giving the best fit to the experimental powder XRD data.

Structure Refinement

The structure solution giving the best fit to the experimental powder XRD data (i.e. lowest R_{wp}) was used as the initial structural model for Rietveld refinement.[206] In the refinement, a common isotropic displacement parameter was refined for the non-hydrogen atoms of each molecule, and the value for hydrogen atoms was set as 1.2 times that for the non-hydrogen atoms in the same molecule. Standard restraints were applied to bond lengths and bond angles (based on geometric information from MOGUL,[207] with values for bonds involving hydrogen taken from Allen *et al.*[169]). Planar restraints were applied to the carboxylic acid group of (*S*)-ibuprofen, the

carboxylate group of L-proline and the aromatic ring of (*S*)-ibuprofen. The final Rietveld refinement gave a good quality fit between calculated and experimental powder XRD data (R_{wp} = 3.58%, R_p = 2.61%; Figure 5.8b), with the following refined lattice parameters: a = 14.429(33) Å, b = 5.809(15) Å, c = 21.816(10) Å, β = 97.12(26)°, V = 1814.57(12) Å^3.

The final refined structure was subjected to geometry optimization (with fixed unit cell) using periodic DFT-D calculations in the program CASTEP[170] (Academic Release version 8.0). The geometry optimized structure shows only very minor differences (RMSD = 0.33 Å for non-hydrogen atoms) from the refined structure, giving further validation of the correctness of the final refined structure.

5.3.4 Structure Determination of the QH Phase from Powder XRD Data

Indexing and Profile Fitting

The powder XRD pattern of the **QH** phase was indexed using the program FJZN[208] in the CRYSFIRE package, giving the following unit cell with monoclinic metric symmetry: a = 33.11 Å, b = 5.69 Å, c = 20.29 Å, β = 100.85°, V = 3760 Å^3. Recalling that both (*S*)-ibuprofen and L-proline molecules in the **QH** phase are single enantiomers, the space group must be chiral. On the basis of systematic absences, the space group was assigned as *C*2. Profile fitting for space group *C*2 using the Le Bail method[149] in the GSAS software[150] gave a good-quality fit to the experimental powder XRD data (R_{wp} = 1.84%, R_p = 1.37%; Figure 5.9a) with the following refined unit cell parameters: a = 33.1324(9) Å, b = 5.6947(13) Å, c = 20.2865(5) Å, β = 100.8491(21)°, V = 3759.22(17) Å^3.

Structure Solution

Structure solution for the **QH** phase was carried out using the direct-space GA technique implemented in the program EAGER. For the **QH** phase, density considerations suggest that the unit cell contains eight molecules of (*S*)-ibuprofen and eight molecules of L-proline, and therefore the asymmetric unit comprises two molecules of (*S*)-ibuprofen and two molecules of L-proline. This conclusion is in agreement with the assignment of the contents of the asymmetric unit from solid-state ^{13}C NMR data. In addition, from the water stoichiometry determined from the TGA data, we deduce that there is one half molecule of water in the asymmetric unit. For

space group *C*2, we deduce that the half molecule of water is located with the oxygen atom on a 2-fold rotation axis, with one hydrogen atom of the water molecule in the asymmetric unit and the other hydrogen atom generated by the 2-fold rotation axis.

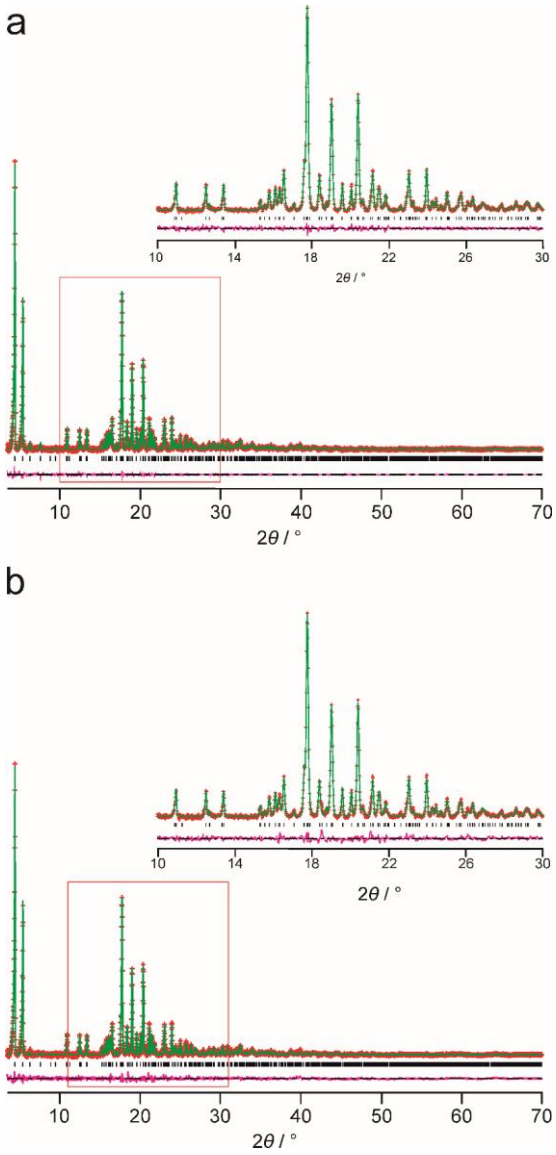

Figure 5.9. *(a) Le Bail fitting and (b) final Rietveld refinement for the* ***QH*** *phase. Red crosses, experimental data following background subtraction; green line, calculated data; magenta line, difference plot; black tick marks, predicted peak positions.*

In the GA structure solution calculations, the (*S*)-ibuprofen and L-proline molecules were defined in the same way as in the structure solution calculations for the **AH** phase (see Section 5.3.3). The half molecule of water was defined by 2 structural variables (1 positional, 1 orientational), allowing the water fragment (O–H) to move along the 2-fold rotation axis (parallel to the *b*-axis) and rotate around this

axis. Again, the position of one L-proline molecule was fixed along the *b*-axis. Thus, the total number of structural variables in GA structure solution calculation was 35. The GA calculations involved the evolution of a population size of 500 trial structures for 500 generations, with 50 mating operations and 250 mutation operations per generation. In total, 16 independent GA calculations were carried out in parallel. Four calculations generated a very similar structure, giving the best fit to the experimental powder XRD data.

Structure Refinement

The structure giving the best fit to the experimental powder XRD data (i.e. lowest R_{wp}) was used as the initial structural model for Rietveld refinement. A common isotropic displacement parameter was refined for the non-hydrogen atoms of each molecule, with the value for the hydrogen atoms assigned as 1.2 times of the value of non-hydrogen atoms. Standard restraints were applied to bond lengths and bond angles in the (*S*)-ibuprofen, L-proline and water molecules (using bond lengths and bond angles extracted from MOGUL,[207] with values for bonds involving hydrogen taken from Allen *et al.*[169]). Planar restraints were applied to the carboxylic acid group and aromatic ring of (*S*)-ibuprofen, and the carboxylate group of L-proline.

In the initial Rietveld refinement, a good quality of fit between the calculated and experimental powder XRD patterns was obtained (R_{wp} = 2.93%, R_p = 2.11%). However, an unfavourable short contact was present between an L-proline molecule and an (*S*)-ibuprofen molecule, which was resolved by carrying out a DFT-D geometry-optimization calculation (with fixed unit cell). The unfavourable short contact was alleviated, leading to a geometrically reasonable hydrogen-bonding scheme.

The structure obtained following the DFT-D geometry optimization was then used as the initial structural model for the final Rietveld refinement, which gave an improved fit to the experimental powder XRD data (Figure 5.9b; R_{wp} = 2.51%, R_p = 1.79%), with the following final refined parameters: a = 33.138(14) Å, b = 5.694(19) Å, c = 20.291(7) Å, β = 100.864(32)°, V = 3760.52(25) Å^3.

5.3.5 Structural Properties of the AH Phase

The crystal structure of the **AH** phase (Figure 5.10) is described in terms of a one-dimensional ribbon-like hydrogen-bonding arrangement running along the *b*-axis (Figure 5.11).

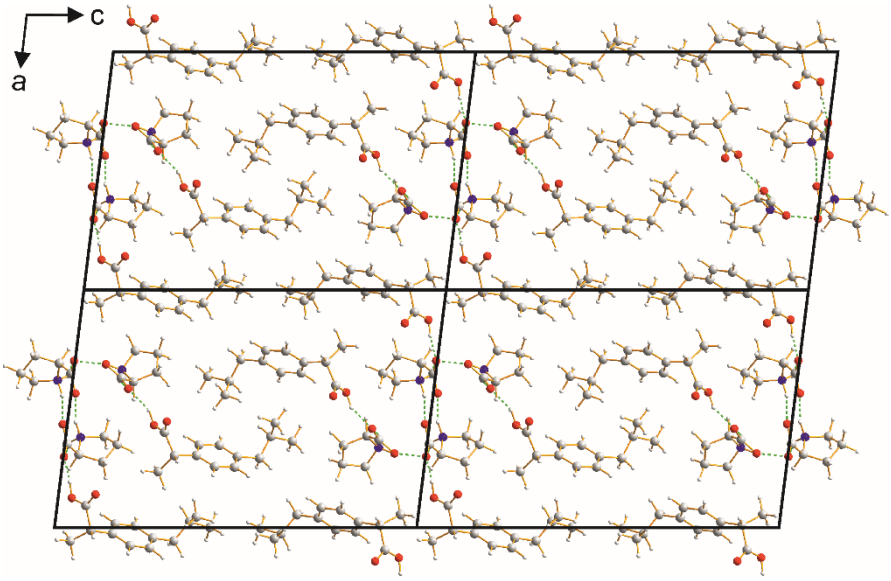

Figure 5.10. *Crystal structure of* ***AH*** *viewed along the b-axis. Hydrogen bonds are indicated by green dashed lines.*

The ribbon is constructed from two chains of L-proline molecules. Within each chain, adjacent L-proline molecules are related by translation along the *b*-axis and are linked by N–H···O hydrogen bonds between the ammonium group (N–H donor) of one molecule and the carboxylate group (O acceptor) of the other molecule. Furthermore, the two chains are cross-linked by additional N–H···O hydrogen bonds between ammonium groups (N–H donor) and carboxylate groups (O acceptors) of L-proline molecules in the two chains; each L-proline molecule is engaged in two cross-linking N–H···O hydrogen bonds of this type, in one case as the N–H donor and in the other case as the O acceptor, involving two different L-proline molecules in the other chain. In addition, (*S*)-ibuprofen molecules are arranged along the periphery of the ribbon (at each of the two edges of the ribbon). Each of these (*S*)-ibuprofen molecules forms an O–H···O hydrogen bond with an L-proline molecule in the ribbon, involving the carboxylic acid group of the (*S*)-ibuprofen molecule (O–H donor) and the carboxylate group of the L-proline molecule (O acceptor).

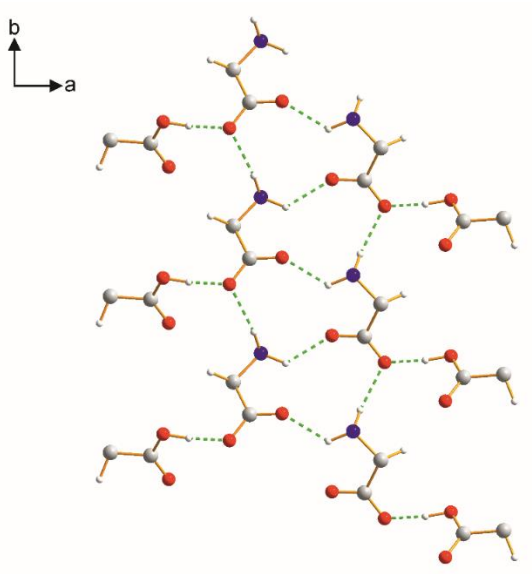

Figure 5.11. *Hydrogen-bonding arrangement in the* ***AH*** *phase. For clarity, only the carboxylate and ammonium groups of* L*-proline and the carboxylic acid group of (S)-ibuprofen and are shown. Green dashed lines indicate hydrogen bonding.*

The conformations of the two independent (*S*)-ibuprofen molecules and the two independent L-proline molecules in the asymmetric unit are shown in Figure 5.12.

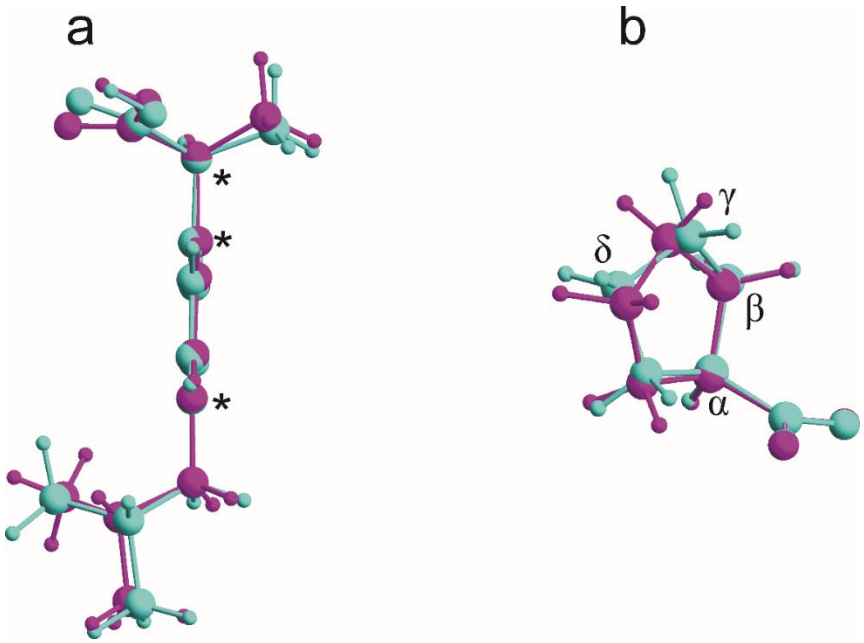

Figure 5.12. *Overlay of the two independent molecules of (a) (S)-ibuprofen and (b)* L*-proline in the structure of the* ***AH*** *phase. For (S)-ibuprofen, carbon atoms indicated by black asterisks are superimposed. For* L*-proline, the three atoms of the carboxylate group are superimposed.*

It can be seen that the two crystallographically independent (*S*)-ibuprofen molecules and the two crystallographically independent L-proline molecules show similar conformations. The conformations of the five-membered rings of the two independent L-proline molecules are close to "envelope" conformations (in this context, an "envelope" conformation is defined when four atoms of the five-membered ring are co-planar and the fifth atom (the "flap") is out of the plane; Figure 5.12b).

5.3.6 Structural Properties of the QH Phase

The crystal structure of the **QH** phase (Figure 5.13) may be described in terms of two hydrogen-bonded regions: one region contains the water molecules (denoted region W; enclosed by the red dotted line in Figure 5.14) and the other region does not contain water molecules (denoted region N; enclosed by the blue dotted line in Figure 5.14).

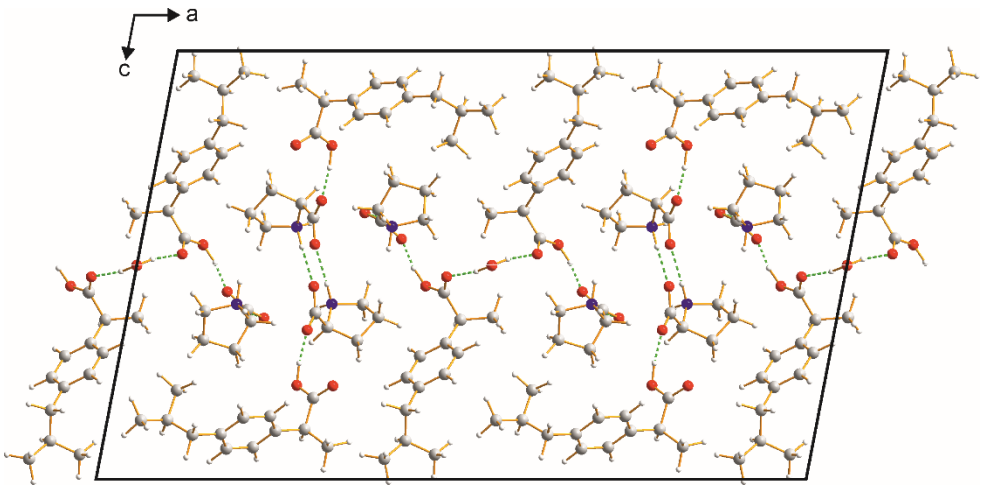

Figure 5.13. *Crystal structure of the* ***QH*** *phase viewed along the b-axis. Hydrogen bonding is indicated by green dashed lines.*

The asymmetric unit of the **QH** phase comprises two molecules of (*S*)-ibuprofen (one molecule in each region), two molecules of L-proline (one molecule in each region), and one half molecule of water (in region W). The two independent molecules of (*S*)-ibuprofen and the two independent molecules of L-proline have significant differences in molecular conformations (Figure 5.15), in contrast to the situation for the **AH** phase.

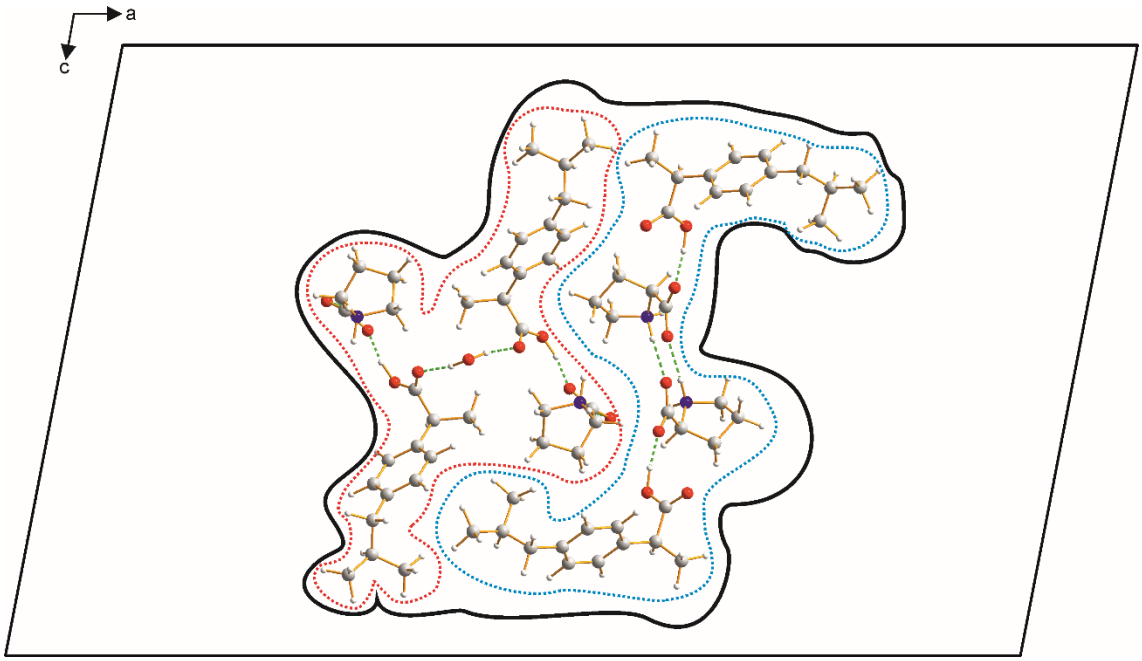

Figure 5.14. *The two hydrogen-bonded regions in the crystal structure of the* ***QH*** *phase, indicated by the blue dotted line (region N) and the red dotted line (region W). Hydrogen bonds are indicated by green dashed lines.*

The conformations of the five-membered rings in the two independent molecules of L-proline in the **QH** phase are described as distorted rings (Figure 5.15b), in contrast to the nearly envelope conformations in the **AH** phase.

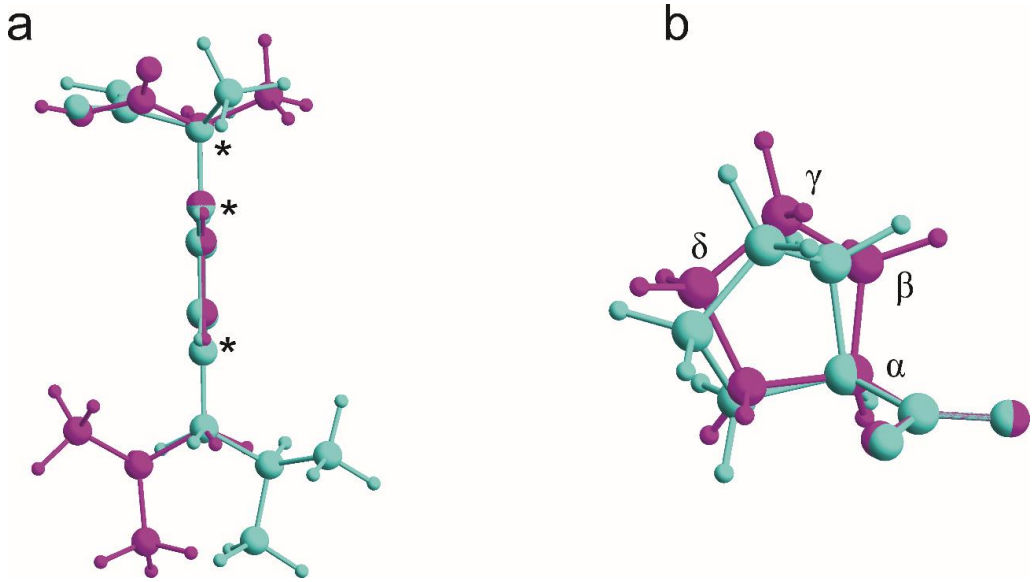

Figure 5.15. *Overlay of the two independent molecules of (a) (S)-ibuprofen and (b) L-proline in the* ***QH*** *phase. For (S)-ibuprofen, carbon atoms indicated by black asterisks are superimposed. For L-proline, the carboxylate groups are superimposed.*

Figure 5.16 shows an overlay between one L-proline molecule in the **AH** phase and one L-proline molecule in the **QH** phase, displaying the difference between the envelope and distorted ring conformations (while four atoms of the five-membered ring are co-planar and the flap projects out of this plane in envelope conformation, the four atoms are distorted from planarity in the distorted ring conformation).

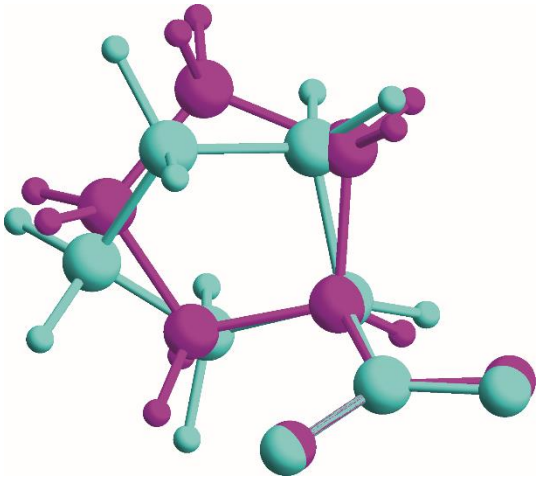

Figure 5.16. *Overlay of a molecule of L-proline from the* ***AH*** *phase (flat envelope conformation; magenta) and a molecule of L-proline from the* ***QH*** *phase (distorted ring conformation; cyan). The three atoms of the carboxylate group are superimposed.*

The oxygen atom of the water molecule is located on a 2-fold rotation axis parallel to the *b*-axis (Figure 5.17).

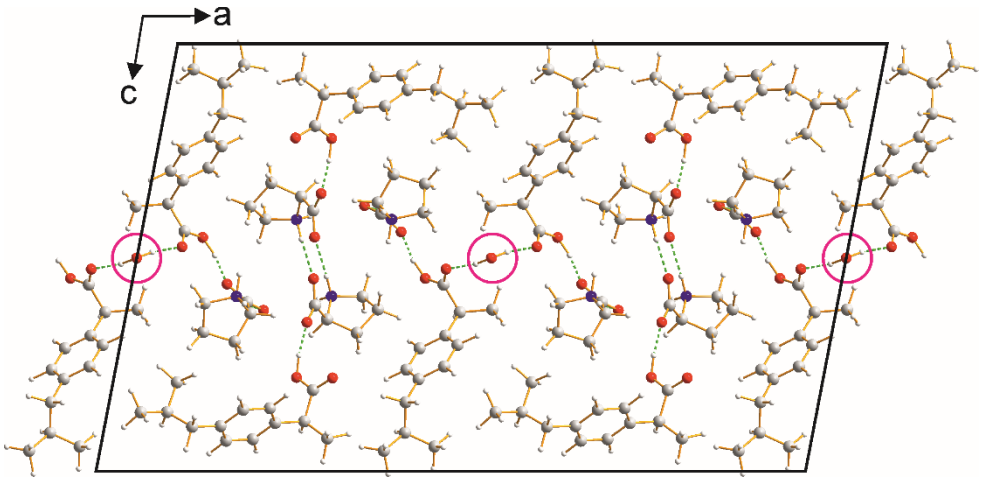

Figure 5.17*. Structure of the* ***QH*** *phase viewed along the b-axis. The water molecules (highlighted by magenta circles) are located on 2-fold rotation axes parallel to the b-axis.*

The hydrogen-bonding in region N can be described in terms of hydrogen-bonded ribbons running along the *b*-axis (Figure 5.18a). In terms of the hydrogen bonding connectivity, these ribbons are identical to those observed in the **AH** phase (see the discussion in Section 5.3.5 and Figure 5.11). Thus, the ribbons in region N of the **QH** phase contains two chains of L-proline molecules, with intermolecular N–H···O hydrogen bonds between ammonium groups (N–H donor) and carboxylate groups (O acceptors) of L-proline molecules linking adjacent molecules along each chain, and cross-linking between molecules in different chains. Furthermore, (*S*)-ibuprofen molecules are arranged along the periphery of the ribbon (at each of the two edges of the ribbon), with each (*S*)-ibuprofen molecule forming an O–H···O hydrogen bond with an L-proline molecule in the ribbon. Importantly, the two ribbons shown in Figure 5.11 (**AH** phase) and Figure 5.18a (**QH** phase) are identical (although they run in opposite directions vertically in the figures shown).

The hydrogen-bonding in region W (Figure 5.18b) can also be described as a ribbon running along the *b*-axis, but the hydrogen-bonding arrangement is significantly different from those in region N and in the **AH** phase. In region W, the periphery at each edge of the ribbon comprises a chain of L-proline molecules running along the *b*-axis. Within each chain, adjacent L-proline molecules are related by translation and are linked by N–H···O hydrogen bonds between the ammonium group (N–H donor) of one molecule and the carboxylate group (O acceptor) of the other molecule. In the "inner" part of the ribbon (between the two L-proline chains), each L-proline molecule is engaged in an O–H···O hydrogen bond with an (*S*)-ibuprofen molecule, involving the carboxylic acid group of (*S*)-ibuprofen (O–H donor) and the carboxylate group of L-proline (O acceptor). Furthermore, pairs of these (*S*)-ibuprofen molecules are bridged by a water molecule, which acts as the donor in O–H···O hydrogen bonds to each of the two (*S*)-ibuprofen molecules (O acceptor).

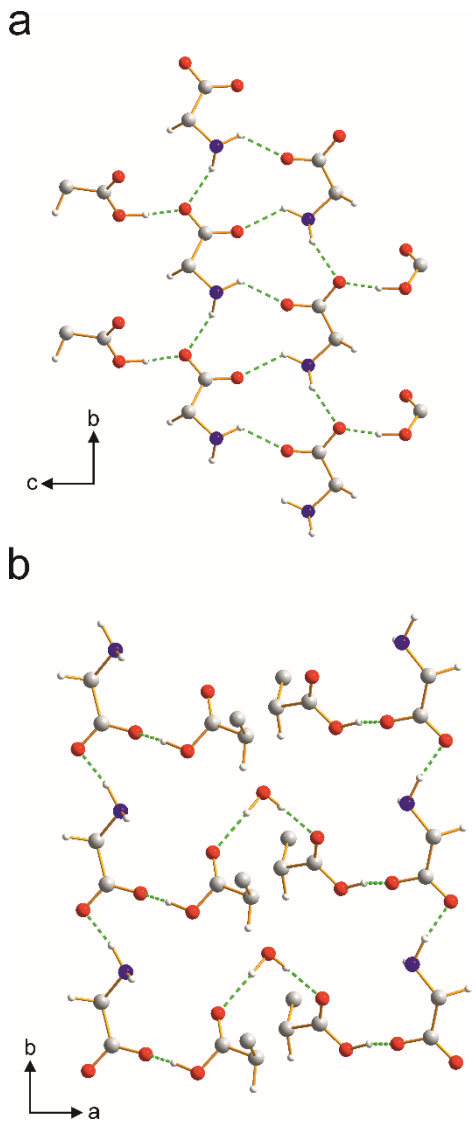

Figure 5.18. *Hydrogen-bonding arrangements in (a) region N and (b) region W of the* ***QH*** *phase. For clarity, only the carboxylate and ammonium groups of L-proline and the carboxylic acid group of (S)-ibuprofen are shown. Green dashed lines indicate hydrogen bonding.*

5.3.7 Dehydration Studies of the QH Phase

As the two phases reported in this chapter are an anhydrous phase (**AH**) and a quarter-hydrate phase (**QH**), it is relevant to investigate the possibility that these phases may interconvert *via* hydration/dehydration processes, particularly with regard to potential hydration of the **AH** phase and dehydration of the **QH** phase, and to assess whether these processes are reversible or irreversible. However, due to the fact that the **AH** phase was obtained only once and with only a limited amount of sample, it was not possible to carry out investigations on the hydration behaviour of this phase.

On the other hand, dehydration of the **QH** phase has been investigated, as now described.

TGA data (Figures 5.4) show that the **QH** phase dehydrates over a range of temperatures on heating, starting close to ambient temperature. An important aspect of such dehydration processes is to establish the nature of the solid phase produced following dehydration. In the present case, one possible outcome of dehydration of the **QH** phase could be the formation of the known anhydrous phase, namely the **AH** phase. However, it is possible that transformation pathways to other anhydrous phases may occur upon dehydration of the **QH** phase.

To investigate this issue, a powder sample of the **QH** phase was sealed in a capillary at ambient temperature and the powder XRD pattern was recorded first at ambient temperature and then after heating (following opening the capillary) to 80 °C (Figure 5.19), recalling that the TGA data suggest that loss of water from the **QH** phase is essentially complete at 80 °C (in the relatively rapid heating process used in the TGA experiment). The powder XRD pattern recorded at 80 °C is similar to the powder XRD pattern characteristic of the **QH** phase recorded at ambient temperature, but not identical. The small differences between these powder XRD patterns suggest that the sample had undergone minor structural changes on heating to 80 °C, presumably as a consequence of dehydration and with only minor structural relaxation following loss of the water molecules. This result also suggests that the **QH** phase does *not* transform to the **AH** phase upon dehydration, as the powder XRD pattern recorded at 80 °C is significantly different from the powder XRD pattern characteristic of the **AH** phase.

Although the resolution of the powder XRD data used in the study of dehydration of the **QH** phase was not as good as the resolution of the powder XRD data used for structure determination, the resolution was sufficiently good to observe small changes between the powder XRD data recorded at ambient temperature and 80 °C in Figure 5.19, suggesting that small structural changes occur upon heating.

It is clear from the results of the experiments discussed in this section that the phase produced on dehydration of the **QH** phase does *not* correspond to the **AH** phase. The fact that the powder XRD pattern of the material produced upon dehydration of the **QH** phase shows only minor changes compared to the powder XRD pattern of the

QH phase suggests that the structure of the dehydrated phase may have a close resemblance to the structure of the **QH** phase. However, structure determination of the dehydrated phase from powder XRD data was not carried out in the present work.

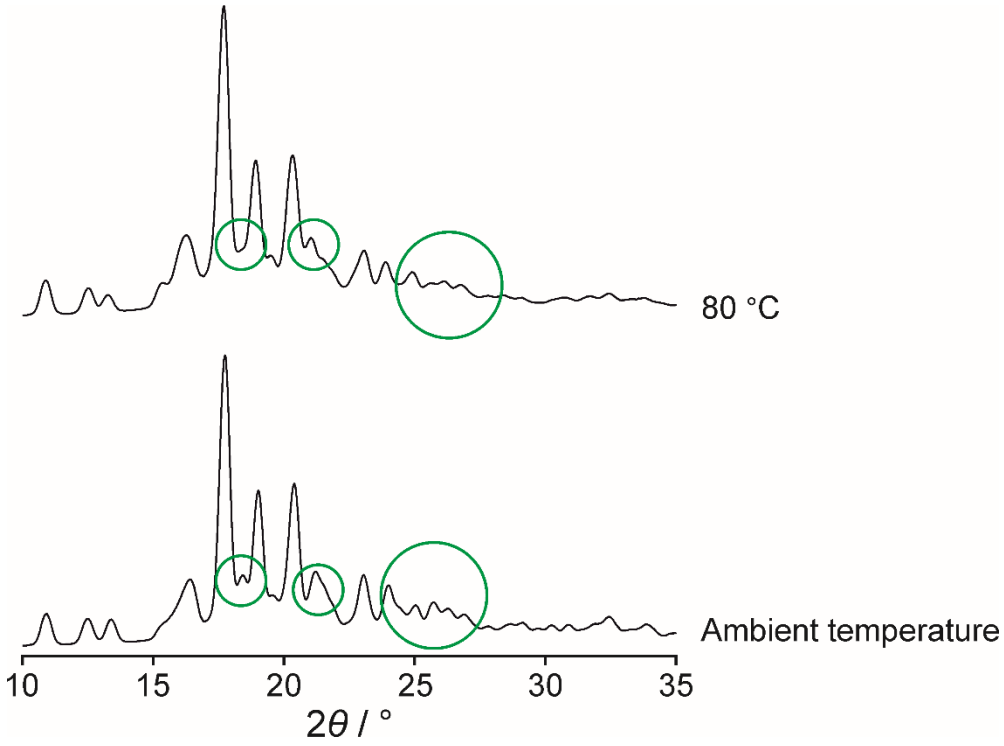

Figure 5.19. *Powder XRD data recorded for a sample of the* ***QH*** *phase in a sealed capillary. The data were recorded first at ambient temperature and then on heating (following opening the capillary) to 80 °C. Regions showing small differences between the data recorded at ambient temperature and 80 °C are highlighted by green open circles.*

5.4 Concluding Remarks

In conclusion, the structural properties of an anhydrous (**AH**) phase and a quarter-hydrate (**QH**) phase of (*S*)-ibuprofen:L-proline co-crystals are reported in this chapter. While the formation of the **AH** phase is elusive, the **QH** phase can be prepared reproducibly. The hydration level of each phase was determined by thermal analysis (TGA) and further confirmed by structure determination from powder XRD data. As both phases were produced as polycrystalline powders, structure determination was carried out directly from powder XRD data, using the direct-space GA strategy for structure solution followed by Rietveld refinement. The crystal structures of both phases contain one-dimensional ribbon-like hydrogen-bonding arrangements. However, while the **AH** phase has only one hydrogen-bonding array, the **QH** phase

has two distinct hydrogen-bonded regions, one of which incorporates the water molecule.

Although it was not possible to study the hydration/dehydration behaviour of the **AH** phase due to the limited amount of sample available, the dehydration behaviour of the **QH** phase was studied. TGA data suggest that the **QH** phase undergoes dehydration close to ambient temperature, and powder XRD data suggest that minor structural changes occur upon heating the **QH** phase (consistent with dehydration and only minor structural relaxation). Significantly, the results reported here suggest that dehydration of the **QH** phase does *not* produce the **AH** phase.

Chapter 6: Polymorphism of L-Tryptophan

6.1 Introduction

Polymorphism arises when a given molecule can crystalize in two or more different crystal structures.[2, 66, 209-213] As a consequence, polymorphs differ in their physicochemical properties and relative thermodynamic stabilities. From a fundamental perspective, polymorphism provides an opportunity to explore fundamental issues concerning the relationships between structure and properties of molecular solids. From an applied perspective, it is crucial to identify and characterize the range of polymorphs available to a given molecule, and to utilize the optimal polymorph in specific materials applications. As such, polymorphism plays an important role in many industrial fields including pharmaceuticals, pigments and explosives industries.

As amino acids play important roles in biological systems, there is significant interest in the structural properties of this family of materials. All 20 directly encoded proteinogenic amino acids have now had a crystal structure determined, following recently reported structures of L-arginine,[132] L-tryptophan[214] and L-lysine.[200] However, structurally characterized polymorphs have so far been reported only for L-cysteine,[215-217] L-glutamic acid,[218-219] glycine,[220-222] L-histidine,[223-224] L-isoleucine,[225-226] L-leucine,[227-228] L-phenylalanine,[229-230] L-proline[205, 231] and L-serine.[232-234] This chapter is focused on L-tryptophan (L-Trp; molecular structure, Figure 6.1), for which only one crystal structure has been reported previously,[214] a remarkably complex structure containing 16 independent molecules in the asymmetric unit, with space group *P*1.

While crystallization from solution is the most common approach for preparing crystalline phases of organic materials (and presents wide-ranging opportunities for the discovery of new polymorphs by varying experimental conditions, such as the choice of solvent and the rate of cooling or evaporation), another method that may produce new polymorphs is crystallization from the gas phase (following sublimation). Evidence has been reported[235] for the formation of a new solid form of L-Trp using this strategy for crystallization, although the crystal structure was not determined.

In this chapter, the structural properties of a new polymorph of L-Trp prepared by crystallization from the gas phase following sublimation are reported. L-Trp has attracted the attention of researchers, as this amino acid is the precursor to the neurotransmitter serotonin, which has an essential role not only as an antidepressant but also in cognitive improvement.[236] As the material produced by crystallization from the gas phase is a microcrystalline powder, structure determination was carried out directly from powder XRD data.[85, 88, 139, 237] Although structure determination from powder XRD data is more challenging than from single-crystal XRD data, advances in structure determination from powder XRD data, particularly the development of the direct-space strategy for structure solution,[83-85, 88, 139, 162] are such that structure determination of organic solids of moderate complexity is now feasible. The new polymorph of L-Trp is designated as the β polymorph and the previously reported polymorph is designated as the α polymorph.

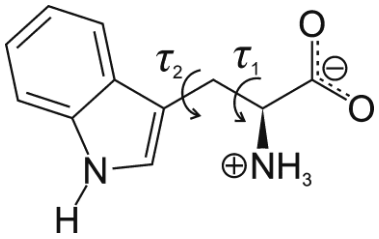

Figure 6.1. *Molecular structure of L-Trp. The torsion angles τ_1 and τ_2 are discussed subsequently.*

6.2 Experimental Section

6.2.1 Crystallization from the Gas Phase

The β polymorph of L-Trp was prepared by crystallization from the gas phase, following sublimation of a powder sample (*ca*. 200 mg) of the α polymorph. The sample was heated under vacuum inside a cylindrical curved-bottom flask containing a cold finger. A schematic diagram of the sublimation apparatus is shown in Figure 1.14 (Chapter 1). The cold finger was filled with acetone/dry ice at –78 °C (dry ice was added periodically to maintain the temperature at –78 °C). The temperature of the sample was increased to 240 °C, with sublimation observed to occur at this temperature. After a few hours, a microcrystalline powder had formed on the cold finger and on the outer glass tube (see Figure 1.14).

6.2.2 Laboratory X-ray Powder Diffraction Data for Structure Determination

High-quality powder XRD data for structure determination of the β polymorph of L-Trp were recorded at ambient temperature (294 K) using a Bruker D8 diffractometer (CuKα_1, Ge-monochromated) operating in transmission mode. The powder sample was packed into three glass capillaries, which were flame-sealed and attached to the disc sample holder of the powder XRD instrument (2θ range, 4° – 70°; step size, 0.016°; total time, 17 hr).

6.2.3 Variable-Temperature Synchrotron X-ray Powder Diffraction Data

Synchrotron X-ray powder diffraction data were recorded as a function of temperature for a sample of the β polymorph using beamline I11 at Diamond Light Source.[238] The sample was contained in a borosilicate glass capillary (0.7 mm), which was rotated around the capillary axis to reduce the effects of preferred orientation. Temperature was controlled using an Oxford Cryostream Plus. Powder XRD data were recorded at 290 K and at intervals of 50 K on cooling (at 360 K/hr) to 140 K using a Position-Sensitive Detector (PSD) on I11 (λ = 0.82462 Å; step size, 0.004°; 2θ range, 1° – 92°; data collection time *ca*. 1 s). A high-quality powder XRD pattern was then recorded at 123 K using a Multi-Analyser-Crystal (MAC) detector on I11 (λ = 0.824656 Å; step size, 0.001°; 2θ range, 1° – 150°; data collection time, 15 min). Powder XRD data were then recorded using the PSD detector on heating (at 360 K/hr) to 440 K at intervals of 50 K. To allow the data recorded using the MAC detector to be used in the program GSAS, the total data size was reduced by binning into groups of 10 points to give an effective step size of 0.01°.

6.2.4 Solid-state ^{13}C NMR Spectroscopy

High-resolution solid-state ^{13}C NMR spectra were recorded for the β polymorph of L-Trp using a Bruker AVANCE III spectrometer (^{13}C Larmor frequency, 213.82 MHz; 3.2 mm HXY probe in double-resonance mode; zirconia rotor; 20 °C) at the UK 850 MHz High-Field Solid-State NMR Facility. The ^{13}C NMR spectra were recorded using ramped ^{1}H→^{13}C cross-polarization[190] together with ^{1}H decoupling using SPINAL-64[108] and magic-angle spinning (MAS) at 12 kHz and 15 kHz.

6.2.5 Periodic DFT-D Calculations

Periodic DFT-D calculations carried out in conjunction with structure solution from powder XRD data utilized the program CASTEP (Academic Release version 8.0).[170] The geometry-optimization calculations used ultrasoft pseudopotentials,[193] PBE functional,[172] semi-empirical dispersion corrections (TS correction scheme),[174] fixed unit cell, preserved space group symmetry, periodic boundary conditions, a basis set cut-off energy of 700 eV and a Monkhorst-Pack grid[192] of minimum sample spacing $0.05 \times 2\pi$ Å^{-1}. Convergence criteria for geometry optimization were 0.01 eV Å^{-1} for forces, 0.00001 eV per atom for energy and 0.001 Å for atomic displacements. Calculation of NMR parameters used the same basis set cut-off energy and Monkhorst-Pack grid.

For comparison of the relative energies of the α and β polymorphs, single-point energy calculations of the geometry-optimized crystal structures (at 123 K and ambient temperature) were carried out using the FHI-aims program (date stamp: 190813),[239] due its efficiency for periodic hybrid-DFT calculations.[240-241] Both generalized gradient approximation (GGA) and hybrid-GGA exchange-correlation functionals were considered, specifically PBE[172] and PBE0,[173] coupled with either the Tkatchenko-Scheffler (TS)[174] or the many-body dispersion (MBD)[242] methods for dispersion correction. Thus, the complete set of exchange-correlation functionals considered in this work were: PBE-TS, PBE-MBD, PBE0-TS and PBE0-MBD. The electronic structure calculations were carried out with an "intermediate" basis set and relativistic effects were included *via* the scaled zeroth order regular approximation.[239] A Γ-centred k-grid was used with a minimum sample spacing of 0.05 Å^{-1}; testing with a denser k-grid sampling of 0.04 Å^{-1} gives changes in the relative energies of < 1 meV. The electronic structure self-consistent field (SCF) cycle was considered to be converged when changes in the electron density, the total energy and the sum of the eigenvalue energies were below 10^{-6} e a_0^{-3}, 10^{-6} eV and 10^{-6} eV, respectively.

6.2.6 Single-crystal X-ray Diffraction of the α Polymorph of L-Trp at Ambient Temperature

To allow structural comparison between the β polymorph and the α polymorph of L-Trp at ambient temperature, it was necessary to carry out single-crystal X-ray diffraction on the α polymorph at ambient temperature. For this work, single crystals

of the α polymorph were prepared as follows. A solution was prepared by dissolving L-Trp (10 mg) in a water:ethanol mixture (1:1 by mass; total mass, 1 g). An amount (60 mg) of this solution was transferred to a small vial which was then covered with parafilm. A few holes were made in the parafilm and the small vial was placed in a bigger vial containing acetonitrile (1 ml) as anti-solvent. The bigger vial was sealed and covered with parafilm and left several days for slow anti-solvent crystallization. Plate-like crystals were collected after several days.

Single-crystal XRD data for the α polymorph were measured at ambient temperature (298 K) using a fine-focus sealed-tube Rigaku XtaLAB PRO dual source (CuKα) diffractometer equipped with a PILATUS 200 detector. Data collection parameters: $-13 \leq h \leq 13$, $-13 \leq k \leq 13$, $-43 \leq l \leq 43$; frame scan width, 0.5°; scan speed, 1.0° per 10.0 s for low resolution and 1.0° per 32.0 s for high resolution; 87632 reflections collected; 26208 independent reflections (R_{int} = 0.0639). The single crystal of the α polymorph was a colourless plate with dimensions 0.418 × 0.281 × 0.057 mm^3. Data were processed using CrysAlis^{PRO} (Rigaku), giving the following unit cell: a = 11.4948(2) Å, b = 11.4979(2) Å, c = 35.7666(6) Å, α = 84.497(1)°, β = 86.796(1)°, γ = 60.068(2)°; V = 4077.56(14) $Å^3$ (see Table 7.1 for crystallographic information).

6.3 Results and Discussion

Powder XRD analysis of samples of L-Trp produced by crystallization from the gas phase were found to be predominantly the new β polymorph, although a small amount of the α polymorph was also present. In spite of extensive attempts to obtain a pure phase of the β polymorph, a monophasic sample of the β polymorph was not obtained. Powder XRD patterns of the α and β polymorphs are shown in Figure 6.2, from which it is clear that the sample of the β polymorph prepared in this work contained a small amount of the α polymorph (the small amount of the α polymorph was also detected in high-resolution solid-state ^{13}C NMR spectra; Figure 6.4). We note that the sample deposited on the side walls of the sublimation apparatus (Figure 1.14) contained a lower proportion of the α polymorph than the sample deposited on the cold finger and was therefore used to record high-quality powder XRD data for structure determination of the β polymorph.

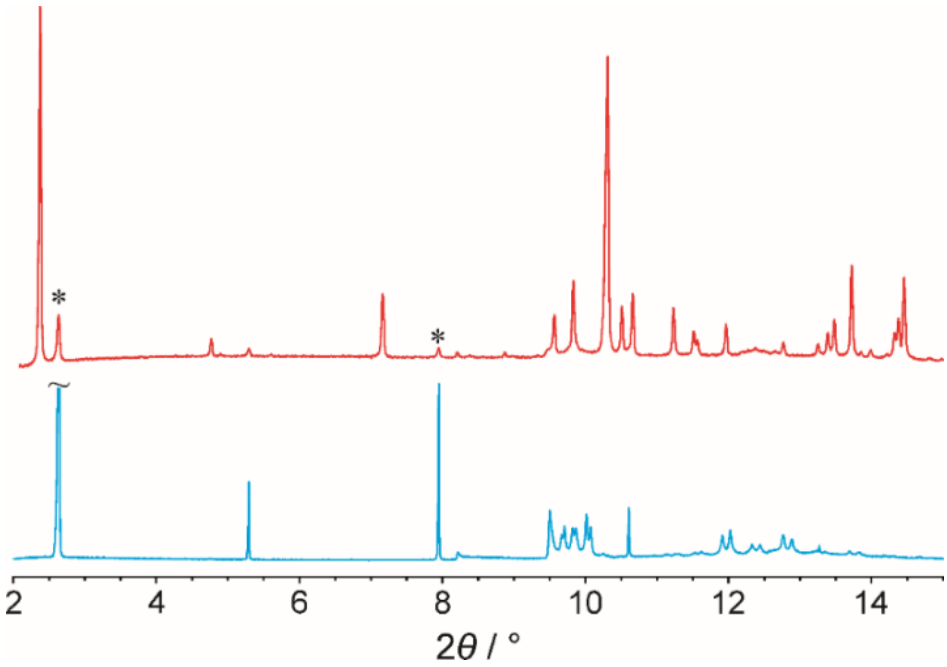

Figure 6.2. *Powder XRD data for the β polymorph (red) and the α polymorph (blue) of* L*-Trp. For the α polymorph, the very strong peak at ca. 2.6° has been truncated. Peaks indicated with black asterisks in the sample of the β polymorph are due to an impurity amount of the α polymorph.*

We note that a previous study[235] gave evidence (from powder XRD data) for the formation of a new solid form of L-Trp, obtained by crystallization from the gas phase, although the crystal structure was not determined in the previous study. At the initial stage of the present work, it was unclear whether the material obtained by crystallization from the gas phase in the present work was the same as, or different from, the material obtained previously,[235] as significant differences are apparent between the powder XRD pattern recorded for the β polymorph in the present work and the powder XRD pattern reported in the previous work (see Figure 6.3). This issue was resolved after completing the structure determination of the β polymorph in the present work. It was then clear that the peaks with significant intensity in the powder XRD data reported previously[235] correspond to the (00*l*) reflections from the β polymorph, suggesting that the material obtained previously has the same *c*-axis as the β polymorph reported here. A comparison between the powder XRD pattern obtained in this study and the powder pattern of the new form obtained previously is shown in Figure 6.3. Therefore, in all probability, the sample obtained previously[235] was indeed the β polymorph, but exhibiting severe preferred orientation in its powder XRD pattern.

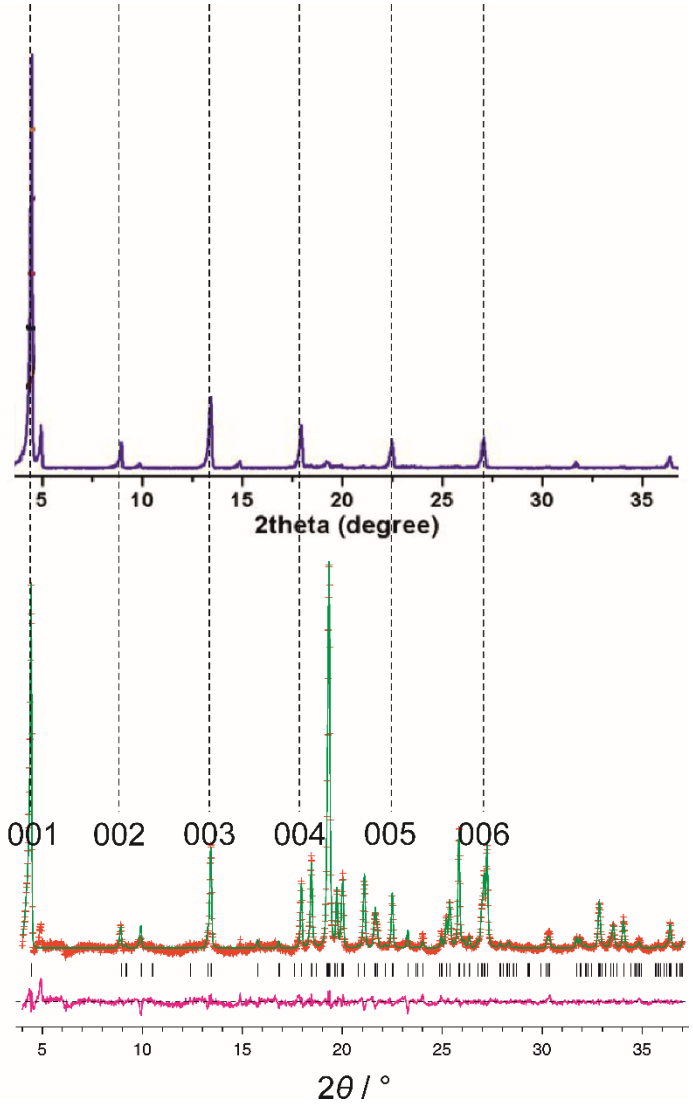

Figure 6.3. *Comparison between the powder XRD pattern of the β polymorph of* L*-Trp prepared in the present work (bottom) and the powder XRD pattern of a new polymorph of* L*-Trp reported in ref. 232 (top; data taken from Figure 2 of ref. 232). Clearly, there is severe preferred orientation in the powder XRD pattern reported in ref. 232.*

6.3.1 High-resolution Solid-state ^{13}C NMR Spectroscopy

The high-resolution solid-state ^{13}C NMR spectrum of the β polymorph of L-Trp (recorded for the same sample used for structure determination from powder XRD data) is shown in Figure 6.4. The solid-state ^{13}C NMR spectrum has two peaks in the region between 175 and 180 ppm assigned to the carbon of the carboxylate group (CO_2^- group) of L-Trp. In addition, there are two peaks in the region *ca*. 55 ppm assigned to the methylene group (CH_2 group) of L-Trp. These results suggest that the

β polymorph of L-Trp has two crystallographically-independent molecules in the asymmetric unit, which allows the correct number of fragments to be used in the structure solution calculations from powder XRD data. As the sample contained a small impurity amount of the α polymorph, extra peaks due to the α polymorph are observed in the solid-state ^{13}C NMR spectrum (indicated by cyan asterisks in Figure 6.4).

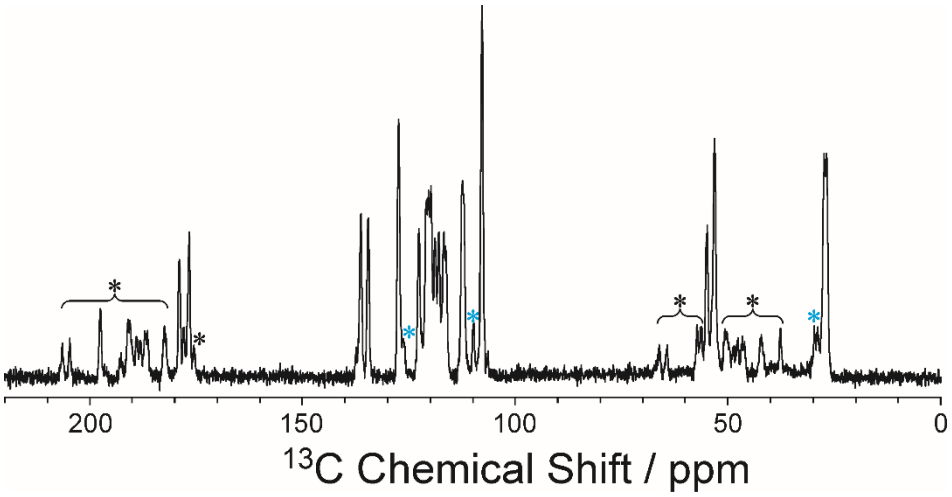

Figure 6.4. *High-resolution solid-state ^{13}C NMR spectrum of the β polymorph of L-Trp. Peaks due to a small impurity amount of the α polymorph are indicated by cyan asterisks. Spinning sidebands are indicated by black asterisks.*

6.3.2 Structure Determination from Powder XRD Data

Indexing and Profile Fitting

The powder XRD pattern of the β polymorph was indexed using the program DICVOL91[199] within the CRYSFIRE package,[141] giving the following unit cell with monoclinic metric symmetry: a = 9.63 Å, b = 5.21 Å, c = 19.79 Å, β = 94.0°, V = 995.6 Å^3. Profile fitting and unit cell refinement were carried out using the Le Bail method[149] in the program GSAS.[150] On the basis of systematic absences, the space group was assigned as $P2_1$ (we note that the space group for L-Trp must be chiral). Density considerations suggest that there are four molecules of L-Trp in the unit cell (Z = 4). Given the assignment of the space group as $P2_1$, which has a multiplicity of 2, the asymmetric unit must contain two molecules of L-Trp (Z' = 2), consistent with the results from high-resolution solid-state ^{13}C NMR. Profile fitting for space group $P2_1$ gave a good quality of fit to the experimental powder XRD data, with the

following refined lattice parameters: a = 9.60857(27) Å, b = 5.20196(13) Å, c = 19.7499(5) Å, β = 93.9601(33)°, V = 984.81(5) Å^3 (R_{wp} = 0.73%, R_p = 0.54%; see Figure 6.5). The main discrepancies in the profile fitting arise from peaks due to the small amount of the α polymorph present in the sample (indicated by cyan asterisks in Figure 6.5).

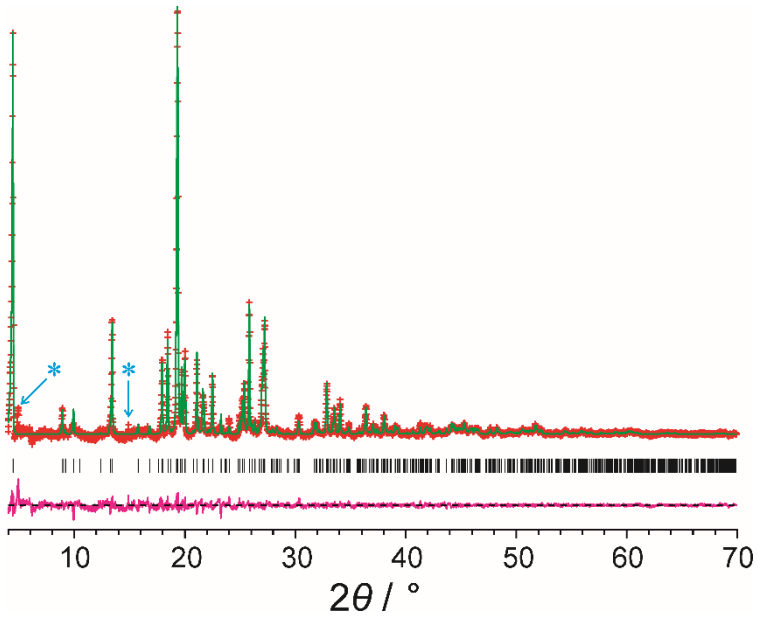

Figure 6.5. *Le Bail fitting of the powder XRD data for the β polymorph of* L*-Trp (red crosses, experimental powder XRD pattern following background subtraction; green line, calculated powder XRD pattern; black tick marks, predicted peak positions; magenta line, difference plot). Peaks marked with cyan asterisks are due to a small impurity amount of the α polymorph.*

Structure Solution

Structure solution of the β polymorph of L-Trp was carried out using the direct-space strategy[85] implemented using a genetic algorithm (GA) in the program EAGER.[81, 98-99, 139, 196-197, 243] In the structure solution calculations, one of the two molecules of L-Trp in the asymmetric unit was defined by 8 structural variables (2 positional, 3 orientational and 3 torsion-angle variables; for $P2_1$, the position of one molecule along the b-axis may be fixed) and the other molecule was defined by 9 structural variables (3 positional, 3 orientational and 3 torsion-angle variables). Thus the total number of structural variables in the GA calculation was 17. Standard bond lengths and bond angles were taken from the Cambridge Structural Database using MOGUL[244] and bond lengths involving hydrogen atoms were taken from Allen *et*

al.[169] Each GA calculation involved the evolution of a population of 100 trial structures, and was run for 200 generations. In each generation, 10 mating operations and 50 mutation operations were applied. A total of 40 independent GA calculations were carried out in parallel, with 29 calculations producing essentially the same structure giving the best fit to the experimental powder XRD data (i.e. with lowest R_{wp}).

Structure Refinement

The trial structure with lowest R_{wp} obtained in the structure solution calculations was used as the initial structural model for Rietveld refinement.[167] In the refinement, standard restraints were applied to bond lengths and bond angles, and planar restraints were used for the carboxylate group and indole ring. A common isotropic displacement parameter was refined for all non-hydrogen atoms, and the value for hydrogen atoms was set at 1.2 times this value. The initial Rietveld refinement produced a good fit (R_{wp} = 0.94%, R_p = 0.67%) although two hydrogen atoms in one molecule (the gauche molecule) were unacceptably close to each other. This unacceptable short contact was resolved by carrying out a periodic DFT-D geometry-optimization calculation (with fixed unit cell). The geometry-optimized structure was very similar to the structure from the Rietveld refinement (RMSD = 0.36 Å for non-hydrogen atoms). The structure following geometry optimization was then used as the initial structural model for further Rietveld refinement, with additional intermolecular distance restraints applied to preserve the hydrogen-bonding geometry found in the geometry-optimized structure.

The final Rietveld refinement for the β polymorph (Figure 6.6) produced a high-quality fit (R_{wp} = 0.82%, R_p = 0.61%), comparable to the quality of fit obtained in profile fitting (Figure 6.5), with the following refined lattice parameters: a = 9.60888(27) Å, b = 5.20179(14) Å, c = 19.7495(6) Å, β = 93.9505(33)°, V = 984.80(6) Å^3. The main discrepancies in the Rietveld refinement (see the difference profile in Figure 6.6) arise due to peaks from the impurity of the α polymorph. The solid-state ^{13}C NMR spectrum calculated (using the strategy described elsewhere[245]) for the final refined structure is in good agreement with the experimental solid-state ^{13}C NMR spectrum (Figure 6.7), giving further validation for the correctness of the structure.

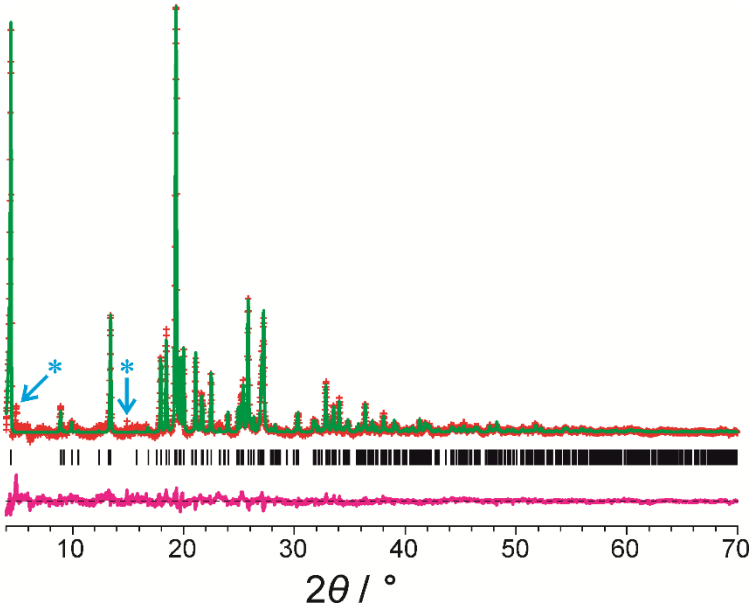

Figure 6.6. *Final Rietveld refinement for the β polymorph of L-Trp (red crosses, experimental powder XRD pattern after background subtraction; green line, calculated powder XRD pattern; black tick marks, predicted peak positions; magenta line, difference plot). Blue asterisks indicate the main peaks due to a small impurity amount of the α polymorph.*

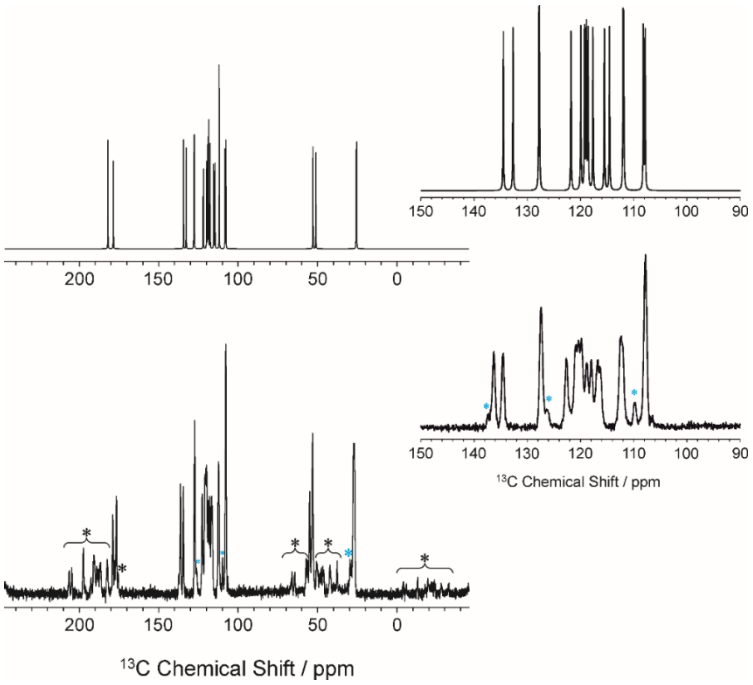

Figure 6.7 *Calculated (top) and experimental (bottom) solid-state ^{13}C NMR spectra for the β polymorph of L-Trp. Insets show expanded regions of the spectra. Cyan asterisks indicate peaks due to the impurity of the α polymorph.*

Given the presence of the small impurity amount of the α polymorph, Le Bail and Rietveld refinement of the β polymorph was also attempted in which the α polymorph was included as a second phase in the refinement. However, these two-phase refinements were unstable. Even though the α polymorph is only a minor phase in the sample, the large unit cell (giving rise to a large number of predicted peak positions) and the structural complexity of the α polymorph contribute to this problem. For this reason, the Rietveld refinement was carried out using only the β polymorph, as described above. The low intensity peaks due to the α polymorph in the experimental powder XRD pattern are therefore not fitted in the refinement and remain as minor discrepancies in the Rietveld difference plot (Figure 6.6).

The Rietveld refinement of the β polymorph described above was carried out using laboratory powder XRD data recorded at ambient temperature, and the discussion of the crystal structure of the β polymorph (Section 6.3.3) is based on the final structure obtained in this refinement. Le Bail and Rietveld refinement of the β polymorph was also carried out at 123 K, using the synchrotron X-ray powder diffraction data recorded at 123 K (part of this powder XRD pattern is shown in Figure 6.14). In Le Bail fitting of the β polymorph at 123 K (in which the α polymrrph was included as a second phase), the unit cell parameters and space group obtained for the β polymorph at room temprature were used together with the reported unit cell parameters and space group of the α polymorph (Figure 6.8a; R_{wp} = 3.95%, R_p = 2.78%). The refined unit cell parameters were as follows: a = 9.603(14) Å, b = 5.181(6) Å, c = 19.727(27) Å, β = 94.50(21)°, V = 978.35(27) Å^3. In the final Rietveld refinement of β-L-Trp at 123 K, the structure of the β polymorph determined at ambient temperature was used as the initial structural model. Rietveld refinement of the β polymorph at 123 K gave a fit shown in Figure 6.8b (R_{wp} = 4.64%, R_p = 3.13%) with the following refined unit cell paramters: a = 9.606(16) Å, b = 5.179(8) Å, c = 19.726(31) Å, β = 94.48(20)°, V = 978.50(30) Å^3.

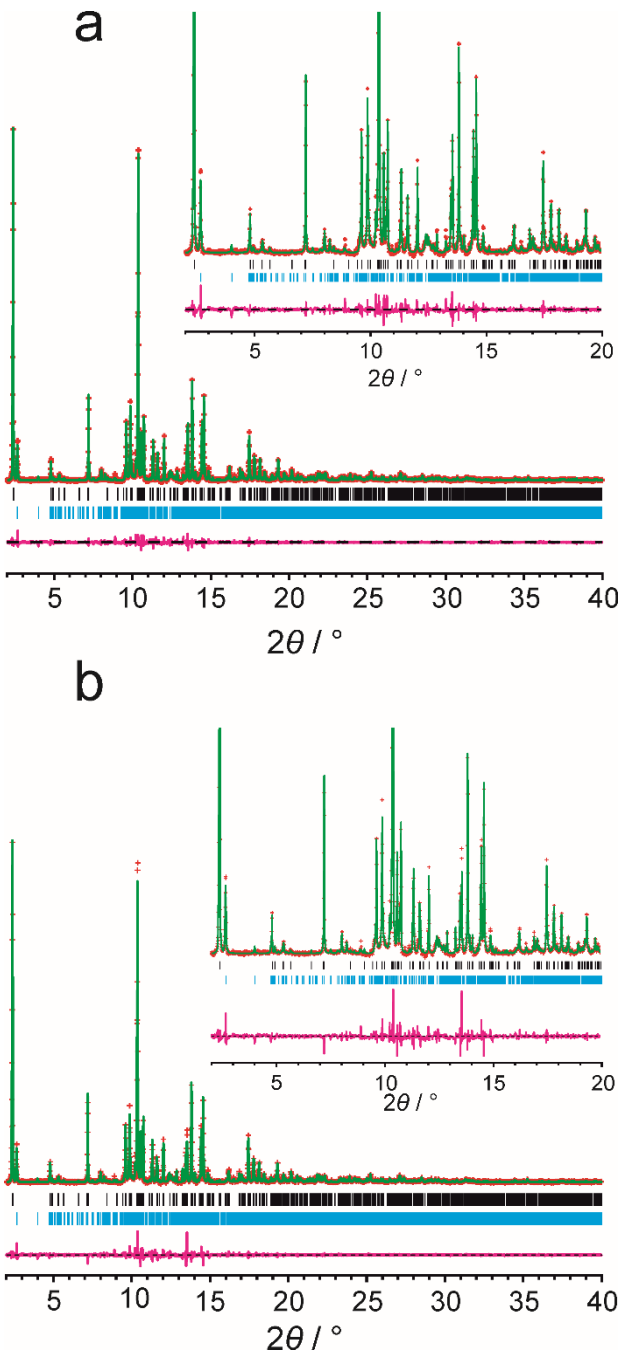

Figure 6.8. *(a) Le Bail fitting for the β polymorph of L-Trp at 123 K (b) final Rietveld refinement for the β polymorph of L-Trp at 123 K (red crosses, experimental powder XRD pattern after background subtraction; green line, calculated powder XRD pattern; black tick marks, predicted peak positions for the β polymorph; cyan tick marks, predicted peak position for the α polymorph; magenta line, difference plot).*

This Rietveld refinement led to essentially the same fractional atomic coordinates as the structure determined at ambient temperature. However, the quality of fit obtained in the Le Bail and Rietveld refinements using the synchrotron X-ray powder diffraction data at 123 K was not as good as that obtained in the refinement

using the laboratory powder XRD data at ambient temperature. This situation can be attributed to the fact that the sample used in the synchrotron X-ray powder diffraction study contained a higher amount of the α polymorph than the sample used in the laboratory powder XRD study. Nevertheless, the structure of the β polymorph determined from the Rietveld refinement at 123 K was used as the starting structure for geometry optimization using periodic DFT-D calculations, and was used to establish the information shown in Tables 6.1 and 6.3 for the β polymorph at 123 K.

6.3.3 Structural Properties of the β polymorph of L-Trp

In common with several other amino acids, the crystal structure of the β polymorph is a layered structure with alternating hydrophilic and hydrophobic regions (Figure 6.9). The two independent molecules in the asymmetric unit have different conformations (Figure 6.10), described as *trans* (τ_1 = 179.4°) and *gauche* (τ_1 = 52.1°), on the basis of the N–Cα–Cβ–Cγ torsion angle (τ_1 in Figure 6.1).

Table 6.1. *Crystallographic data for the α and β polymorphs of L-Trp at 123 K and ambient temperature.*

	***T* = 123 K**		**Ambient temperature**	
	α polymorph	**β polymorph**	**α polymorph**	**β polymorph**
Reference	[214]	This work	This work	This work
Space Group	*P*1	$P2_1$	*P*1	$P2_1$
Z	16	4	16	4
Z'	16	2	16	2
a / Å	11.430	9.606	11.495	9.609
b / Å	11.464	5.180	11.498	5.202
c / Å	35.606	19.726	35.767	19.751
α / °	84.42	90	84.50	90
β / °	87.69	94.48	86.80	93.95
γ / °	60.10	90	60.07	90
V / Å	4025.31	978.50	4077.56	984.88

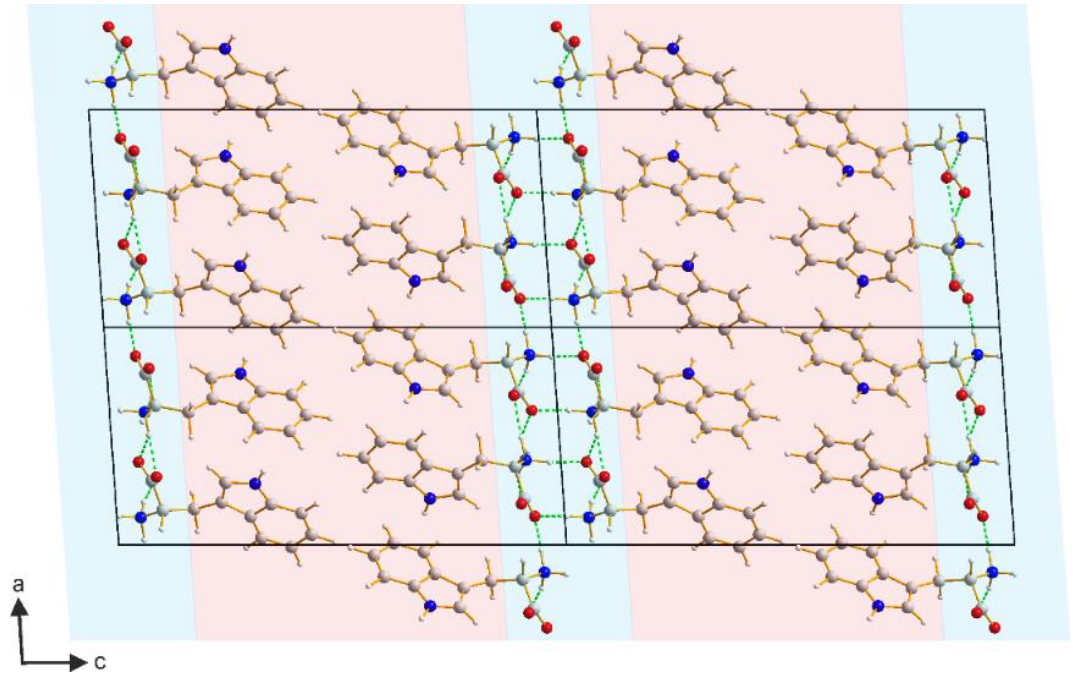

Figure 6.9. *Crystal structure of the β polymorph of L-Trp viewed along the b-axis (hydrophilic region, cyan shading; hydrophobic region, pink shading).*

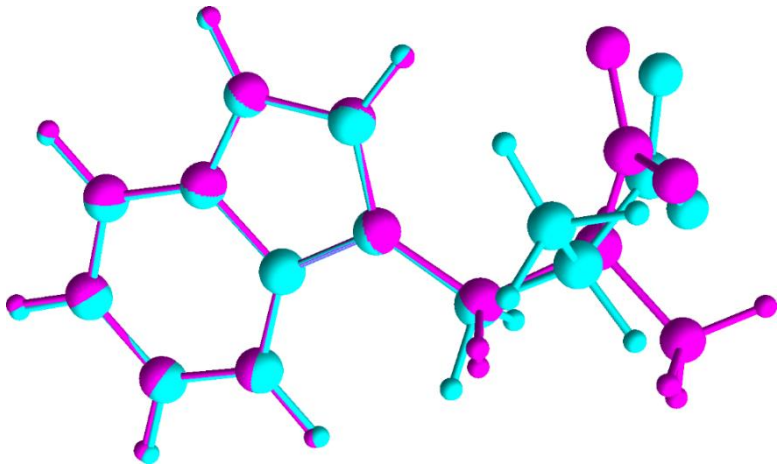

Figure 6.10. *Overlay of the two crystallographically independent molecules of L-Trp in the crystal structure of the β polymorph. The two conformations are described as gauche (blue) and trans (purple), as defined by the N–Cα–Cβ–Cγ torsion angle. The indole rings of the two molecules are superimposed in the overlay.*

The hydrophilic layer comprises two hydrogen-bonded sheets (each sheet is parallel to the *ab*-plane), related to each other by the 2_1 screw axis along the *b*-axis. As shown in Figure 6.11, a given sheet is constructed from three types of cyclic N–H···O hydrogen bonded array, described as $R_4^3(14)$, $R_4^4(16)$ and $R_1^2(4)$ in graph set notation.[246]

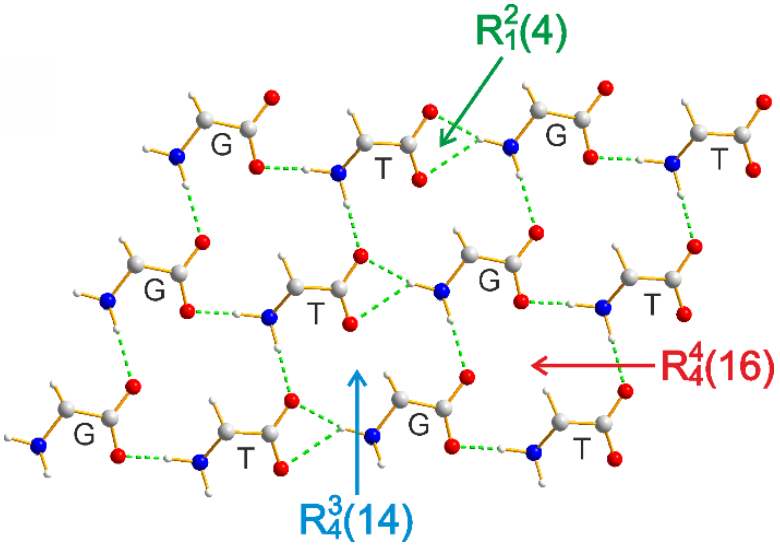

Figure 6.11. *Hydrogen-bonding arrangement in a single sheet of the hydrophilic region in the β polymorph of* L*-Trp (gauche and trans molecules are labelled G and T respectively). The indole rings are omitted for clarity. Green dashed lines indicate hydrogen bonding.*

For each molecule, one N–H bond of the ammonium group connects adjacent sheets through an N–H···O hydrogen bond. The hydrophobic region in the β polymorph is a "bilayer" involving the indole rings of L-Trp molecules (Figure 6.9). Within one layer of the bilayer, the indole rings of the *trans* and *gauche* molecules form a nearly perpendicular arrangement, as shown in Figure 6.12.

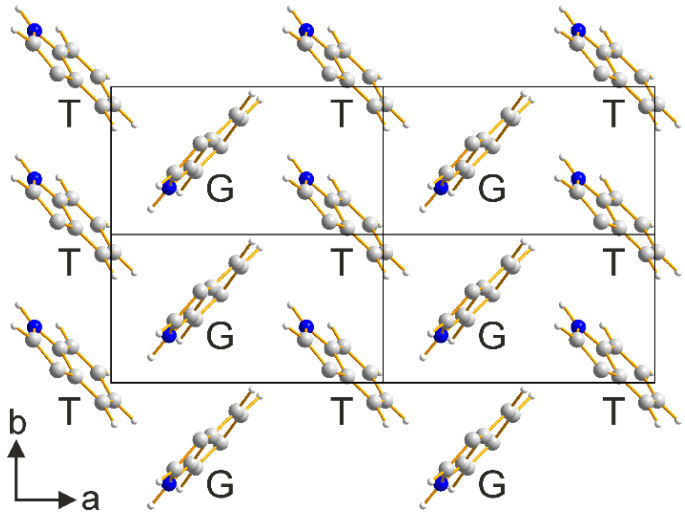

Figure 6.12. *The arrangement of indole rings of the* L*-Trp molecules in a single layer of the hydrophobic bilayer in the β polymorph viewed along the c-axis (gauche and trans molecules are labelled G and T respectively).*

According to the classification system of Görbitz *et al.*,[247] the β polymorph has the L2-L2 hydrogen-bonding arrangement, which is reported to be the most energetically favourable hydrogen-bonding scheme for enantiopure amino acids. While the L2-L2 scheme is also reported for L-isoleucine (both polymorphs),[225-226] L-leucine (polymorph I),[227] L-lysine,[200] L-methionine[248] and L-valine,[249] the β polymorph of L-Trp is the first case of an amino acid containing an aromatic side-chain that adopts the L2-L2 hydrogen-bonding scheme, representing a counter-example to the suggestion[247] that amino acids with aromatic side-chains cannot form this hydrogen bonding arrangement *"owing to inevitable steric conflict"*. The conformational features that allow L-Trp to adopt the L2-L2 arrangement in the β polymorph by avoiding undesirable steric conflict are discussed below.

Now the structural properties of the α and β polymorphs of L-Trp are compared. Each structure comprises alternating hydrophobic and hydrophilic layers, but with significant differences in the hydrogen-bonding scheme in the hydrophilic region and in the arrangement of indole rings in the hydrophobic region. The asymmetric unit of the β polymorph has one *gauche* molecule and one *trans* molecule (defined by the N–Cα–Cβ–Cγ torsion angle; τ_1 in Figure 6.1), while the asymmetric unit of the α polymorph has eight *gauche* molecules and eight *trans* molecules.[214] An important difference in molecular conformations between the α and β polymorphs (see Figure 6.13) concerns the Cα–Cβ–Cγ–CH(ring) torsion angle (τ_2 in Figure 6.1), which defines the orientation of the indole ring relative to the amino acid head-group. For the β polymorph, τ_2 is relatively close to zero (*trans* molecule, $\tau_2 = -37.5°$; *gauche* molecule, $\tau_2 = 8.7°$), which means that the plane of the indole ring lies close to the Cα–Cβ–Cγ plane. In contrast, for the α polymorph, the values of τ_2 are substantially larger (for *trans* molecules, τ_2 ranges from –112.2° to –115.2°; for *gauche* molecules, τ_2 ranges from 109.6° to 113.6°), such that the indole ring is tilted significantly away from the Cα–Cβ–Cγ plane. A comparison of all the torsion angles of the α and β polymorphs is given in Table 6.2.

As the Cα–Cβ–Cγ plane is essentially perpendicular to the plane of the hydrogen-bonded layer (*ab*-plane), the indole rings in the β polymorph project almost perpendicular to the hydrogen-bonded layer, allowing efficient packing of L-Trp molecules in the *ab*-plane and facilitating the formation of the L2-L2 hydrogen-bonding arrangement without unfavourable steric conflict. As a

consequence, the area per molecule in the *ab*-plane is significantly lower for the β polymorph than the α polymorph (Table 6.3) and the "thickness" of the hydrophobic bilayer is larger for the β polymorph (Table 6.3).

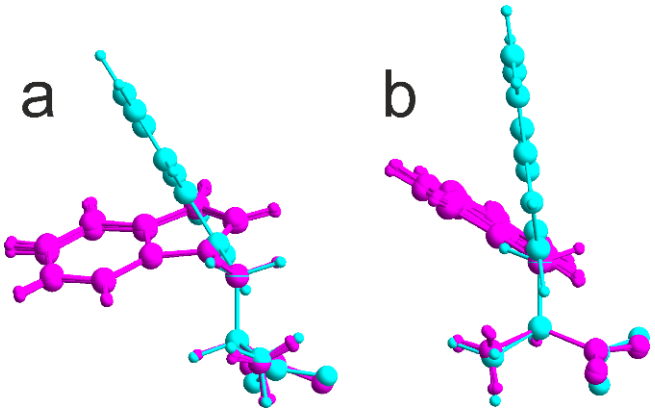

Figure 6.13. *Overlays of (a) the 8 trans molecules in the α polymorph (magenta) and the trans molecule in the β polymorph (cyan), and (b) the 8 gauche molecules in the α polymorph (magenta) and the gauche molecule in the β polymorph (cyan). The N, Cα and Cβ atoms of the head-group are superimposed in the overlay.*

Table 6.2. *Full list of torsion angles in the α and β polymorphs of L-Trp (table continues on the next page).*

β polymorph

	O-CO-Cα-Cβ	**CO-Cα-Cβ-Cγ**	**Cα-Cβ-Cγ-CH(ring)**	**N-Cα-Cβ-Cγ**
Trans	85.8	61.8	–37.5	179.4
Gauche	–59.4	–77.5	8.7	52.1

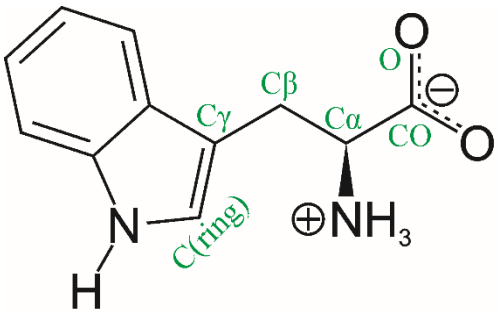

α polymorph

	O-CO-Cα-Cβ	**CO-Cα-Cβ-Cγ**	**Cα-Cβ-Cγ-CH(ring)**	**N-Cα-Cβ-Cγ**
Trans1	99.1	64.7	–112.5	–173.4
Trans2	99.2	65.8	–115.2	–173.4
Trans3	102.3	65.8	–113.4	–173.2

Table 6.2. (cont.)

Trans4	102.5	65.1	–113.2	–173.6
Trans5	98.4	65.8	–114.1	–173.2
Trans6	99.9	65.4	–114.6	–173.7
Trans7	103.2	65.3	–114.8	–172.8
Trans8	101.4	64.8	–112.2	–174.1
Gauche1	–71.4	157.7	111.7	–78.6
Gauche2	–72.2	158.1	111.3	–79.1
Gauche3	–75.9	157.8	113.3	–79.6
Gauche4	–76.4	159.0	109.9	–78.3
Gauche5	–73.4	159.3	109.6	–77.7
Gauche6	–71.8	158.0	113.6	–80.0
Gauche7	–74.6	158.2	111.0	–79.0
Gauche8	–76.1	158.2	112.0	–79.0

6.3.4 Relative Stabilities of the Polymorphs of L-Trp

The relative stabilities of the α and β polymorphs have been assessed, both at 123 K and ambient temperature, using periodic DFT-D energy calculations. Initially, geometry-optimization calculations with fixed unit cell were carried out using PBE-TS. The initial structures used in these calculations were as follows: (i) α polymorph at 123 K: structure from single-crystal XRD reported previously;[214] (ii) β polymorph at 123 K: structure determined from powder XRD in the present work; (iii) α polymorph at ambient temperature: unit cell determined from single-crystal XRD in the present work together with the fractional coordinates reported[214] for the structure at 123 K; (iv) β polymorph at ambient temperature: structure determined from powder XRD in the present work.

The energies of the resultant geometry-optimized structures were then calculated using PBE-TS, PBE-MBD, PBE0-TS and PBE0-MBD. Among these methods, PBE0-MBD is considered[176, 250] to give the most reliable assessment of the relative energies of polymorphs of organic materials. From the PBE0-MBD results, the calculated energy (per mol of L-Trp molecules) is lower for the β polymorph by 1.1 kJ mol^{-1} at ambient temperature and by 0.3 kJ mol^{-1} at 123 K (Table 6.3). These results suggest that the β polymorph may be more stable than the α polymorph (although the differences in energy may be comparable to the errors inherent in the computational approach used, including the neglect of entropic factors). Furthermore, the β polymorph has higher density (Table 6.3) than the α polymorph (by 2.8% at 123

K and 3.5% at ambient temperature), indicating that the β polymorph has the more efficient packing arrangement.

To investigate the possible occurrence of polymorphic phase transitions, powder XRD data were recorded on beamline I11 at Diamond Light Source for a sample of the β polymorph containing a small amount of the α polymorph, with data recorded (Figure 6.14) on cooling from 290 K to 123 K and then on heating from 123 K to 440 K. Throughout this temperature cycle, no changes were observed in the relative intensities of the powder XRD patterns due to the α and β polymorphs. Thus, there is no evidence for any polymorphic transformations in this temperature range.

Table 6.3. *Properties of the α and β polymorphs of L-Trp at 123 K and ambient temperature. Energies (per mole of L-Trp molecules) from periodic DFT-D calculations are given relative to the α polymorph at 123 K.*[251] *Density is calculated from the experimental unit cell volume (Table 6.1) and the number of molecules in the unit cell. The area per molecule in the hydrogen-bonded layer is calculated from the geometry of the ab-plane. The thickness of the bilayer is estimated from the perpendicular distance between the planes of adjacent hydrophilic layers (for the α polymorph, the average of the values for the two crystallographically distinct bilayers is given). Energy calculations were carried by Andrew Logsdail, Cardiff University.*[251]

Temperature	**123 K**		**Ambient**	
Polymorph	**α**	**β**	**α**	**β**
Energy (PBE-TS) / kJ mol^{-1}	0	–0.3	1.1	0.3
Energy (PBE-MBD) / kJ mol^{-1}	0	1.0	0.7	1.2
Energy (PBE0-TS) / kJ mol^{-1}	0	–1.2	1.6	–0.4
Energy (PBE0-MBD) / kJ mol^{-1}	0	–0.3	1.3	0.2
Density / g cm^{-3}	1.348	1.386	1.331	1.377
Area per molecule in hydrogen-bonded sheet / Å^2	28.40	24.88	28.63	24.99
Thickness of bilayer / Å	17.72	19.67	17.80	19.70

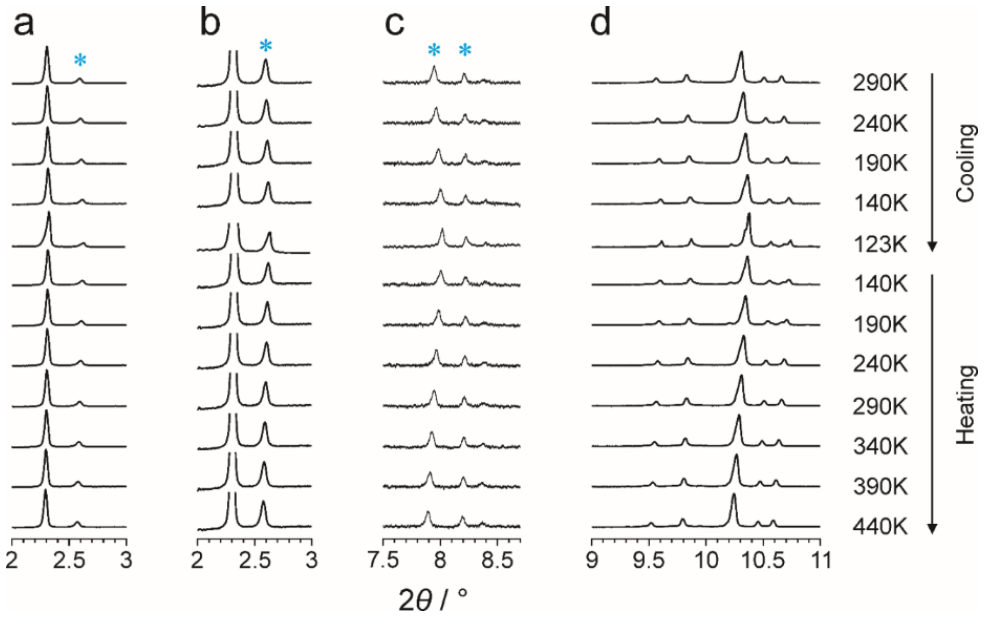

Figure 6.14. *Selected regions of the variable-temperature synchrotron powder X-ray diffraction data recorded for a sample of the β polymorph containing a small amount of the α polymorph (peaks due to the α polymorph are indicated by blue asterisks). Data were recorded on cooling from 290 K to 123 K and then on heating from 123 K to 440 K. The intensity scales in (b) and (c) are expanded relative to those in (a) and (d) in order to emphasize the peaks due to the small amount of the α polymorph.*

6.4. Concluding Remarks

In conclusion, the new β polymorph of L-Trp has been prepared by crystallization from the gas phase. The crystal structure of the β polymorph, determined directly from powder XRD data, represents the first example of an amino acid with an aromatic side-chain that adopts the energetically favourable L2-L2 hydrogen-bonding arrangement. Periodic DFT-D calculations suggest that the β polymorph may be more stable than the α polymorph. Finally, it is worth emphasizing the opportunity to exploit crystallization from the gas phase as a method to produce new polymorphs of other organic materials in the future. In this regard, we note that crystallization from the gas phase eliminates the solvent effects that can have a significant influence on crystallization processes from solution.

Chapter 7: Characterization of Solid-State Phase Transitions in 1-Iodoadamantane (1-IA)

7.1 Introduction

While most crystalline materials are usually characterized by a high degree of positional and orientational order, there is a class of crystalline materials that are positionally ordered but with significant reorientational dynamics. Rotator phases or plastic crystals are examples of these types of material, which exhibit reorientational degrees of freedom.[252] In these materials, crystallization does not supress molecular reorientational dynamics, as the molecules are positionally ordered (characteristic of the crystalline phase) but with reorientational dynamics (characteristic of the liquid phase), meaning that these rotator phase solids still have some liquid phase characteristics. These materials usually have a high-symmetry orientationally disordered structure at high temperature and a more ordered low-symmetry structure at low temperature.

Rotator phase solids usually undergo phase transitions on heating and cooling. The transition from the disordered phase (high-temperature phase) to the ordered phase (low-temperature phase) arises from molecular motions becoming "frozen" on cooling across the transition, which may lead to lowering of symmetry. Hence, these transitions can be classified as group to subgroup transitions. In the disordered phases, the reorientational dynamics may result in certain atoms having random site occupancies. However, on cooling, atoms tend to have non-random site occupancies due to reducing the reorientational degrees of freedom. Examples of rotator phases include hexamethylbenzene,[253-256] adamantane[257-263] and tetrakis (trimethylsilyl) silane.[264-266] In addition, urea[267-270] and thiourea[271-273] inclusion compounds typically exhibit order-disorder phase transitions. At high temperature, the guest molecules are dynamically disordered inside the host structure, while at low temperature, the guest dynamics become frozen and there is a lowering of the symmetry of the structure.

In this chapter, we investigate the phase transition behaviour of 1-iodoadamantane (1-IA; Figure 7.1) as a function of temperature. Although it has been noted in the literature that 1-IA is a rotator phase material,[252] the structural properties of 1-IA as a function of temperature have yet not been reported. Only one

crystal structure of 1-IA has been reported[274] (the same structure has been determined at both ambient temperature and at 256 K, corresponding to phase A in this chapter). However, DSC data recorded in the present work show that this material undergoes several phase transitions as a function of temperature. We note that the temperature dependent structural properties of other 1-haloadamantane derivatives (1-fluoroadamantane,[275-279] 1-chloroadamantane[280-283] and 1-bromoadamantane[284-286]) have been reported.

We demonstrate here using single-crystal XRD, powder XRD and DSC that 1-IA undergoes several phase transitions on cooling and heating. The crystal structures of different solid phases arising from phase transitions on cooling have been determined by single-crystal XRD; however, at this stage, the crystal structures of the solid phases arising from phase transition on heating have not yet been determined. In addition, although powder XRD data were recorded as a function of temperature on heating, it was not possible to determine the crystal structures from powder XRD data as it was not possible to index the powder XRD patterns.

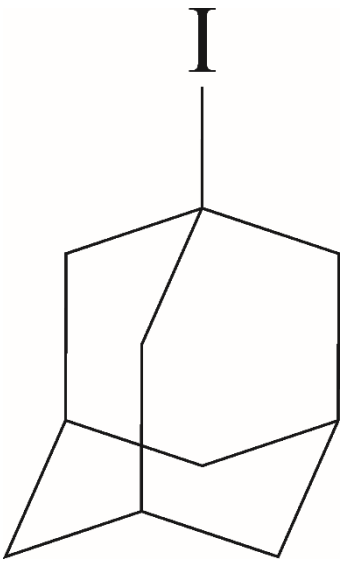

Figure 7.1. *Molecular structure of 1-IA.*

7.2 Experimental Section

7.2.1 Single Crystal Preparation

Single crystals of 1-IA were prepared by evaporation of solvent from a solution of 1-IA in ethanol. The solution was placed in a vial sealed with parafilm, with a few

holes made in the parafilm to allow slow solvent evaporation. Large single crystals were collected after one day.

Several other crystallization methods, including crash cooling, slow cooling and anti-solvent methods, were also used to explore the possible formation of different phases. In crash cooling, 1-IA was dissolved in ethanol at 343 K followed by quenching in ice. In slow cooling, a hot solution of 1-IA in ethanol was placed in an incubator at 343 K and cooled to 283 K at 0.01 K/min. In the anti-solvent method, a solution of 1-IA in ethanol was placed in a small vial sealed with parafilm containing a few holes. This vial was then placed inside a bigger vial containing water as an anti-solvent. The bigger vial was capped and sealed with parafilm, allowing slow diffusion of the water from the vapour phase into the ethanol solution in the small vial.

7.2.2 Differential Scanning Calorimetry (DSC)

DSC data were recorded for a sample of 1-IA (typically *ca*. 5 – 10 mg) in a hermetically sealed aluminium pan using a TA Instruments Q100 differential scanning calorimeter. Starting from ambient temperature, the sample was cooled to 190 K and then heated to 360 K. DSC data were recorded both for heating/cooling rates of 5 K/min and 20 K/min. In another experiment, a sample of 1-IA was heated from ambient temperature to 370 K at 20 K/min. Each DSC experiment was repeated three times.

7.2.3 Synchrotron Powder XRD

Synchrotron X-ray powder diffraction data were recorded as a function of temperature for a sample of 1-IA using beamline I11 at Diamond Light Source.[238] The sample was packed in a borosilicate glass capillary (0.7 mm), which was rotated around the capillary axis to reduce the effects of preferred orientation. Temperature was controlled using an Oxford Cryostream Plus. Powder XRD data were recorded at 293 K and at intervals of 10 K on cooling (at 360 K/hr) to 123 K using a Position Sensitive Detector (PSD) on I11 (λ = 0.82462 Å; step size, 0.004°; 2θ range, 1° to 92°; data collection time *ca*. 1 s). The sample was then heated at the same rate back to 293 K and powder XRD data were recorded at intervals of 10 K on heating. Since the material is beam-sensitive, a 1 mm attenuation was applied to reduce the intensity of X-rays and hence to reduce the beam damage.

7.2.4 Laboratory Powder XRD

Powder XRD data using a laboratory source were also recorded as a function of temperature on heating, starting from ambient temperature (for a sample that had not previously been cooled below ambient temperature) up to the melting temperature. The sample was packed in a glass capillary and data were collected on an Agilent SuperNova Dual Atlas diffractometer with a mirror monochromator using Cu K_α radiation (λ = 1.5418 Å). Temperature was controlled using an Oxford Cryosystems 700 Series Cryostream, with powder XRD data recorded at intervals of 5 K on heating. Two-dimensional diffraction images were recorded for five detector and sample positions with sample rotation about the capillary axis for each position. Intensity integration of the images produced a conventional one-dimensional powder XRD pattern (showing intensity *versus* 2θ) in the 2θ range from 6° to 120°.

7.2.5 Single-crystal XRD

Following selection under a microscope, crystals were attached to a sample pin using an adhesive. Single-crystal XRD data were collected on an Agilent SuperNova Dual Atlas diffractometer with a mirror monochromator using either Cu (λ = 1.5418 Å) or Mo (λ = 0.7107 Å) radiation. Sample temperature was controlled using an Oxford Cryosystems cooling apparatus. Crystal structures were generally solved and refined using SHELXS and SHELXL.[287-288] For disordered structures, restraints were applied to molecular geometry and displacement parameters during refinement. Non-hydrogen atoms were refined with anisotropic displacement parameters. Hydrogen atoms were inserted in idealized positions, and a riding model was used with Uiso(H) set at 1.2 or 1.5 times the value of Ueq for the atom to which they are bonded.

7.3 Results and Discussion

All crystallization experiments (by evaporation, crash cooling, slow cooling and anti-solvent methods) produced the same phase, which we designate as phase A (also referred to as the high-temperature phase). This phase corresponds to the published crystal structure of 1-IA (determined at both ambient temperature and 256 K).[272] On cooling, phase A was found to transform to either of two low-temperature phases, designated as phase B and phase C. The structure of each phase and their

transformation behaviour are discussed in more detail in Sections 7.3.3, 7.3.4 and 7.3.5.

7.3.1 DSC Results

The DSC data for 1-IA recorded using a cooling/heating rate of 20 K/min are shown in Figure 7.2 (DSC data recorded using cooling/heating rates of 5 K/min and 20 K/min are shown in the Appendix B). On cooling 1-IA, two exothermic events assigned as solid-solid phase transitions are observed at *ca*. 230 K and *ca.* 208 K. On subsequent heating, three thermal events, which are also assigned as solid-solid phase transitions, are observed at *ca.* 211 K, 257 K and 285 K. A large endothermic peak at *ca.* 348 K is attributed to melting.

In another DSC experiment (Figure 7.3), a sample of 1-IA (which had not previously been cooled below ambient temperature) was heated from ambient temperature to the melting temperature. No phase solid-state phase transitions were observed in this temperature range (prior to melting).

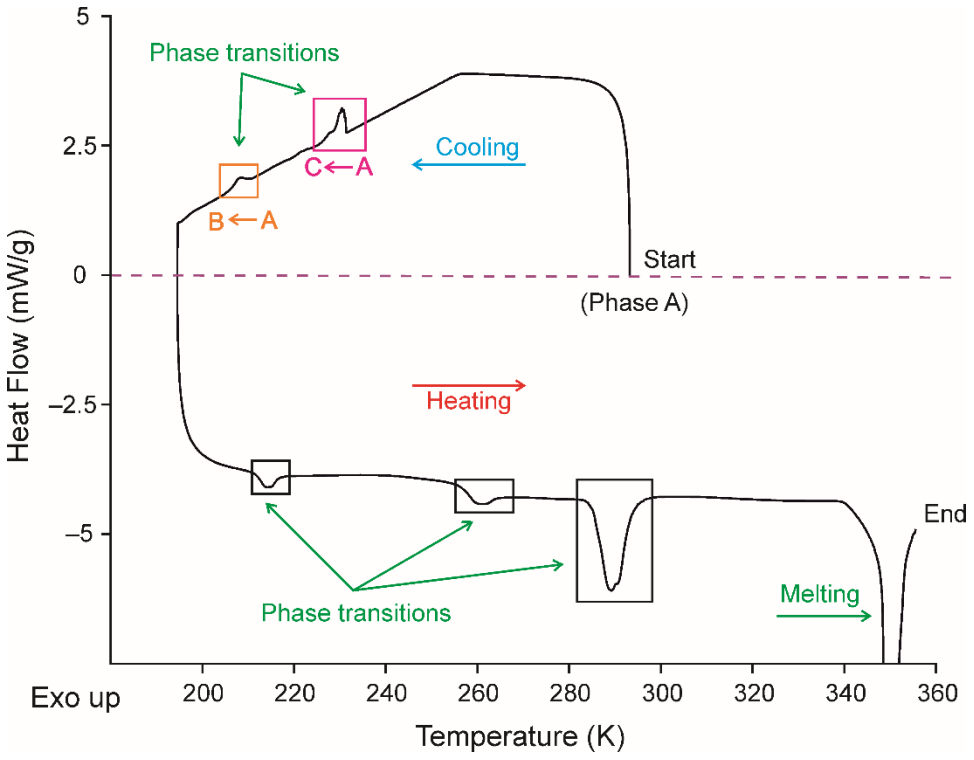

Figure 7.2. *DSC data for 1-IA recorded using cooling/heating rates of 20 K/min. The assignments of the structural changes associated with the phase transitions on cooling are discussed in Sections 7.3.3 and 7.3.4. In order to emphasize the small peaks observed on cooling, the large peak due to melting is truncated.*

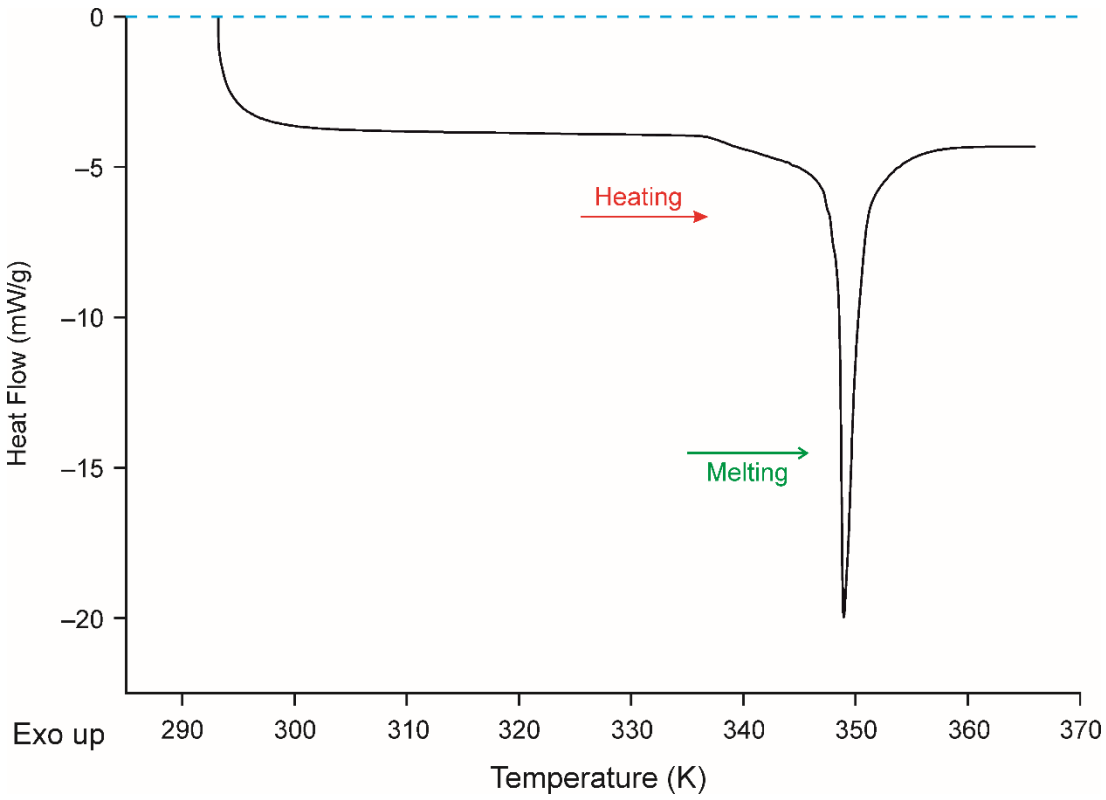

Figure 7.3. *DSC data for 1-IA recorded on heating from ambient temperature to above the melting temperature.*

7.3.2 Variable-temperature Powder XRD

To study the structural properties of 1-IA as a function of temperature, powder XRD data were recorded as a function of temperature on both cooling and heating on beamline I11 at Diamond Light Source. In addition, laboratory powder XRD data where recorded as a function of temperature on heating from ambient temperature to the melting temperature.

Synchrotron Powder XRD Data as a Function of Temperature on Cooling

DSC data (Figure 7.2) show that 1-IA undergoes two phase transitions on cooling, which was confirmed by variable-temperature powder XRD (Figures 7.4 and 7.5). For each powder XRD pattern, Le Bail fitting was carried out to confirm the phase (A, B or C) present at each temperature, using the unit cell parameters and space group determined for each phase from single-crystal XRD data (structure determination of each phase is discussed in Section 7.3.3).

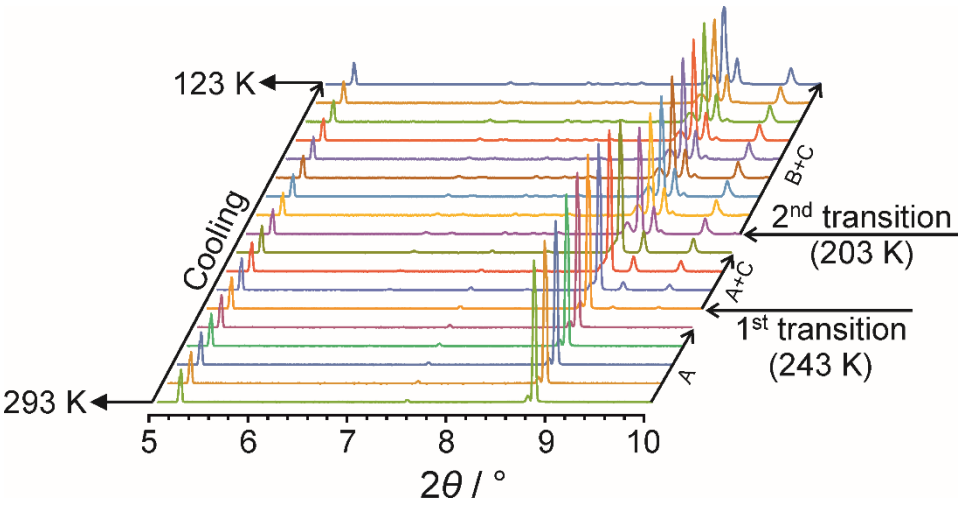

Figure 7.4. *Powder XRD data recorded for 1-IA (in the range 2θ = 5 – 10°) as a function of temperature on cooling from 293 K to 123 K in steps of 10 K.*

At 293 K, the powder XRD data (Figures 7.4 and 7.5) indicate that 1-IA exists as a monophasic sample of phase A. No changes are observed in the powder XRD data down to 253 K. However, at 243 K there is evidence of the emergence of peaks corresponding to phase C, suggesting that phase A had started to transform to phase C (this transition was also identified by single-crystal XRD; see Sections 7.3.3 and 7.3.4).

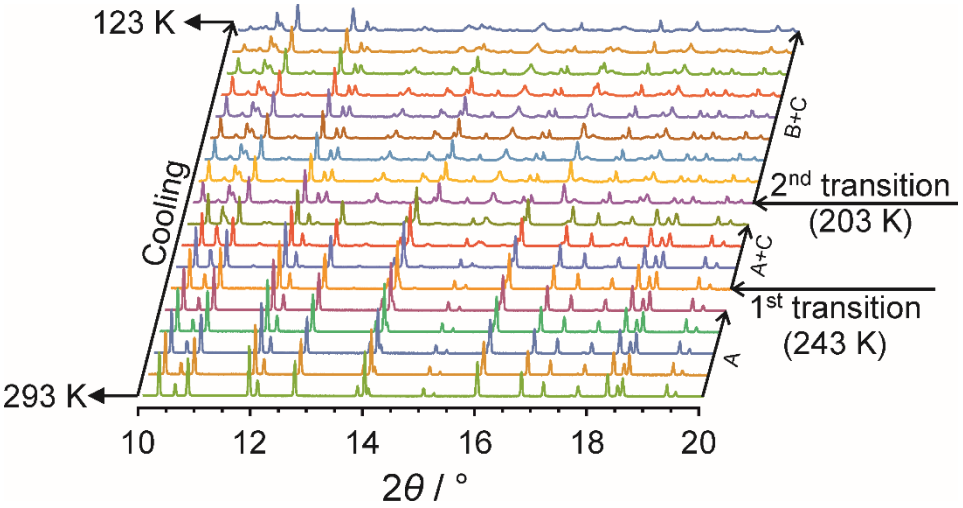

Figure 7.5. *Powder XRD data recorded for 1-IA (in the range 2θ = 10 – 20°) as a function of temperature on cooling from 293 K to 123 K in steps of 10 K.*

The fact that this transition is observed at a different temperature from that observed in the DSC data (230 K; Figure 7.2) may be due to the different cooling schedules used in the DSC and powder XRD experiments. The peaks due to phase C

continue to grow as temperature is decreased to 213 K, but the sample is still a mixture of phase A and phase C. At 203 K, the remaining amount of phase A in the sample is observed to transform to phase B (this transition was also identified by single-crystal XRD). At the lowest temperature studied (123 K), the sample comprises a mixture of phase B and phase C.

Synchrotron Powder XRD Study as a Function of Heating

DSC data (Figure 7.2) show that 1-IA undergoes three phase transitions on heating at *ca.* 211 K, 257 K and 285 K. These transitions were also observed in variable-temperature powder XRD data recorded on heating (Figures 7.6 and 7.7), with the three transitions observed at the following temperatures: 213 K, 263 K and 283 K. The crystal structures of the solid phases involved in these transitions have not been determined in the present work.

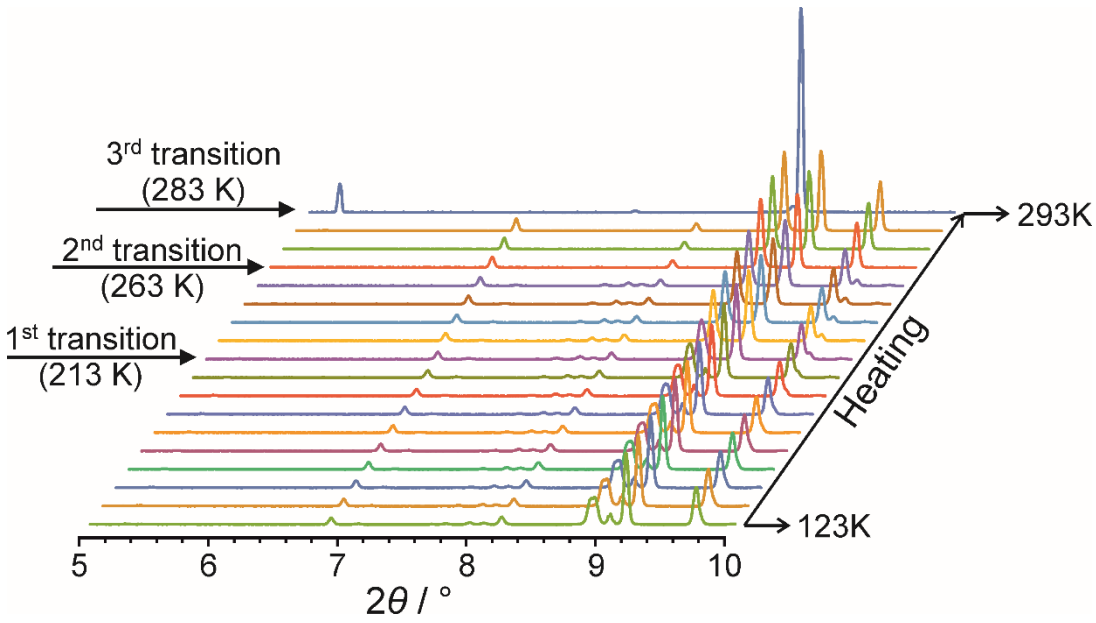

Figure 7.6. *Powder XRD data recorded for 1-IA (in the range 2θ = 5 – 10°) as a function of temperature on heating from 123 K to 293 K.*

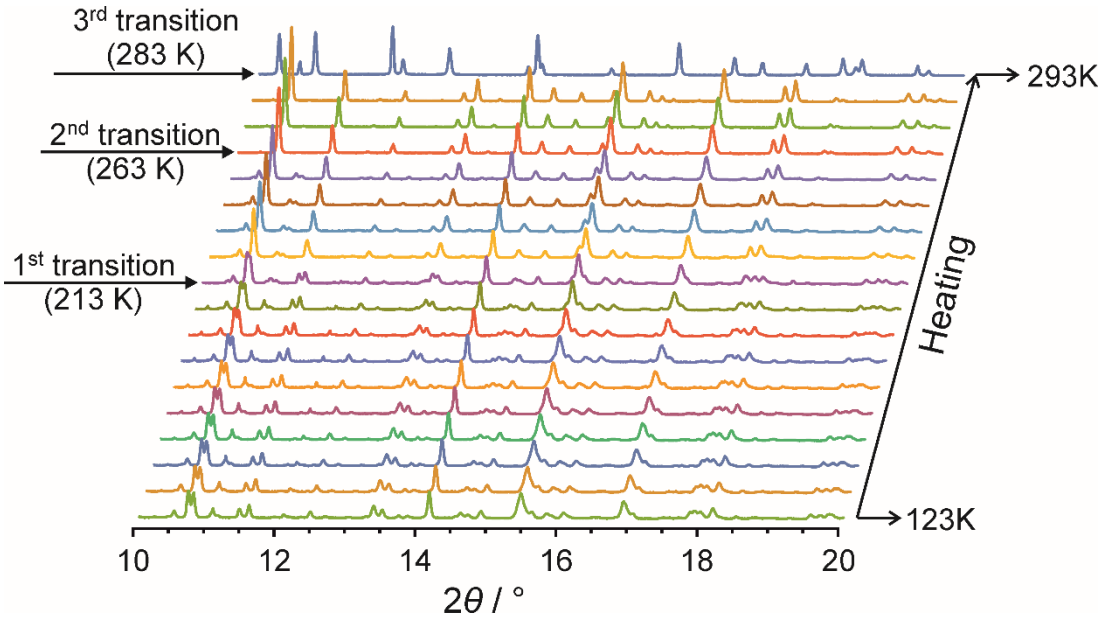

Figure 7.7. *Powder XRD data recorded for 1-IA (in the range 2θ = 10 – 20°) as a function of temperature on heating from 123 K to 293 K.*

Laboratory Powder XRD Study as a Function of Temperature on Heating from Ambient Temperature

DSC data (Figure 7.3) show that, on heating from ambient temperature, 1-IA does not exhibit any phase transitions before melting. This behaviour was confirmed by a variable-temperature powder XRD study in which a sample of phase A of 1-IA (which had not previously been cooled below ambient temperature) was heated from ambient temperature to the melting temperature (Figure 7.8). Clearly, no changes occur in the powder XRD data throughout this temperature range, and the sample remains as a monophasic sample of phase A up to the melting temperature.

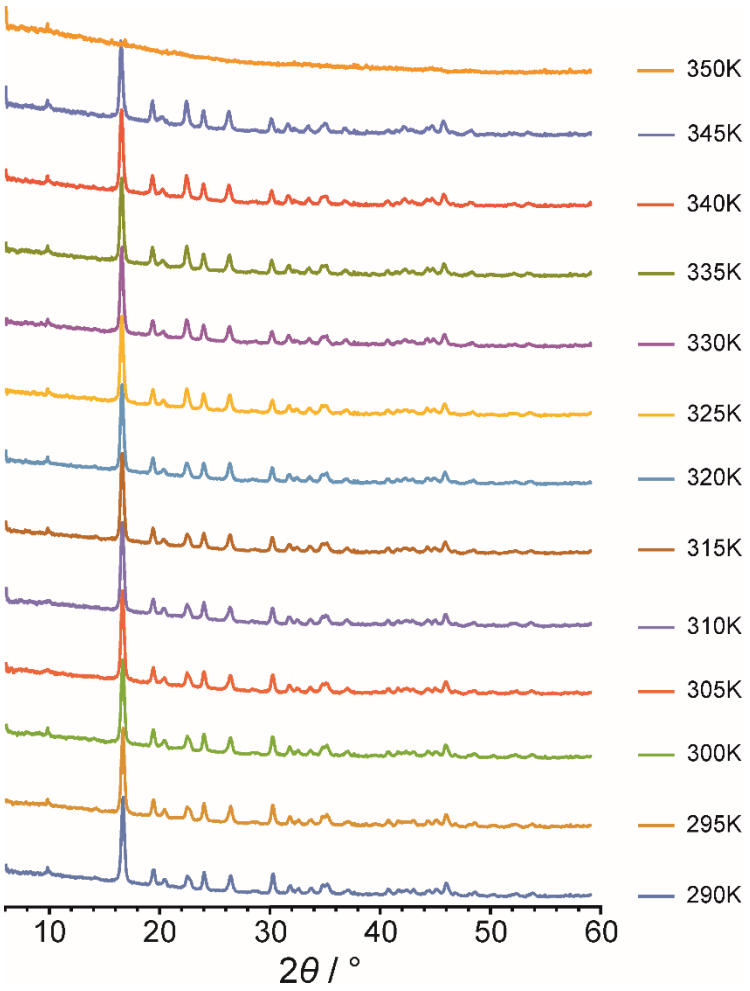

Figure 7.8. *Powder XRD data recorded for 1-IA as a function of temperature on heating from 290 K to 350 K.*

7.3.3 Structural Properties of 1-IA Phases

It is clear from the powder XRD study, a sample of phase A of 1-IA transforms into two different low-temperature phases (denoted phase B and phase C) on cooling. To determine the crystal structures of phase B and phase C, we have carried out low-temperature single-crystal XRD studies. As now discussed, a significant finding from this work is that individual single crystals of 1-IA that exist as phase A at ambient temperature can show two distinct types of behaviour on cooling. Specifically, some crystals of 1-IA are found to undergo a transition to low-temperature phase B on cooling below 203 K (corresponding to one of the transition temperatures observed in DSC data on cooling; Figure 7.2). However, other single crystals of 1-IA are found to undergo a transition to low-temperature phase C on cooling below 220 K (corresponding to the other transition temperature observed in DSC data on cooling;

Figure 7.2). Table 7.1 summarizes the crystallographic data for the high-temperature phase (phase A) and the low-temperature phases (phase B and phase C) of 1-IA.

Table 7.1. *Crystallographic data for phases A, B and C of 1-IA (table continues in the next page).*

Empirical formula	$C_{10}H_{15}I$		
Formula weight (g/mol)	262.12	262.12	262.12
Temperature (K)	293(2)	200(2)	220(2)
Phase	Phase A	Phase B	Phase C
Crystal system	Orthorhombic	Monoclinic	Monoclinic
Space group	$Pmn2_1$	$P2_1$	$P2_1/n$
λ/Å	0.71073	1.54184	0.71073
Crystal size/mm^3	0.524 × 0.314 × 0.068	0.091 × 0.077 × 0.056	0.580 × 0.466 × 0.237
***a* (Å)**	6.6977(12)	6.575(4)	6.9402(16)
***b* (Å)**	8.8476(11)	8.5096(4)	13.826(3)
***c* (Å)**	8.6709(12)	8.8262(5)	10.278(3)
α (°)	90	90	90
β (°)	90	94.411(5)	90.14(2)
γ (°)	90	90	90
V (Å^3)	513.83(13)	492.37(5)	986.22(4)
Density (g/cm^3)	1.694	1.768	1.765
Z	2	2	4
Absorption coefficient (mm^{-1})	3.057	25.025	3.186
F(000)	256	256	512
Theta range for data collection (°)	3.29 – 29.789	6.754 – 74.241	3.538 – 29.621
Index ranges	$-9 \leq h \leq 8$	$-8 \leq h \leq 7$	$-9 \leq h \leq 9$
	$-11 \leq k \leq 9$	$-10 \leq k \leq 10$	$-18 \leq k \leq 17$
	$-11 \leq l \leq 8$	$-10 \leq l \leq 10$	$-9 \leq l \leq 13$

Table 7.1 (cont.)

Reflections collected	2116	2511	3387
Independent reflections	1025 [R(int) = 0.0204]	1550 [*R*(int) = 0.0334]	1945 [R(int) = 0.0755]
Refinement method	Full-matrix least-squares on F^2	Full-matrix least-squares on F^2	Full-matrix least-squares on F^2
Data / restraints / parameters	1025 / 17 / 58	1550 / 63 / 100	1945 / 518 / 183
Goodness-of-fit on F^2	1.081	1.113	1.047
Final R indices [I>2σ(I)]	R1 = 0.0347, wR2 = 0.0838	R1 = 0.0548, wR2 = 0.1369	R1 = 0.0922, wR2 = 0.2345
R indices (all data)	R1 = 0.0579, wR2 = 0.0942	R1 = 0.0627, wR2 = 0.1448	R1 = 0.1382, wR2 = 0.2822
Absolute structure parameter	0.55(4)	0.49(4)	
Extinction coefficient	n/a	n/a	0.004(2)
Largest diff. peak and hole (e.Å^{-3})	0.666 and –0.592	0.830 and –0.909	1.795 and –2.413

Structural Properties of Phase A

The high-temperature phase (phase A) is orthorhombic with space group *P*mn2_1. The crystal structure (Figure 7.9) can be described in terms of rows (chains) of molecules of 1-IA parallel to the *b*-axis in which the C–I bonds are aligned in the same direction for all molecules in the chain. Neighbouring chains related by translation along the *a*-axis or the *c*-axis are clearly parallel to each other. However, nearest-neighbour chains (displaced by the vector $\boldsymbol{a}/2 + \boldsymbol{c}/2$ in the projection shown in Figure 7.9b) are anti-parallel to each other. Thus, for one set of chains, the C–I bonds of all molecules point in the *positive* direction along the *b*-axis, whereas for the other set of chains, the C–I bonds of all molecules point in the *negative* direction along the *b*-axis.

In each type of chain, the molecular symmetry axis is parallel to the *b*-axis and perpendicular to the *ac*-plane, and the 1-IA molecules are located on a crystallographic

mirror plane. Thus the asymmetric unit comprises one half molecule of 1-IA with the other half generated by the mirror symmetry. As this phase is believed to be a rotator phase, it is expected that the 1-IA molecule is dynamic *via* 3-fold 120° jumps around the molecular symmetry axis (i.e. the C–I bond axis). Thus, the structure appears to be ordered from the "XRD perspective" because the symmetry of the jump process (3-fold 120° jumps) matches one of the molecular symmetry elements (3-fold axis parallel to the C–I bond).

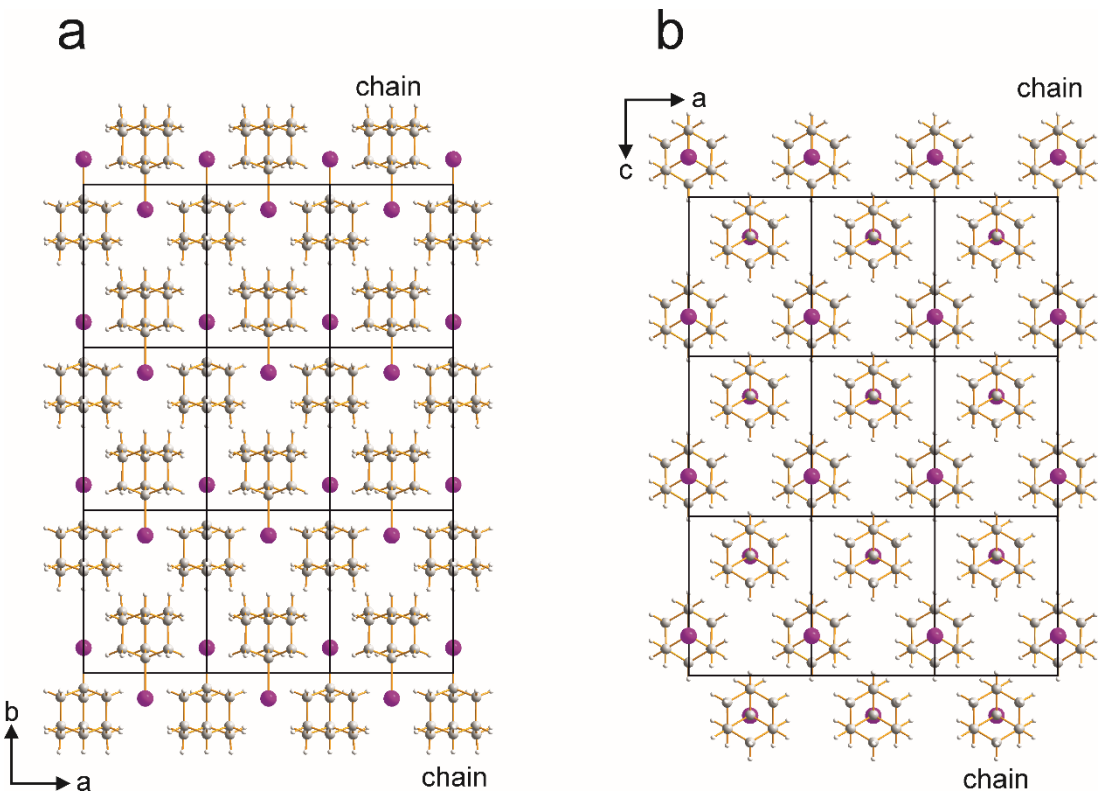

Figure 7.9. *Crystal structure of phase A at 290 K viewed (a) along the c-axis and (b) along the b-axis.*

Structural Properties of Phase B

Phase B is monoclinic with space group $P2_1$. The crystal structure is shown in Figure 7.10. It is clear from Figures 7.9 and 7.10 and Table 7.1 that phase A and phase B have similar unit cell parameters, although the symmetry is lowered from orthorhombic in phase A to monoclinic in phase B. To facilitate comparison between phase A and phase B, the unit cell parameters for phase B were transformed so that the *c*-axis is the unique axis. Similar to phase A, the structure of phase B can also be described in terms of rows (chains) of molecules with the molecular axes aligned

parallel to each other. In these chains, adjacent molecules are related by translation along the *b*-axis. The molecular axes (and C–I bond axes) of all molecules in a given chain are parallel to each other, but (unlike phase A) the molecular axis are tilted slightly away from the *b*-axis. Again, there are two different orientations of these chains. For one set of chains, the C–I bonds of all molecules are oriented close to the *positive* direction along the *b*-axis, whereas for the other set of chains, the C–I bonds of all molecules are oriented close to the *negative* direction along the *b*-axis.

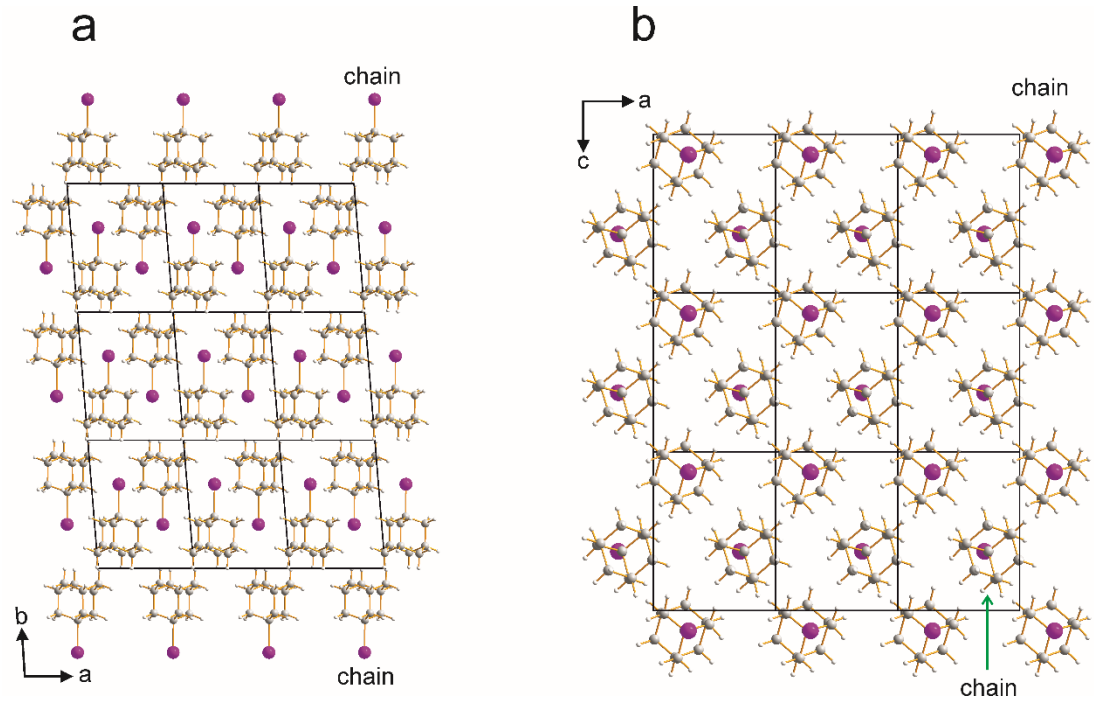

Figure 7.10. *Crystal structure of phase B at 175 K viewed along (a) the c-axis and (b) the b-axis.*

Structural Properties of Phase C

Phase C is monoclinic with space group $P2_1/n$, and exhibits a significantly different crystal structure than phase A and phase B. In the crystal structure (Figure 7.11), there are four distinct molecular orientations with significantly different directions of the C–I bond axes (labelled 1 – 4 in Figure 7.11). The directions of the C–I bonds of molecules 1 and 3 are anti-parallel to each other, and the directions of the C–I bonds of molecules 2 and 4 are anti-parallel to each other, while the directions of the C–I bonds for molecules 1 and 3 are essentially perpendicular to those for molecules 2 and 4. We note that other 1-haloadamantanes (such as the low-temperature phase of 1-bromoadamantane[286] and the low-temperature ordered

phase III of 1-chloroadamantane[289]) are isostructural with phase C of 1-IA. Clearly, the structure of phase C is significantly different from both phase A (which contains chains of molecules with the C–I bond axes parallel to the *b*-axis) and phase B (which contains chains of molecules with the C–I bond axes nearly parallel to the *b*-axis).

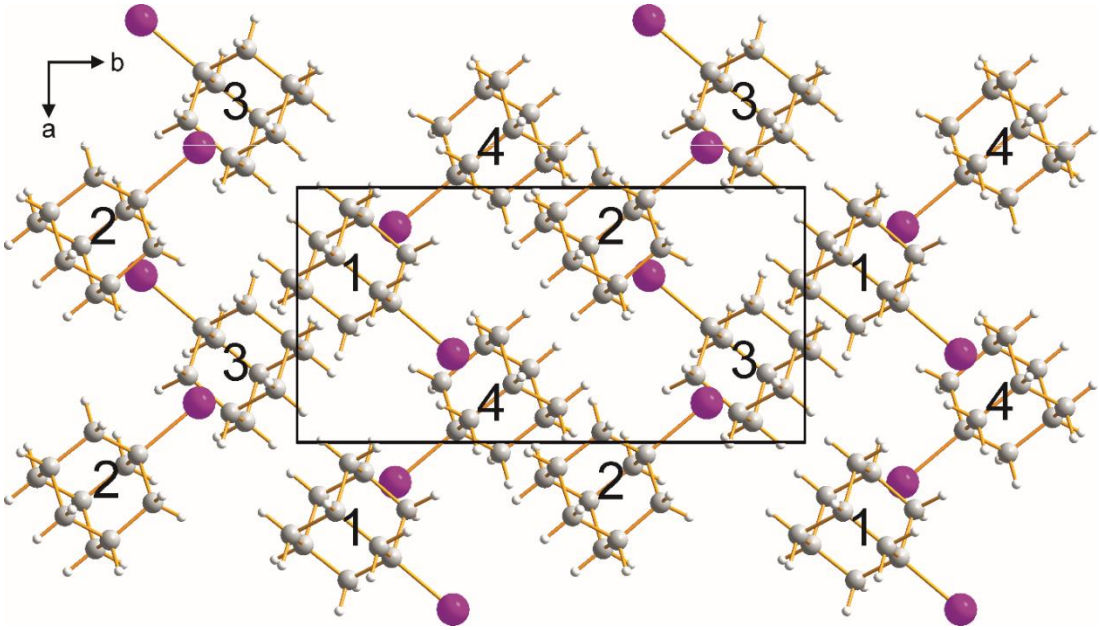

Figure 7.11. *Crystal structure of phase C at 220 K viewed along the c-axis.*

7.3.4 Structural Relations between the High-Temperature Phase and the Low-Temperature Phases of 1-IA

Relation between Phase A and Phase B

Comparison of the crystal structures of phase A and phase B (see Figures 7.12 – 7.14) shows that these phases share several common structural features, although with some significant differences. In particular, on transforming from phase A to phase B, the 1-IA molecules undergo a slight tilting of the C–I bonds away from the *b*-axis (we recall that, in phase A, the C–I bond axes of all molecules are exactly parallel to the *b*-axis).

In addition, on transforming from phase A to phase B, the 1-IA molecules undergo a small rotation around the molecular symmetry axes, corresponding to loss of the mirror plane and the lowering of symmetry from $P\mathrm{mn}2_1$ (phase A) to $P2_1$ (phase B); this type of phase transition may be described as a group-subgroup transition. As a consequence, the 1-IA molecule does not lie on a crystallographic mirror plane in phase B and the asymmetric unit comprises one whole molecule of 1-IA (in contrast,

the asymmetric unit of phase A comprises one half 1-IA molecule). We note that 1-fluoroadamantane shows group-subgroup phase transitions.[275]

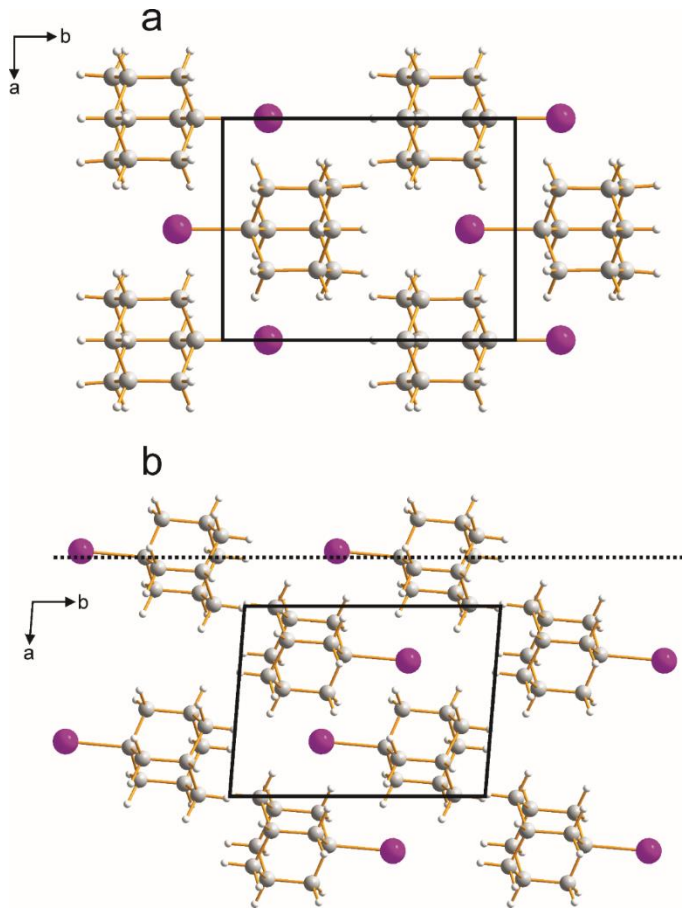

Figure 7.12. *Comparison of the crystal structures of (a) phase A and (b) phase B viewed along the c-axis, showing both a slight rotation of the 1-IA molecules in phase B around the molecular symmetry axis and a slight tilting of the molecular symmetry axis in phase B away from the b-axis.*

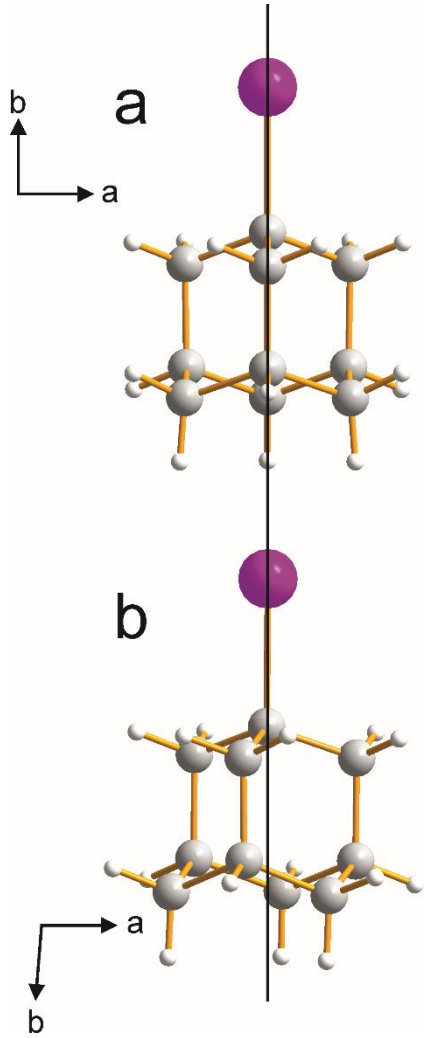

Figure 7.13. *The 1-IA molecule in (a) phase A and (b) phase B, showing that the molecule lies on a mirror plane in phase A, whereas the slight rotation of the molecule around the C–I bond axis in phase B corresponds to loss of the mirror symmetry.*

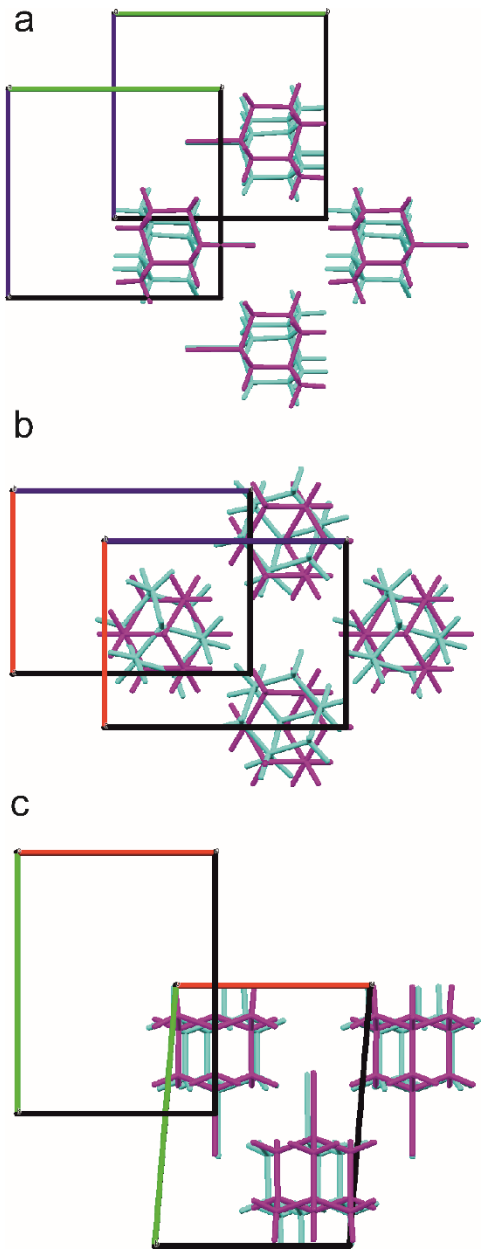

Figure 7.14. *Overlay of the structures of phase A (magenta) and phase B (cyan) viewed along (a) the a-axis, (b) the b-axis, and (c) the c-axis. The symmetry is $Pmn2_1$ for phase A and $P2_1$ for phase B. The transition from phase A to phase B can be described as a group to subgroup transition.*

To investigate the order of the A → B phase transition, the volume per molecule in the crystal structure is plotted against temperature in Figure 7.15 (these data were established from single-crystal XRD studies as a function of temperature). At the phase transition temperature 207 K, a discontinuity in the volume per molecule is observed, indicating the first-order character of this transition.

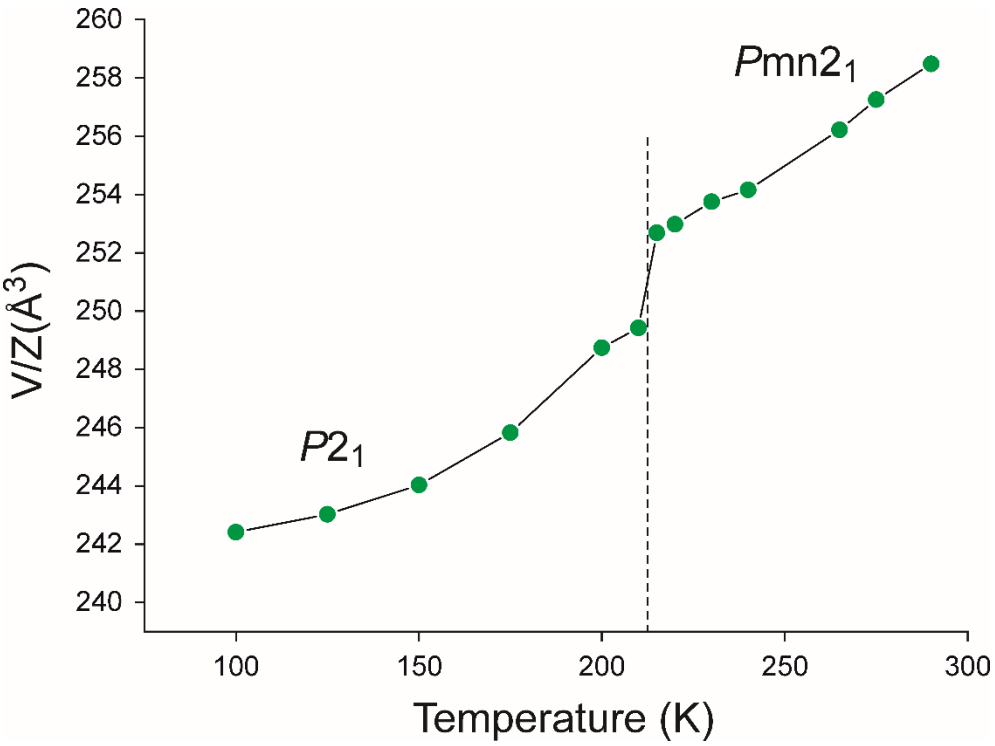

Figure 7.15. *Volume per molecule as a function of temperature for the transformation from phase A to phase B.*

Relation between Phase A and Phase C

Structural comparison of phase A and phase C is shown in Figures 7.16 and 7.17. The transition from phase A to phase C involves significant reorientation of the 1-IA molecules, by *ca*. 45° around the *c*-axis, which is substantially greater than the changes in molecular orientations associated with the transition from phase A to phase B. As a consequence, the structure of phase C is significantly different from that of phase A.

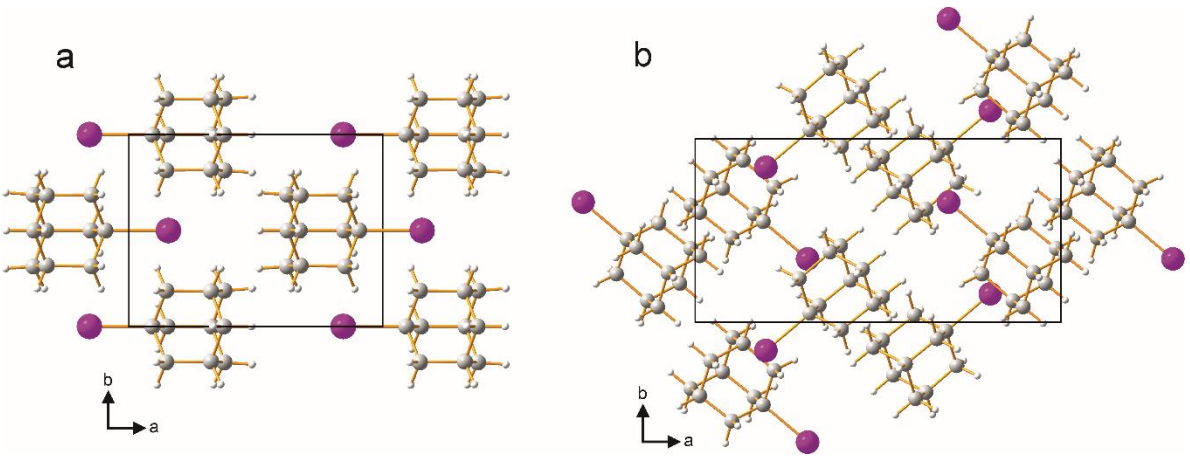

Figure 7.16. *Comparison between the structures of (a) phase A and (b) phase C.*

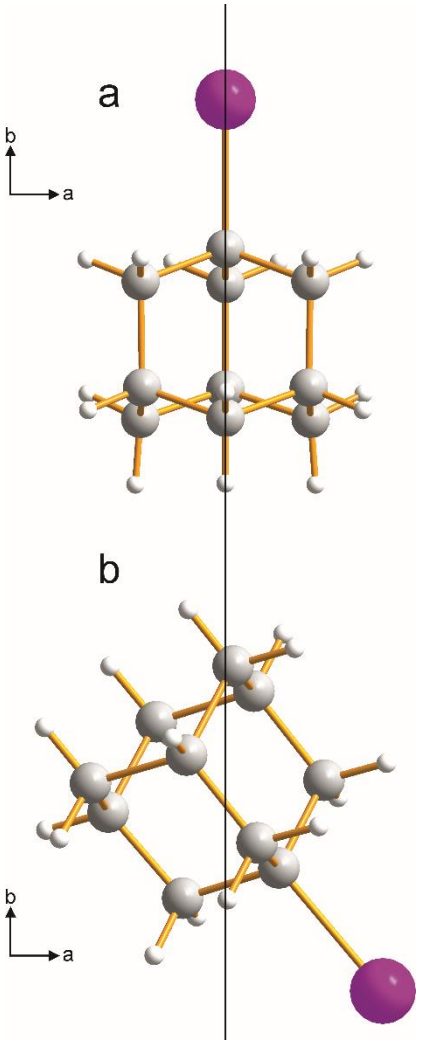

Figure 7.17. *The 1-IA molecule in (a) phase A and (b) phase C, showing that the whole molecule in phase C has rotated around the c-axis.*

Again to investigate the order of the A → C phase transition, the volume per molecule in the crystal structure is plotted against temperature in Figure 7.18 (these data were also established from single-crystal XRD studies as a function of temperature). Across the A → C transition, a discontinuity in the volume per molecule is observed, indicating the first-order character of this transition.

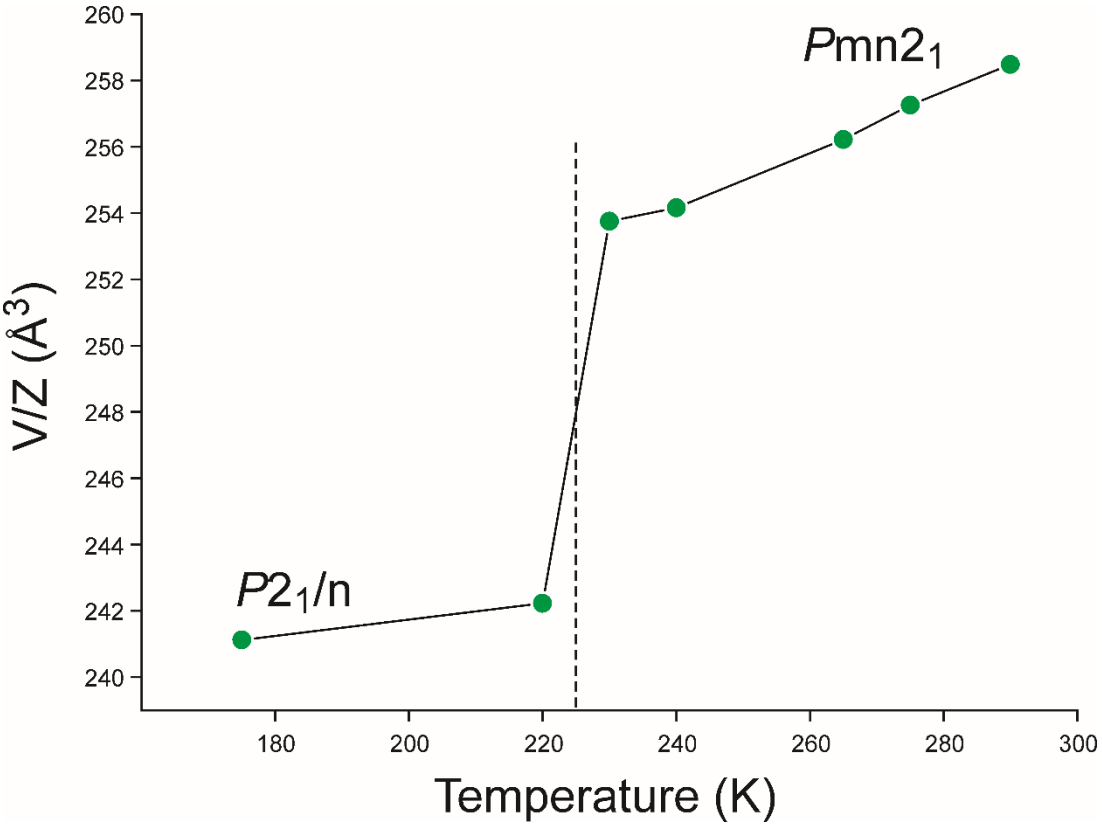

Figure 7.18. *Volume per molecule as a function of temperature for the transformation from phase A to phase C.*

7.3.5 Phase Behaviour

The structural behaviour of 1-IA as a function of temperature is clearly complex. While a polycrystalline sample shows two phase transitions on cooling and three phase transitions on heating (in agreement with DSC data), it is clear from single-crystal XRD data that individual single crystals do *not* show all the transitions observed in the DSC data. In particular, we have found from single-crystal XRD that, on cooling, some single crystals show the A → B transition, while other single crystals show the A → C transition. It appears that, in this case, individual crystals in phase A that are identical at the level of information probed by X-ray diffraction must differ from each other in other aspects (such as size, surface properties and/or defects) that can significantly influence the behaviour of the crystals with regard to low-temperature phase transitions. As a consequence, some individual crystals undergo the transition from phase A to phase B on cooling, while other crystals undergo the transition from phase A to phase C on cooling. Clearly, other experimental strategies are needed to explore the reasons for the different phase transition behaviour of different crystals of

phase A that appear to be identical with regard to X-ray diffraction. Such studies should be the focus of future research.

7.4 Conclusion

In conclusion, we have shown that 1-IA exhibits complex phase transition behaviour on both cooling and heating, and we have focused on rationalizing the structural consequences of the phase transitions observed on cooling. While polycrystalline samples of 1-IA show two phase transitions on cooling (evident from DSC and from variable-temperature powder XRD), it is clear from single-crystal XRD that individual single crystals undergo only one phase transition on cooling, which is either the transition from phase A to phase B or the transition from phase A to phase C. These observations are fully consistent with the results of variable-temperature powder XRD, in which it is observed that a powder sample of phase A transforms to a mixture of phase A and phase C (at a temperature corresponding to the A → C transition), which then transforms to a mixture of phase B and phase C (at a temperature corresponding to the A → B transition).

The crystal structures of all phases A, B and C have been determined in this work from single-crystal XRD. The transformation from phase A to phase B involves only relatively minor changes in molecular orientations (specifically, a small rotation of the 1-IA molecule around the molecular symmetry axis and a slight tilting of the molecular symmetry axis). However, the transformation from phase A to phase C involves significantly greater reorientation of the molecule, leading to a substantially different structure.

The A→C transformation is clearly a first-order solid-solid phase transition, both because a significant discontinuity in the volume per molecule is observed at the phase transition temperature (see Figure 7.18) and because the two phases are not related by a group-subgroup relationship (phase A, $Pmn2_1$; phase C, $P2_1/n$). For the A→B transformation, it is clear from Table 7.2 and Figures 7.12 to 7.14 that the transition from phase A to phase B involves only subtle structural changes, with the two phases related by a group-subgroup relationship (phase A, $Pmn2_1$; phase B, $P2_1$), which may suggest that the transition has significant second order character. On the other hand, the data showing the dependence of the volume per molecule as a function of temperature (Figure 7.15) suggests that there is a small discontinuity in volume at

the phase transition temperature, suggesting that the transition from phase A to phase B has first order character. However, in order to definitively confirm that the volume per molecule exhibits a discontinuity at the phase transition temperature, measurement of the unit cell volume at a greater number of temperatures in the vicinity of the phase transition temperature would be required. For this reason, we refrain from assigning the order of the transition from phase A to phase B on the basis of the experimental data currently available.

Chapter 8: Future Work

While solid-state properties (including structural and thermal properties) of many organic materials are reported in this thesis, the results generate several opportunities for future studies to gain deeper understanding of the systems of interest.

In Chapter 4, the structural properties, thermal properties and hydration-dehydration behaviour of the **IL-AH** and **IL-MH** co-crystal phases are reported. The **IL-AH** co-crystal was found to undergo a reversible solid-solid phase transition as a function of temperature (the high-temperature phase is denoted **IL-X**). While the structural properties of the ambient-temperature phase (**IL-AH**) have been determined from powder XRD data and reported in this thesis, the structural properties of the high-temperature phase (**IL-X**) have yet not been determined. Future work must focus on this issue. Although the powder XRD pattern of **IL-X** has been indexed and an initial structural model has been obtained from structure solution calculations, the current Rietveld refinement of this phase is not yet considered satisfactory. One possible explanation for the fact that the Rietveld fit is currently unsatisfactory could be the effects of preferred orientation on the powder XRD data (which could mean that the structure obtained in the structure solution calculation is too far from the correct structure to allow a satisfactory Rietveld refinement). It is therefore important to focus on this aspect, for example to check experimentally if there is preferred orientation in the powder sample of the **IL-X** phase, and to adopt experimental protocols to ensure that powder XRD data can be recorded in which the effects of preferred orientation are minimized. Successful determination of the structural properties of **IL-X** will allow a detailed understanding of the structural relations between the **IL-AH** and **IL-X** phases, and hence an understanding of the phase transition behaviour.

With regard to the work reported in Chapter 5, it was found that dehydration of the **QH** phase does not give the **AH** phase but rather gives a new "dehydrated phase" (which we designate as the **DP** phase). From the similarity of the powder XRD data of the **QH** and **DP** phases, we believe that the **QH** and **DP** phases may have similar structural properties. It is important to focus on the structural characterization of the **DP** phase, in order to extend our structural understanding of this system. As discussed

in Chapter 5, only very low resolution powder XRD data were used to study dehydration of the **QH** phase, and the quality of the powder XRD data is not adequate for carrying out structure determination of the **DP** phase. A major priority is therefore to record high-resolution powder XRD data to determine the structural properties of the **DP** phase.

While the co-crystal phases reported in this thesis were prepared on the basis of a trial and error approach, an important line of research is to develop strategies to predict which co-formers are suitable for a specific API (in the context of the pharmaceutical industry, such strategies may lead to significant savings in time and cost). There are several geometric, kinetic and thermodynamic factors that affect the possibility to form a co-crystal between a co-former and an API. These factors are still poorly understood and it is important to develop models that predict the possibility to form a specific co-crystal based on understanding the effect of these factors on the interactions between the API and the co-former. It is therefore recommended that future work should focus on this area, in order to gain deeper understanding of the rational design of co-crystals.

In this thesis, the two co-formers used to prepare the pharmaceutical co-crystals were L-lysine and L-proline. Here, some pertinent questions may be raised. For example, why does (*S*)-ibuprofen form co-crystals with these two amino acids, when it does not form co-crystals with other amino acids? What factors dictate the interaction between the API and the co-former? Other relevant questions concerns the specific enantiomers of the ibuprofen and amino acids present in the co-crystals. For example, does (*R*)-ibuprofen form co-crystals with L-amino acids, and can co-crystals be formed between racemic (*RS*)-ibuprofen and racemic DL-amino acids? Clearly, the answers to these questions will provide a deeper understanding of the role of the chirality of both the API and the co-former in controlling the feasibility of co-crystal formation.

The structural properties of a new phase of L-tryptophan, prepared by crystallization from the gas phase following sublimation, are reported in Chapter 6, allowing detailed comparison of the structural properties of the new polymorph (β polymorph) and the one polymorph reported previously (α polymorph). Periodic DFT-D calculations and density considerations suggest that the new polymorph may be more stable than the previously reported polymorph. However, the crystal structure

of the previously reported α polymorph is complex, and future work should focus on understanding the structural properties of this material in more depth. In regard to carrying out more detailed structure re-determination of the α polymorph, the use of other techniques in conjunction with X-ray diffraction is critical, including electron diffraction data (which allows significantly smaller crystals to be studied than X-ray diffraction). In addition, future work must focus on investigating the reasons that crystallization from the gas phase appears to produce new polymorphs of amino acids that cannot be obtained by conventional crystallization from solution. For example, the surface of the cold template, on which crystallization from the gas phase occurs, may have a significant impact on the type of polymorph produced. In this regard, different types of cold surface could be used in future research to explore the opportunity to obtain more new polymorphs of L-tryptophan and other amino acids.

The phase transition behaviour of 1-iodoadamantane (1-IA) as a function of temperature is discussed in Chapter 7, focusing on the structural changes that occur on cooling 1-IA from ambient temperature. Two phase transitions were identified from DSC and powder XRD studies, and the crystal structures of the solid phases corresponding to these phase transitions were determined by single-crystal XRD. The results have revealed complex behaviour as a function of temperature on cooling, as it was found that some individual crystals undergo the A → B transition on cooling, whereas other individual crystals undergo the A → C transition on cooling, in spite of all the original crystals of phase A having the same crystal structure, as determined by single-crystal XRD. The underlying reasons for this fascinating behaviour are yet to be established, and future work must focus on understanding this aspect. For example, more detailed characterization of single crystals of phase A of 1-IA by other techniques (for example, studying surface properties using atomic force microscopy or characterizing defect properties using electron microscopy) may allow an understanding of why different single crystals exhibit different phase transition behaviour. In addition, although the occurrence of several phase transitions on the heating cycle (after cooling from ambient temperature) was demonstrated, both by DSC and powder XRD, the crystal structures of the solid phases corresponding to each phase transition were not determined. Future work must also focus on the heating cycle, with the aim of structurally characterizing the solid phases corresponding to each transition.

References

[1] B. C. Hancock, M. Parks, *Pharm. Res.* **2000**, *17*, 397-404.
[2] S. L. Price, *Acc. Chem. Res.* **2009**, *42*, 117-126.
[3] D. Zhou, G. G. Zhang, D. Law, D. J. Grant, E. A. Schmitt, *J. Pharm. Sci.* **2002**, *91*, 1863-1872.
[4] S. R. Vippagunta, H. G. Brittain, D. J. W. Grant, *Adv. Drug. Deliver. Rev.* **2001**, *48*, 3-26.
[5] P. Vishweshwar, J. A. McMahon, J. A. Bis, M. J. Zaworotko, *J. Pharm. Sci.* **2006**, *95*, 499-516.
[6] J. D. Dunitz, *CrystEngComm* **2003**, *5*, 506-506.
[7] S. N. Black, E. A. Collier, R. J. Davey, R. J. Roberts, *J. Pharm. Sci.* **2007**, *96*, 1053-1068.
[8] R. Löbenberg, G. L. Amidon, *Eur. J. Pharm. Biopharm.* **2000**, *50*, 3-12.
[9] in *http://www.fda.gov/Food/FoodIngredientsPackaging/GenerallyRecognizedasSafeGRAS/default.htm (date accessed: 8.12.2019).*
[10] M. Lusi, *Cryst. Growth Des.* **2018**, *18*, 3704-3712.
[11] M. A. Khoj, C. E. Hughes, K. D. M. Harris, B. M. Kariuki, *Cryst. Growth Des.* **2017**, *17*, 1276-1284.
[12] W. A. McNaught A D, *IUPAC. Compendium of Chemical Terminology (the "Gold Book")*, 2nd ed., Blackwell Scientific Publications, Oxford, **1997**.
[13] S. L. Childs, L. J. Chyall, J. T. Dunlap, V. N. Smolenskaya, B. C. Stahly, G. P. Stahly, *J. Am. Chem. Soc.* **2004**, *126*, 13335-13342.
[14] J. F. Remenar, S. L. Morissette, M. L. Peterson, B. Moulton, J. M. MacPhee, H. R. Guzmán, Ö. Almarsson, *J. Am. Chem. Soc.* **2003**, *125*, 8456-8457.
[15] D. P. McNamara, S. L. Childs, J. Giordano, A. Iarriccio, J. Cassidy, M. S. Shet, R. Mannion, E. O'Donnell, A. Park, *Pharm. Res.* **2006**, *23*, 1888-1897.
[16] N. Variankaval, R. Wenslow, J. Murry, R. Hartman, R. Helmy, E. Kwong, S.-D. Clas, C. Dalton, I. Santos, *Cryst. Growth Des.* **2006**, *6*, 690-700.
[17] Z. Zhou, W. Li, W. J. Sun, T. Lu, H. H. Y. Tong, C. C. Sun, Y. Zheng, *Int. J. Pharm.* **2016**, *509*, 391-399.
[18] R. Spogli, M. Bastianini, F. Ragonese, R. G. Iannitti, L. Monarca, F. Bastioli, I. Nakashidze, G. Brecchia, L. Menchetti, M. Codini, C. Arcuri, L. Mancinelli, B. Fioretti, *Nutrients* **2018**, *10*, 1925.
[19] D. R. Weyna, T. Shattock, P. Vishweshwar, M. J. Zaworotko, *Cryst. Growth Des.* **2009**, *9*, 1106-1123.
[20] Q. Fu, Y. Han, Y. F. Xie, N. B. Gong, F. Guo, *J. Mol. Struct.* **2018**, *1168*, 145-152.
[21] I. A. Cuadra, A. Cabanas, J. A. R. Cheda, C. Pando, *J. Supercrit. Fluids* **2018**, *136*, 60-69.
[22] S. Draguta, M. S. Fonari, S. N. Bejagam, K. Storms, J. Lindline, T. V. Timofeeva, *Struct. Chem.* **2016**, *27*, 1303-1315.
[23] A. V. Trask, *Mol. Pharm.* **2007**, *4*, 301-309.
[24] J. M. Chen, S. Li, T. B. Lu, *Cryst. Growth Des.* **2014**, *14*, 6399-6408.
[25] A. Y. Woo, M. M. Waye, S. K. Tsui, S. T. Yeung, C. H. Cheng, *J. Pharmacol. Exp. Ther.* **2008**, *325*, 226-235.
[26] L. Cui, F. Qiu, N. L. Wang, X. S. Yao, *Chem. Pharm. Bull.* **2004**, *52*, 772-775.
[27] K. Suresh, N. R. Goud, A. Nangia, *Chem Asian J* **2013**, *8*, 3032-3041.
[28] Z.-Z. Wang, J.-M. Chen, T.-B. Lu, *Cryst. Growth Des.* **2012**, *12*, 4562-4566.

[29] N. K. Duggirala, A. J. Smith, L. Wojtas, R. D. Shytle, M. J. Zaworotko, *Cryst. Growth Des.* **2014**, *14*, 6135-6142.
[30] J. F. Cade, *Med J Aust* **1949**, *2*, 349-352.
[31] G. P. Hartigan, *Br J Psychiatry* **1963**, *109*, 810-814.
[32] P. J. Barnes, *Ann. Am. Thorac. Soc.* **2005**, *2*, 334-339.
[33] E. Shefter, H.-L. Fung, O. Mok, *J. Pharm. Sci.* **1973**, *62*, 791-794.
[34] J. Herman, J. P. Remon, N. Visavarungroj, J. B. Schwartz, G. H. Klinger, *Int. J. Pharm.* **1988**, *42*, 15-18.
[35] M. Otsuka, N. Kaneniwa, *Chem. Pharm. Bull.* **1988**, *36*, 4914-4920.
[36] E. Suzuki, K. Shimomura, K. Sekiguchi, *Chem. Pharm. Bull.* **1989**, *37*, 493-497.
[37] S. Puttipipatkhachorn, E. Yonemochi, T. Oguchi, K. Yamamoto, Y. Nakai, *Chem. Pharm. Bull.* **1990**, *38*, 2233-2236.
[38] N. Rodríguez-Hornedo, D. Lechuga-Ballesteros, W. Hsiu-Jean, *Int. J. Pharm.* **1992**, *85*, 149-162.
[39] C. O. Agbada, P. York, *Int. J. Pharm.* **1994**, *106*, 33-40.
[40] S. P. Duddu, N. G. Das, T. P. Kelly, T. D. Sokoloski, *Int. J. Pharm.* **1995**, *114*, 247-256.
[41] H. Zhu, C. Yuen, D. J. W. Grant, *Int. J. Pharm.* **1996**, *135*, 151-160.
[42] N. V. Phadnis, R. Suryanarayanan, *J. Pharm. Sci.* **1997**, *86*, 1256-1263.
[43] E. Suihko, J. Ketolainen, A. Poso, M. Ahlgren, J. Gynther, P. Paronen, *Int. J. Pharm.* **1997**, *158*, 47-55.
[44] M. D. Ticehurst, R. A. Storey, C. Watt, *Int. J. Pharm.* **2002**, *247*, 1-10.
[45] A. V. Trask, W. D. S. Motherwell, W. Jones, *Int. J. Pharm.* **2006**, *320*, 114-123.
[46] P. A. Wood, N. Feeder, M. Furlow, P. T. A. Galek, C. R. Groom, E. Pidcock, *CrystEngComm* **2014**, *16*, 5839-5848.
[47] L. Fábián, *Cryst. Growth Des.* **2009**, *9*, 1436-1443.
[48] S. L. James, C. J. Adams, C. Bolm, D. Braga, P. Collier, T. Friscic, F. Grepioni, K. D. M. Harris, G. Hyett, W. Jones, A. Krebs, J. Mack, L. Maini, A. G. Orpen, I. P. Parkin, W. C. Shearouse, J. W. Steed, D. C. Waddell, *Chem. Soc. Rev.* **2012**, *41*, 413-447.
[49] T. Friščić, S. L. Childs, S. A. A. Rizvi, W. Jones, *CrystEngComm* **2009**, *11*, 418-426.
[50] R. J. Davey, S. L. M. Schroeder, J. H. ter Horst, *Angew. Chem. Int. Ed.* **2013**, *52*, 2166-2179.
[51] T. Kleetz, R. Scheel, G. Schembecker, K. Wohlgemuth, *Cryst. Growth Des.* **2018**, *18*, 4906-4910.
[52] C. Rodriguez-Navarro, E. Doehne, *Earth Surf. Process. Landf* **1999**, *24*, 191-209.
[53] H. J. M. Kramer, G. M. van Rosmalen, in *Encyclopedia of Separation Science* (Ed.: I. D. Wilson), Academic Press, Oxford, **2000**, pp. 64-84.
[54] S. Kudo, H. Takiyama, *J. Chem. Eng. Data* **2018**, *63*, 451-458.
[55] N. Takata, K. Shiraki, R. Takano, Y. Hayashi, K. Terada, *Cryst. Growth Des.* **2008**, *8*, 3032-3037.
[56] S. J. Nehm, B. Rodríguez-Spong, N. Rodríguez-Hornedo, *Cryst. Growth Des.* **2006**, *6*, 592-600.
[57] G. G. Zhang, R. F. Henry, T. B. Borchardt, X. Lou, *J. Pharm. Sci.* **2007**, *96*, 990-995.
[58] S. Zhang, A. C. Rasmuson, *Cryst. Growth Des.* **2013**, *13*, 1153-1161.

[59] D. Hasa, E. Miniussi, W. Jones, *Cryst. Growth Des.* **2016**, *16*, 4582-4588.
[60] D. J. Berry, C. C. Seaton, W. Clegg, R. W. Harrington, S. J. Coles, P. N. Horton, M. B. Hursthouse, R. Storey, W. Jones, T. Friščić, N. Blagden, *Cryst. Growth Des.* **2008**, *8*, 1697-1712.
[61] J. D. Green, in *Encyclopedia of Separation Science* (Ed.: I. D. Wilson), Academic Press, Oxford, **2000**, pp. 1113-1117.
[62] N. Kamali, C. O'Malley, M. F. Mahon, A. Erxleben, P. McArdle, *Cryst. Growth Des.* **2018**, *18*, 3510-3516.
[63] M. A. Solomos, C. Capacci-Daniel, J. F. Rubinson, J. A. Swift, *Cryst. Growth Des.* **2018**, *18*, 6965-6972.
[64] P. M. J. Szell, S. A. Gabriel, E. Caron-Poulin, O. Jeannin, M. Fourmigue, D. L. Bryce, *Cryst. Growth Des.* **2018**, *18*, 6227-6238.
[65] S. Shen, G. M. Xia, Z. J. Jiang, Q. Q. Shao, W. Z. Shan, H. M. Wang, *Cryst. Growth Des.* **2019**, *19*, 320-327.
[66] J. Bernstein, *Polymorphism in Molecular Crystals*, Oxford University Press, Oxford, **2002**.
[67] L. J. Wang, Y. Song, *J. Mol. Struct.* **2019**, *1183*, 217-223.
[68] Q. H. Yang, T. M. Ren, S. Yang, X. Q. Li, Y. N. Chi, Y. Yang, J. K. Gu, C. W. Hu, *Cryst. Growth Des.* **2016**, *16*, 6060-6068.
[69] S. Z. Ismail, C. L. Anderton, R. C. B. Copley, L. S. Price, S. L. Price, *Cryst. Growth Des.* **2013**, *13*, 2396-2406.
[70] G. K. Bertram, B. M. Susan, J. T. Anthony, *Basic and Clinical Pharmacology*, 12th ed., The McGraw-Hill Companies, Inc., New York, **2012**.
[71] N. Boden, in *The Plastically Crystalline State* (Ed.: J. N. Sherwood), John Wiley & Sons, **1979**, pp. 147-214.
[72] D.-K. Bučar, R. W. Lancaster, J. Bernstein, *Angew. Chem. Int. Ed. Engl.* **2015**, *54*, 6972-6993.
[73] J. Bauer, S. Spanton, R. Henry, J. Quick, W. Dziki, W. Porter, J. Morris, *Pharm. Res.* **2001**, *18*, 859-866.
[74] J. Haleblian, W. McCrone, *J. Pharm. Sci.* **1969**, *58*, 911-929.
[75] W. C. Röntgen, Nature, **1895**, pp. 274-276.
[76] B. Shah, V. K. Kakumanu, A. K. Bansal, *J. Pharm. Sci.* **2006**, *95*, 1641-1665.
[77] W. L. Bragg, W. H. Bragg, *Proc. R. Soc. London, Ser. A* **1913**, *89*, 248-277.
[78] P. A. Doyle, P. S. Turner, *Acta Crystallogr., Sect. A* **1968**, *24*, 390-397.
[79] G. E. Bacon, *Neutron diffraction 3 edition*, Clarendon Press, United Kingdom, **1975**.
[80] K. D. M. Harris, P. A. Williams, in *Structure from Diffraction Methods*, 1st ed. (Eds.: W. D. Bruce, D. O'Hare, I. R. Walton), Jhon Wiley & Sons, Ltd, West Sussex, **2014**.
[81] D. Albesa-Jové, B. M. Kariuki, S. J. Kitchin, L. Grice, E. Y. Cheung, K. D. M. Harris, *ChemPhysChem* **2004**, *5*, 414-418.
[82] K. Fujii, A. L. Garay, J. Hill, E. Sbircea, Z. Pan, M. Xu, D. C. Apperley, S. L. James, K. D. M. Harris, *Chem. Commun.* **2010**, *46*, 7572-7574.
[83] K. D. M. Harris, *Mater. Manuf. Processes* **2009**, *24*, 293-302.
[84] K. D. M. Harris, *Comput. Mater. Sci.* **2009**, *45*, 16-20.
[85] K. D. M. Harris, M. Tremayne, P. Lightfoot, P. G. Bruce, *J. Am. Chem. Soc.* **1994**, *116*, 3543-3547.
[86] P. Lightfoot, M. Tremayne, K. D. M. Harris, P. G. Bruce, *J. Chem. Soc., Chem. Commun.* **1992**, 1012-1013.

[87] Z. Pan, M. Xu, E. Y. Cheung, K. D. M. Harris, E. C. Constable, C. E. Housecroft, *J. Phys. Chem. B* **2006**, *110*, 11620-11623.
[88] K. D. M. Harris, *Top. Curr. Chem.* **2012**, *315*, 133-178.
[89] K. D. M. Harris, S. Habershon, E. Y. Cheung, R. L. Johnston, *Z. Kristallogr.* **2004**, *219*, 838-846.
[90] K. Fujii, M. T. Young, K. D. M. Harris, *J. Struct. Biol.* **2011**, *174*, 461-467.
[91] F. Guo, E. Y. Cheung, K. D. M. Harris, V. R. Pedireddi, *Cryst. Growth Des.* **2006**, *6*, 846-848.
[92] F. Guo, K. D. M. Harris, *J. Am. Chem. Soc.* **2005**, *127*, 7314-7315.
[93] S. Habershon, K. D. M. Harris, R. L. Johnston, *J. Comp. Chem.* **2003**, *24*, 1766-1774.
[94] K. D. M. Harris, *Cryst. Growth Des.* **2003**, *3*, 887-895.
[95] K. D. M. Harris, R. L. Johnston, B. M. Kariuki, *Acta Crystallogr., Sect. A* **1998**, *54*, 632-645.
[96] K. D. M. Harris, M. Tremayne, *Chem. Mater.* **1996**, *8*, 2554-2570.
[97] K. D. M. Harris, M. Tremayne, B. M. Kariuki, *Angew. Chem. Int. Ed.* **2001**, *40*, 1626-1651.
[98] B. M. Kariuki, P. Calcagno, K. D. M. Harris, D. Philp, R. L. Johnston, *Angew. Chem. Int. Ed.* **1999**, *38*, 831-835.
[99] B. M. Kariuki, K. Psallidas, K. D. M. Harris, R. L. Johnston, R. W. Lancaster, S. E. Staniforth, S. M. Cooper, *Chem. Commun.* **1999**, 1677-1678.
[100] B. M. Kariuki, H. Serrano-González, R. L. Johnston, K. D. M. Harris, *Chem. Phys. Lett.* **1997**, *280*, 189-195.
[101] B. M. Kariuki, D. M. S. Zin, M. Tremayne, K. D. M. Harris, *Chem. Mater.* **1996**, *8*, 565-569.
[102] J. Martí-Rujas, A. Morte-Ródenas, F. Guo, N. Thomas, K. Fujii, B. M. Kariuki, K. D. M. Harris, *Cryst. Growth Des.* **2010**, *10*, 3176-3181.
[103] F. Guo, J. Martí-Rujas, Z. Pan, C. E. Hughes, K. D. M. Harris, *J. Phys. Chem. C* **2008**, *112*, 19793-19796.
[104] R. Jenkins, R. Manne, R. Robin, C. Senemaud, *Pure Appl. Chem.* **1991**, *63*, 735-746.
[105] P. Willmott, *An Introduction to Synchrotron Radiation: Techniques and Applications*, John Wiley & Sons, Ltd, **2011**.
[106] M. J. Duer, *Solid-State NMR Spectroscopy Principles and Applications.*, Blackwell Science, **2002**.
[107] A. Pines, M. G. Gibby, J. S. Waugh, *J. Chem. Phys.* **1973**, *59*, 569-590.
[108] B. M. Fung, A. K. Khitrin, K. Ermolaev, *J. Magn. Reson.* **2000**, *142*, 97-101.
[109] G. Höhne, Hemminger, Wolfgang F., Flammersheim, H.-J., *Differential Scanning Calorimetry*, Springer, **2003**.
[110] D. Faroongsarng, *Aaps Pharmscitech* **2016**, *17*, 572-577.
[111] E. Gil-Gonzalez, A. Perejon, P. E. Sanchez-Jimenez, S. Medina-Carrasco, J. Kupcik, J. Subrt, J. M. Criado, L. A. Perez-Maqueda, *Cryst. Growth Des.* **2018**, *18*, 3107-3116.
[112] P. J. Glusker, N. K. Trueblood, *Crystal Structure Analysis: A Primer.*, Oxford University Press, Oxford, **1985**.
[113] D. J. Dunitz, *X-ray Analysis and the Structure of Organic Molecules*, Verlag Helvetica Chimica Acta, Basel, **1995**.
[114] G. Sheldrick, *Acta Crystallogr., Sect. A* **2008**, *64*, 112-122.
[115] Y. Zhou, F. Guo, C. E. Hughes, D. L. Browne, T. R. Peskett, K. D. M. Harris, *Cryst. Growth Des.* **2015**, *15*, 2901-2907.

[116] A. K. Cheetham, A. P. Wilkinson, *J. Phys. Chem. Solids* **1991**, *52*, 1199-1208.
[117] A. K. Cheetham, A. P. Wilkinson, *Angew. Chem. Int. Ed. Engl.* **1992**, *31*, 1557-1570.
[118] W. I. F. David, K. Shankland, L. B. McCusker, C. Bärlocher, *Structure Determination from Powder Diffraction Data.*, IUCr/OUP, Oxford, **2002**.
[119] K. D. M. Harris, M. Tremayne, B. M. Kariuki, *Angew. Chem. Int. Ed.* **2001**, *40*, 1626-1651.
[120] K. D. M. Harris, M. Tremayne, P. Lightfoot, P. G. Bruce, *J. Am. Chem. Soc.* **1994**, *116*, 3543-3547.
[121] D. M. Poojary, A. Clearfield, *Acc. Chem. Res.* **1997**, *30*, 414-422.
[122] P. R. Rudolf, *Mater. Chem. Phys.* **1993**, *35*, 267-272.
[123] M. Tremayne, B. M. Kariuki, K. D. M. Harris, *J. Mater. Chem.* **1996**, *6*, 1601-1604.
[124] M. Tremayne, B. M. Kariuki, K. D. M. Harris, *J. Appl. Crystallogr.* **1996**, *29*, 211-214.
[125] M. Tremayne, B. M. Kariuki, K. D. M. Harris, *Acta Crystallogr. A* **1996**, *52*, C59-C59.
[126] H. Tsue, M. Horiguchi, R. Tamura, K. Fujii, H. Uekusa, *J. Synth. Org. Chem. Jpn.* **2007**, *65*, 1203-1212.
[127] W. I. F. David, K. Shankland, *Acta Crystallogr., Sect. A* **2008**, *64*, 52-64.
[128] M. L. Peterson, S. L. Morissette, C. McNulty, A. Goldsweig, P. Shaw, M. LeQuesne, J. Monagle, N. Encina, J. Marchionna, A. Johnson, J. Gonzalez-Zugasti, A. V. Lemmo, S. J. Ellis, M. J. Cima, Ö. Almarsson, *J. Am. Chem. Soc.* **2002**, *124*, 10958-10959.
[129] A. J. Florence, B. Baumgartner, C. Weston, N. Shankland, A. R. Kennedy, K. Shankland, W. I. F. David, *J. Pharm. Sci.* **2003**, *92*, 1930-1938.
[130] A. E. Watts, K. Maruyoshi, C. E. Hughes, S. P. Brown, K. D. M. Harris, *Cryst. Growth Des.* **2016**, *16*, 1798-1804.
[131] K. D. M. Harris, in *Advanced X-Ray Crystallography*, *Vol. 315* (Ed.: K. Rissanen), Springer-Verlag Berlin, Berlin, **2012**, pp. 133-177.
[132] E. Courvoisier, P. A. Williams, G. K. Lim, C. E. Hughes, K. D. M. Harris, *Chem. Commun.* **2012**, *48*, 2761-2763.
[133] Z. F. Zhou, K. D. M. Harris, *Comput. Mater. Sci.* **2009**, *45*, 118-121.
[134] A. J. Hanson, E. Y. Cheung, K. D. M. Harris, *J. Phys. Chem. B* **2007**, *111*, 6349-6356.
[135] Z. F. Zhou, V. Siegler, E. Y. Cheung, S. Habershon, K. D. M. Harris, R. L. Johnston, *Chemphyschem* **2007**, *8*, 650-653.
[136] Z. G. Pan, E. Y. Cheung, K. D. M. Harris, E. C. Constable, C. E. Housecroft, *Cryst. Growth Des.* **2005**, *5*, 2084-2090.
[137] D. Albesa-Jove, B. M. Kariuki, S. J. Kitchin, L. Grice, E. Y. Cheung, K. D. M. Harris, *Chemphyschem* **2004**, *5*, 414-418.
[138] S. Habershon, D. Albesa-Jove, E. Y. Cheung, G. W. Turner, R. L. Johnston, K. D. M. Harris, in *European Powder Diffraction Epdic 8, Vol. 443-4* (Eds.: Y. Andersson, E. J. Mittemeijer, U. Welzel), Trans Tech Publications Ltd, Durnten-Zurich, **2004**, pp. 11-21.
[139] K. D. M. Harris, E. Y. Cheung, *Chem. Soc. Rev.* **2004**, *33*, 526-538.
[140] B. M. Kariuki, R. L. Johnston, K. D. M. Harris, K. Psallidas, S. Ahn, H. Serrano-Gonzalez, *Commun. Math. Comp. Chem.* **1998**, 123-135.
[141] R. Shirley, *The CRYSFIRE System for Automatic Powder Indexing: User's Manual*, The Lattice Press, Guildford, U.K., **1999**.

[142] R. Shirley, *CRYSFIRE Suite of Programs for Indexing Powder Diffraction Paterns*, University of Surrey, **1999**.
[143] J. Visser, *J. Appl. Crystallogr.* **1969**, *2*, 89-95.
[144] P.-E. Werner, L. Eriksson, M. Westdahl, *J. Appl. Crystallogr.* **1985**, *18*, 367-370.
[145] A. Boultif, D. Louer, *J. Appl. Crystallogr.* **1991**, *24*, 987-993.
[146] R. Shirley, *A modified version of Visser's ITO zone-indexing program, using the Ishida & Watanabe PM criterion for zone evaluation, (not yet published)*, , **1999.**
[147] M. Neumann, *J. Appl. Crystallogr.* **2003**, *36*, 356-365.
[148] G. Pawley, *J. Appl. Crystallogr.* **1981**, *14*, 357-361.
[149] A. Le Bail, H. Duroy, J. L. Fourquet, *Mat. Res. Bull.* **1988**, *23*, 447-452.
[150] A. C. Larson, R. B. Von Dreele, *Los Alamos National Laboratory Report* **2004**, LAUR 86-748.
[151] M. F. C. Ladd;, R. A. Palmer;, *Theory and Practice of Direct Methods in Crystallography*, Plenum Press, New York, **1980**.
[152] M. Woolfson, *Acta Crystallogr., Sect. A* **1987**, *43*, 593-612.
[153] A. L. Patterson, *Phys. Rev.* **1934**, *46*, 372-376.
[154] G. Oszlanyi, A. Suto, *Acta Crystallogr., Sect. A* **2004**, *60*, 134-141.
[155] G. Oszlanyi, A. Suto, *Acta Crystallogr., Sect. A* **2005**, *61*, 147-152.
[156] C. Baerlocher, B. McCusker Lynne, L. Palatinus, in *Z. Kristallogr., Vol. 222*, **2007**, p. 47.
[157] Y. G. Andreev, P. Lightfoot, P. G. Bruce, *J. Appl. Crystallogr.* **1997**, *30*, 294-305.
[158] M. Falcioni, M. W. Deem, *J. Chem. Phys.* **1999**, *110*, 1754-1766.
[159] M. Shinozuka, *Comput. Struct.* **1972**, *2*, 855-874.
[160] C. C. Seaton, M. Tremayne, *Chem. Commun.* **2002**, 880-881.
[161] S. Y. Chong, M. Tremayne, *Chem. Commun.* **2006**, 4078-4080.
[162] K. D. M. Harris, R. L. Johnston, B. M. Kariuki, *Acta Crystallogr., Sect. A* **1998**, *54*, 632-645.
[163] B. M. Kariuki, K. Psallidas, K. D. M. Harris, R. L. Johnston, R. W. Lancaster, S. E. Staniforth, S. M. Cooper, *Chem. Commun.* **1999**, 1677-1678.
[164] B. M. Kariuki, C. L. Bauer, K. D. M. Harris, S. J. Teat, *Angew. Chem. Int. Ed.* **2000**, *39*, 4485-4488.
[165] F. Guo, K. D. M. Harris, *J. Am. Chem. Soc.* **2005**, *127*, 7314-7315.
[166] Z. Pan, M. Xu, E. Y. Cheung, K. D. M. Harris, E. C. Constable, C. E. Housecroft, *J. Phys. Chem. B.* **2006**, *110*, 11620-11623.
[167] H. M. Rietveld, *J. Appl. Crystallogr.* **1969**, *2*, 65-71.
[168] F. A. Allen, *Acta Crystallogr., Sect. B: Struct. Sci.* **2002**, *58*, 380-388.
[169] F. H. Allen, O. Kennard, D. G. Watson, L. Brammer, A. G. Orpen, R. Taylor, *J. Chem. Soc., Perkin Trans. 2* **1987**, S1-S19.
[170] S. J. Clark, M. D. Segall, C. J. Pickard, P. J. Hasnip, M. J. Probert, K. Refson, M. C. Payne, *Z. Kristallogr.* **2005**, *220*, 567-570.
[171] G. R. Parr, Y. Weitao, *Density-Functional Theory of Atoms and Molecules*, Oxford University Press, New York, **1989**.
[172] J. P. Perdew, K. Burke, M. Ernzerhof, *Phys. Rev. Lett.* **1996**, *77*, 3865-3868.
[173] C. Adamo, V. Barone, *J. Chem. Phys.* **1999**, *110*, 6158-6170.
[174] A. Tkatchenko, M. Scheffler, *Phys. Rev. Lett.* **2009**, *102*, 073005.
[175] A. M. Reilly, A. Tkatchenko, *Chem. Sci.* **2015**, *6*, 3289-3301.

[176] J. Hoja, H. Y. Ko, M. A. Neumann, R. Car, R. A. DiStasio, Jr., A. Tkatchenko, *Sci Adv* **2019**, *5*, eaau3338.
[177] F. de Vries, E. Setakis, T. P. van Staa, *Br. J. Clin. Pharmacol.* **2010**, *70*, 429-438.
[178] K. D. Rainsford, *Int. J. Clin. Pract. Suppl.* **2013**, 9-20.
[179] M. A. Filippa, E. I. Gasull, *Fluid Phase Equilib.* **2013**, *354*, 185-190.
[180] A. Tilborg, B. Norberg, J. Wouters, *Eur. J. Med. Chem* **2014**, *74*, 411-426.
[181] H. H. Tung, S. Waterson, S. D. Reynolds, *Vol. Formation and resolution of ibuprofen lysinate*, 1991 US Patent Number: 4994604.
[182] C. Vladiskovic, N. Masciocchi, *J. Pharm. Biomed. Anal.* **2015**, *107*, 394-402.
[183] W. I. F. David, K. Shankland, L. B. McCusker, C. Baerlocher, IUCr/OUP, **2002**.
[184] V. Favre-Nicolin, R. Černý, *Z. Kristallogr.* **2004**, *219*, 847-856.
[185] M. Tremayne, *Philos. Trans. R. Soc. A* **2004**, *362*, 2691-2707.
[186] V. Brodski, R. Peschar, H. Schenk, *J. Appl. Crystallogr.* **2005**, *38*, 688-693.
[187] H. Tsue, M. Horiguchi, R. Tamura, K. Fujii, H. Uekusa, *J. Synth. Org. Chem. Jpn.* **2007**, *65*, 1203-1212.
[188] K. D. Harris, *Top Curr Chem* **2012**, *315*, 133-177.
[189] G. W. Turner, E. Tedesco, K. D. M. Harris, R. L. Johnston, B. M. Kariuki, *Chem. Phys. Lett.* **2000**, *321*, 183-190.
[190] G. Metz, X. L. Wu, S. O. Smith, *J. Magn. Reson. A* **1994**, *110*, 219-227.
[191] B. M. Fung, A. K. Khitrin, K. Ermolaev, *J Magn Reson* **2000**, *142*, 97-101.
[192] H. J. Monkhorst, J. D. Pack, *Phys. Rev. B* **1976**, *13*, 5188-5192.
[193] D. Vanderbilt, *Phys. Rev. B* **1990**, *41*, 7892-7895.
[194] R. Shirley, D. Louër, *Acta Cryst.* **(1978)**, *A34*, S382.
[195] R. Shirley, *The CRYSFIRE System for Automatic Powder Indexing: User's Manual,, Vol. Guildford, UK*, **(1999)**.
[196] E. Tedesco, G. W. Turner, K. D. M. Harris, R. L. Johnston, B. M. Kariuki, *Angew. Chem. Int. Ed.* **2000**, *39*, 4488-4491.
[197] F. Guo, J. Martí-Rujas, Z. Pan, C. E. Hughes, K. D. M. Harris, *J. Phys. Chem. C* **2008**, *112*, 19793-19796.
[198] J. Martí-Rujas, L. Meazza, G. K. Lim, G. Terraneo, T. Pilati, K. D. M. Harris, P. Metrangolo, G. Resnati, *Angew. Chem. Int. Ed.* **2013**, *52*, 13444-13448.
[199] A. Boultif, D. Louër, *J. Appl. Cryst.* **1991**, *24*, 987-993.
[200] P. A. Williams, C. E. Hughes, K. D. M. Harris, *Angew. Chem. Int. Ed.* **2015**, *54*, 3973-3977.
[201] B. M. Kariuki, H. Serrano-González, R. L. Johnston, K. D. M. Harris, *Chem. Phys. Lett.* **1997**, *280*, 189-195.
[202] G. Metz, X. L. Wu, S. O. Smith, *J. Magn. Reson. A* **1994**, *110*, 219-227.
[203] P.-E. Werner, Eriksson, L. & Westdahl, M. , *J. Appl. Cryst.* **1985**, *18*, 367-370.
[204] E. Y. Cheung, E. E. McCabe, K. D. M. Harris, R. L. Johnston, E. Tedesco, K. M. P. Raja, P. Balaram, *Angew. Chem. Int. Ed.* **2002**, *41*, 494-496.
[205] R. L. Kayushina, B. K. Vainshtein, *Kristallografiya* **1965**, *10*, 833-844.
[206] H. Rietveld, *J. Appl. Crystallogr.* **1969**, *2*, 65-71.
[207] I. J. Bruno, J. C. Cole, M. Kessler, J. Luo, W. D. S. Motherwell, L. H. Purkis, B. R. Smith, R. Taylor, R. I. Cooper, S. E. Harris, A. G. Orpen, *J. Chem. Inf. Comput. Sci.* **2004**, *44*, 2133-2144.
[208] R. Shirley, *The Cysfire 2002 System for Automatic Powder Indexing: User's Manual*, The Lattice Press, Guildford, Surrey, UK., **2002**.
[209] R. J. Davey, *Chem. Commun.* **2003**, 1463-1467.

[210] D. Braga, F. Grepioni, *Chem. Commun.* **2005**, 3635-3645.
[211] S. Y. Ahn, F. Guo, B. M. Kariuki, K. D. M. Harris, *J. Am. Chem. Soc.* **2006**, *128*, 8441-8452.
[212] L. A. Yu, *Acc. Chem. Res.* **2010**, *43*, 1257-1266.
[213] P. A. Williams, C. E. Hughes, G. K. Lim, B. M. Kariuki, K. D. M. Harris, *Cryst. Growth Des.* **2012**, *12*, 3104-3113.
[214] C. H. Görbitz, K. W. Törnroos, G. M. Day, *Acta Crystallogr., Sect. B: Struct. Sci.* **2012**, *68*, 549-557.
[215] M. M. Harding, H. A. Long, *Acta Crystallogr., Sect. B: Struct. Crystallogr. Cryst. Chem.* **1968**, *24*, 1096-1102.
[216] K. A. Kerr, J. P. Ashmore, *Acta Crystallogr., Sect. B: Struct. Crystallogr. Cryst. Chem.* **1973**, *29*, 2124-2127.
[217] S. A. Moggach, D. R. Allan, S. J. Clark, M. J. Gutmann, S. Parsons, C. R. Pulham, L. Sawyer, *Acta Crystallogr., Sect. B: Struct. Sci.* **2006**, *62*, 296-309.
[218] S. Hirokawa, *Acta Crystallogr.* **1955**, *8*, 637-641.
[219] M. S. Lehmann, A. C. Nunes, *Acta Crystallogr., Sect. B: Struct. Crystallogr. Cryst. Chem.* **1980**, *36*, 1621-1625.
[220] G. Albrecht, R. B. Corey, *J. Am. Chem. Soc.* **1939**, *61*, 1087-1103.
[221] Y. Iitaka, *Acta Crystallogr.* **1960**, *13*, 35-45.
[222] Y. Iitaka, *Acta Crystallogr.* **1961**, *14*, 1-10.
[223] J. J. Madden, E. L. McGandy, N. C. Seeman, *Acta Crystallogr., Sect. B: Struct. Crystallogr. Cryst. Chem.* **1972**, *B 28*, 2382-2389.
[224] J. J. Madden, N. C. Seeman, E. L. McGandy, *Acta Crystallogr., Sect. B: Struct. Crystallogr. Cryst. Chem.* **1972**, *B 28*, 2377-2382.
[225] K. Torii, Y. Iitaka, *Acta Crystallogr., Sect. B: Struct. Crystallogr. Cryst. Chem.* **1971**, *B 27*, 2237-2246.
[226] S. Curland, E. Meirzadeh, Y. Diskin-Posner, *Acta Crystallogr., Sect. E* **2018**, *74*, 776-779.
[227] M. M. Harding, R. M. Howieson, *Acta Crystallogr., Sect. B: Struct. Sci. Cryst. Eng. Mater.* **1976**, *32*, 633-634.
[228] M. Yamashita, S. Inomata, K. Ishikawa, T. Kashiwagi, H. Matsuo, S. Sawamura, M. Kato, *Acta Crystallogr., Sect. E: Cryst. Commun.* **2007**, *63*, O2762-O2764.
[229] P. A. Williams, C. E. Hughes, A. B. M. Buanz, S. Gaisford, K. D. M. Harris, *J. Phys. Chem. C* **2013**, *117*, 12136-12145.
[230] F. S. Ihlefeldt, F. B. Pettersen, A. von Bonin, M. Zawadzka, C. H. Gorbitz, *Angew. Chem. Int. Ed.* **2014**, *53*, 13600-13604.
[231] N. Tumanova, N. Tumanov, K. Robeyns, F. Fischer, L. Fusaro, F. Morelle, V. Ban, G. Hautier, Y. Filinchuk, J. Wouters, T. Leyssens, F. Emmerling, *Cryst. Growth Des.* **2018**, *18*, 954-961.
[232] T. J. Kistenmacher, G. A. Rand, R. E. Marsh, *Acta Crystallogr., Sect. B: Struct. Sci. Cryst. Eng. Mater.* **1974**, *30*, 2573-2578.
[233] S. A. Moggach, D. R. Allan, C. A. Morrison, S. Parsons, L. Sawyer, *Acta Crystallogr., Sect. B: Struct. Sci.* **2005**, *61*, 58-68.
[234] S. A. Moggach, W. G. Marshall, S. Parsons, *Acta Crystallogr., Sect. B: Struct. Sci.* **2006**, *62*, 815-825.
[235] Z. Liu, C. Li, *Biophys Chem* **2008**, *138*, 115-119.
[236] T. A. Jenkins, J. C. D. Nguyen, K. E. Polglaze, P. P. Bertrand, *Nutrients* **2016**, *8*, 56.

[237] K. D. M. Harris, S. Habershon, E. Y. Cheung, R. L. Johnston, *Z. Kristallogr.* **2004**, *219*, 838-846.
[238] S. P. Thompson, J. E. Parker, J. Potter, T. P. Hill, A. Birt, T. M. Cobb, F. Yuan, C. C. Tang, *Rev. Sci. Instrum.* **2009**, *80*, 075107.
[239] V. Blum, R. Gehrke, F. Hanke, P. Havu, V. Havu, X. Ren, K. Reuter, M. Scheffler, *Comput. Phys. Commun.* **2009**, *180*, 2175-2196.
[240] X. Ren, P. Rinke, V. Blum, J. Wieferink, A. Tkatchenko, A. Sanfilippo, K. Reuter, M. Scheffler, *New J. Phys* **2012**, *14*, 053020.
[241] S. V. Levchenko, X. Ren, J. Wieferink, R. Johanni, P. Rinke, V. Blum, M. Scheffler, *Comput. Phys. Commun.* **2015**, *192*, 60-69.
[242] A. Ambrosetti, A. M. Reilly, R. A. D. Jr., A. Tkatchenko, *J. Chem. Phys* **2014**, *140*, 18A508.
[243] C. E. Hughes, G. N. M. Reddy, S. Masiero, S. P. Brown, P. A. Williams, K. D. M. Harris, *Chem. Sci.* **2017**, *8*, 3971-3979.
[244] I. J. Bruno, J. C. Cole, M. Kessler, J. Luo, W. D. S. Motherwell, L. H. Purkis, B. R. Smith, R. Taylor, R. I. Cooper, S. E. Harris, A. G. Orpen, *J. Chem. Inf. Comput. Sci.* **2004**, *44*, 2133-2144.
[245] D. V. Dudenko, P. A. Williams, C. E. Hughes, O. N. Antzutkin, S. P. Velaga, S. P. Brown, K. D. M. Harris, *J. Phys. Chem. C* **2013**, *117*, 12258-12265.
[246] M. C. Etter, J. C. Macdonald, J. Bernstein, *Acta Crystallogr., Sect. B: Struct. Sci.* **1990**, *46*, 256-262.
[247] C. H. Görbitz, K. Vestli, R. Orlando, *Acta Crystallogr., Sect. B: Struct. Sci. Cryst. Eng. Mater.* **2009**, *65*, 393-400.
[248] K. Torii, Y. Iitaka, *Acta Crystallogr., Sect. B: Struct. Sci. Cryst. Eng. Mater.* **1973**, *29*, 2799-2807.
[249] K. Torii, Y. Iitaka, *Acta Crystallogr., Sect. B: Struct. Crystallogr. Cryst. Chem.* **1970**, *B 26*, 1317-1326.
[250] A. G. Shtukenberg, Q. Zhu, D. J. Carter, L. Vogt, J. Hoja, E. Schneider, H. Song, B. Pokroy, I. Polishchuk, A. Tkatchenko, A. R. Oganov, A. L. Rohl, M. E. Tuckerman, B. Kahr, *Chem. Sci.* **2017**, *8*, 4926-4940.
[251] O. Al Rahal, C. E. Hughes, P. A. Williams, A. J. Logsdail, Y. Diskin-Posner, K. D. M. Harris, *Angew. Chem. Int. Ed.* **2019**, *58*, 18788-18792.
[252] N. Boden, in *The Plastically Crystalline State: Orientationally Disordered Crystals* (Ed.: J. N. Sherwood), John Wiley & Sons, New York, **1979**, pp. 147-214.
[253] E. R. Andrew, *J. Chem. Phys* **1950**, *18*, 607-618.
[254] W. C. Hamilton, J. W. Edmonds, A. Tippe, *Faraday Discuss.* **1969**, *48*, 192-204.
[255] G. Celotti, F. Bertinelli, C. Stremmenos, *Acta Crystallogr., Sect. A* **1975**, *31*, 582-585.
[256] J. Tang, L. Sterna, A. Pines, *J. Magn. Reson.* **1980**, *41*, 389-394.
[257] C. E. Nordman, D. L. Schmitkons, *Acta Crystallogr.* **1965**, *18*, 764-767.
[258] H. A. Resing, *J. Chem. Phys* **1965**, *43*, 1828-1829.
[259] H. A. Resing, *Mol. Cryst. Liq. Cryst.* **1969**, *9*, 101-132.
[260] J. D. Graham, J. K. Choi, *J. Chem. Phys* **1975**, *62*, 2509-2511.
[261] M. Meyer, G. Ciccotti, *Mol. Phys.* **1985**, *56*, 1235-1248.
[262] M. Meyer, C. Marhic, G. Ciccotti, *Mol. Phys.* **1986**, *58*, 723-733.
[263] J. P. Amoureux, M. Foulon, *Acta Crystallogr., Sect. B* **1987**, *43*, 470-479.
[264] A. E. Aliev, K. D. M. Harris, D. C. Apperley, *J. Chem. Soc., Chem. Commun.* **1993**, 251-253.

[265] M. J. Jones, F. Guillaume, K. D. M. Harris, A.-j. Dianoux, *Proc. Royal Soc. A* **1996**, *452*, 701-714.
[266] R. E. Dinnebier, W. A. Dollase, X. Helluy, J. Kummerlen, A. Sebald, M. U. Schmidt, S. Pagola, P. W. Stephens, S. van Smaalen, *Acta Crystallogr., Sect. B* **1999**, *55*, 1014-1029.
[267] K. D. M. Harris, P. Jonsen, *Chem. Phys. Lett.* **1989**, *154*, 593-598.
[268] F. Guillaume, S. P. Smart, K. D. M. Harris, A. J. Dianoux, *J. Phys.: Condens. Matter* **1994**, *6*, 2169-2184.
[269] A. E. Aliev, S. P. Smart, I. J. Shannon, K. D. M. Harris, *J. Chem. Soc., Faraday Trans.* **1996**, *92*, 2179-2185.
[270] L. Yeo, B. M. Kariuki, H. Serrano-González, K. D. M. Harris, *J. Phys. Chem. B* **1997**, *101*, 9926-9931.
[271] A. Desmedt, S. J. Kitchin, F. Guillaume, M. Couzi, K. D. M. Harris, E. H. Bocanegra, *Phys. Rev. B* **2001**, *64*, 054106.
[272] Z. Pan, A. Desmedt, E. J. MacLean, F. Guillaume, K. D. M. Harris, *J. Phys. Chem. C* **2008**, *112*, 839-847.
[273] B. A. Palmer, B. M. Kariuki, A. Morte-Ródenas, K. D. M. Harris, *Cryst. Growth Des.* **2012**, *12*, 577-582.
[274] M. Foulon, C. Gors, *Acta Crystallogr., Sect. B* **1988**, *44*, 156-163.
[275] L. Yuan, S. Clevers, A. Burel, P. Negrier, M. del Barrio, B. Ben Hassine, D. Mondieig, V. Dupray, J. L. Tamarit, G. Coquerel, *Cryst. Growth Des.* **2017**, *17*, 3395-3401.
[276] B. Ben Hassine, P. Negrier, M. Romanini, M. Barrio, R. Macovez, A. Kallel, D. Mondieig, J. L. Tamarit, *Phys. Chem. Chem. Phys.* **2016**, *18*, 10924-10930.
[277] N. T. Kawai, D. F. R. Gilson, I. S. Butler, *Can. J. Chem* **1991**, *69*, 1758-1765.
[278] M. Bee, J. P. Amoureux, *Mol. Phys.* **1983**, *50*, 585-602.
[279] J. P. Amoureux, M. Bee, J. L. Sauvajol, *Acta Crystallogr., Sect. B: Struct. Sci.* **1982**, *38*, 1984-1989.
[280] A. Vispa, D. Monserrat, G. J. Cuello, F. Fernandez-Alonso, S. Mukhopadhyay, F. Demmel, J. L. Tamarit, L. C. Pardo, *Phys. Chem. Chem. Phys.* **2017**, *19*, 20259-20266.
[281] R. Decressain, L. Carpentier, E. Cochin, J. P. Amoureux, *Eur. Phys. J. B* **2007**, *58*, 223-230.
[282] M. Bee, J. P. Amoureux, *Mol. Phys.* **1983**, *48*, 63-79.
[283] J. P. Amoureux, M. Bee, J. L. Sauvajol, *Mol. Phys.* **1982**, *45*, 709-719.
[284] M. Kosmowska, J. Tarasiewicz, H. A. Kolodziej, *J. Mol. Struct.* **2012**, *1016*, 8-12.
[285] A. B. Bazyleva, A. V. Blolchin, G. J. Kabo, A. G. Kabo, Y. U. Paulechka, *J. Chem. Thermodyn.* **2005**, *37*, 643-657.
[286] R. Betz, P. Klufers, P. Mayer, *Acta Crystallogr., Sect. E: Cryst. Commun.* **2009**, *65*, O101-U2143.
[287] G. M. Sheldrick, *Acta Crystallogr A* **2008**, *64*, 112-122.
[288] G. M. Sheldrick, *Acta Crystallogr., Sect. C* **2015**, *71*, 3-8.
[289] M. Foulon, T. Belgrand, C. Gors, M. More, *Acta Crystallogr., Sect. B* **1989**, *45*, 404-411.

Appendix A: Atomic Parameters for Crystal Structures Determined During the Course of This PhD.

	x	*y*	*z*	U_{iso}
O1	0.7903(24)	0.6449(22)	0.9771(9)	0.0341(17)
O2	0.6801(20)	0.7926(21)	1.0275(8)	0.0341(17)
C3	0.7227(19)	0.7554(17)	0.9852(7)	0.0341(17)
N4	0.5643(21)	0.9526(24)	0.9374(8)	0.0461(17)
H5	0.479(6)	0.899(6)	0.953(5)	0.0575(22)
H6	0.601(6)	1.039(7)	0.962(5)	0.0575(22)
H7	0.525(9)	0.990(13)	0.8987(14)	0.0575(22)
C8	0.6920(19)	0.8537(20)	0.9352(7)	0.0697(17)
H9	0.664(4)	0.783(4)	0.8993(11)	0.0881(22)
C10	0.8334(22)	0.9330(23)	0.9282(8)	0.0409(17)
H11	0.802(4)	1.0449(26)	0.9165(24)	0.0506(22)
H12	0.904(4)	0.934(7)	0.9679(9)	0.0506(22)
C13	0.9274(26)	0.8643(23)	0.8849(10)	0.0310(17)
H14	0.854(4)	0.849(7)	0.8461(13)	0.0377(22)
H15	0.973(5)	0.7589(30)	0.8993(27)	0.0377(22)
C16	1.0550(24)	0.9647(23)	0.8749(10)	0.0360(17)
H17	1.008(5)	1.0709(32)	0.8622(28)	0.0443(22)
H18	1.132(4)	0.977(7)	0.9130(13)	0.0443(22)
C19	1.1419(26)	0.9157(26)	0.8327(8)	0.0155(17)
H20	1.211(5)	1.005(4)	0.8211(23)	0.0177(22)

Table A.1: *Atomic coordinates and isotropic displacement parameters (U_{iso}) for* ***IL-AH*** *phase (continues on the next page).*

H21	1.066(5)	0.879(6)	0.7970(11)	0.0177(22)
N22	1.2397(22)	0.7949(22)	0.8565(9)	0.0125(17)
H23	1.258(14)	0.804(9)	0.8984(9)	0.0138(22)
H24	1.188(9)	0.6967(30)	0.846(5)	0.0138(22)
H25	1.341(7)	0.799(10)	0.842(5)	0.0138(22)
O26	0.0357(21)	0.5415(23)	0.1699(8)	0.0250(17)
O27	–0.0090(20)	0.3194(20)	0.1983(8)	0.0250(17)
C28	–0.0561(18)	0.4368(18)	0.2001(6)	0.0250(17)
C29	–0.2180(22)	0.2967(19)	0.2607(7)	–0.0214(17)
H30	–0.282(12)	0.245(8)	0.2272(14)	–0.0303(22)
H31	–0.124(4)	0.231(5)	0.275(5)	–0.0303(22)
H32	–0.286(14)	0.307(4)	0.292(4)	–0.0303(22)
C33	–0.1659(19)	0.4507(18)	0.2428(6)	0.0439(17)
H34	–0.2658(28)	0.5094(34)	0.2236(12)	0.0545(22)
C35	–0.0953(18)	0.5456(19)	0.2901(6)	0.0439(17)
C36	–0.1641(19)	0.6717(22)	0.3034(7)	0.0439(17)
H37	–0.2693(20)	0.7051(35)	0.2798(10)	0.0545(22)
C38	–0.1030(19)	0.7567(19)	0.3488(7)	0.0439(17)
H39	–0.1610(29)	0.8558(22)	0.3570(13)	0.0545(22)
C40	0.0232(18)	0.7247(20)	0.3802(6)	0.0439(17)
C41	0.0947(18)	0.6000(23)	0.3693(7)	0.0439(17)
H42	0.1979(21)	0.569(4)	0.3946(10)	0.0545(22)
C43	0.0367(19)	0.5107(20)	0.3250(7)	0.0482(17)

Table A.1: (cont.)

H44	0.0983(29)	0.4130(22)	0.3179(13)	0.0601(22)
C45	0.0726(20)	0.8212(23)	0.4260(7)	0.0614(17)
H46	0.106(5)	0.753(4)	0.4618(11)	0.0773(22)
H47	–0.0235(31)	0.889(5)	0.4325(20)	0.0773(22)
C48	0.2003(23)	0.9219(21)	0.4180(7)	0.1223(17)
C49	0.3490(24)	0.8264(31)	0.4171(10)	0.1223(17)
H50	0.351(10)	0.782(14)	0.3776(22)	0.1565(22)
H51	0.351(8)	0.740(11)	0.445(5)	0.1565(22)
H52	0.4458(32)	0.892(5)	0.428(6)	0.1565(22)
H53	0.168(4)	0.973(4)	0.3778(10)	0.1565(22)
C54	0.2250(29)	1.0474(21)	0.4609(10)	0.0240(17)
H55	0.167(10)	1.025(5)	0.4944(24)	0.0287(22)
H56	0.3414(34)	1.059(8)	0.4753(34)	0.0287(22)
H57	0.184(11)	1.146(4)	0.4421(18)	0.0287(22)

Table A.1: (cont.)

	x	*y*	*z*	U_{iso}
O1	1.425(10)	0.0237(11)	0.554(4)	0.0863(19)
O2	1.035(12)	-0.003(1)	0.578(4)	0.0863(19)
C1	1.195(10)	0.0195(8)	0.5946(25)	0.0863(19)
N1	0.843(11)	0.0397(13)	0.722(5)	0.0863(19)
H1	0.864(13)	0.023(9)	0.804(31)	0.1036(23)
H2	0.74(4)	0.028(11)	0.641(21)	0.1036(23)
H3	0.742(27)	0.0607(16)	0.76(5)	0.1036(23)
C2	1.111(9)	0.0488(10)	0.6812(32)	0.0863(19)
H4	1.225(13)	0.0480(15)	0.776(4)	0.1036(23)
C3	1.147(10)	0.0824(10)	0.618(6)	0.0863(19)
H5	1.357(10)	0.0857(23)	0.604(12)	0.1036(23)
H6	1.086(24)	0.1005(12)	0.694(7)	0.1036(23)
C4	1.001(12)	0.0899(8)	0.485(5)	0.0863(19)
H7	0.822(17)	0.1030(21)	0.511(9)	0.1036(23)
H8	1.119(24)	0.1076(15)	0.428(7)	0.1036(23)
C5	0.932(10)	0.0625(13)	0.387(4)	0.0863(19)
H9	0.745(8)	0.0687(27)	0.339(7)	0.1036(23)
H10	0.900(23)	0.0396(14)	0.442(6)	0.1036(23)
C6	1.132(7)	0.0586(15)	0.276(5)	0.0863(19)
H11	1.248(17)	0.0808(27)	0.266(8)	0.1036(23)
H12	1.267(19)	0.0387(31)	0.299(8)	0.1036(23)
N2	1.020(8)	0.0521(15)	0.137(5)	0.0863(19)

Table A.2: *Atomic coordinates and isotropic displacement parameters (U_{iso}) for* ***IL-MH*** *phase (continues on the next page).*

H13	1.145(10)	0.0365(27)	0.079(8)	0.1036(23)
H14	1.006(29)	0.0734(22)	0.082(8)	0.1036(23)
H15	0.827(9)	0.0427(34)	0.143(8)	0.1036(23)
O3	0.665(8)	0.8995(10)	1.597(4)	0.0863(19)
O4	0.329(9)	0.9189(9)	1.496(4)	0.0863(19)
C7	0.447(8)	0.8950(6)	1.5421(24)	0.0863(19)
C8	0.413(14)	0.8390(12)	1.672(5)	0.0863(19)
H16	0.27(8)	0.82(1)	1.682(35)	0.1036(23)
H17	0.40(12)	0.854(4)	1.765(6)	0.1036(23)
H18	0.61(5)	0.827(13)	1.671(32)	0.1036(23)
C9	0.364(6)	0.8589(6)	1.541(4)	0.0863(19)
H19	0.156(6)	0.8593(12)	1.519(6)	0.1036(23)
C10	0.500(7)	0.8458(6)	1.413(4)	0.0863(19)
C11	0.404(5)	0.8533(5)	1.280(5)	0.0863(19)
H20	0.234(6)	0.8688(6)	1.273(7)	0.1036(23)
C12	0.516(7)	0.8417(7)	1.157(4)	0.0863(19)
H21	0.431(10)	0.8485(10)	1.058(5)	0.1036(23)
C13	0.737(7)	0.8213(6)	1.161(4)	0.0863(19)
C14	0.831(6)	0.8136(5)	1.294(5)	0.0863(19)
H22	1.001(6)	0.7981(6)	1.302(7)	0.1036(23)
C15	0.719(7)	0.8255(7)	1.416(4)	0.0863(19)
H23	0.804(10)	0.8185(10)	1.515(5)	0.1036(23)
C16	0.861(8)	0.8081(8)	1.031(5)	0.0863(19)

Table A.2: (cont.)

H24	0.872(21)	0.8273(10)	0.952(6)	0.1036(23)
H25	1.063(6)	0.8012(19)	1.053(9)	0.1036(23)
C17	0.721(8)	0.7788(8)	0.966(4)	0.0863(19)
C18	0.606(14)	0.7541(13)	1.066(6)	0.0863(19)
H26	0.72(8)	0.732(7)	1.07(6)	0.1036(23)
H27	0.41(5)	0.748(13)	1.04(4)	0.1036(23)
H28	0.60(12)	0.763(7)	1.172(12)	0.1036(23)
H29	0.56(1)	0.7887(16)	0.904(6)	0.1036(23)
C19	0.914(13)	0.7637(13)	0.866(6)	0.0863(19)
H30	1.04(7)	0.746(10)	0.919(14)	0.1036(23)
H31	0.816(20)	0.751(11)	0.781(30)	0.1036(23)
H32	1.04(7)	0.7821(30)	0.82(4)	0.1036(23)
O5	0.428(7)	0.5206(8)	0.915(4)	0.0863(19)
H33	0.507(12)	0.501(6)	0.96(4)	0.1036(23)
H34	0.48(8)	0.539(5)	0.975(18)	0.1036(23)
O6	1.44(1)	–0.0307(10)	–0.062(4)	0.0863(19)
O7	1.056(11)	–0.0019(9)	–0.081(4)	0.0863(19)
C20	1.209(9)	–0.0253(8)	–0.1022(27)	0.0863(19)
N3	0.874(11)	–0.0508(13)	–0.254(6)	0.0863(19)
H35	0.88(4)	–0.029(6)	–0.31(4)	0.1036(23)
H36	0.719(14)	–0.049(12)	–0.185(8)	0.1036(23)
H37	0.84(4)	–0.070(7)	–0.32(4)	0.1036(23)
C21	1.128(9)	–0.0554(9)	–0.186(4)	0.0863(19)

Table A.2: (cont.)

H38	1.270(13)	–0.0587(14)	–0.270(5)	0.1036(23)
C22	1.108(12)	–0.0873(9)	–0.108(6)	0.0863(19)
H39	1.302(13)	–0.0934(21)	–0.069(9)	0.1036(23)
H40	1.056(22)	–0.1063(11)	–0.182(7)	0.1036(23)
C23	0.911(10)	–0.0870(12)	0.009(5)	0.0863(19)
H41	0.728(10)	–0.0761(30)	–0.026(6)	0.1036(23)
H42	0.864(22)	–0.1124(14)	0.033(8)	0.1036(23)
C24	0.996(11)	–0.0702(17)	0.142(5)	0.0863(19)
H43	0.986(32)	–0.0437(15)	0.132(8)	0.1036(23)
H44	1.198(9)	–0.076(4)	0.166(8)	0.1036(23)
C25	0.820(12)	–0.0814(13)	0.257(5)	0.0863(19)
H45	0.616(11)	–0.080(4)	0.227(8)	0.1036(23)
H46	0.861(34)	–0.1066(10)	0.287(8)	0.1036(23)
N4	0.846(9)	–0.0611(11)	0.383(5)	0.0863(19)
H47	1.026(19)	–0.051(5)	0.392(12)	0.1036(23)
H48	0.821(31)	–0.0762(16)	0.468(5)	0.1036(23)
H49	0.698(30)	–0.0434(32)	0.383(5)	0.1036(23)
O8	0.704(7)	–0.8944(10)	–1.137(4)	0.0863(19)
O9	0.402(8)	–0.9205(9)	–1.017(4)	0.0863(19)
C26	0.500(6)	–0.8956(6)	–1.0703(26)	0.0863(19)
C27	0.318(13)	–0.8428(12)	–1.176(5)	0.0863(19)
H50	0.112(17)	–0.840(11)	–1.202(33)	0.1036(23)
H51	0.41(9)	–0.854(6)	–1.266(13)	0.1036(23)

Table A.2: (cont.)

H52	0.40(9)	–0.818(4)	–1.160(19)	0.1036(23)
C28	0.351(6)	–0.8640(6)	–1.047(4)	0.0863(19)
H53	0.159(6)	–0.8710(12)	–1.008(6)	0.1036(23)
C29	0.502(7)	–0.8498(6)	–0.928(4)	0.0863(19)
C30	0.404(6)	–0.8568(6)	–0.796(5)	0.0863(19)
H54	0.232(6)	–0.8718(6)	–0.787(7)	0.1036(23)
C31	0.520(8)	–0.8448(7)	–0.676(4)	0.0863(19)
H55	0.435(11)	–0.851(1)	–0.576(4)	0.1036(23)
C32	0.744(8)	–0.8250(7)	–0.683(4)	0.0863(19)
C33	0.841(6)	–0.8180(6)	–0.816(5)	0.0863(19)
H56	1.013(6)	–0.8031(6)	–0.827(7)	0.1036(23)
C34	0.725(7)	–0.8302(7)	–0.937(4)	0.0863(19)
H57	0.809(10)	–0.824(1)	–1.036(5)	0.1036(23)
C35	0.868(10)	–0.8126(9)	–0.551(5)	0.0863(19)
H58	0.912(23)	–0.8334(12)	–0.483(7)	0.1036(23)
H59	1.056(7)	–0.8016(22)	–0.576(9)	0.1036(23)
C36	0.710(8)	–0.7881(9)	–0.466(4)	0.0863(19)
C37	0.679(14)	–0.7581(13)	–0.556(6)	0.0863(19)
H60	0.81(8)	–0.738(5)	–0.52(4)	0.1036(23)
H61	0.479(31)	–0.749(8)	–0.55(5)	0.1036(23)
H62	0.73(12)	–0.763(4)	–0.664(12)	0.1036(23)
H63	0.516(10)	–0.7987(17)	–0.449(7)	0.1036(23)
C38	0.823(12)	–0.7792(15)	–0.326(4)	0.0863(19)

Table A.2: (cont.)

H64	0.95(7)	–0.758(8)	–0.334(11)	0.1036(23)
H65	0.670(18)	–0.773(11)	–0.252(14)	0.1036(23)
H66	0.94(8)	–0.799(5)	–0.282(23)	0.1036(23)
O10	0.536(10)	–0.5165(9)	–0.325(4)	0.0863(19)
H67	0.52(5)	–0.501(9)	–0.406(30)	0.1036(23)
H68	0.466(22)	–0.505(7)	–0.244(19)	0.1036(23)

Table A.2: (cont.)

	x	*y*	*z*	U_{iso}
N1	0.6632(21)	0.453(5)	0.8677(11)	0.062(5)
H2	0.6182(27)	0.589(6)	0.8701(31)	0.075(5)
H3	0.687(5)	0.394(8)	0.9115(10)	0.075(5)
C4	0.7437(19)	0.531(7)	0.8373(16)	0.062(5)
H5	0.8092(19)	0.468(17)	0.8623(23)	0.075(5)
H6	0.744(6)	0.720(7)	0.837(4)	0.075(5)
C7	0.7318(24)	0.436(7)	0.7736(14)	0.062(5)
H8	0.7975(26)	0.354(16)	0.765(4)	0.075(5)
H9	0.713(6)	0.570(10)	0.7390(20)	0.075(5)
C10	0.6540(27)	0.261(5)	0.7703(10)	0.062(5)
H11	0.681(5)	0.089(5)	0.7627(28)	0.075(5)
H12	0.6002(35)	0.308(13)	0.7326(14)	0.075(5)
C13	0.6143(12)	0.264(4)	0.8316(11)	0.062(5)
H14	0.5397(13)	0.302(6)	0.8236(22)	0.075(5)
C15	0.6298(11)	0.0385(34)	0.8661(9)	0.062(5)
O16	0.5842(16)	–0.131(4)	0.8434(12)	0.062(5)
O17	0.6872(17)	0.040(5)	0.9136(10)	0.062(5)
N18	0.3803(19)	0.526(4)	0.9586(11)	0.062(5)
H19	0.362(4)	0.662(7)	0.9850(22)	0.075(5)
H20	0.4444(22)	0.462(8)	0.9769(24)	0.075(5)
C21	0.3839(23)	0.605(5)	0.8939(15)	0.062(5)
H22	0.4554(32)	0.650(12)	0.8869(25)	0.075(5)

Table A.3: *Atomic coordinates and isotropic displacement parameters (U_{iso}) for* ***AH*** *phase (continues on the next page).*

H23	0.338(5)	0.753(5)	0.8832(23)	0.075(5)
C24	0.3503(23)	0.404(6)	0.8547(10)	0.062(5)
H25	0.4071(31)	0.282(9)	0.8510(29)	0.075(5)
H26	0.320(4)	0.460(10)	0.8089(11)	0.075(5)
C27	0.2769(18)	0.297(4)	0.8887(11)	0.062(5)
H28	0.272(4)	0.113(5)	0.8798(19)	0.075(5)
H29	0.2097(19)	0.380(10)	0.8745(20)	0.075(5)
C30	0.3085(12)	0.342(4)	0.9573(9)	0.062(5)
H31	0.2493(21)	0.405(6)	0.9792(17)	0.075(5)
C32	0.3509(13)	0.1334(32)	0.9929(7)	0.062(5)
O33	0.2986(17)	–0.032(4)	0.9973(12)	0.062(5)
O34	0.4352(15)	0.140(5)	1.0123(12)	0.062(5)
O35	–0.1407(16)	0.220(4)	0.1025(12)	0.0611(34)
O36	–0.1263(16)	0.509(4)	0.0382(9)	0.0611(34)
H37	–0.1927(17)	0.482(6)	0.0275(14)	0.073(4)
C38	–0.0938(11)	0.3716(30)	0.0796(8)	0.0611(34)
C39	0.0551(12)	0.491(6)	0.0483(7)	0.0611(34)
H40	0.050(13)	0.360(20)	0.012(5)	0.073(4)
H41	0.017(9)	0.644(19)	0.031(7)	0.073(4)
H42	0.1270(31)	0.53(4)	0.0629(32)	0.073(4)
C43	0.0107(10)	0.3907(32)	0.1020(8)	0.0611(34)
H44	0.0390(21)	0.218(4)	0.1114(14)	0.073(4)
C45	0.0244(11)	0.5278(34)	0.1622(7)	0.0611(34)
C46	–0.0169(11)	0.740(4)	0.1667(8)	0.0611(34)

Table A.3: (cont.)

H47	–0.0577(13)	0.811(5)	0.1267(11)	0.073(4)
C48	–0.0081(11)	0.8615(35)	0.2221(10)	0.0611(34)
H49	–0.0404(14)	1.028(4)	0.2239(16)	0.073(4)
C50	0.0422(11)	0.772(4)	0.2750(8)	0.0611(34)
C51	0.0846(11)	0.558(4)	0.2699(9)	0.0611(34)
H52	0.1250(13)	0.485(6)	0.3098(12)	0.073(4)
C53	0.0739(11)	0.4365(35)	0.2153(10)	0.0611(34)
H54	0.1071(14)	0.272(4)	0.2133(16)	0.073(4)
C55	0.0550(14)	0.910(5)	0.3344(10)	0.0611(34)
H56	0.067(4)	1.089(5)	0.3232(20)	0.073(4)
H57	0.1163(16)	0.845(10)	0.3633(14)	0.073(4)
C58	–0.0257(13)	0.902(4)	0.3714(8)	0.0611(34)
C59	–0.0020(22)	1.043(5)	0.4297(12)	0.0611(34)
H60	0.050(12)	1.168(24)	0.424(5)	0.073(4)
H61	0.024(14)	0.931(12)	0.4658(19)	0.073(4)
H62	–0.063(4)	1.126(30)	0.441(5)	0.073(4)
H63	–0.0876(19)	0.973(8)	0.3440(16)	0.073(4)
C64	–0.0456(25)	0.658(5)	0.3885(15)	0.0611(34)
H65	–0.027(14)	0.635(12)	0.4364(24)	0.073(4)
H66	–0.118(4)	0.624(13)	0.377(9)	0.073(4)
H67	–0.007(11)	0.542(5)	0.364(8)	0.073(4)
O68	0.5536(16)	0.085(4)	0.2747(11)	0.0611(34)
O69	0.5687(15)	0.431(4)	0.2404(9)	0.0611(34)
H70	0.5057(16)	0.401(7)	0.2210(11)	0.073(4)

Table A.3: (cont.)

C71	0.5981(10)	0.2627(31)	0.2718(7)	0.0611(34)
C72	0.7636(17)	0.390(5)	0.2675(12)	0.0611(34)
H73	0.762(13)	0.303(30)	0.225(5)	0.073(4)
H74	0.744(10)	0.563(12)	0.260(11)	0.073(4)
H75	0.8319(33)	0.38(4)	0.291(6)	0.073(4)
C76	0.6967(10)	0.2748(31)	0.3070(8)	0.0611(34)
H77	0.7212(21)	0.100(4)	0.3174(14)	0.073(4)
C78	0.6958(10)	0.4047(32)	0.3678(8)	0.0611(34)
C79	0.7425(11)	0.3128(31)	0.4217(10)	0.0611(34)
H80	0.7776(13)	0.1503(34)	0.4203(16)	0.073(4)
C81	0.7453(11)	0.4271(35)	0.4768(9)	0.0611(34)
H82	0.7810(14)	0.350(5)	0.5178(12)	0.073(4)
C83	0.7007(11)	0.6374(32)	0.4810(9)	0.0611(34)
C84	0.6531(11)	0.7332(31)	0.4275(11)	0.0611(34)
H85	0.6187(14)	0.8964(34)	0.4296(17)	0.073(4)
C86	0.6509(11)	0.6187(35)	0.3714(10)	0.0611(34)
87	0.6147(14)	0.695(5)	0.3304(12)	0.073(4)
C88	0.7075(12)	0.759(4)	0.5427(11)	0.0611(34)
H89	0.7444(29)	0.920(6)	0.5386(22)	0.073(4)
H90	0.7481(22)	0.651(9)	0.5770(13)	0.073(4)
C91	0.6161(14)	0.813(4)	0.5665(10)	0.0611(34)
C92	0.6361(21)	0.939(5)	0.6278(14)	0.0611(34)
H93	0.671(12)	1.095(14)	0.6208(34)	0.073(4)
H94	0.679(11)	0.836(17)	0.6595(24)	0.073(4)

Table A.3: (cont.)

H95	0.5730(29)	0.975(28)	0.646(4)	0.073(4)
H96	0.5756(25)	0.926(7)	0.5331(16)	0.073(4)
C97	0.5593(18)	0.598(5)	0.5740(15)	0.0611(34)
H98	0.602(5)	0.475(13)	0.599(9)	0.073(4)
H99	0.502(8)	0.640(11)	0.598(9)	0.073(4)
H100	0.535(12)	0.532(24)	0.5301(19)	0.073(4)

Table A.3: (cont.)

	x	*y*	*z*	U_{iso}
H1	0.2675(11)	0.990(5)	0.5977(26)	0.1622(35)
N1	0.2850(6)	1.140(5)	0.5897(11)	0.1131(23)
C1	0.28483(28)	1.3206(34)	0.6438(8)	0.1131(23)
C2	0.3288(8)	1.067(5)	0.5907(16)	0.1131(23)
H2	0.2727(12)	1.215(8)	0.5433(10)	0.1622(35)
C3	0.26411(25)	1.5447(34)	0.6111(8)	0.1131(23)
C4	0.3305(4)	1.353(5)	0.6754(10)	0.1131(23)
C5	0.3538(5)	1.279(6)	0.6204(13)	0.1131(23)
H3	0.2669(5)	1.251(4)	0.6797(11)	0.1622(35)
H4	0.3317(12)	1.017(11)	0.5397(22)	0.1622(35)
H5	0.3352(13)	0.913(5)	0.6235(29)	0.1622(35)
H6	0.3368(7)	1.534(6)	0.6931(24)	0.1622(35)
H7	0.3380(7)	1.235(9)	0.7189(11)	0.1622(35)
H8	0.3531(13)	1.418(8)	0.5826(19)	0.1622(35)
H9	0.3861(4)	1.235(10)	0.6396(23)	0.1622(35)
O1	0.25735(31)	1.710(4)	0.6507(11)	0.1131(23)
O2	0.2549(4)	1.555(5)	0.5487(8)	0.1131(23)
H10	0.3357(10)	0.474(4)	0.3928(25)	0.1622(35)
N2	0.3490(8)	0.312(5)	0.4098(10)	0.1131(23)
C6	0.32460(33)	0.116(4)	0.3700(6)	0.1131(23)
C7	0.3919(6)	0.314(6)	0.3934(14)	0.1131(23)
H11	0.3506(14)	0.298(8)	0.4617(11)	0.1622(35)
C8	0.3395(6)	0.166(5)	0.3044(6)	0.1131(23)

Table A.4: *Atomic coordinates and isotropic displacement parameters (U_{iso}) for* ***QH*** *phase (continues on the next page).*

C9	0.3323(4)	-0.142(4)	0.3965(6)	0.1131(23)
C10	0.3862(5)	0.183(6)	0.3265(13)	0.1131(23)
H12	0.2918(4)	0.157(5)	0.3657(14)	0.1622(35)
H13	0.4009(13)	0.499(7)	0.3899(30)	0.1622(35)
H14	0.4130(10)	0.229(12)	0.4342(17)	0.1622(35)
H15	0.3298(11)	0.028(8)	0.2674(11)	0.1622(35)
H16	0.3262(9)	0.333(7)	0.2833(16)	0.1622(35)
H17	0.3998(11)	0.007(7)	0.3341(24)	0.1622(35)
H18	0.4011(10)	0.274(10)	0.2900(18)	0.1622(35)
O3	0.3069(5)	–0.300(4)	0.3775(9)	0.1131(23)
O4	0.3656(5)	–0.190(5)	0.4388(7)	0.1131(23)
H19	0.8464(4)	0.424(18)	0.912(6)	0.1622(35)
C11	0.8174(5)	0.494(4)	0.9224(11)	0.1131(23)
C12	0.7803(4)	0.3618(13)	0.8826(4)	0.1131(23)
H20	0.8178(27)	0.474(20)	0.9763(10)	0.1622(35)
H21	0.8159(27)	0.681(5)	0.910(5)	0.1622(35)
C13	0.7398(4)	0.4836(23)	0.8861(5)	0.1131(23)
C14	0.7842(4)	0.3263(20)	0.8092(5)	0.1131(23)
H22	0.7788(6)	0.1850(19)	0.9041(7)	0.1622(35)
C15	0.7126(5)	0.3884(24)	0.9242(5)	0.1131(23)
C16	0.7283(4)	0.6942(24)	0.8516(5)	0.1131(23)
O5	0.7576(5)	0.1663(22)	0.7797(8)	0.1131(23)
O6	0.8085(5)	0.4311(32)	0.7809(11)	0.1131(23)
C17	0.6754(5)	0.4996(32)	0.9276(6)	0.1131(23)
C18	0.6910(5)	0.8042(23)	0.8553(5)	0.1131(23)

Table A.4: (cont.)

H23	0.7208(8)	0.2247(24)	0.9515(5)	0.1622(35)
H24	0.7485(6)	0.7752(33)	0.8213(5)	0.1622(35)
H25	0.755(7)	0.17(4)	0.7280(14)	0.1622(35)
C19	0.6637(4)	0.7107(32)	0.8932(7)	0.1131(23)
H26	0.6551(6)	0.419(4)	0.9578(7)	0.1622(35)
H27	0.6832(7)	0.9677(24)	0.8279(6)	0.1622(35)
C20	0.6238(4)	0.837(4)	0.8953(9)	0.1131(23)
C21	0.5844(4)	0.7112(31)	0.8607(8)	0.1131(23)
H28	0.6214(7)	0.866(9)	0.9481(10)	0.1622(35)
H29	0.6248(7)	1.0133(27)	0.8729(22)	0.1622(35)
C22	0.5475(6)	0.872(5)	0.8614(15)	0.1131(23)
C23	0.5902(8)	0.634(6)	0.7910(11)	0.1131(23)
H30	0.5808(9)	0.552(5)	0.8903(17)	0.1622(35)
H31	0.5282(17)	0.887(13)	0.8112(22)	0.1622(35)
H32	0.5279(15)	0.806(11)	0.896(4)	0.1622(35)
H33	0.5575(12)	1.051(5)	0.878(4)	0.1622(35)
H34	0.5613(20)	0.65(4)	0.7543(26)	0.1622(35)
H35	0.613(5)	0.747(22)	0.773(5)	0.1622(35)
H36	0.601(6)	0.452(13)	0.791(4)	0.1622(35)
H37	0.0345(6)	0.250(12)	0.653(4)	0.1622(35)
C24	0.0152(4)	0.378(6)	0.6208(12)	0.1131(23)
C25	–0.0298(4)	0.3455(29)	0.62704(27)	0.1131(23)
H38	0.0196(9)	0.352(18)	0.5691(17)	0.1622(35)
H39	0.0256(7)	0.555(8)	0.637(4)	0.1622(35)
C26	–0.06026(31)	0.4012(26)	0.56245(34)	0.1131(23)

Table A.4: (cont.)

C27	–0.0439(4)	0.4890(27)	0.68172(30)	0.1131(23)
H40	–0.0348(8)	0.1593(28)	0.6372(8)	0.1622(35)
C28	–0.0768(4)	0.4150(23)	0.7114(5)	0.1131(23)
C29	–0.02437(35)	0.6993(31)	0.7038(6)	0.1131(23)
O7	–0.0877(4)	0.2334(29)	0.5479(8)	0.1131(23)
O8	–0.0609(4)	0.5772(27)	0.5262(7)	0.1131(23)
C30	–0.08964(34)	0.5462(28)	0.7614(5)	0.1131(23)
C31	–0.0373(5)	0.8305(23)	0.7539(6)	0.1131(23)
H41	–0.0924(6)	0.2507(24)	0.6948(8)	0.1622(35)
H42	–0.1096(30)	0.282(12)	0.506(5)	0.1622(35)
H43	0.0013(4)	0.763(4)	0.6819(9)	0.1622(35)
C32	–0.0700(5)	0.7580(26)	0.7837(4)	0.1131(23)
H44	–0.11530(35)	0.483(4)	0.7835(7)	0.1622(35)
H45	–0.0216(7)	0.9947(25)	0.7704(9)	0.1622(35)
C33	–0.0820(7)	0.9113(32)	0.8376(5)	0.1131(23)
C34	–0.0748(5)	0.8103(28)	0.9091(6)	0.1131(23)
H46	–0.1149(9)	0.955(8)	0.8234(8)	0.1622(35)
H47	–0.0654(14)	1.0798(25)	0.8386(9)	0.1622(35)
C35	–0.0995(8)	0.952(6)	0.9515(12)	0.1131(23)
C36	–0.0294(6)	0.810(6)	0.9414(12)	0.1131(23)
H48	–0.0862(11)	0.628(4)	0.9063(13)	0.1622(35)
H49	–0.1320(9)	0.898(14)	0.942(5)	0.1622(35)
H50	–0.0871(23)	0.930(15)	1.0054(10)	0.1622(35)
H51	–0.0987(23)	1.141(6)	0.940(4)	0.1622(35)
H52	–0.0247(13)	0.744(20)	0.9932(24)	0.1622(35)

Table A.4: (cont.)

H53	–0.0113(11)	0.700(18)	0.913(4)	0.1622(35)
H54	–0.0165(15)	0.989(8)	0.943(5)	0.1622(35)
H55	0.0204(5)	0.797(5)	0.4860(15)	0.1622(35)
O9	0	0.903(5)	0.5	0.1131(23)

Table A.4: (cont.)

	x	*y*	*z*	U_{iso}
C1	0.8028(6)	0.0857(11)	0.76354(21)	0.0403(15)
C2	0.8347(6)	–0.0739(11)	0.82577(20)	0.0403(15)
H1	0.9371(8)	–0.1650(15)	0.8212(4)	0.0483(17)
H2	0.7604(9)	–0.2351(16)	0.82700(29)	0.0483(17)
C3	0.8414(8)	0.0531(15)	0.89645(15)	0.0403(15)
H3	0.9278(9)	0.1914(20)	0.9014(4)	0.0483(17)
N1	0.8733(15)	–0.1589(22)	0.9462(4)	0.0403(15)
H4	0.9769(31)	–0.231(10)	0.9419(29)	0.0483(17)
H5	0.803(5)	–0.309(7)	0.9370(23)	0.0483(17)
H6	0.866(8)	–0.090(4)	0.9954(4)	0.0483(17)
C4	0.7052(8)	0.1782(18)	0.91635(14)	0.0403(15)
O1	0.6184(10)	0.0332(22)	0.94311(16)	0.0403(15)
O2	0.6874(9)	0.4154(18)	0.90520(18)	0.0403(15)
C5	0.7130(5)	0.2906(12)	0.7516(4)	0.0403(15)
H7	0.6442(6)	0.3833(18)	0.7853(6)	0.0483(17)
C6	0.8681(5)	0.0435(10)	0.70109(24)	0.0403(15)
C7	0.9678(5)	–0.1332(12)	0.6805(5)	0.0403(15)
H8	1.0126(7)	–0.2786(11)	0.7153(7)	0.0483(17)
C8	1.0089(6)	–0.1199(19)	0.6144(5)	0.0403(15)
H9	1.0861(7)	–0.2556(23)	0.5980(8)	0.0483(17)
C9	0.9524(10)	0.0661(22)	0.56828(35)	0.0403(15)
H10	0.9870(13)	0.0712(30)	0.5169(4)	0.0483(17)

Table A.5: *Atomic coordinates and isotropic displacement parameters (U_{iso}) for* ***β-L-Trp*** *phase at ambient temperature (continues on the next page).*

C10	0.8535(10)	0.2429(18)	0.58714(26)	0.0403(15)
H11	0.8099(13)	0.3866(20)	0.5516(4)	0.0483(17)
C11	0.8121(6)	0.2296(11)	0.65346(28)	0.0403(15)
N2	0.7184(6)	0.3755(9)	0.6859(4)	0.0403(15)
H12	0.6611(7)	0.5249(9)	0.6655(6)	0.0483(17)
C12	0.3286(6)	0.6146(11)	0.76809(20)	0.0403(15)
C13	0.3888(5)	0.7846(10)	0.82357(20)	0.0403(15)
H13	0.3542(9)	0.9841(11)	0.81403(34)	0.0483(17)
H14	0.5030(5)	0.7910(16)	0.8212(4)	0.0483(17)
C14	0.3599(7)	0.7254(14)	0.89695(13)	0.0403(15)
H15	0.4322(8)	0.8480(16)	0.92783(26)	0.0483(17)
N3	0.3900(11)	0.4590(14)	0.92175(26)	0.0403(15)
H16	0.4947(9)	0.4149(26)	0.9152(21)	0.0483(17)
H17	0.3224(17)	0.3170(18)	0.9018(13)	0.0483(17)
H18	0.381(5)	0.4605(20)	0.97451(30)	0.0483(17)
C15	0.2138(7)	0.8092(18)	0.91329(10)	0.0403(15)
O3	0.1319(9)	0.6352(22)	0.93314(13)	0.0403(15)
O4	0.1887(9)	1.0445(19)	0.90537(15)	0.0403(15)
C16	0.2332(5)	0.4160(12)	0.7671(4)	0.0403(15)
H19	0.1767(7)	0.3322(18)	0.8075(5)	0.0483(17)
C17	0.3685(5)	0.6413(9)	0.69989(24)	0.0403(15)
C18	0.4610(5)	0.8083(11)	0.6698(5)	0.0403(15)

Table A.5: (cont.)

H20	0.5194(6)	0.9538(10)	0.6997(7)	0.0483(17)
C19	0.4769(7)	0.7844(18)	0.6008(5)	0.0403(15)
H21	0.5484(8)	0.9131(22)	0.5769(7)	0.0483(17)
C20	0.4023(10)	0.5972(21)	0.56148(31)	0.0403(15)
H22	0.4177(13)	0.5848(28)	0.50752(32)	0.0483(17)
C21	0.3101(9)	0.4291(16)	0.59005(30)	0.0403(15)
H23	0.2527(11)	0.2847(18)	0.5594(5)	0.0483(17)
C22	0.2941(5)	0.4531(10)	0.65963(30)	0.0403(15)
N4	0.2129(5)	0.3194(8)	0.7020(4)	0.0403(15)
H24	0.1472(5)	0.1716(9)	0.6881(6)	0.0483(17)

Table A.5: (cont.)

	x	*y*	*z*	U_{iso}
C1	0.8041(6)	0.0806(12)	0.76509(20)	0.1240(24)
C2	0.8397(6)	–0.0830(12)	0.82653(19)	0.1240(24)
H1	0.9423(8)	–0.1721(14)	0.8212(4)	0.1487(29)
H2	0.7663(9)	–0.2462(16)	0.82794(28)	0.1487(29)
C3	0.8484(8)	0.0452(16)	0.89726(14)	0.1240(24)
H3	0.9341(9)	0.1859(20)	0.9017(4)	0.1487(29)
N1	0.8833(16)	–0.1666(23)	0.9472(4)	0.1240(24)
H4	0.9942(17)	–0.192(6)	0.9551(16)	0.1487(29)
H5	0.838(4)	–0.3392(27)	0.9291(10)	0.1487(29)
H6	0.846(4)	–0.121(4)	0.9937(7)	0.1487(29)
C4	0.7116(8)	0.1695(19)	0.91641(14)	0.1240(24)
O1	0.6277(10)	0.0209(24)	0.94381(16)	0.1240(24)
O2	0.6895(10)	0.4063(20)	0.90443(18)	0.1240(24)
C5	0.7118(5)	0.2845(13)	0.7560(4)	0.1240(24)
H7	0.6447(6)	0.3708(18)	0.7914(6)	0.1487(29)
C6	0.8652(5)	0.0482(11)	0.70135(22)	0.1240(24)
C7	0.9648(5)	–0.1228(13)	0.6779(4)	0.1240(24)
H8	1.0133(7)	–0.2715(12)	0.7110(6)	0.1487(29)
C8	1.0010(7)	–0.0993(20)	0.6112(5)	0.1240(24)
H9	1.0779(8)	–0.2307(25)	0.5926(7)	0.1487(29)
C9	0.9398(11)	0.0914(23)	0.56719(31)	0.1240(24)
H10	0.9706(14)	0.1042(31)	0.51532(34)	0.1487(29)

Table A.6: *Atomic coordinates and isotropic displacement parameters (U_{iso}) for* ***β-L-Trp*** *phase at 123 K (continues on the next page).*

C10	0.8410(10)	0.2630(18)	0.58888(26)	0.1240(24)
H11	0.7937(13)	0.4104(20)	0.5550(4)	0.1487(29)
C11	0.8047(7)	0.2393(12)	0.65585(28)	0.1240(24)
N2	0.7123(6)	0.3784(10)	0.6908(5)	0.1240(24)
H12	0.6525(8)	0.5289(10)	0.6723(6)	0.1487(29)
C12	0.3373(6)	0.6159(11)	0.77250(19)	0.1240(24)
C13	0.3985(5)	0.7793(10)	0.82970(20)	0.1240(24)
H13	0.3697(9)	0.9829(11)	0.82063(33)	0.1487(29)
H14	0.5132(5)	0.7756(15)	0.8300(4)	0.1487(29)
C14	0.3614(8)	0.7151(14)	0.90152(12)	0.1240(24)
H15	0.4314(9)	0.8341(17)	0.93521(26)	0.1487(29)
N3	0.3929(12)	0.4433(15)	0.92266(27)	0.1240(24)
H16	0.4971(9)	0.4013(20)	0.9147(19)	0.1487(29)
H17	0.3242(15)	0.3040(18)	0.9013(15)	0.1487(29)
H18	0.387(5)	0.4346(26)	0.9756(4)	0.1487(29)
C15	0.2131(8)	0.8001(18)	0.91392(9)	0.1240(24)
O3	0.1286(11)	0.6265(22)	0.93145(12)	0.1240(24)
O4	0.1873(10)	1.0363(18)	0.90560(12)	0.1240(24)
C16	0.2407(5)	0.4180(12)	0.7715(4)	0.1240(24)
H19	0.1856(7)	0.3330(17)	0.8121(5)	0.1487(29)
C17	0.3745(5)	0.6455(10)	0.70394(22)	0.1240(24)
C18	0.4665(5)	0.8128(12)	0.6737(4)	0.1240(24)

Table A.6: (cont.)

H20	0.5271(6)	0.9566(11)	0.7036(6)	0.1487(29)
C19	0.4791(7)	0.7913(18)	0.6041(4)	0.1240(24)
H21	0.5501(8)	0.9203(22)	0.5801(7)	0.1487(29)
C20	0.4016(10)	0.6060(20)	0.56461(28)	0.1240(24)
H22	0.4144(13)	0.5954(27)	0.51036(29)	0.1487(29)
C21	0.3098(9)	0.4376(16)	0.59341(28)	0.1240(24)
H23	0.2502(11)	0.2948(18)	0.5627(4)	0.1487(29)
C22	0.2972(6)	0.4591(11)	0.66343(28)	0.1240(24)
N4	0.2172(5)	0.3242(9)	0.7060(4)	0.1240(24)
H24	0.1502(6)	0.1776(9)	0.6919(6)	0.1487(29)

Table A.6: (cont.)

	x	*y*	*z*		
C1	0	0.9070(7)	0.7469(17)	0.0430(18)	U_{ani}
C2	0	0.8488(13)	0.5810(15)	0.092(5)	U_{ani}
H2A	0.11744	0.885145	0.52709	0.11	U_{iso}
H2B	–0.11744	0.885145	0.52709	0.11	U_{iso}
C3	0	0.6729(15)	0.5850(12)	0.105(10)	U_{ani}
H3	0	0.632891	0.479568	0.126	U_{iso}
C4	0.1872(19)	0.6239(14)	0.6678(12)	0.135(7)	U_{ani}
H4A	0.197991	0.514582	0.664682	0.161	U^{iso}
H4B	0.303058	0.666036	0.616298	0.161	U_{iso}
C5	0.1829(14)	0.6762(11)	0.8328(10)	0.103(6)	U_{ani}
H5	0.301784	0.638511	0.886335	0.123	U_{iso}
C6	0.1864(16)	0.8532(9)	0.8318(15)	0.101(4)	U_{ani}
H6A	0.186754	0.891597	0.936606	0.121	U_{iso}
H6B	0.305368	0.889461	0.779878	0.121	U_{iso}
C7	0	0.6258(19)	0.9177(17)	0.111(9)	U_{ani}
H7A	–1E-06	0.668491	1.0207	0.133	U_{iso}
H7B	0.000001	0.516561	0.926852	0.133	U_{iso}
I1	0	1.15551(7)	0.7503(10)	0.0913(4)	U_{ani}

Table A.7: *Atomic coordinates and atomic displacement parameters for phase A of 1-IA.*

	x	*y*	*z*		
C1	0.744(2)	0.382(4)	0.5938(15)	0.021(3)	U_{ani}
C2	0.909(3)	0.481(2)	0.644(2)	0.031(4)	U_{ani}
H2A	0.881932	0.589355	0.606427	0.038	U_{iso}
H2B	1.035225	0.443261	0.601892	0.038	U_{iso}
C3	0.938(3)	0.482(2)	0.822(2)	0.032(4)	U_{ani}
H3	1.047082	0.559368	0.856377	0.039	U_{iso}
C4	0.997(3)	0.3178(17)	0.881(3)	0.040(5)	U_{ani}
H4A	1.12827	0.284833	0.842678	0.048	U_{iso}
H4B	1.012355	0.317522	0.993352	0.048	U_{iso}
C5	0.826(3)	0.205(2)	0.823(2)	0.034(4)	U_{ani}
H5	0.862014	0.097336	0.861215	0.041	U_{iso}
C6	0.799(3)	0.200(2)	0.651(2)	0.027(3)	U_{ani}
H6A	0.686272	0.127703	0.616795	0.032	U_{iso}
H6B	0.925343	0.163375	0.608215	0.032	U_{iso}
C7	0.537(3)	0.415(2)	0.651(2)	0.039(5)	U_{ani}
H7A	0.438557	0.331723	0.617513	0.046	U_{iso}
H7B	0.483126	0.517245	0.6115	0.046	U_{iso}
C8	0.566(3)	0.420(2)	0.828(2)	0.038(5)	U_{ani}
H8	0.435837	0.452775	0.870719	0.046	U_{iso}
C9	0.626(3)	0.252(3)	0.883(2)	0.031(4)	U_{ani}
H9A	0.639061	0.249847	0.995846	0.037	U_{iso}
H9B	0.518476	0.176694	0.847468	0.037	U_{iso}

Table A.8: *Atomic coordinates and atomic displacement parameters for phase B of 1-IA (table continues in the next page).*

C10	0.735(3)	0.534(2)	0.876(2)	0.032(4)	U_{ani}
H10A	0.747354	0.541538	0.988734	0.038	U_{iso}
H10B	0.699757	0.639177	0.835021	0.038	U_{iso}
I1	0.71260(16)	0.3717(5)	0.34300(10)	0.0380(3)	U_{ani}

Table A.8: (cont.)

	x	*y*	*z*		
C1	–0.0487(17)	0.3140(8)	0.2496(12)	0.0497(19)	U_{ani}
C2	–0.091(2)	0.3387(11)	0.3918(11)	0.051(3)	U_{ani}
H2A	0.029633	0.354825	0.437034	0.061	U_{iso}
H2B	–0.14877	0.282844	0.435352	0.061	U_{iso}
C3	–0.229(2)	0.4249(11)	0.3968(19)	0.051(3)	U_{ani}
H3	–0.2566	0.441302	0.488635	0.061	U_{iso}
C4	–0.138(3)	0.5125(10)	0.3292(18)	0.053(3)	U_{ani}
H4A	–0.01736	0.529989	0.372905	0.064	U_{iso}
H4B	–0.2257	0.567993	0.334289	0.064	U_{iso}
C5	–0.098(3)	0.4878(11)	0.1857(17)	0.052(3)	U_{ani}
H5	–0.0408	0.543951	0.140097	0.062	U_{iso}
C6	0.0393(18)	0.4002(10)	0.1813(15)	0.051(3)	U_{ani}
H6A	0.066334	0.383351	0.09056	0.061	U_{iso}
H6B	0.16155	0.417146	0.223451	0.061	U_{iso}
C7	–0.2373(19)	0.2843(9)	0.1816(15)	0.050(3)	U_{ani}
H7A	–0.29269	0.228054	0.225805	0.06	U_{iso}
H7B	–0.21052	0.266213	0.091295	0.06	U_{iso}
C8	–0.383(2)	0.3689(13)	0.1843(18)	0.053(3)	U_{ani}
H8	–0.5047	0.351313	0.14018	0.063	U_{iso}
C9	–0.417(2)	0.3973(15)	0.3272(19)	0.051(3)	U_{ani}
H9A	–0.50656	0.452153	0.330335	0.061	U_{iso}
H9B	–0.4773	0.342949	0.3729	0.061	U_{iso}

Table A.9: *Atomic coordinates and atomic displacement parameters for phase C of 1-IA (table continues in the next page).*

C10	–0.289(2)	0.4577(12)	0.121(2)	0.052(3)	U_{ani}
H10A	–0.37908	0.512151	0.124684	0.063	U_{iso}
H10B	–0.26465	0.443572	0.028756	0.063	U_{iso}
I1	0.15462(15)	0.19299(6)	0.24990(11)	0.0595(6)	U_{ani}

Table A.9: (cont.)

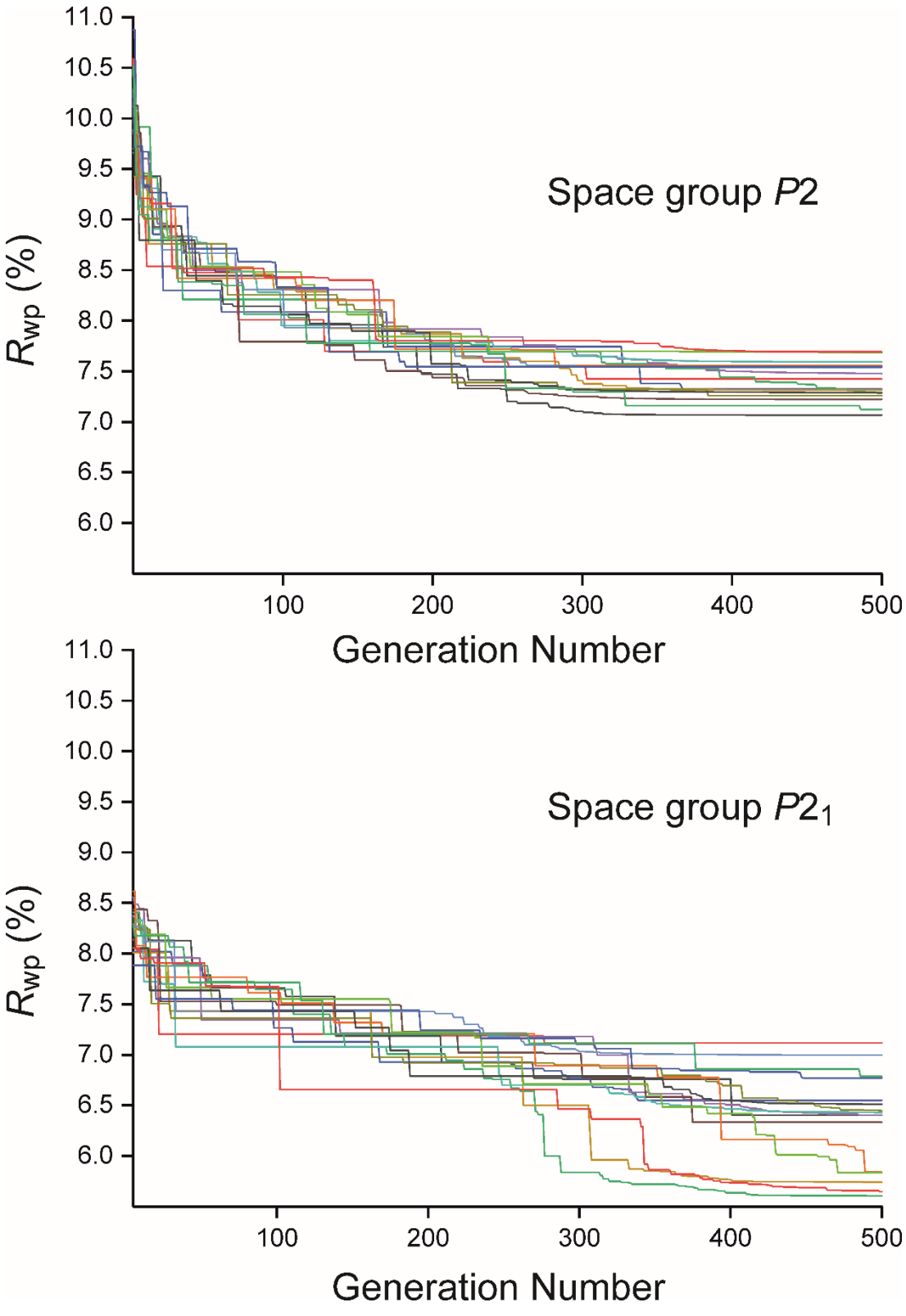

Figure A.1: *Results from the GA structure solution calculations for the* ***AH*** *phase using space group P2 and P21. The plots show that the lowest* R_{wp} *in the population versus generation number for the 16 independent GA calculations that were run on different processors. Clearly, the structure solution calculations converge on a significantly lower value of* R_{wp} *for space group P21 than for space group P2.*

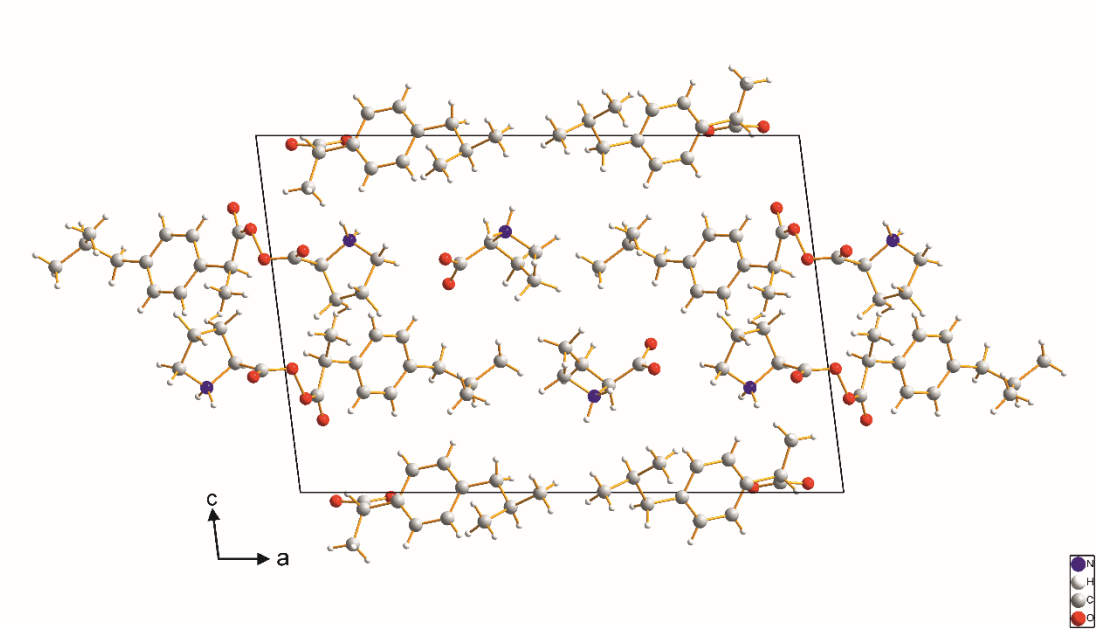

Figure A.2: *The structure solution with the lowest R_{wp} obtained in the GA structure solution calculations for the* ***AH*** *phase using space group P2 viewed along the b-axis. Clearly, there is significant overlap between molecules suggesting that P2 is the wrong space group.*

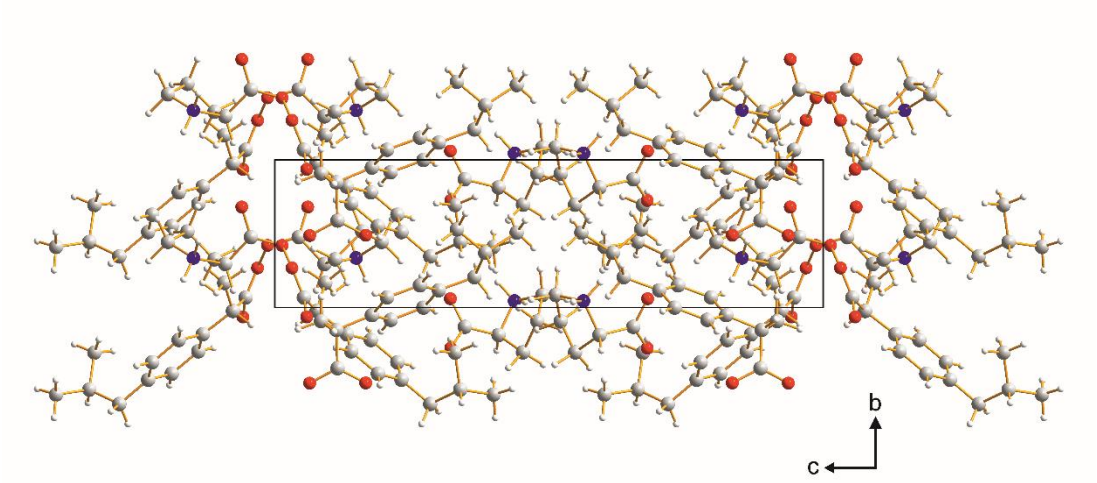

Figure A.3: *The structure solution with the lowest R_{wp} obtained in the GA structure solution calculations for the* ***AH*** *phase using space group P2 viewed along the a-axis. Clearly, there is significant overlap between molecules suggesting that P2 is the wrong space group.*

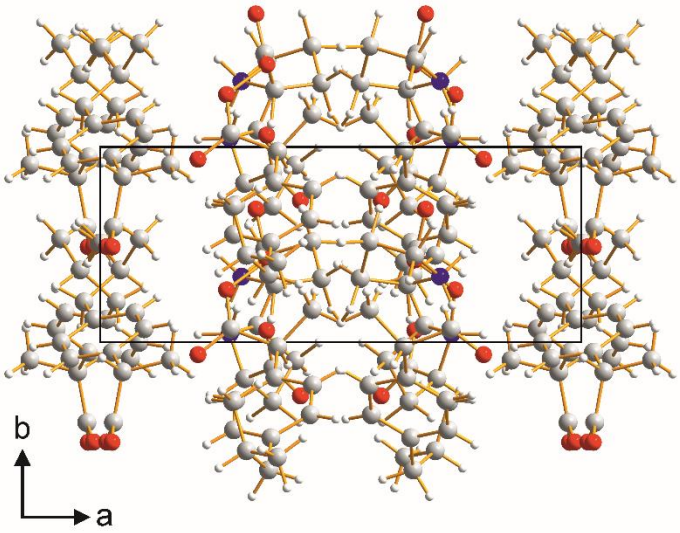

Figure A.4: *The structure solution with the lowest R_{wp} obtained in the GA structure solution calculations for the* ***AH*** *phase using space group P2 viewed along the c-axis. Clearly, there is significant overlap between molecules suggesting that P2 is the wrong space group.*

Appendix B: DSC Thermograms of Different Systems Reported in this Thesis

(S)-ibuprofen:L-lysine Co-crystal System

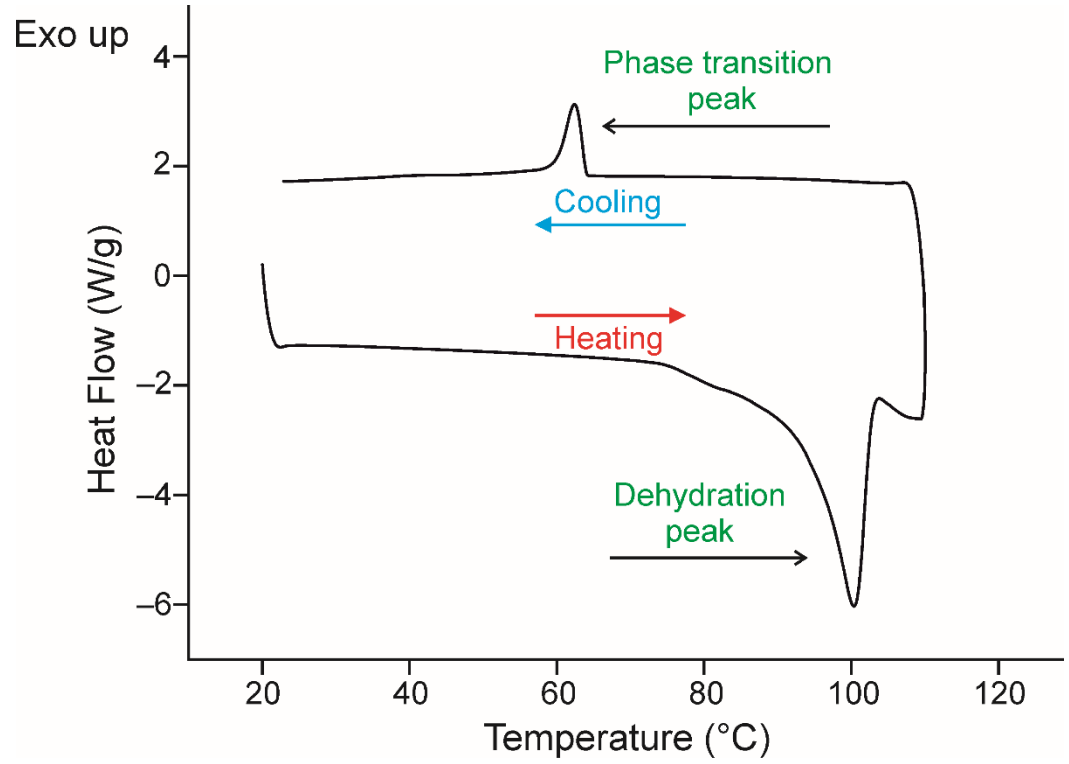

***Figure B.1**: DSC thermogram of **IL-MH** phase showing the dehydration peak on heating and the phase transition peak on cooling.*

(S)-ibuprofen:L-proline Co-crystal System

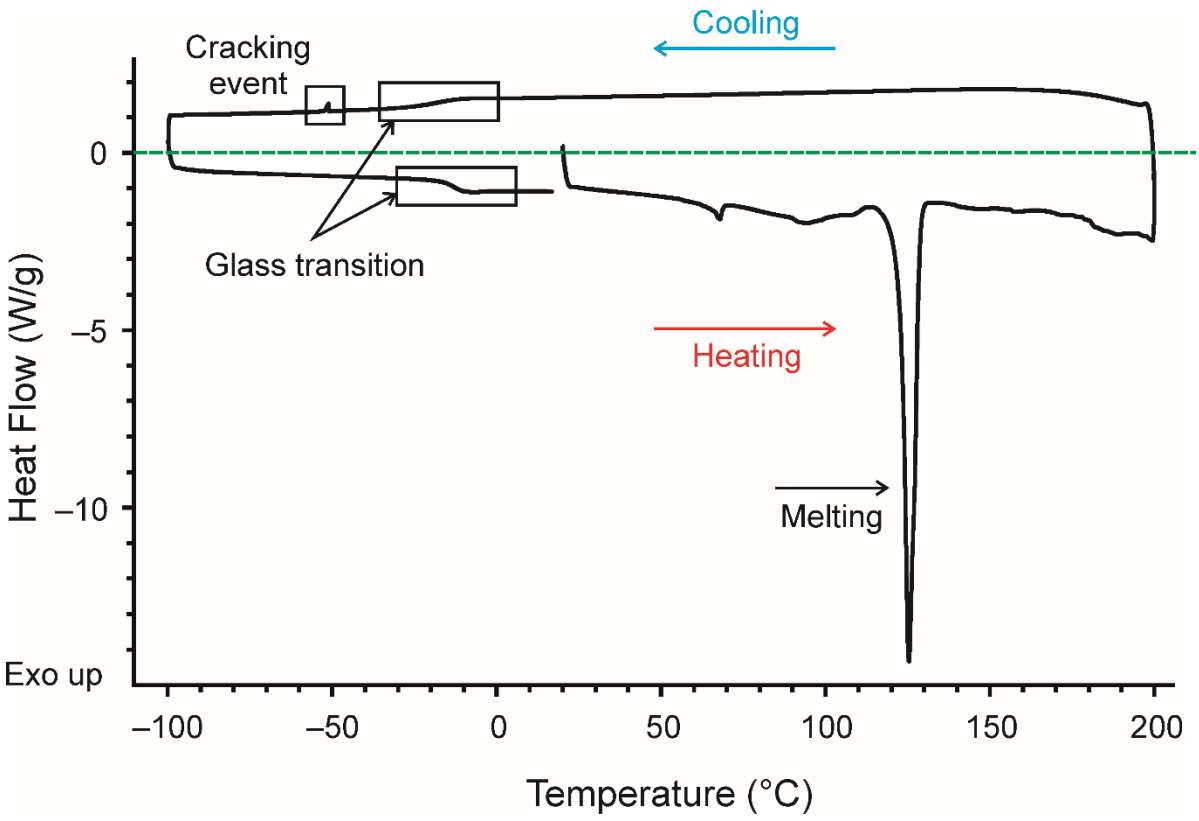

***Figure B.2**: DSC thermogram of **QH** phase.*

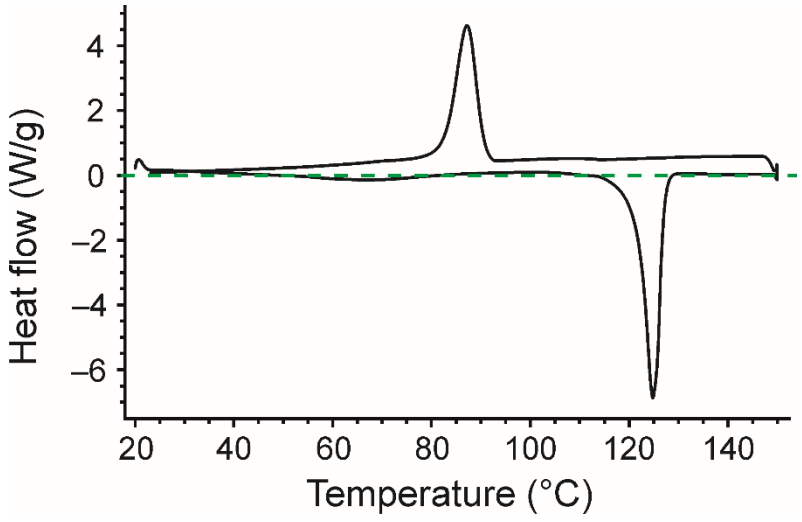

***Figure B.3**: Another DSC thermogram of **QH** phase.*

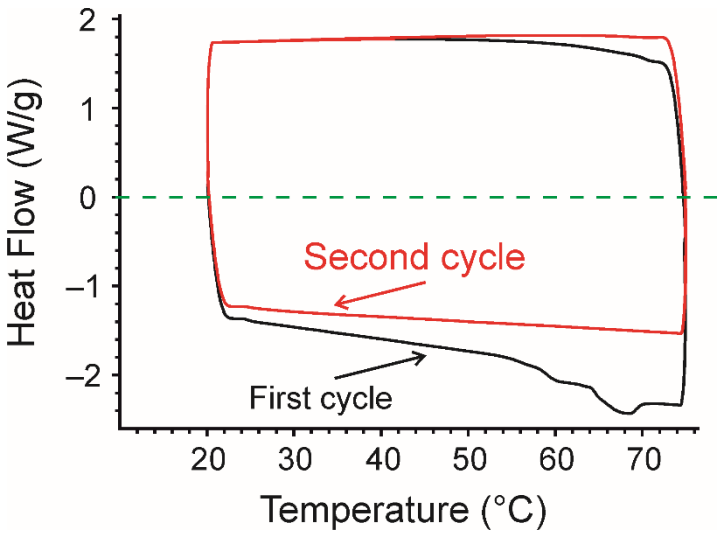

***Figure B.4**: Two cycles of heating/cooling of the **QH** phase.*

1-IA System

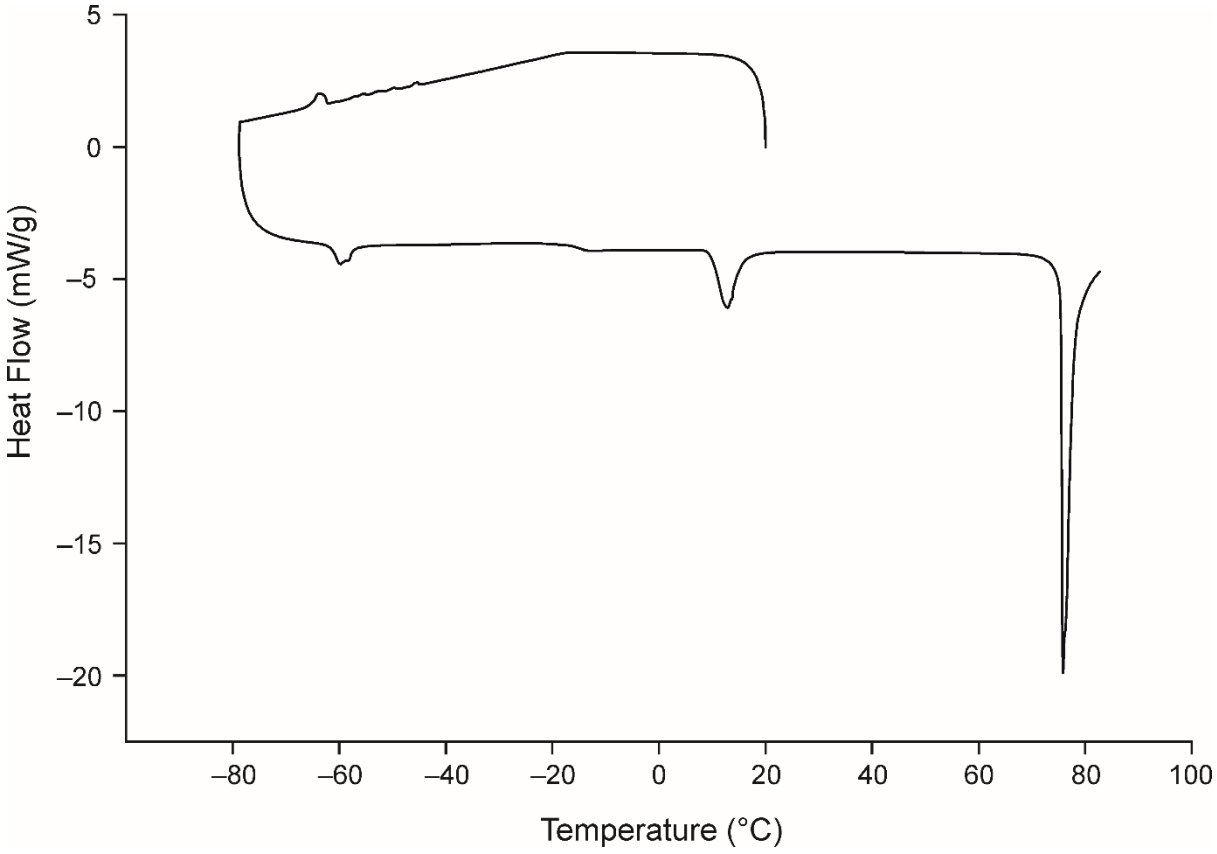

***Figure B.5:** DSC theromgram of 1-IA using 20 °C/min. Exothermic up.*

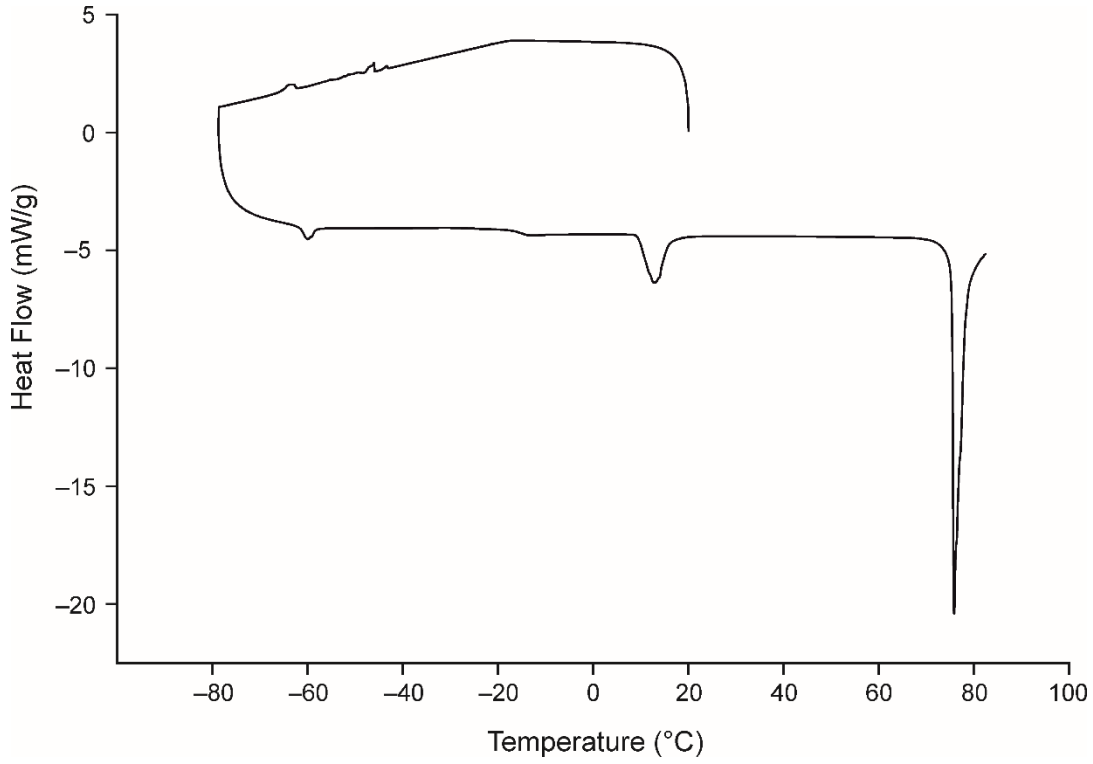

Figure B.6: *DSC theromgram of 1-IA using 20 °C/min. Exothermic up.*

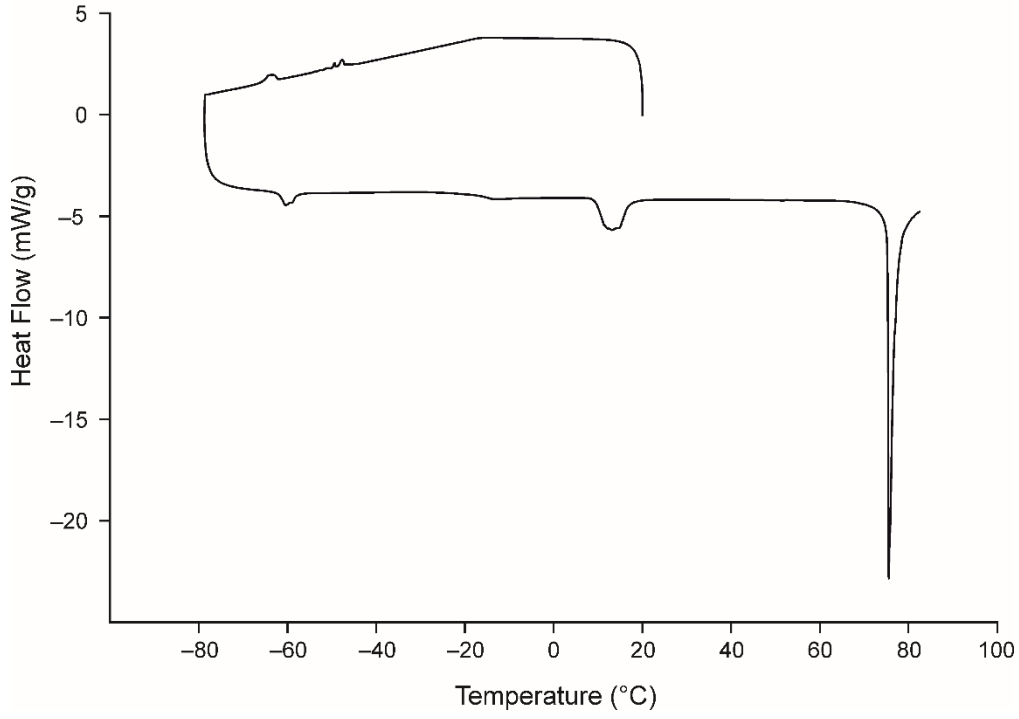

Figure B.7: *DSC theromgram of 1-IA using 20 °C/min. Exothermic up.*

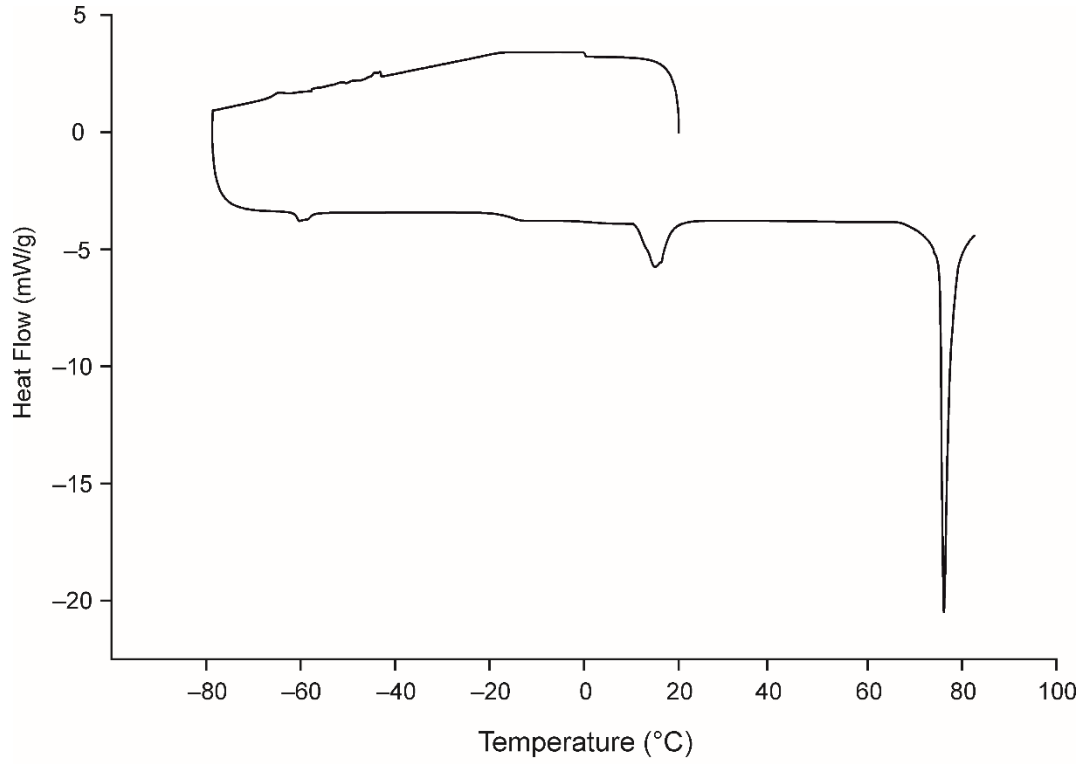

Figure B.8: *DSC theromgram of 1-IA using 20 °C/min. Exothermic up.*

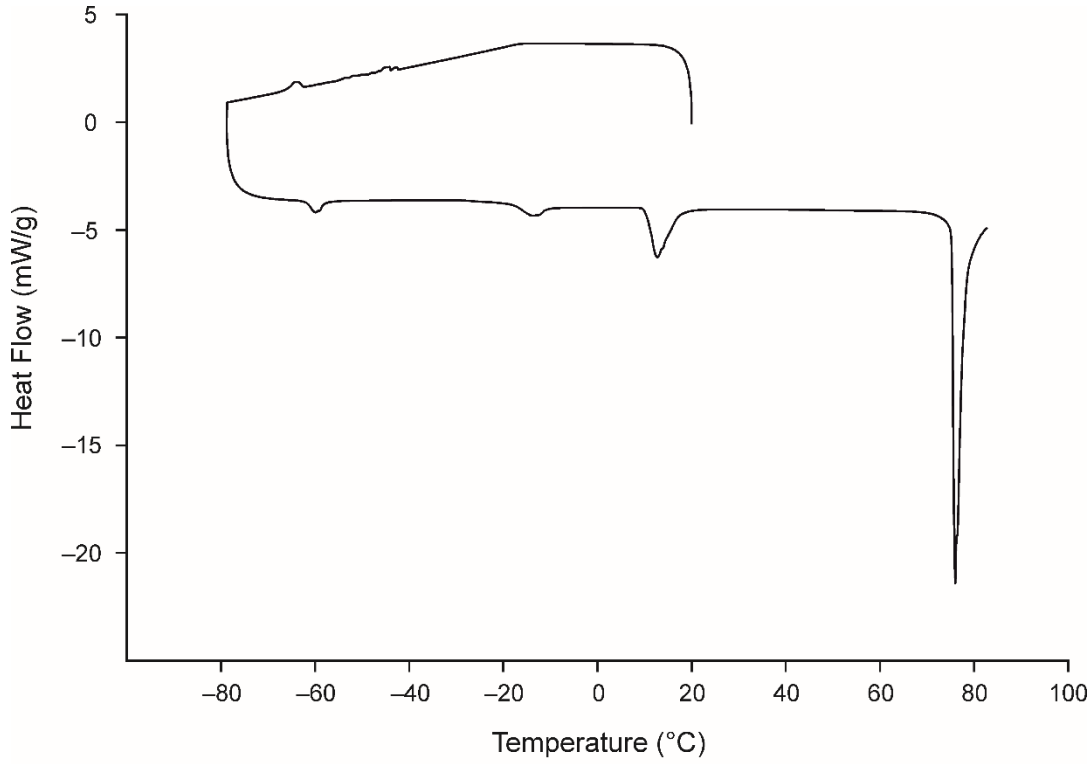

Figure B.9: *DSC theromgram of 1-IA using 20 °C/min. Exothermic up.*

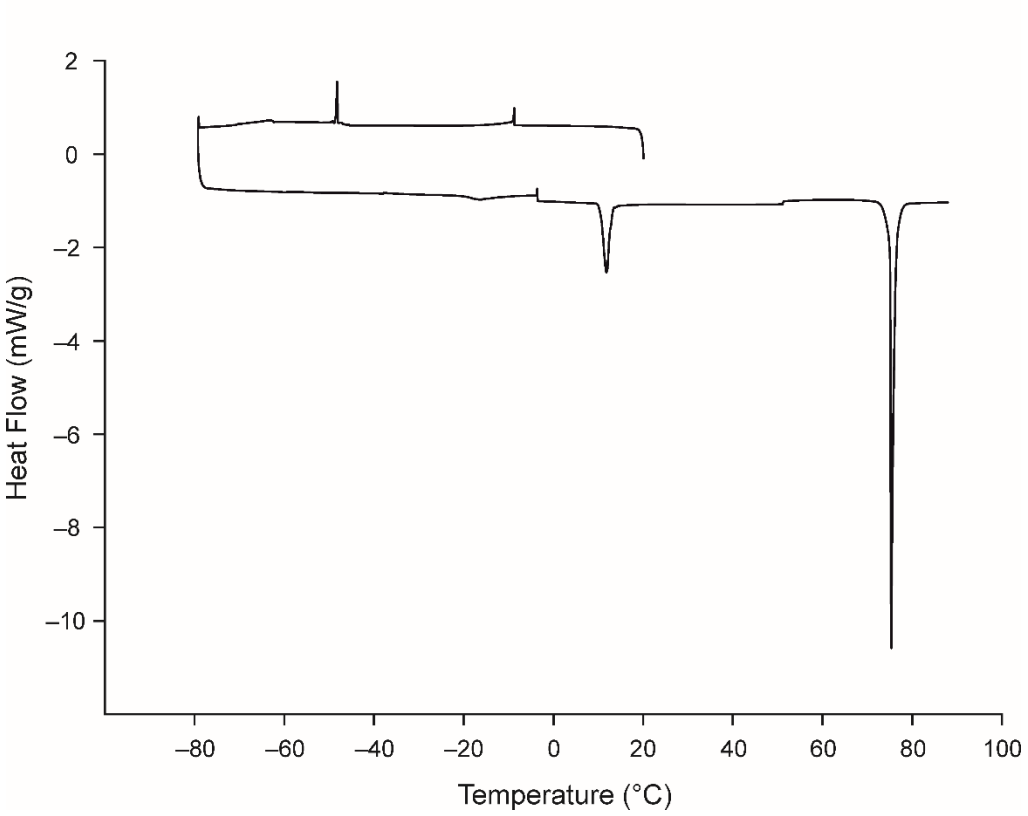

Figure B.10: *DSC theromgram of 1-IA using 5 °C/min. Exothermic up.*

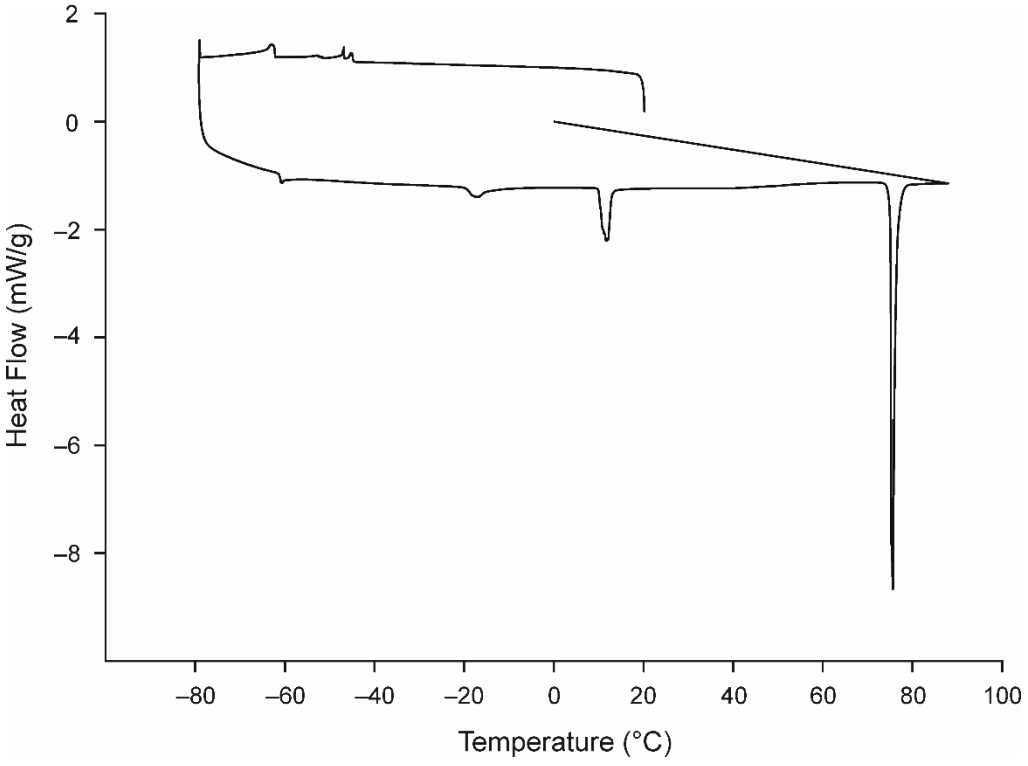

Figure B.11: *DSC theromgram of 1-IA using 5 °C/min. Exothermic up.*

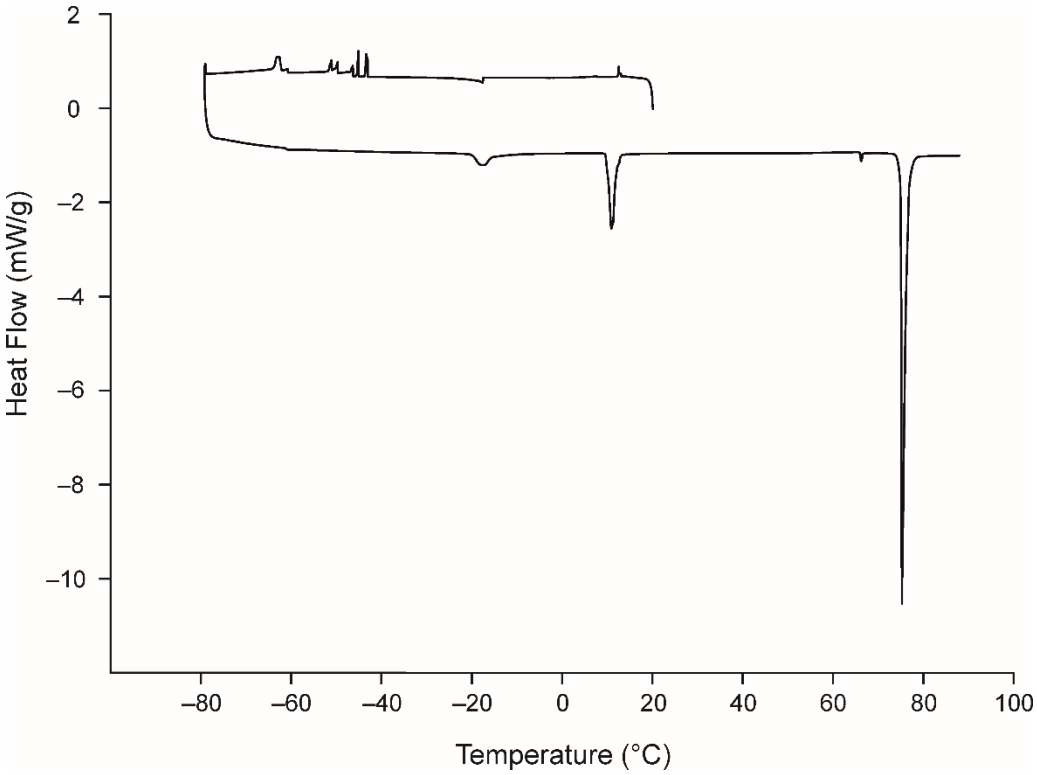

Figure B.12: *DSC theromgram of 1-IA using 5 °C/min. Exothermic up.*

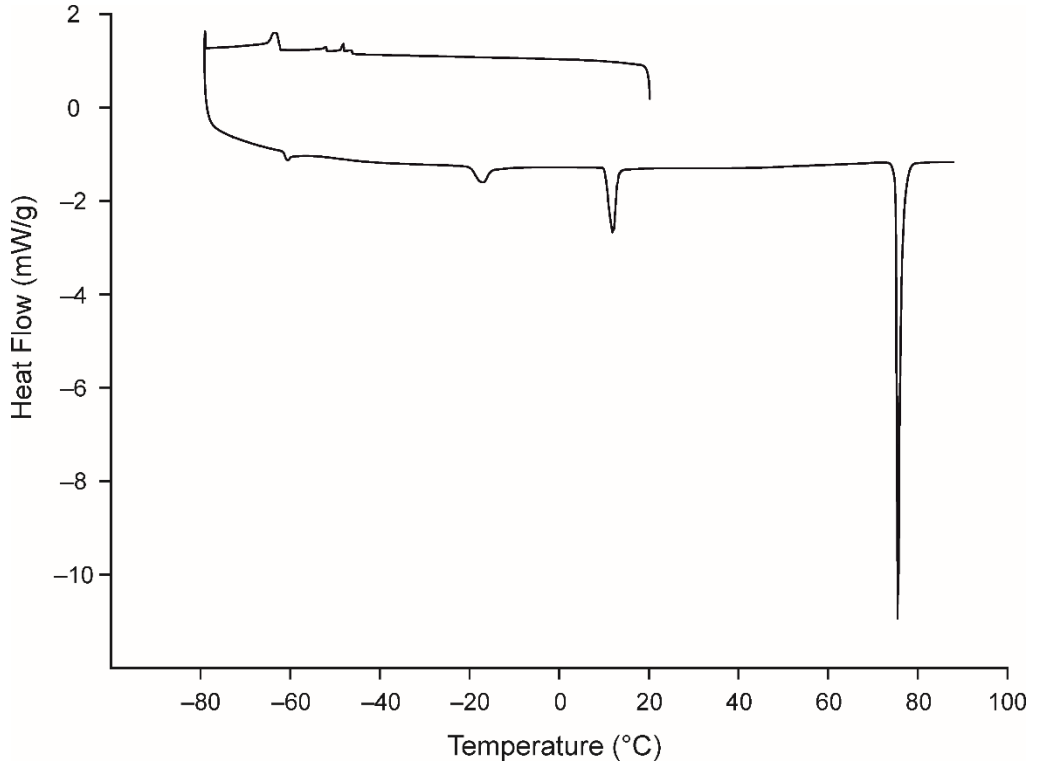

Figure B.13: *DSC theromgram of 1-IA using 5 °C/min. Exothermic up.*

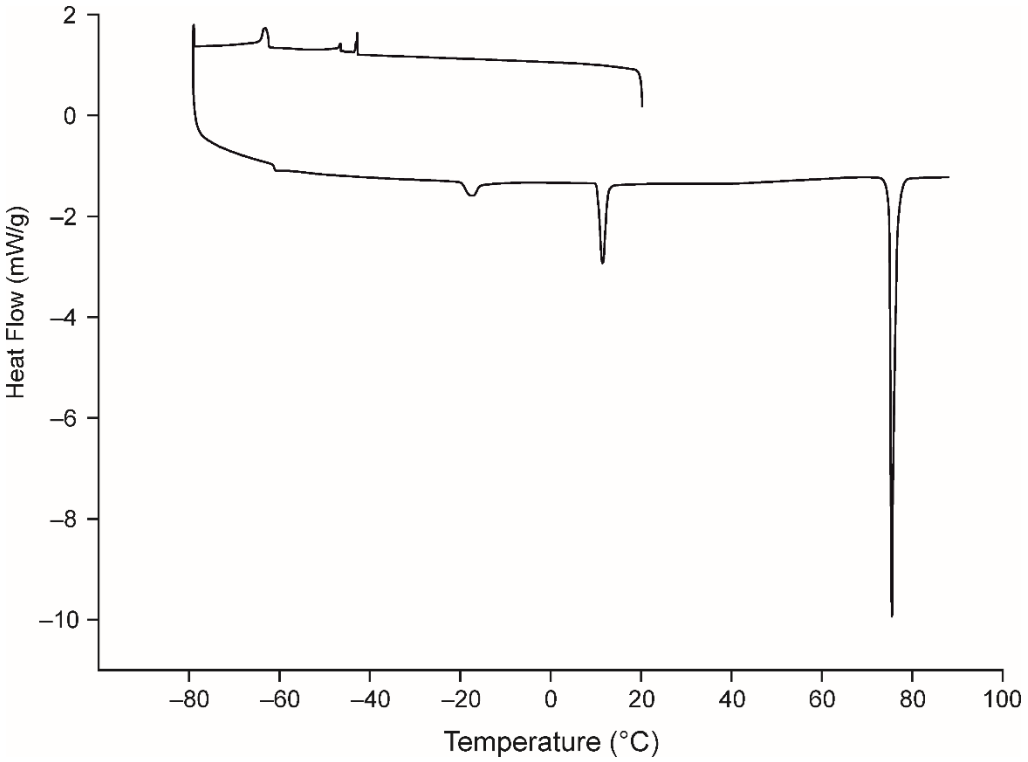

Figure B.14: *DSC theromgram of 1-IA using 5 °C/min. Exothermic up.*

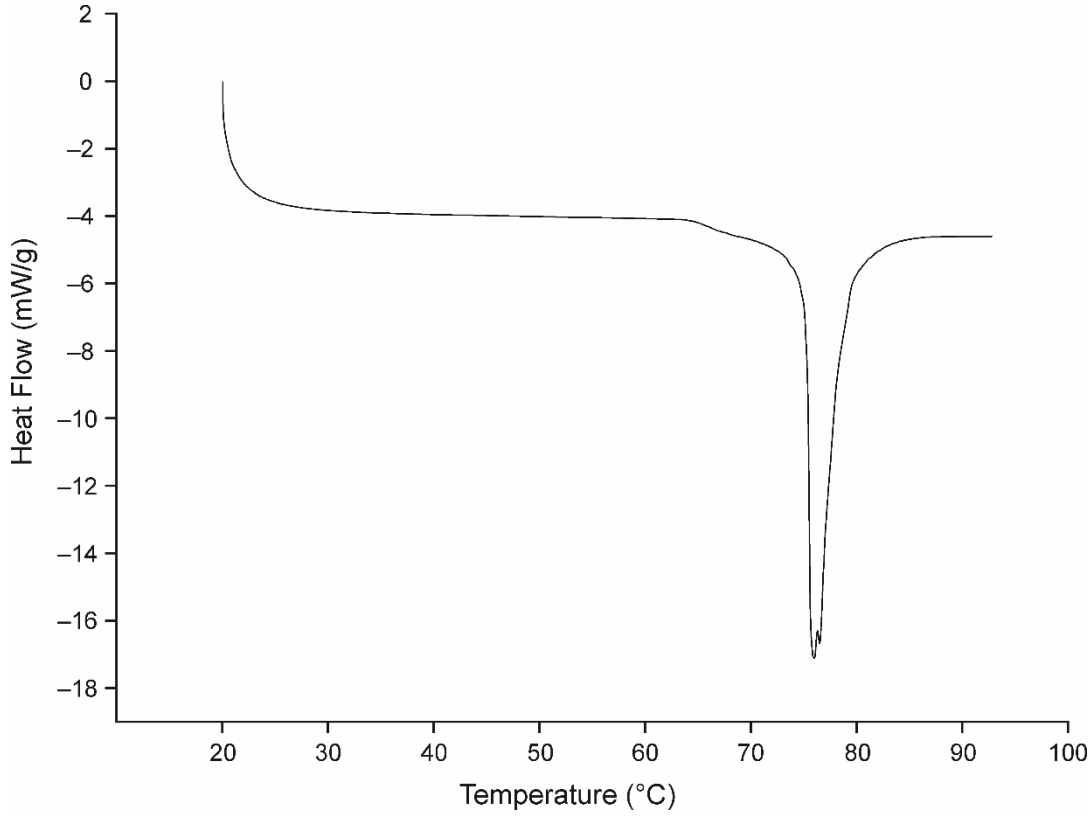

Figure B.15: *DSC theromgram of 1-IA using 20 °C/min. Exothermic up.*

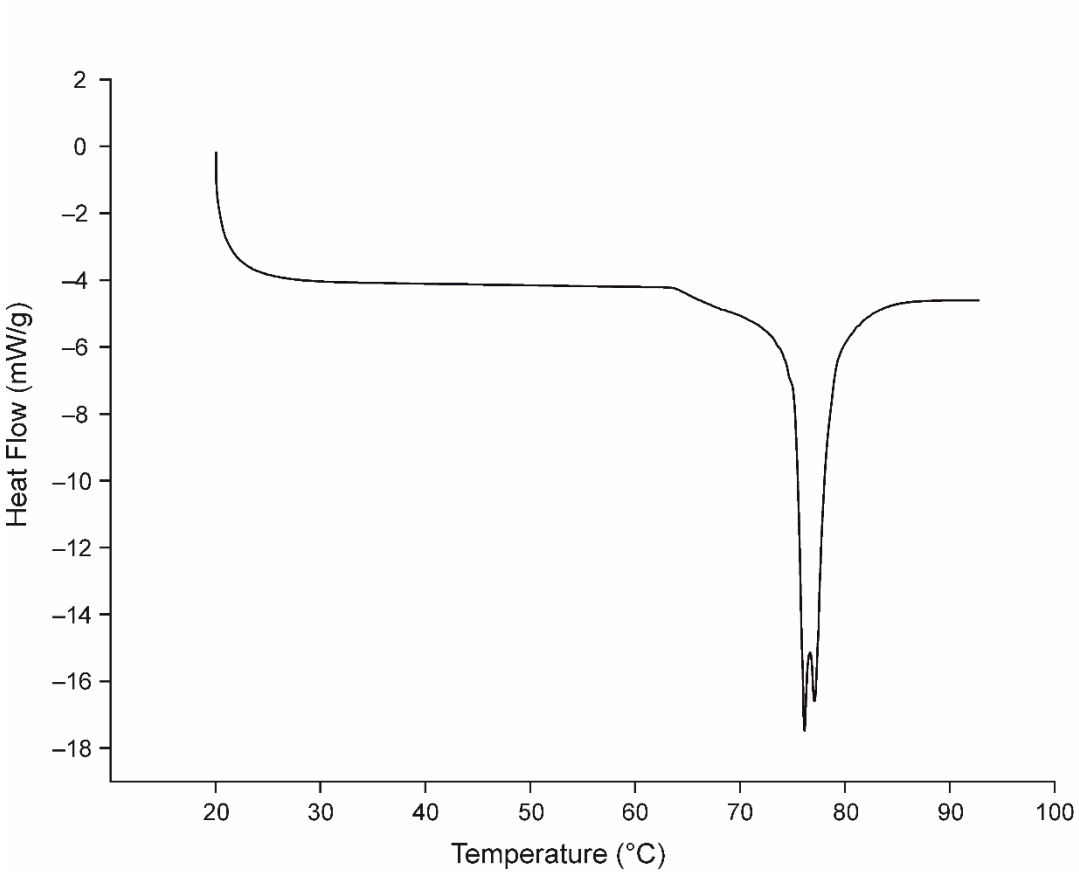

Figure B.16: *DSC theromgram of 1-IA using 20 °C/min. Exothermic up.*

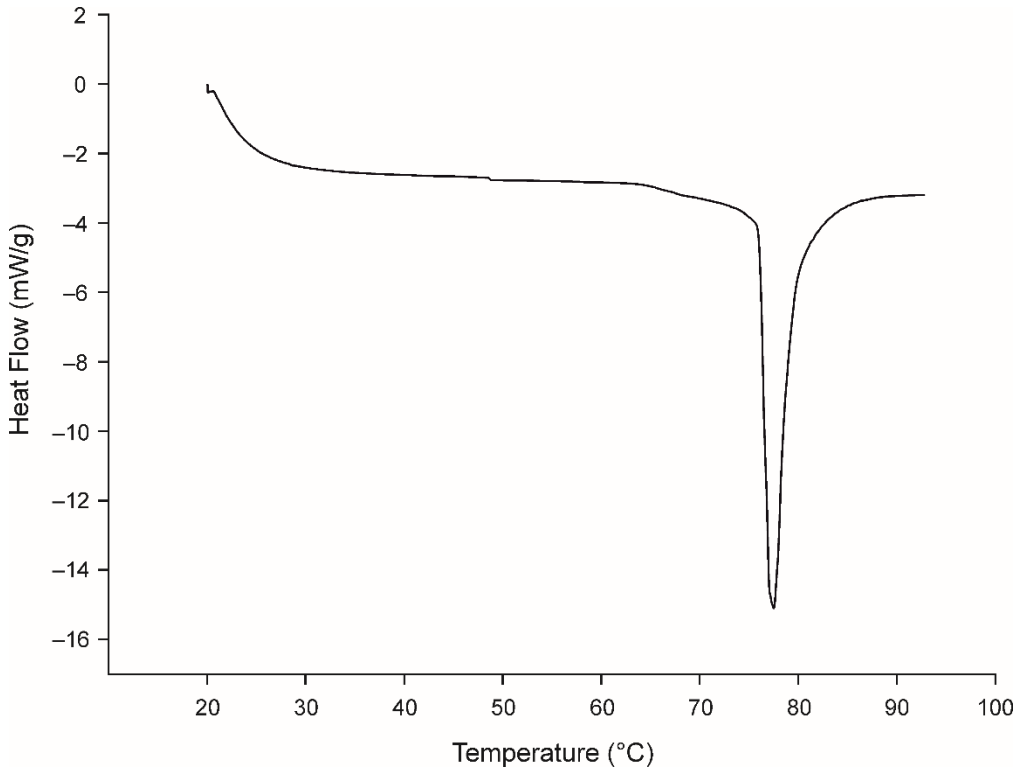

Figure B.17: *DSC theromgram of 1-IA using 20 °C/min. Exothermic up.*

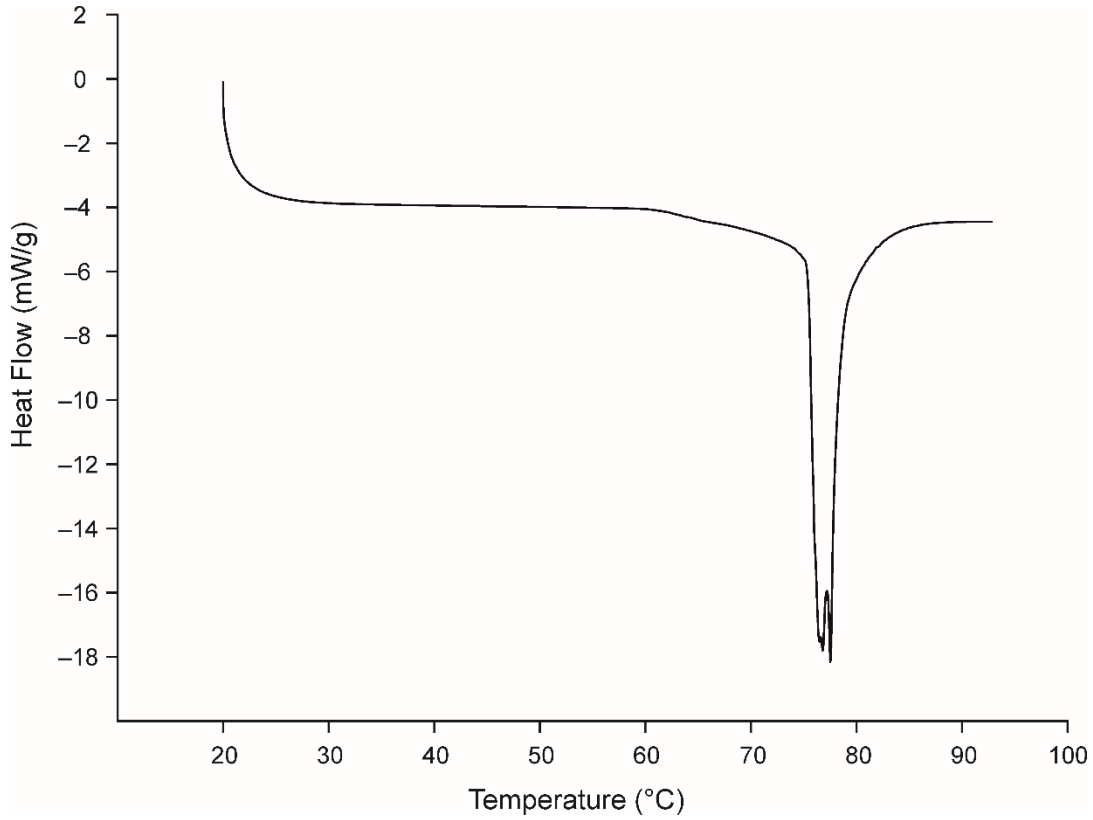

Figure B.18: *DSC theromgram of 1-IA using 20 °C/min. Exothermic up.*

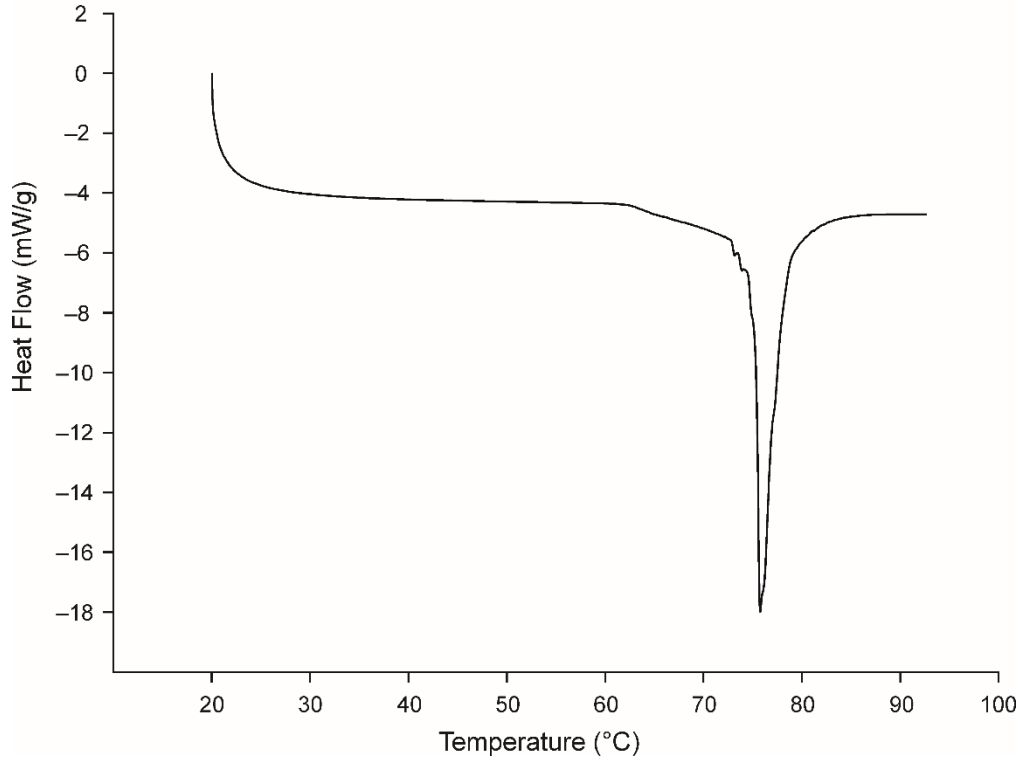

Figure B.19: *DSC theromgram of 1-IA using 20 °C/min. Exothermic up.*

Appendix C: Table of Bond Distances for Different Phases Reported in this Thesis

Atom #1	Atom #2	Length (Å)
C29	H32	1.057
C29	C33	1.574
C29	H30	1.054
C29	H31	1.058
O27	C28	1.231
C28	C33	1.55
C33	C35	1.526
C33	H34	1.096
C43	H44	1.082
O26	C28	1.248
C35	C43	1.403
C35	C36	1.375
C41	C43	1.411
C41	H42	1.082
O1	C3	1.214
C36	H37	1.083
C36	C38	1.416
C40	C45	1.46
C40	C41	1.359
C3	C8	1.527
C38	C40	1.315
C38	H39	1.082
O2	C3	1.215
N22	H25	1.024
N22	H23	1.032
N22	H24	1.031
C45	H46	1.094
C45	H47	1.094
C45	C48	1.508
C49	H50	1.063
C49	H51	1.051
C49	H52	1.061
C8	H9	1.102
C8	C10	1.495
C13	H14	1.096
C13	C16	1.518

Table C.1: *Bond distances for* ***IL-AH*** *phase (continues in the next page).*

C13	H15	1.092
C19	N22	1.485
C19	H20	1.091
C19	H21	1.092
C48	C54	1.563
C48	C49	1.6
C48	H53	1.103
C10	H12	1.094
C10	H11	1.094
C10	C13	1.587
N4	H5	1.03
N4	H7	1.034
N4	C8	1.47
N4	H6	1.027
C16	H18	1.095
C16	C19	1.461
C16	H17	1.092
C54	H56	1.061
C54	H57	1.061
C54	H55	1.061

***Table C.1:** (cont.)*

Atom #1	Atom #2	Length (Å)
O9	C26	1.257
C26	C28	1.531
O8	C26	1.24
C28	C29	1.514
C28	H53	1.102
C30	H54	1.088
C30	C31	1.402
C29	C30	1.408
C29	C34	1.412
C31	C32	1.42
C31	H55	1.096
C27	H51	1.097
C27	H52	1.118
C27	H50	1.103
C27	C28	1.537
C34	H57	1.085
C32	C33	1.415
C32	C35	1.522
C33	H56	1.087
C33	C34	1.413
C35	C36	1.539
C35	H58	1.106
C35	H59	1.101
C36	H63	1.108
C36	C37	1.523
C36	C38	1.525
C38	H65	1.099
C38	H64	1.097
C38	H66	1.103
C37	H62	1.1
C37	H60	1.127
C37	H61	1.103
O10	H68	0.987
O10	H67	1.017
C22	H40	1.097
C22	C23	1.526
C22	H39	1.103
C23	H41	1.103
C23	C24	1.53
C23	H42	1.1

Table C.2: *Bond distances for* ***IL-MH*** *phase (continues in the next page).*

C25	H45	1.098
C25	H46	1.1
C25	N4	1.489
C24	H44	1.098
C24	H43	1.098
C24	C25	1.513
N4	H48	1.042
N4	H49	1.058
N4	H47	1.025
C21	H38	1.106
C21	C22	1.521
N3	H37	1.034
N3	H36	1.048
N3	H35	1.051
N3	C21	1.484
O6	C20	1.278
C20	C21	1.542
O2	C1	1.254
O7	C20	1.265
C1	C2	1.535
O1	C1	1.266
N1	C2	1.491
N1	H1	1.058
N1	H2	1.066
N1	H3	1.077
C2	H4	1.094
C2	C3	1.527
N2	H14	1.03
N2	H13	1.072
N2	H15	1.074
C6	H11	1.099
C6	N2	1.494
C6	H12	1.101
C5	H9	1.105
C5	H10	1.097
C5	C6	1.503
C3	C4	1.529
C3	H5	1.104
C3	H6	1.096
C4	H7	1.102
C4	H8	1.101

Table C.2: (cont.)

C4	C5	1.52
O5	H34	0.994
O5	H33	1.006
C18	H26	1.086
C18	H27	1.076
C18	H28	1.093
C19	H32	1.096
C19	H31	1.102
C19	H30	1.106
C17	C19	1.526
C17	C18	1.528
C17	H29	1.107
C16	H25	1.105
C16	H24	1.104
C16	C17	1.544
C14	C15	1.407
C14	H22	1.091
C13	C16	1.517
C13	C14	1.417
C15	H23	1.096
C8	H18	1.134
C8	H17	1.096
C8	C9	1.535
C8	H16	1.082
C12	H21	1.094
C12	C13	1.421
C10	C11	1.418
C10	C15	1.41
C11	C12	1.411
C11	H20	1.09
C9	H19	1.098
C9	C10	1.527
C7	C9	1.549
O3	C7	1.263
O4	C7	1.243

Table C.2: (cont.)

Atom #1	Atom #2	Length (Å)
C15	O16	1.252
C15	O17	1.244
O68	C71	1.221
C32	O33	1.233
C32	O34	1.238
O35	C38	1.252
C10	C13	1.519
C10	H12	1.093
C10	H11	1.093
C71	C76	1.532
C13	C15	1.514
C13	H14	1.091
C76	H77	1.09
C76	C78	1.528
C27	H29	1.093
C27	C30	1.532
C27	H28	1.087
C79	C81	1.369
C79	H80	1.074
C30	H31	1.092
C30	C32	1.526
C38	C43	1.53
C72	H74	1.051
C72	H73	1.054
C72	C76	1.526
C72	H75	1.055
C43	C45	1.528
C43	H44	1.093
C24	H25	1.094
C24	C27	1.501
C24	H26	1.09
C78	C86	1.409
C78	C79	1.388
C81	H82	1.073
C81	C83	1.389
O69	H70	0.97
O69	C71	1.238
C7	H9	1.095
C7	H8	1.098
C7	C10	1.51

Table C.3: *Bond distances for* ***AH*** *phase (table continues in the next page)*

C53	H54	1.072
N1	C13	1.478
N1	H3	1.033
N1	C4	1.478
N1	H2	1.028
C39	H41	1.088
C39	H40	1.094
C39	H42	1.071
C39	C43	1.519
O36	H37	0.97
O36	C38	1.252
N18	C30	1.486
N18	H20	1.03
N18	H19	1.031
N18	C21	1.491
C45	C46	1.378
C45	C53	1.389
C4	H6	1.098
C4	C7	1.485
C4	H5	1.094
C51	C53	1.377
C51	H52	1.073
C97	H98	1.051
C97	H100	1.051
C97	H99	1.06
C21	H22	1.093
C21	H23	1.093
C21	C24	1.492
C86	H87	1.074
C83	C88	1.513
C83	C84	1.395
C64	H65	1.055
C64	H67	1.06
C64	H66	1.062
C84	C86	1.39
C84	H85	1.074
C46	H47	1.073
C46	C48	1.392
C88	H90	1.09
C88	H89	1.085
C88	C91	1.509

Table C.3: (cont.)

C50	C51	1.396
C50	C55	1.516
C91	C97	1.514
C91	H96	1.094
C91	C92	1.52
C48	H49	1.077
C48	C50	1.386
C58	C59	1.516
C58	C64	1.502
C58	H63	1.092
C55	H57	1.088
C55	H56	1.087
C55	C58	1.497
C92	H94	1.055
C92	H95	1.058
C92	H93	1.057
C59	H62	1.059
C59	H60	1.062
C59	H61	1.054

Table C.3: (cont.)

Atom #1	Atom #2	Length (Å)
C9	O3	1.243
C9	O4	1.293
C6	H12	1.099
C6	C9	1.569
C6	C8	1.531
C8	H16	1.1
C8	H15	1.093
C8	C10	1.531
O5	H25	1.037
C10	H17	1.098
C10	H18	1.095
O7	H42	1.046
H37	C24	1.1
N2	C6	1.518
N2	C7	1.52
N2	H11	1.047
C7	C10	1.529
C7	H13	1.101
C7	H14	1.091
C14	O6	1.228
C14	O5	1.329
C25	H40	1.099
C25	C26	1.529
C25	C27	1.521
C12	C14	1.532
C12	H22	1.102
C12	C13	1.524
C24	H39	1.095
C24	H38	1.096
C24	C25	1.531
C15	C17	1.399
C15	H23	1.092
C26	O7	1.314
C26	O8	1.241
C28	H41	1.091
C28	C30	1.39
H19	C11	1.097
H10	N2	1.052
C13	C15	1.402

Table C.4: *Bond distances for* ***QH*** *phase (table continues in the next page).*

C13	C16	1.405
C27	C29	1.394
C27	C28	1.406
C11	H21	1.093
C11	H20	1.097
C11	C12	1.535
C17	C19	1.407
C17	H26	1.093
C30	H44	1.094
C30	C32	1.404
C23	H36	1.096
C23	H35	1.106
C23	H34	1.101
C16	C18	1.4
C16	H24	1.093
C29	C31	1.393
C29	H43	1.093
C19	C20	1.513
C21	C22	1.53
C21	C23	1.527
C21	H30	1.106
C32	C33	1.51
H55	O9	0.987
C18	C19	1.398
C18	H27	1.09
C36	H52	1.099
C36	H53	1.102
C36	H54	1.103
C34	C36	1.524
C34	C35	1.525
C34	H48	1.102
C31	C32	1.399
C31	H45	1.092
C20	H29	1.105
C20	H28	1.102
C20	C21	1.538
C22	H33	1.105
C22	H31	1.099
C22	H32	1.108
C33	H47	1.104
C33	H46	1.102

Table C.4: (cont.)

C33	C34	1.537
C35	H51	1.103
C35	H50	1.101
C35	H49	1.102
H1	N1	1.062
C2	H4	1.095
C2	H5	1.097
C2	C5	1.523
N1	C1	1.505
N1	H2	1.044
N1	C2	1.506
C5	H9	1.097
C5	H8	1.099
C1	C4	1.539
C1	C3	1.539
C1	H3	1.097
C4	H7	1.1
C4	C5	1.531
C4	H6	1.098
C3	O1	1.284
C3	O2	1.247

Table C.4: (cont.)

Atom #1	Atom #2	Length (Å)
N1	H4	1.073
N1	H5	1.04
N1	H6	1.043
C7	H8	1.09
C7	C8	1.391
C8	C9	1.412
C8	H9	1.089
C2	H2	1.103
C2	C3	1.542
C2	H1	1.101
C6	C7	1.408
C6	C11	1.429
C3	C4	1.537
C3	N1	1.495
C3	H3	1.098
C9	H10	1.09
C9	C10	1.392
C1	C5	1.381
C1	C6	1.439
C1	C2	1.497
C4	O1	1.267
C4	O2	1.263
C11	N2	1.37
C10	H11	1.089
C10	C11	1.397
C5	H7	1.083
C5	N2	1.375
N4	H24	1.02
N2	H12	1.019
C16	N4	1.382
C16	H19	1.087
C21	C22	1.399
C21	H23	1.09
C22	N4	1.372
N3	H17	1.043
N3	H16	1.049
N3	H18	1.052
C20	H22	1.088
C20	C21	1.392

Table C.5: *Bond distances for* ***β-L-Trp*** *phase at ambient temperature (table continues in the next page).*

C12	C16	1.38
C12	C13	1.493
C12	C17	1.432
C17	C18	1.404
C17	C22	1.422
C14	C15	1.526
C14	H15	1.097
C14	N3	1.491
C19	H21	1.09
C19	C20	1.41
C13	H14	1.102
C13	H13	1.102
C13	C14	1.526
C18	H20	1.091
C18	C19	1.387
C15	O4	1.255
C15	O3	1.279

Table C.5: (cont.)

Atom #1	Atom #2	Length (Å)
N1	H4	1.073
N1	H5	1.045
N1	H6	1.038
C7	H8	1.09
C7	C8	1.392
C8	C9	1.413
C8	H9	1.089
C2	H2	1.103
C2	C3	1.542
C2	H1	1.101
C3	H3	1.098
C3	C4	1.537
C3	N1	1.495
C6	C7	1.408
C6	C11	1.429
C1	C6	1.438
C1	C5	1.382
C1	C2	1.496
C9	C10	1.392
C9	H10	1.089
C4	O1	1.266
C4	O2	1.264
C11	N2	1.37
C10	H11	1.09
C10	C11	1.398
C5	H7	1.083
C5	N2	1.375
N4	H24	1.02
N2	H12	1.019
C16	N4	1.382
C16	H19	1.087
C21	C22	1.4
C21	H23	1.09
N3	H16	1.048
N3	H17	1.044
N3	H18	1.051
C22	N4	1.373
C20	H22	1.088
C20	C21	1.393
C12	C16	1.382

Table C.6: *Bond distances for* ***β-L-Trp*** *phase at 123K (table continues in the next page).*

C12	C13	1.494
C12	C17	1.434
C17	C18	1.404
C17	C22	1.425
C14	C15	1.529
C14	H15	1.097
C14	N3	1.493
C13	H13	1.101
C13	H14	1.102
C13	C14	1.524
C19	C20	1.411
C19	H21	1.089
C15	O3	1.277
C15	O4	1.257
C18	H20	1.09
C18	C19	1.392

Table C.6: (cont.)

Atom #1	Atom #2	Length (Å)
C4	H4A	0.97
C4	H4B	0.97
C4	C5	1.504
C7	H7A	0.97
C7	H7B	0.97
C3	C4	1.508
C3	C4	1.508
C3	H3	0.98
C5	C7	1.497
C5	H5	0.98
C2	C3	1.557
C2	H2B	0.97
C2	H2A	0.97
C6	C5	1.566
C6	H6B	0.97
C6	H6A	0.97
C1	I1	2.199
C1	C2	1.528
C1	C6	1.525
C1	C6	1.525

Table C.7: *Bond distances of* ***1-IA*** *(phase A).*

Atom #1	Atom #2	Length (Å)
C9	H9b	0.99
C9	H9a	0.99
C4	H4a	0.99
C4	H4b	0.99
C4	C5	1.541
C10	H10b	0.99
C10	H10a	0.99
C8	C10	1.539
C8	C9	1.588
C8	H8	1.00
C5	H5	1.00
C5	C6	1.543
C5	C9	1.449
C3	C4	1.532
C3	H3	1.00
C3	C10	1.488
C6	H6b	0.99
C6	H6a	0.99
C7	H7b	0.99
C7	H7a	0.99
C7	C8	1.555
C2	H2b	0.99
C2	H2a	0.99
C2	C3	1.563
C1	I1	2.23
C1	C7	1.473
C1	C6	1.585
C1	C2	1.485
C1	C6	1.585
C1	C7	1.473
C1	I1	2.23
C1	C2	1.485
C2	H2b	0.99
C2	C3	1.563
C2	H2a	0.99
C7	C8	1.555
C7	H7b	0.99
C7	H7a	0.99
C6	H6a	0.99
C6	H6b	0.99

Table C.8: *Bond distances for* ***1-IA*** *(phase B). Table continues in the next page.*

C3	C4	1.532
C3	H3	1.00
C3	C10	1.488
C5	H5	1
C5	C6	1.543
C5	C9	1.449
C8	C9	1.588
C8	H8	1
C8	C10	1.539
C10	H10b	0.99
C10	H10a	0.99
C4	H4a	0.99
C4	H4b	0.99
C4	C5	1.541
C9	H9b	0.99
C9	H9a	0.99

Table C.8: (cont.)

Atom #1	Atom #2	Length
C7	H7B	0.979
C7	H7A	0.98
C7	C8	1.546
C1	I1	2.189
C1	C7	1.538
C1	C2	1.53
C1	C6	1.513
C2	C3	1.53
C2	H2A	0.982
C2	H2B	0.979
C8	H8	0.988
C9	C8	1.539
C9	H9B	0.981
C9	H9A	0.981
C6	C5	1.542
C6	H6B	0.98
C6	H6A	0.98
C3	C9	1.535
C3	C4	1.533
C3	H3	0.99
C10	C8	1.536
C10	H10A	0.979
C10	H10B	0.983
C5	H5	0.99
C5	C10	1.539
C4	H4B	0.981
C4	C5	1.54
C4	H4A	0.98

Table C.9: *Bond distances for* ***1-IA*** *(phase C).*

Appendix D: Publications

O. Al Rahal, C. E. Hughes, P. A. Williams, A. J. Logsdail, Y. Diskin-Posner, K. D. M. Harris., Polymorphism of L-Tryptophan., *Angew.Chem.Int.Ed.*, **2019**, 58, 18788-18792